THE UNIVERSITY OF QUEENSLAND

AUSTRALIA

Effects of flow non-uniformities on the drag reduction by boundary layer combustion

Chan Yong Khang, Wilson
DipEng (Mech), BEng (Hons)

A thesis submitted for the degree of Doctor of Philosophy at

The University of Queensland in August 2012

School of Mechanical and Mining Engineering,
Centre for Hypersonics

Abstract

The proportion of the overall drag force on a flight vehicle that can be attributed to skin friction drag is much higher on hypersonic vehicles than for vehicles operating at lower speeds. Consequently, controlling skin friction drag is a major obstacle to the successful development of an operational scramjet-powered flight vehicle. To date, many techniques have been proposed for the reduction of skin friction. Of the many methods available, the combustion of hydrogen in supersonic turbulent boundary layers has been experimentally, numerically and theoretically shown to be a promising method of reducing skin friction drag in hypervelocity applications. However, one key issue that can affect the implementation of the boundary layer combustion technique in a realistic scramjet is the presence of highly non-uniform flow entering the combustion chamber from the inlet. The aim of this project is to investigate if and how flow non-uniformities entering a scramjet combustor can affect the potential for boundary layer combustion to reduce skin friction. To achieve this aim, the project is approached experimentally and numerically.

Experiments were conducted on a circular constant-area combustor that was attached downstream of a Rectangular-to-Elliptical Shape Transition (REST) inlet and an injector designed to deliver hydrogen into the boundary layer. Using a stress wave force balance, the integrated skin friction drag on the internal surface of the combustor was measured for three scenarios - one, where fuel is not injected, two, where fuel is injected but combustion is suppressed, and three, where fuel is injected and allowed to burn. The REST inlet was used to produce flow disturbances that are typical of those to be expected in operational scramjet inlets. When the experimental model was tested at on- and off-design conditions, the experimentally measured drag coefficients for the fuel-on tests were 28% - 30% lower than those for the fuel-off tests. The levels of skin friction reduction that are measured in the current experiments are similar to those measured in experiments conducted without a realistic scramjet inlet upstream of the combustor, thus demonstrating that the drag reduction brought about by boundary layer combustion is not significantly affected by the flow disturbances generated from the REST inlet.

In addition, the experimental model was also tested with vortex generators attached in the inlet. These vortex generators were used to generate flow disturbances similar to those brought about by conventional cross-stream fuel injection techniques.

The experimental results show that the level of skin friction reduction is similar to that measured in the tests without the vortex generators, thus demonstrating that flow disturbances similar to those from cross-stream fuel injection in the inlet do not affect the drag reduction potential of boundary layer combustion. These experiments also demonstrate that the levels of drag reduction brought about by film-cooling effects are more easily affected by flow disturbances than those brought about by boundary layer combustion.

To support the analysis of the experiments, non-reacting RANS CFD simulations of the internal flowfield in the experimental model were conducted using an in-house code called Eilmer3. To facilitate the simulations of the types of flows relevant to this study, the latest version of Wilcox's k-ω turbulence model was implemented in Eilmer3. However, because this version of Wilcox's k-ω model has yet to be thoroughly validated for hypersonic applications, a series of simulations had to be conducted to validate it against test cases that have flowfields representative of those to be expected in this project. A generally good agreement between the numerical and experimental results is obtained for all the six cases that were tested.

Simulations of the internal flowfield in the experimental model were conducted with varying levels of inflow disturbances to assess the levels of flow disturbances that may be required to sweep the fuel layer out from the boundary layer. The numerical results demonstrate that, even in the presence of strong flow disturbances, most of the injected fuel remains in the region of the flowfield that will induce a reduction in skin friction if the fuel burns. Additional simulations also demonstrate that for the drag reduction potential of the boundary layer combustion technique to be realised, heat addition must be occur in regions of the boundary layer where there are large near-wall values of Reynolds shear stress.

Declaration by Author

This thesis is composed of my original work, and contains no material previously published or written by another person except where due reference has been made in the text. I have clearly stated the contribution by others to jointly-authored works that I have included in my thesis.

I have clearly stated the contribution of others to my thesis as a whole, including statistical assistance, survey design, data analysis, significant technical procedures, professional editorial advice, and any other original research work used or reported in my thesis. The content of my thesis is the result of work I have carried out since the commencement of my research higher degree candidature and does not include a substantial part of work that has been submitted to qualify for the award of any other degree or diploma in any university or other tertiary institution. I have clearly stated which parts of my thesis, if any, have been submitted to qualify for another award.

I acknowledge that an electronic copy of my thesis must be lodged with the University Library and, subject to the General Award Rules of The University of Queensland, immediately made available for research and study in accordance with the *Copyright Act 1968*.

I acknowledge that copyright of all material contained in my thesis resides with the copyright holder(s) of that material.

Chan Yong Khang, Wilson

Publications during candidature

Chan, W.Y.K.; Jacobs, P.A.; Nap, J.P.; Mee, D.J. and Kirchhartz, R.M. (2010).
"The k-ω turbulence model in Eilmer3: User guide and test cases". In *The University of Queensland, School of Mechanical & Mining Engineering Research Report Number 2010/01*. – Chan was responsible for 60% of the analysis, 60% of the interpretation of the data and 70% of drafting and writing. Jacobs was responsible for 15% of the analysis, 20% of the interpretation of the data and 15% of drafting and writing. Nap was responsible for 10% of the analysis. Mee was responsible for 10% of the analysis, 15% of the interpretation of the data and 15% of drafting and writing. Kirchhartz was responsible for 5% of the analysis and 5% of the interpretation of the data.

Chan, W.Y.K.; Mee, D.J.; Smart, M.K.; Turner, J.C and Stalker, R.J. (2010).
"Boundary layer combustion for viscous drag reduction in practical scramjet configurations". In *27th Congress of The International Council for the Aeronautical Sciences, Nice, France*. – Chan was responsible for 60% of the analysis, 60% of the interpretation of the data and 75% of drafting and writing. Mee was responsible for 20% of the analysis, 20% of the interpretation of the data and 25% of drafting and writing. Smart was responsible for 10% of the analysis. Turner was responsible for 10% of the analysis and 10% of the interpretation of the data. Stalker was responsible for 10% of the interpretation of the data.

Chan, W.Y.K.; Jacobs, P.A. and Mee, D.J. (2011).
"Suitability of the k-ω turbulence model for scramjet flowfield simulations". In *International Journal for Numerical Methods in Fluids*. – Chan was responsible for 80% of the analysis, 60% of the interpretation of the data and 70% of drafting and writing. Jacobs was responsible for 10% of the analysis, 20% of the interpretation of the data and 15% of drafting and writing. Mee was responsible for 10% of the analysis, 20% of the interpretation of the data and 15% of drafting and writing.

Chan, W.Y.K.; Mee, D.J.; Smart, M.K. and Turner, J.C (2012).
"Effects of flow disturbances from cross-stream fuel injection on the drag reduction by boundary layer combustion". In *18th AIAA/3AF International Space Planes and Hypersonic Systems and Technologies Conference, Tours , France*. – Chan was responsible for 60% of the analysis, 70% of the interpretation of the data and 75% of drafting and writing. Mee was responsible for 20% of the analysis, 20% of the

interpretation of the data and 25% of drafting and writing. Smart was responsible for 10% of the analysis. Turner was responsible for 10% of the analysis and 10% of the interpretation of the data.

Publications included in this thesis

Chan, W.Y.K.; Jacobs, P.A.; Nap, J.P.; Mee, D.J. and Kirchhartz, R.M. (2010).
"The k-ω turbulence model in Eilmer3: User guide and test cases". In *The University of Queensland, School of Mechanical & Mining Engineering Research Report Number 2010/01*. – Parts of the report are included in Chapter 4.

Chan, W.Y.K.; Mee, D.J.; Smart, M.K.; Turner, J.C. and Stalker, R.J. (2010).
"Boundary layer combustion for viscous drag reduction in practical scramjet configurations". In *27th Congress of The International Council for the Aeronautical Sciences, Nice, France*. – Parts of the paper are included in Chapters 3 and 5.

Chan, W.Y.K.; Jacobs, P.A. and Mee, D.J. (2011).
"Suitability of the k-ω turbulence model for scramjet flowfield simulations". In *International Journal for Numerical Methods in Fluids*. – Incorporated in Chapter 4.

Chan, W.Y.K.; Mee, D.J.; Smart, M.K. and Turner, J.C. (2011).
"Effects of flow disturbances from cross-stream fuel injection on the drag reduction by boundary layer combustion". In *18th AIAA/3AF International Space Planes and Hypersonic Systems and Technologies Conference, Tours , France*. – Parts of the paper are included in Chapters 3 and 5.

Contributions by others to the thesis

No contributions by others.

Statement of parts of the thesis submitted to qualify for the award of another degree

None.

Acknowledgements

My most utmost and sincere gratitude goes to my PhD supervisor, Professor David Mee. Thanks for sharing your enthusiasm and passion for research and your knowledge and experience in this field, for offering advice that more than often is correct, for your encouragement and guidance throughout my five-year candidature, for supporting me financially when my scholarship ran out, and for being such an awesome teacher.

To my associate supervisor Professor Michael Smart, thanks for sharing your expertise on REST inlets, for offering advice on the many topics in the hypersonics field, and for being supportive of the work that has been conducted in this project.

To Dr Peter Jacobs, thanks for sharing your expertise on your code Eilmer3 and also on the various aspects of CFD and my project. Thanks too for the many enriching chats during the afternoon-coffee sessions and Friday-drinks sessions. To Professor Ray Stalker, thanks for sharing your expertise on free-piston shock tunnels and the boundary layer combustion technique.

To the T4 technicians Keith Hitchcock and Grant Tayles for manufacturing the test model and for all the technical advice. To the T4 operators, Dylan, Luke, Drew, thanks for putting your blood, sweat and tears to make my T4 campaign a successful one.

To Rainer "*Größe Mann*", James, Mel, thanks for being such awesome mentors to me during my stay at the Centre for Hypersonics and for sharing your advice on not only technical topics, but also on the many aspects of life.

To my other really close buddies at UQ, Tom "*Tonight's gonna be a good night*" Manfred, Fabs, Jenny, Drew, "*postal*" Sarah, Katsu, Luke "*Skywalker*", David G., Arianna, Oana, Dave Petty, "*fifi*" Philippe, Dylan, Carolyn, thanks for the many enjoyable chats and laughs during my stay at UQ.

Many thanks also go out to the NCI National Facility at the ANU, the Pawsey-funded iVEC Infrastructure at Murdoch University, the HPC Facility at UQ and the UQ Centre for Hypersonics Blackhole cluster admin team for granting the computational resources for the CFD work in this project. Thanks also to all the IT experts, Steve Kimball, David Gwynne, Rik Taylor and David Green, for making IT matters a breeze to deal with.

Finally to my loving family members, Dad, Mom, Dad-in-law, Mom-in-law, Brother, Rhonda, Wei Yen, thanks for being supportive to me in so many ways for the past 30 years of my life. I would not be where I am now without all of you.

Keywords

scramjet, hypersonics, airbreathing propulsion, boundary layer combustion, skin friction, drag reduction, supersonic combustion, flow non-uniformities, k-ω turbulence model, CFD validation

Australian and New Zealand Standard Research Classifications (ANZSRC)

090107 Hypersonic Propulsion and Hypersonic Aerodynamics, 100%

Fields of Research (FoR) Classification

0901 Aerospace Engineering, 100%

This thesis is dedicated to the memory of Wei Ling (1982 - 2007). Thank you for all the precious memories of the ten years that we have shared together. And thanks for being such a wonderful friend and an awesome buddy who was always there when I needed you. Most importantly, thanks for being such a loving and caring wife. I am forever grateful to have spent a part of my life with you.

Contents

List of Figures **xv**

List of Tables **xxi**

Nomenclature **xxiii**

1 Introduction **1**

1.1 Scramjets & skin friction drag 1

1.2 Aims 4

1.3 Outline of thesis 5

2 Literature Review **7**

2.1 Boundary layer combustion 7

2.2 Flow disturbances & their effects on boundary layer combustion 20

3 Details of Experiments **25**

3.1 Experimental model 25

3.1.1 REST inlet 26

3.1.2 Fuel injector & supply system 28

3.1.3 Vortex generators 28

3.1.4 Combustor 30

3.1.5 Stress wave force balance 32

3.2 Test facility 35
3.3 Test conditions 39
3.3.1 Test conditions 39
3.3.2 Fuel injection conditions 41
3.4 Data reduction 44
3.4.1 Pressure measurements 44
3.4.2 Drag measurements 45

4 Details of Numerical & Analytical Tools 47

4.1 Numerical tools 47
4.1.1 Flow solver - Eilmer3 48
4.1.2 The modelling of turbulence 48
4.1.3 Test case 1 - 2D flat plate 52
4.1.4 Test case 2 - Axisymmetric hollow cylinder 55
4.1.5 Test case 3 - Backward-facing step 60
4.1.6 Test case 4 - Mixing of coaxial jets 65
4.1.7 Test case 5 - Shock-wave-turbulent-boundary-layer interaction . 71
4.1.8 Test case 6 - Boundary layer combustion experiments of Kirchhartz 73
4.2 Analytical tools 75
4.2.1 Turbulent skin friction theories 76
4.2.2 Modification of theories to account for flows with pressure gradients 79

5 Results & Discussions **83**

5.1 Tests at design point - 4.8 MJ/kg condition 84

5.1.1 Verification of the performance of the inlet against its design point 84

5.1.2 Inlet & combustor pressure measurements 88

5.1.3 Combustor drag measurements 90

5.1.4 Comparison with Kirchhartz's direct-connect experiments 95

5.2 Simulating the effects of inlet fuel injection 98

5.2.1 Inlet & combustor pressure measurements 98

5.2.2 Combustor drag measurements 100

5.3 Simulating the effects of throat fuel injection 102

5.3.1 Inlet & combustor pressure measurements 102

5.3.2 Combustor drag measurements 103

5.4 Tests at off-design conditions 105

5.5 Summary 106

6 Characterisation of the Effects of Flow Disturbances **109**

6.1 Undisturbed case 113

6.2 Vortex generator case 115

6.3 Increased vorticity case 118

6.4 Thin inflow boundary layer case 118

6.5 Hydrogen injection at matched pressures case 121

6.6 Summary 121

7 Conclusions and Future Work **125**

7.1 Conclusions 125

7.2 Recommendations for Future Work 128

References **131**

A A lower Pitot-to-nozzle-supply pressure ratio for N_2 tests **147**

B Uncertainty Analysis **149**

B.1 Uncertainties in the test conditions 149

B.2 Uncertainties in the fuelling conditions 150

C Estimation of flight-equivalent conditions **155**

D Detailed shot summary **157**

E Conditions at the exit of the fuel injector nozzle **161**

F A comparison of the strain gauges used **165**

G The use of 10% driver gas contamination to limit test times **169**

H Drag coefficient in terms of Pitot pressure **175**

I Integral form of the Navier-Stokes equations **177**

J Tests conducted at off-design conditions **181**

J.1 Tests at lower stagnation enthalpies - H_s = 3.7 MJ/kg 181

J.1.1 Inlet & combustor pressure measurements 181

J.1.2 Combustor drag measurements 182

J.2 Tests at higher stagnation enthalpies - H_s = 8 MJ/kg 184

J.2.1 Inlet & combustor pressure measurements 184

J.2.2 Combustor drag measurements 184

J.3 Tests at higher Mach numbers 186

J.3.1 Inlet & combustor pressure measurements 186

J.3.2 Combustor drag measurements 187

List of Figures

1.1 Tangential slot injection for the reduction of viscous drag. 2

2.1 Results from analysis of DNS data (adapted from Gomez et al., 2009). . . 9

2.2 Experimental configuration and results (adapted from Goyne et al., 2000). 12

2.3 Fuel injector and combustor design (adapted from Rowan and Paull, 2006). 13

2.4 Effects of equivalence ratio of cross-stream fuel injection and vortex generator height on skin friction coefficient (adapted from Rowan and Paull, 2006). 14

2.5 Comparison of Stalker's theory with experimental and numerical results of Goyne et al. (adapted from Stalker et al., 2005). The experimental configuration for these results is shown in Figure 2.2a. 15

2.6 Experimental setup of Suraweera (2006). Also shown is the computational domain used by Denman (2007) for his LES simulations. 16

2.7 Instantaneous contour plot of static temperature. Flow is from left to right. (adapted from Denman, 2007) 17

2.8 Comparison of localised skin friction coefficients (adapted from Denman, 2007). 18

2.9 Effect of heat addition on Reynolds shear stresses (adapted from Denman, 2007). 19

2.10 Experimental setup of Kirchhartz (2010). 19

2.11 Typical flow disturbances encountered in scramjet flowfields (adapted from Hemsch, 1992). 21

2.12 Complex flowfield resulting from the cross-flow injection of fuel (Viti et al., 2009) 22

3.1 Experimental setup used in the current study. Also shown is the experimental setup of Kirchhartz (2010). 26

3.2 The REST inlet. 27

3.3 Fuel supply and injection system. 29

3.4 Vortex generators. 30

3.5 Vortex generators on the REST inlet. 31

3.6 Vortex generators in injector. 31

3.7 Combustor. 32

3.8 Stress wave force balance. 33

3.9 Layout of strain gauges on the brass sting (taken from Kirchhartz, 2010). Gauges B, C, D and E are the piezo-electric film strain gauges, while gauges SSGA, SSGB and SSGOld are the semi-conductor strain gauges. . 35

3.10 T4 Stalker tube 36

3.11 Uniform test flow core (estimated from a Pitot survey of the Mach 6 nozzle) shown in relation with the test model. Note that measurements have been replicated about the axis of the nozzle. 38

3.12 Ludwieg tube fill pressure versus discharge coefficient 42

3.13 Timing of fuel injection for test 10567 42

3.14 Typical pressure trace from shot 10568. 44

3.15 Typical drag trace from shot 10568. 46

4.1 Overview of selected test cases. 52

4.2 Schematic of the flat plate experiments. 53

4.3 Grid convergence for the 2D flat plate test case. 54

4.4 Comparison of experimental, theoretical and numerical results. Numerical results are from simulations that have been conducted using freestream turbulence intensities listed in Table 4.1. 55

4.5 Schematic of the axisymmetric hollow cylinder experiments, where $x = 0$ m corresponds to the leading edge of the cylinder. 56

4.6 Comparison of results from grids with different resolutions. 57

4.7 Comparison of results from grids with different y^+ values. 58

4.8 Surface heat flux values at $x = 0.3$ m for different y^+ values. 58

4.9 Comparison of results from grids with different maximum cell aspect ratios. 59

4.10 Comparison of experimental and numerical results. 60

4.11 Schematic of the backward-facing step experiments. 61

4.12 Comparison of profiles at x/H = -1. Note that temperatures and velocities have been normalised using freestream quantities quoted in the main text. 61

4.13 Grid convergence for the 2D backward-facing step test case. 62

4.14 Comparison between **(a)** experimentally measured and **(b)** numerically simulated pressure contours, and **(c)** experimentally measured and **(d)** numerically simulated temperature contours. Note that the iso-contours have been normalised using freestream static properties. 63

4.15 Boundary layer profiles at several x/H locations. Note that pressures, temperatures and velocities have been normalised using freestream quantities. 64

4.16 Schematic of the coaxial jets experiments. 65

4.17 He-O_2 mole fractions at several x-locations. 67

4.18 Pitot pressure at several x-locations. 68

4.19 x-velocity at several x-locations. 69

4.20 Comparison of experimental turbulence intensity $\sqrt{\overline{u'^2}}$ from the experiments of Cutler et. al. and numerical turbulence intensity $\sqrt{2/3\,k}$ from Eilmer3 simulations. 70

4.21 Schematic of the shock-wave-turbulent-boundary-layer interaction experiments. 71

4.22 Static pressure on the flat plate surface at $r = 0.0889$ m. Note that static pressures have been normalised against freestream quantities. 72

4.23 Comparison of experimental and numerical results. 74

4.24 Schematic for the concept of local similarity (Anderson, 2006). 79

4.25 Comparison of experimental, numerical and theoretical results. 80

5.1 Pressure coefficients in the inlet 84

5.2 Effects of leading edge bluntness on cowl shock impingment location. . 85

5.3 Comparison of results from the numerical simulations of the current experiments and Kirchhartz's experiments. 87

5.4 Pressure coefficients in the inlet and combustor for $H_s = 4.8$ MJ/kg condition. 89

5.5 Combustor drag coefficients for $H_s = 4.8$ MJ/kg condition. 90

5.6 CFD simulations of a circular constant-area duct with heat addition at different locations in the flowfield. 92

5.7 Effects of heat addition at different locations in the flowfield. 93

5.8 Comparison of the weighted Reynolds shear stress profiles at several x-locations. The false zero offset between each set of weighted Reynolds shear stress profiles is equivalent to 8500 kg/m.s^2. 94

5.9 Comparison of re-normalised pressure and drag coefficients for the current experiments and Kirchhartz's experiments. In both plots, the filled symbols and bars are for the current experiments, while the unfilled symbols and bars for Kirchhartz's experiments. 96

5.10 Profiles of hydrogen mass fractions at several x-locations taken from the CFD simulations of Kirchhartz's experiments and of the current experiments. The shaded regions represent the location of the boundary layer. 97

5.11 Pressure coefficients in the inlet and combustor for tests with vortex generators in the inlet (with v.g.) and without vortex generators (without v.g.) at the $H_s = 4.8$ MJ/kg Mach 6.2 test condition. 99

5.12 Comparison of experimentally measured combustor drag coefficients for tests with vortex generators in the inlet (with v.g.) **(a)** with those predicted using skin friction theories and **(b)** with those for tests without vortex generators (without v.g.). 100

5.13 Pressure coefficients in the inlet and combustor for tests with vortex generators in the throat (with v.g.) and without vortex generators (without v.g.) at the $H_s = 4.8\,\mathrm{MJ/kg}$ Mach 6.2 test condition. 102

5.14 Comparison of experimentally measured combustor drag coefficients for tests with vortex generators in the throat (with v.g.) **(a)** with those predicted using skin friction theories and **(b)** with those for tests without vortex generators (without v.g.). 104

5.15 Experimentally measured combustor drag coefficients for tests **(a)** at different stagnation enthalpies and **(b)** at different Mach numbers. 106

6.1 Schematic of computational domain. Dimensions are shown in mm. The vortex generator is not modelled for the undisturbed test case. 110

6.2 Differences in the streamwise vorticity at $x = -0.001$ m between the cases with different inflow boundary layer thicknesses. These cross-sections are with the observer looking upstream at the oncoming flow. The symmetry plane of the vortex generator is on the left of the cross-section. . . 112

6.3 Streamwise slices. 113

6.4 Undisturbed case, where α_{H_2} is the hydrogen mass fraction. 114

6.5 Vortex generator case, where α_{H_2} is the hydrogen mass fraction. 116

6.6 Contours of hydrogen mass fractions near the combustor wall. 117

6.7 Increased vorticity case, where α_{H_2} is the hydrogen mass fraction. 119

6.8 Thin inflow boundary layer case, where α_{H_2} is the hydrogen mass fraction.120

6.9 Hydrogen injection at matched pressures case, where α_{H_2} is the hydrogen mass fraction. 122

A.1 A comparison of the Pitot-to-nozzle-supply pressure ratio for tests with air as the test gas and tests with nitrogen as the test gas. 148

E.1 Schematic of the fuel injector used in the current study. 161

F.1 Method used to generate axial and bending stresses. 166

F.2 Normalised strain gauge output from piezo-electric film strain gauges. . 166

F.3 Normalised strain gauge output from semi-conductor strain gauges. . . 166

G.1 Schematic for the stream-tube one-dimensional finite-rate stream-tube analysis. 169

G.2 Flow variables and H_2O production along the pipe for driver gas with 100% argon. 171

G.3 Flow variables and H_2O production along the pipe for driver gas with 55% argon and 45% helium (by volume). 172

G.4 Flow variables and H_2O production along the pipe for driver gas with 35% argon and 65% helium (by volume). 173

J.1 Pressure coefficients in the inlet and combustor for $H_s = 3.7\,\mathrm{MJ/kg}$ condition 182

J.2 Comparison of experimentally measured combustor drag coefficients for tests at the $H_s = 3.7\,\mathrm{MJ/kg}$ condition with those predicted using skin friction theories and with those for tests at the $H_s = 4.8\,\mathrm{MJ/kg}$ condition. 183

J.3 Pressure coefficients in the inlet and combustor for $H_s = 8\,\mathrm{MJ/kg}$ condition. 185

J.4 Comparison of experimentally measured combustor drag coefficients for tests at the $H_s = 8\,\mathrm{MJ/kg}$ condition condition with those predicted using skin friction theories and with those for tests at the $H_s = 4.8\,\mathrm{MJ/kg}$ condition. 186

J.5 Pressure coefficients in the inlet and combustor for $H_s = 4.8\,\mathrm{MJ/kg}$ $M = 7.4$ condition. 187

J.6 Comparison of experimentally measured combustor drag coefficients for tests at the $M = 7.4$ condition condition with those predicted using skin friction theories and with those for tests at the $M = 6.2$ condition. . 188

List of Tables

3.1 Nominal experimental nozzle-supply, freestream conditions and equivalent flight conditions for tests with air as the test gas. 40

3.2 Nominal experimental nozzle-supply and freestream conditions for tests with nitrogen as the test gas. 40

3.3 Estimated conditions at the fuel injector nozzle exit plane. 43

4.1 Test matrix for the different freestream turbulence properties tested. . . . 53

5.1 Comparison of one-dimensionalised flow properties at 45 mm upstream of fuel injection plane. 88

B.1 Relative sensitivities of the derived quantities F to perturbations in the measured quantities ψ_i. 152

B.2 Relative uncertainties in the measured quantities X_{ψ_i}. 153

B.3 Relative uncertainties in the test conditions. 153

B.4 Relative uncertainties in the measured quantities X_{ψ_i}. 153

B.5 Relative uncertainties in the fuelling conditions. 153

D.1 Nozzle-supply, nozzle-exit and fuelling conditions for each shot. 158

D.2 Freestream chemical composition at the exit of the nozzle for each shot. . 159

G.1 Mass fraction of each individual species of the hydrogen-air mixture for three different driver gas compositions and five different contamination levels. 170

Nomenclature

Roman

a	Parameter in the van Driest II theory
A	Area
A_c	Internal surface area of the combustor
$A^\star$	Effective throat area
b, b_1, b_2	Parameters in the van Driest II theory
c_D	Integrated drag coefficient
c_f	Skin friction coefficient
c_{fn}	Skin friction coefficient without hydrogen injection
c_h	Heat transfer coefficient
c_{hn}	Heat transfer coefficient without hydrogen injection
c_{Hw}	Mass fraction of hydrogen near the wall surface
c_{oe}	Mass fraction of oxygen at the boundary layer edge
c_p	Pressure coefficient
C	Level of contribution
C	Constant
C_{lim}	Stress-limiter coefficient
D	Absolute drag force
D_α	Diffusion coefficient of the α-th species
E	Parameter in the Spalding & Chi theory
f	Relative stoichiometric mass fraction of hydrogen, 0.125
f_β	Vortex-stretching function
$f(\Delta)$	Flow parameter of interest
f_{limit}	Limiting value for a grid with infinite resolution
F	Flow property
F_c	Compressibility parameter in the theory of Spalding & Chi
F_{ψ_i}	Value of the quantity F derived from an input of the measured quantity ψ_i
F_0, F_1, F_2	Parameters in the van Driest II theory
g	Ratio of the velocity at the flame front to the freestream velocity
G	Parameter in the van Driest II theory
h	Altitude
h	Static enthalpy
H	Height of the backward-facing step
H	Stagnation enthalpy
$\overline{I_x}$	Additional terms when flow is inhomogeneous in the streamwise direction
k	Turbulent kinetic energy
K	von Kármán constant, 0.41

l_{tr}	Distance from leading edge of plate where boundary layer transition occurs
L	Length
$\dot{m}$	Mass flow rate
M	Mach number
N	Number of
O	Order of convergence
p	Pressure
Pr	Prandtl number
q	Dynamic pressure
Q	Heat flux
Q, Q_1, Q_2	Parameters in the van Driest II theory
r	Radial distance from the leading edge of the fin
r	Radius of inlet, isolator or combustor
R	Gas constant
Re	Reynolds number
Re_x	Reynolds number based on x-distance
Re_δ	Reynolds number based on boundary layer thickness
S_{ij}	Mean strain-rate tensor
$\overline{S}_{ij}$	Zero-trace Favre-averaged strain-rate tensor
$\hat{S}_{ij}$	Galilean-invariant Favre-averaged strain-rate tensor
$\dot{S}_\alpha$	Production/destruction rate of the α-th species due to chemical reactions
t	Time
$\overline{t}_{ij}$	Viscous stress tensor
T	Temperature
$\breve{u}$	Dimensionless velocity for Equation 2.1, u/u_∞
u^+	Velocity that is non-dimensionalised using van Driest's transformation
u, v, w	Velocity in the x, y, z directions
u', v', w'	Fluctuating velocity components in the x, y, z directions
u'', v'', w''	Favre fluctuating velocity components in the x, y, z directions
$\overline{u'}$, $\overline{v'}$, $\overline{w'}$	Temporal average of fluctuating velocities
$-\overline{u'v'}$	Specific Reynolds shear stress
$-\overline{u''v''}$	Favre-averaged Reynolds shear stress
V	Volume
x, y, z	Cartesian coordinates
X_F	Relative uncertainty of the derived quantity F
X_ψ	Relative uncertainty of the measured quantity ψ
$\breve{y}$	Dimensionless normal distance from the wall for Equation 2.1, $y/(\delta\, l_{tr})$
y^+, z^+	Dimensionless normal distance of the first cell from the wall
y^+_{cell}	Dimensionless normal distance of the cell from the wall
Y_α	Mass fraction of the α-th species

Greek

α	Discharge coefficient of the fuel injector
α	Closure coefficient in the k-ω model
α	Parameter in the skin friction theories
α_{H_2}	Mass fraction of hydrogen
β	Parameter in the skin friction theories
β	Angle of the fin
β, $\beta^\star$, β_o	Closure coefficients in the k-ω model
χ_ω	Vortex-stretching parameter
δ	Boundary layer displacement thickness
$\breve{\delta}$	Dimensionless boundary layer displacement thickness for Equation 2.1, δ/l_{tr}
δ_d	Boundary layer displacement thickness normalised by the boundary layer thickness
δ_{ij}	Kronecker delta
Δ	Representative cell size
ΔQ	Heat of combustion of hydrogen, 120 MJ/kg
ϵ	Dissipation per unit mass
η	Geometrical scaling factor
γ	Ratio of specific heats
μ	Viscosity
$\breve{\mu}$	Dimensionless viscosity for Equation 2.1, μ/μ_∞
ω	Specific dissipation rate
Ω_x	Streamwise vorticity
Ω_{ij}, Ω_{jk}	Rotation tensors
ϕ	Equivalence ratio
ψ	Measured quantity
ρ	Density
σ_d	Cross-diffusion term
σ , $\sigma^\star$, σ_{do}	Closure coefficients in the k-ω model
τ_{ij}	Specific Reynolds stress tensor

Superscript

$\bar{}$	Time-averaged value
$\tilde{}$	Favre-averaged value
$'$	Fluctuations from the mean value

Subscript

∞	Freestream
1	Post-forebody shock conditions entering the scramjet inlet
avg	Mass-flux-weighted averaged value
aw	Adiabatic wall
capture	Area or flow property captured by the REST inlet
cells	Cells
char	Characteristic

C	Compressible term
CT	Compressible-turbulent interaction term
e	Properties at the edge of the boundary layer
f	Flight-equivalent conditions
fan	Expansion fan
ground	Ground test conditions
ignition	Ignition-delay
inc	Incompressible
IT	Inhomogeneous and transient term
jet	Hydrogen jet properties at the exit plane of the injector nozzle
L	Laminar term
LT	Ludwieg tube
LT, f	Final pressure in the Ludwieg tube
LT, i	Initial pressure in the Ludwieg tube
max	Maximum
Pitot	Pitot
plenum	Plenum chamber
s	Nozzle-supply
T	Turbulent term
w	Wall

Acronyms

2D	Two-dimensional
3D	Three-dimensional
AUSMDV	Advection Upwind Splitting Method (flux-Vector-splitting and flux-Difference-splitting)
BL	Boundary Layer
BLC	Boundary Layer Combustion
CEA2	Chemical Equilibrium with Applications 2
CFD	Computational Fluid Dynamics
DNS	Direct Numerical Simulation
EFM	Equilibrium Flux Method
ESTCj	Equilibrium Shock Tube Conditions Junior
FC	Film-Cooling
HIFiRE	Hypersonic International Flight Research Experiment
LES	Large-Eddy Simulation
PLIIF	Planar Laser-Induced Iodine Fluorescence
NASA	National Aeronautics and Space Administration
NATO	North Atlantic Treaty Organization
NENZF	Non-Equilibrium NozZle Flow
RANS	Reynolds-Averaged Navier-Stokes
REST	Rectangular-to-Elliptical Shape Transition
v.g.	Vortex generator
VULCAN	Viscous Upwind ALgorithm for Complex flow ANalysis

"So little is known about the nature of turbulent boundary layers and so much benefit would accrue to aviation from a reduction in turbulent skin friction drag, that all avenues for its reduction should be thoroughly examined."

G. S. Schairer
"Some opportunities for progress in aircraft performance - 27th Wright Brothers Lecture"
Journal of Aircraft, 1964, volume 1, issue 2, pages 49-70.

Chapter 1

Introduction

1.1 Scramjets & skin friction drag

Supersonic combustion ramjets, also known as scramjets, are airbreathing propulsion devices that have the ability to fly at speeds of more than five times the sound speed. Unlike the rocket, its non-airbreathing counterpart that requires a carried oxidiser to function, a scramjet draws in air from the atmosphere for combustion and thus thrust generation. As such, scramjets promise a more economical method for access to space than conventional rockets within the atmosphere. However, because of its need for air, a scramjet can operate only in Earth's atmosphere. As a result of this limitation, a scramjet-powered vehicle will always experience skin friction drag.

Since the advent of scramjets in the late 1950s (Ferri et al., 1964; Swithenbank, 1964; Weber and MacKay, 1958), skin friction drag has remained as one of the few major obstacles to the successful development of an operational scramjet vehicle. Compared to vehicles designed for flight at lower speeds, skin friction drag is particularly significant for hypersonic flight vehicles (Anderson, 2006). Firstly, since skin friction drag increases with flight speed, more skin friction drag occurs on hypersonic flight vehicles than for vehicles travelling at lower speeds. Secondly, flight vehicles designed for sustained hypersonic flights tend to be long and slender for pressure drag reduction purposes. This leads to a larger wetted-surface-to-frontal-area ratio, which in turn results in the skin friction drag becoming a more significant portion of the overall vehicle drag. Thirdly, the size and operating altitudes of hypersonic flight vehicles are likely to be such that predominantly turbulent boundary layers can be expected on the vehicle surfaces (Stalker, 2005). Turbulent boundary layers, in comparison with laminar ones, have higher skin friction drag forces. For hypersonic flight vehicles such as waveriders, Anderson (2006) predicts that the skin friction drag may constitute up to half

of the overall vehicle drag. Similar conclusions were also found from the analysis of experiments conducted on a quasi-axisymmetric scramjet configuration (Paull et al., 1995).

The successful development of scramjet vehicles will depend heavily on the control of these skin frictional drag losses (Paull et al., 1995; Weber and MacKay, 1958). To date, many techniques have been proposed for the reduction of these viscous losses (Bushnell and Hefner, 1990). Of the many methods available, the tangential injection of a gas film along a surface is a promising method of reducing viscous drag in hypervelocity applications. This technique, commonly known as the film-cooling method, was originally used for reducing aerodynamic heating in turbine blades and other aero-engine components (Goldstein, 1971). Dershin et al. (1967); Parthasarathy and Zakkay (1970) and Cary and Hefner (1972) showed that by injecting a gas film with a low molecular weight or at a momentum lower than that in the freestream (as shown in Figure 1.1a), the local skin friction coefficient can be reduced by up to 70% of the no-injection values. However, this large level of reduction occurs only in a small region downstream of the injection point (usually 10 slot heights). As the gas film and mainstream flow mix, the skin friction coefficient increases back to the "no-injection" values.

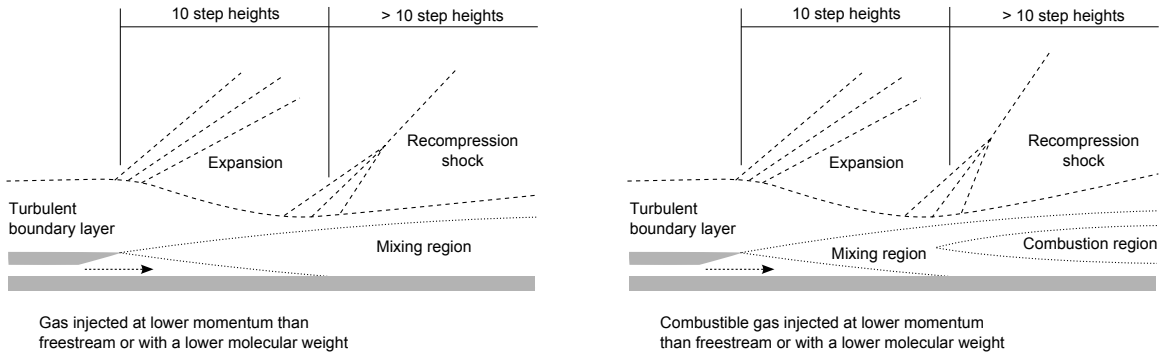

(a) Film-cooling. **(b)** Boundary layer combustion.

Figure 1.1: Tangential slot injection for the reduction of viscous drag.

In 2000, this drag reduction technique was further extended by Goyne et. al. in the Centre for Hypersonics at The University of Queensland. As shown in Figure 1.1b, instead of just injecting gas along the surface, hydrogen is injected into a turbulent boundary layer that is hot enough to allow for the ignition and combustion to occur. When hydrogen burns, the heat energy released from the combustion process increases the temperatures in the boundary layer. The increase in temperatures decreases the

boundary layer densities, which in turn leads to a decrease in Reynolds stresses and an increase in boundary layer displacement thickness. Both these factors contribute to the reduction of skin friction coefficient. The experiments of Goyne et. al. showed that skin friction reductions of up to 80% over 100 step heights are possible when combustion occurs in the boundary layer. These experiments also confirmed the preliminary findings of the numerical simulations of Kazakov et al. (1997) that skin friction coefficient reduction can be achieved with heat addition to boundary layers. The boundary layer combustion technique is an excellent viscous drag reduction method because it combines the high levels of skin friction reduction brought about by the film-cooling effect in the near-field region with those brought about by heat addition in the boundary layer in the far-field regions. Furthermore, because fuel has to be burned, this technique can also be applied in combustors, thus providing not only a possibility of reducing viscous drag but also as a method of releasing heat in the combustor. It is also noteworthy that, due to the high densities present in scramjet combustors, skin friction drag in combustors can account for up to 60% of the overall engine skin friction drag (Paull et al., 1995). As such, the most suitable place to implement the boundary layer combustion technique is in the combustor. Subsequent experiments (Kirchhartz, 2010; Suraweera, 2006), numerical simulations (Denman et al., 2005; Levin and Larin, 2003; Stephensen, 2002), and theoretical analysis (Stalker, 2005) have confirmed this technique's capability for hypervelocity skin friction drag reduction purposes.

Although skin friction reduction by boundary layer combustion has been demonstrated experimentally, theoretically, and numerically, there still remains a question of whether this new technology can be implemented in realistic scramjet configurations. One key issue that can affect the implementation of the boundary layer combustion technique in a realistic scramjet is the presence of highly non-uniform flow entering the combustion chamber from the inlet. This flow non-uniformity, which comes in the form of shock waves and vortices, may be able to sweep the wall fuel layer required for boundary layer combustion into the mainstream. Many researchers involved in the study of boundary layer combustion (Goyne et al., 2000; Kirchhartz, 2010; Rowan, 2003; Stalker et al., 2005; Suraweera, 2006) have indicated the need to investigate the effects of flow non-uniformities on this drag reduction technique. To date, there exists no literature discussing the effects of flow non-uniformities on boundary layer combustion. Although there is literature in the film-cooling industry demonstrating that shock wave impingement (Juhany and Hunt, 1994; Kanda and Ono, 1997; Kanda et al., 1996; Peng and Jiang, 2009; Takita and Masuya, 2000) and mainstream vorticity (Heidmann and Ekkad, 2008) can lift the gas film off the wall, it is not indicated in these studies

as to whether the injected gas gets convected out of the boundary layer. Therefore, the investigation of how flow non-uniformities can affect the boundary layer combustion technique is one of the crucial steps needed to bring this new technology closer to being applied in operational hypersonic vehicles.

1.2 Aims

The main aim of this project is ...

to investigate if and how flow non-uniformities entering a scramjet combustor will affect the potential for boundary layer combustion to reduce skin friction.

To achieve this aim, the project is approached experimentally and numerically.

Experimental approach - Experiments are conducted on a circular constant-area combustor that is attached downstream of a realistic scramjet inlet and an injector designed to inject hydrogen into the boundary layer. Using a stress wave force balance, the integrated skin friction drag on the internal surface of the combustor is measured for three scenarios - one, where fuel is not injected, two, where fuel is injected but combustion is suppressed, and three, where fuel is injected and allowed to burn. The scramjet inlet is used to produce flow disturbances that are typical of those to be expected in operational scramjet inlets. In addition, vortex generators are also used on the inlet to simulate the vorticity generated by conventional cross-stream fuel injection techniques.

Numerical approach - Computational Fluid Dynamics (CFD) simulations of the internal flowfield in the experimental model are conducted using an in-house CFD code called Eilmer3 (Jacobs and Gollan, 2008). When matched to the experimental measurements, these simulations can complement the experiments by revealing more insights into the flowfield in the model. In addition, simulations are also used in this project to quantify the level of flow non-uniformities required to affect the level of drag reduction brought about by boundary layer combustion. However, before the simulations can be conducted, a robust and reliable turbulence model needs to be implemented in Eilmer3. This implementation is validated against test cases that are representative of those to be expected in the current experiments. This is done to validate the suitability of Eilmer3 and the k-ω turbulence model for use in this project.

1.3 Outline of thesis

The thesis is organised into seven chapters. Additional technical information is included in the appendices at the end of this thesis.

Chapter 2 - Literature Review This chapter starts with a review of the current state of research in boundary layer combustion. This chapter is then concluded with a summary of the types of flow non-uniformities that can be encountered in scramjets and a discussion of the possible effects that these disturbances can have on the drag reduction potential of the boundary layer combustion technique.

Chapter 3 - Details of Experiments Details of the experimental program are described in this chapter. This includes details of the experimental model, instrumentation, test facility and test conditions. The methods used for data reduction of the pressure and drag measurements and an analysis of the experimental uncertainties are also presented.

Chapter 4 - Details of Numerical and Analytical Tools This chapter presents details of the numerical and analytical tools used to support the analysis of the experimental data. Details of the flow solver, Eilmer3, and the newly implemented k-ω turbulence model are provided. Results from the validation exercise are also presented. The chapter then continues with a summary of the turbulent skin friction theories that are used in this project, and concludes with an example showing the application of these theories.

Chapter 5 - Results and Discussions This chapter shows the results from the experimental program. The analysis of these results, conducted with supporting CFD simulations and turbulent skin friction theories, are reported here.

Chapter 6 - Characterisation of the levels of flow non-uniformities needed to affect boundary layer combustion This chapter presents results from the simulations conducted to characterise the levels of flow non-uniformities required to affect boundary layer combustion. The simulations include a reference case in which the freestream vorticity is representative of that in undisturbed flow, and cases in which the levels and location of vorticity are varied. A discussion of the implications of these results is presented.

Chapter 7 - Conclusions and Future Work This chapter concludes the thesis by summarising the findings from Chapters 5 and 6 on how flow non-uniformities affect the skin friction reduction brought about by boundary layer combustion. Recommendations for future work are also provided.

Chapter 2

Literature Review

This chapter starts with a review of the current state of research in boundary layer combustion. This is then concluded with a summary of the types of flow non-uniformities that can be encountered in scramjets and a discussion of the possible effects that these disturbances can have on the drag reduction potential of the boundary layer combustion technique.

2.1 Boundary layer combustion

Kazakov et al. (1997) performed numerical simulations to examine the effects on skin friction when heat is added to a supersonic turbulent boundary layer. Two approaches of heat addition were used - one, surface heating and two, volume heat source. It is shown that heat addition to a turbulent boundary layer decreases the skin friction and that for the same amount of heat supplied, volumetric heat addition is more effective at reducing skin friction than surface heating. Kazakov et al. (1997) offer explanations, based on Equation 2.1,

$$c_f = \frac{2}{\check{\delta}\, Re}\, \check{\mu}_w \left(\frac{\partial \check{u}}{\partial \check{y}}\right)_w \tag{2.1}$$

for the reduction of skin friction when heat is added into a boundary layer from the surface. Note that the variables $\check{\delta}$, $\check{\mu}_w$, $\check{u}$ and $\check{y}$ in Equation 2.1 are dimensionless. In the neighbourhood of the heat release zone, the increase of surface temperature causes the dynamic viscosity near the surface to increase. From Equation 2.1, this causes c_f to increase. However, there is also a competing effect which causes c_f to decrease in the presence of heat addition to the boundary layer. When the boundary layer temperature increases, a decrease in density also occurs. This leads to the displacement of streamlines from surface (an increase in boundary layer displacement thickness δ),

a decrease in the transverse velocity component gradient $(\delta u/\delta y)_w$ and hence a decrease in skin friction. Kazakov et al. (1997) postulate that because the increase in δ and decrease in $(\partial u/\partial y)_w$ are more dominant than the increase in μ_w, the skin friction coefficient tends to be decreased. In addition, Kazakov et al. (1997) argue that when heat is added above the surface for the volume heating case, the surface dynamic viscosity μ_w does not increase as much as when heat is added from the surface. As such, they postulate that this explains the better reduction in skin friction seen in the volume heating case than in the surface heating case. Kazakov et al. (1997) also suggest that there exists a "long-term memory" effect in a locally heated boundary layer - that downstream of the heating zone, the skin friction coefficient still remains lower than that for a case without heat addition. This is attributed to the displacement thickness of the boundary layer not returning back to pre-heat-addition values.

In their work, Kazakov et al. (1997) state that the reduction in skin frictional drag in the presence of heat addition to the boundary layer comes about only from decreased densities in the boundary layer. This implies that the levels of skin friction reduction will be the same regardless of whether the boundary layer is laminar or turbulent. However, this is not the case, as suggested by Stalker (2005) and proven by Denman (2007). In 2005, Stalker suggested that the Reynolds stresses play an important role in the skin friction reduction phenomena that occurs in the presence of boundary layer combustion. In laminar boundary layers, when the temperatures rise, the decrease in density increases the boundary layer thickness, tending to reduce the shear stress. However, this tendency is partially offset by the temperature-induced increase in viscosity, leading only to modest reductions in skin friction. In turbulent boundary layers, the shear stress is mainly caused by the Reynolds stresses, which play the role of viscosity in the form of turbulent viscosity in turbulent boundary layers (Stalker, 2005). Since the Reynolds stresses decrease when boundary layer temperatures increase (Denman, 2007), the effective viscosity in turbulent boundary layers tends to be reduced, rather than increased. This, therefore, leads to larger skin friction reductions in turbulent boundary layers than in laminar ones.

It is appropriate, at this juncture, to discuss the importance of near-wall Reynolds stresses in their contribution to skin frictional drag. Fukagata et al. (2002) and Gomez et al. (2009) show in their theoretical analyses that the skin friction drag is primarily dependent on the near-wall Reynolds stresses. In their paper, Fukagata et al. (2002) derive a direct relation between the skin friction coefficient and Reynolds stress distribution. For an incompressible boundary layer on a flat plate with mean zero streamwise

pressure gradient, the skin friction coefficient c_f can be obtained from Equation 2.2.

$$c_f = \underbrace{\frac{4(1-\delta_d)}{Re_\delta}}_{C_L} + \underbrace{2\int_0^1 2(1-y)(-\overline{u'v'})dy}_{C_T} - \underbrace{2\int_0^1 (1-y)^2\left(\overline{I_x} + \frac{\partial \overline{u}}{\partial t}\right)dy}_{C_{IT}} \tag{2.2}$$

The relation in Equation 2.2 shows that the skin friction coefficient can be split into three contributing terms - the quasi-laminar contribution C_L, the turbulent contribution C_T and the inhomogeneous and transient contribution C_{IT}. An extension of Equation 2.2 for compressible flows (as shown in Equation 2.3) is provided by Gomez et al. (2009).

$$\begin{aligned} c_f = & \underbrace{\frac{4(1-\delta_d)}{Re_\delta}}_{C_L} + \underbrace{4\int_0^1 (1-y)\,\overline{\rho}(\overline{u''v''})dy}_{C_T} + \underbrace{\frac{4}{Re_\delta}\int_0^1 (1-y)\,\overline{\mu}\frac{\partial \overline{u}}{\partial y}dy}_{C_C} \\ & + \underbrace{\frac{4}{Re_\delta}\int_0^1 (1-y)\,\overline{\mu'\left(\frac{\partial u'}{\partial y} + \frac{\partial v'}{\partial x}\right)}dy}_{C_{CT}} - \underbrace{2\int_0^1 (1-y)^2\left(\overline{I_x} + \frac{\partial \overline{\rho u}}{\partial t}\right)dy}_{C_{IT}} \end{aligned} \tag{2.3}$$

For compressible flat plate boundary layers, there are two contribution terms in addition to those in Equation 2.2 - the compressible contribution C_C and the compressible-turbulent interaction contribution C_{CT}. Note that the turbulent contribution C_T is essentially a weighted average of the Reynolds stresses $\overline{u'v'}$ in both Equations 2.2 and 2.3. To demonstrate how each term contributes to the skin friction coefficient, Gomez et al. (2009) applied Equation 2.3 to analysis of the data from Direct Numerical Simulations. The results from this analysis are shown in Figure 2.1. Figure 2.1a shows that

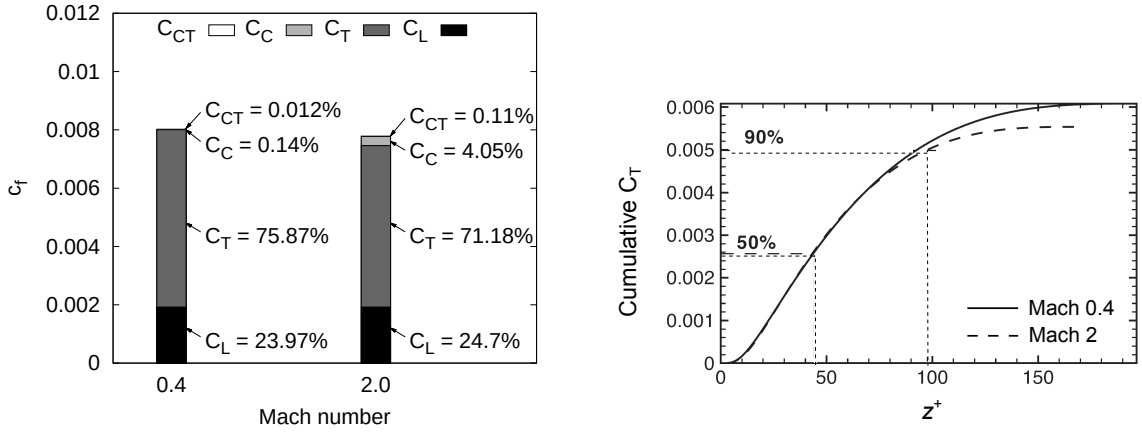

(a) Contributions to the skin friction coefficient. **(b)** Contribution of Reynolds stress to c_f.

Figure 2.1: Results from analysis of DNS data (adapted from Gomez et al., 2009).

the Reynolds stresses contribute to at least 70% of the skin friction coefficient, while Figure 2.1b shows that the Reynolds stresses in the near-wall region (from $z^+ \approx 0$ to $z^+ \approx 100$) are responsible for 90% of the turbulent contribution to skin friction. Both these results clearly show that the near-wall Reynolds stresses contribute significantly to the skin friction in turbulent boundary layers, and that if these near-wall Reynolds stresses are suppressed, a reduction in skin frictional drag can be achieved.

The drag reduction capabilities of the boundary layer combustion technique were demonstrated experimentally for the first time by Goyne et al. in 2000. In their experiments, as shown in Figure 2.2a, hydrogen was injected behind a backward-facing step into a turbulent boundary layer in a 1-m long rectangular duct. Local values of skin friction, heat transfer and static pressure were measured using an array of gauges located along the duct. Figure 2.2b shows the experimentally measured and numerically estimated levels of skin friction coefficient reduction, where c_f is the skin friction coefficient measured when hydrogen was injected and c_{fn} is that measured without hydrogen injection. A value of 0 for the term "$1 - c_f/c_{fn}$" corresponds to no reduction in skin friction coefficient while a value of 1 corresponds to a 100% reduction. The experimental and numerical levels of heat transfer coefficient reduction are presented in a similar way in Figure 2.2c. These experiments demonstrate that when boundary layer combustion occurs, a local skin friction coefficient reduction of up to 70 - 80% can be achieved. It can be observed that the numerical simulations, which were performed using a space-marching finite-volume solver with the k-ϵ turbulence model, estimate the skin friction and heat transfer coefficients reasonably well. One of the questions that commonly arises is the possibility of increased heat transfer to the walls in the presence of boundary layer combustion. Interestingly, Goyne et al. (2000) show that the measured heat transfer coefficient is lower when fuel is burned in the boundary than when no fuel is injected. This was also observed by Takita and Masuya (2000) in their numerical simulations. Stalker et al. (2005) postulate that this occurs because, by virtue of Reynold's analogy, a reduced skin friction coefficient brought about by both the film-cooling and boundary layer combustion effects should result in a reduced heat transfer coefficient. However, in regions where combustion occurs in the boundary layer, the reduction in heat transfer coefficient gets offset by the combustion-related heat release. Figure 2.2c shows that the level of reduction in the numerically estimated heat transfer coefficient for the combustion case deviates from that for the combustion-suppressed case beyond 0.5 m. It is postulated that beyond 0.5 m, the effects of the heat release from combustion starts dominating the surface heat transfer coefficient more than the effects of film-cooling brought about by the surface hydrogen

film.

Using a Navier-Stokes solver coupled with the Cebeci-Smith algebraic turbulence model, Larin and Levin (2001) and Levin and Larin (2003) conducted simulations to investigate the effect of heat addition to a turbulent boundary layer. In their investigations, a bulk thermal energy source was used to model the heat addition to the boundary layer. Their investigations reveal that the addition of bulk thermal energy into a supersonic turbulent boundary layer results in significant amounts of skin friction drag reduction. They show that a local skin friction coefficient reduction of up to 80% and integrated skin friction coefficient reduction of up to 65% is achievable. In addition, their investigations also reveal that bulk thermal energy addition increases the boundary layer thickness and displaces streamlines further away from the wall. An important finding in the work of Larin and Levin (2001) is that when thermal energy is added beyond an optimal amount, the resulting high boundary layer temperatures limit the amount of heat addition by the combustion process, hence reducing the effectiveness of skin friction drag reduction. Larin and Levin (2001) also show that when heat is added to the boundary layer, the heat transfer to the wall increases to about twice the amount that is estimated when no heat is added. This finding is different from that observed in the experiments of Goyne et al. (2000), where the measured heat transfer to the wall was lower with heat addition to the boundary layer. Because the simulations of Larin and Levin (2001) did not account for the injection of hydrogen, the film-cooling effects brought about by hydrogen injection that thermally protected the surface were not present. Hence, the increase in heat transfer to the wall from the addition of heat to the boundary layer seen in the simulations of Larin and Levin (2001) is not unexpected.

Using the same CFD code as that used by Goyne et al. (2000), Stephensen (2002) conducted simulations to parametrically explore the effects of mainstream and injectant conditions on the effectiveness of boundary layer combustion for skin friction reduction. The combustion of hydrogen and oxygen was modelled using the basic NASP 13-reactions finite-rate reaction scheme (Oldenborg et al., 1990). The results indicate that skin friction reduction appears to be slightly more effective for flows at higher freestream Reynolds numbers, pressures and densities. The results also indicate that higher hydrogen mass flow rates improve the levels of skin friction reduction. Two other important observations were also made in this numerical study. Firstly, larger reductions in skin friction can be achieved in lower freestream temperatures when combustion occurs. Similar to the observation made by Larin and Levin (2001), it is postulated that higher freestream temperatures limit the amount of energy released

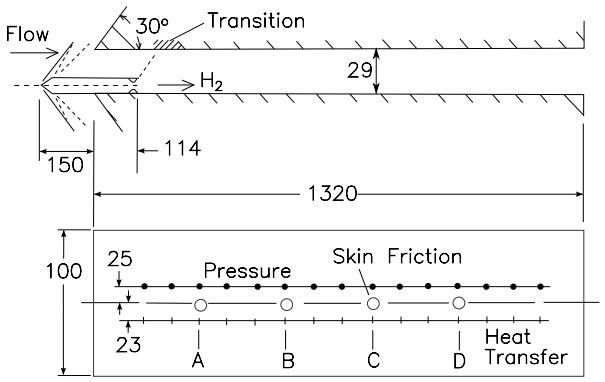

(a) Experimental configuration

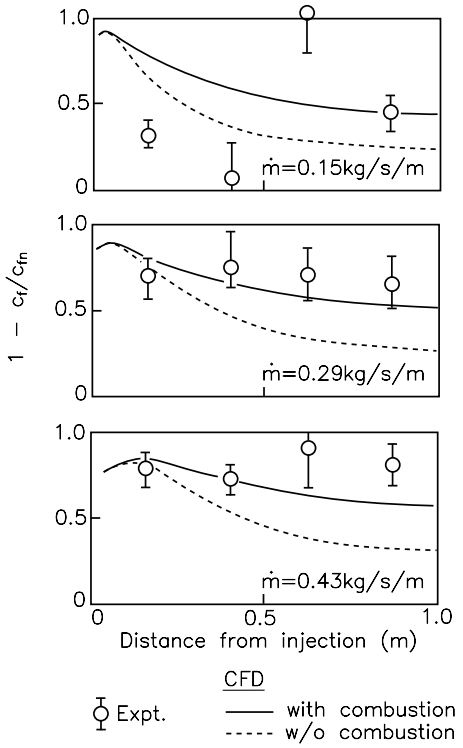

(b) Reductions in skin friction coefficient.

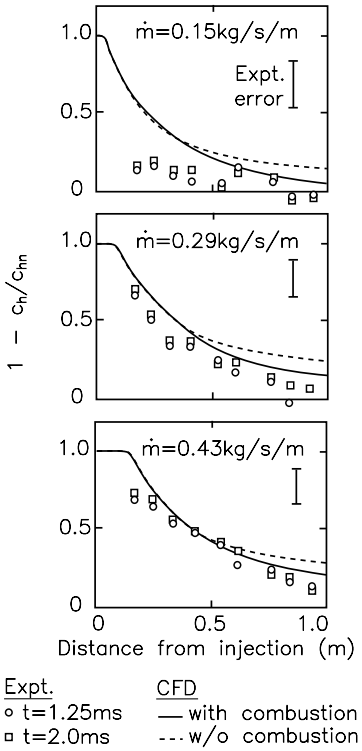

(c) Reductions in heat transfer coefficient.

Figure 2.2: Experimental configuration and results (adapted from Goyne et al., 2000).

into the boundary layer from the combustion process. Secondly, the results show that although a thicker boundary layer does not affect the localised levels of skin friction coefficient reduction, it brings about an earlier ignition of hydrogen in the boundary layer. The earlier ignition of hydrogen is postulated to have been brought about by the higher temperatures present in thicker boundary layers. This has also been observed in the studies by Schetz and Gilreath (1967) and Kirchhartz et al. (2010).

Volchkov et al. (2002) and Perepechko (2003) demonstrated in their numerical simulations that the skin friction reduction potential of boundary layer combustion can also be realised in subsonic flows. The simulations show that when fuel is injected through a porous surface and allowed to burn in a subsonic turbulent boundary layer, the skin friction coefficient decreases significantly from that predicted when no fuel is injected. Volchkov et al. (2002) note that the reduction in skin friction in subsonic flows is brought about by the same factors suggested by Kazakov et al. (1997) for supersonic flows. Once again, the contribution of the reduction in Reynolds stresses to the reduction of skin frictional drag is not mentioned by Volchkov et al. (2002) and Perepechko (2003).

In 2003, Rowan extended the research conducted on the boundary layer combustion technique. Instead of measuring localised skin friction using individual skin friction gauges like in the experiments of Goyne et al. (2000), a stress wave force balance was used to measure the integrated skin friction drag on a circular constant-area combustor. A series of 60.5 mm long injectors, one of which is shown in Figure 2.3, were used to provide different proportions of tangential and cross-stream hydrogen injection. When a 100% tangential fuel injection scheme was used, almost no combustion was observed

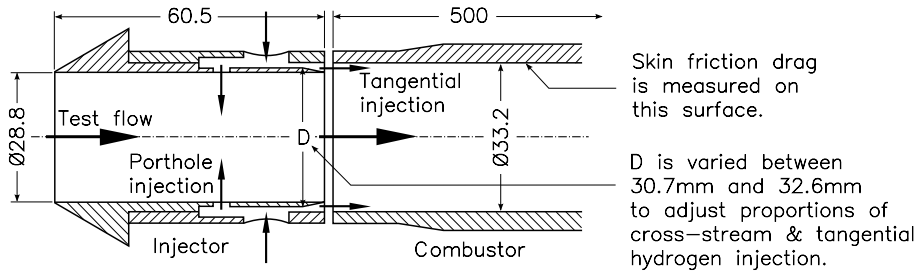

Figure 2.3: Fuel injector and combustor design (adapted from Rowan and Paull, 2006).

within the 500 mm combustor. Rowan postulates that the boundary layer thickness prior to fuel injection is too thin to allow for hydrogen ignition and combustion. This observation supports the finding in the numerical studies of Stephensen (2002) that the thickness of the boundary layer has a significant effect on the ignition of hydro-

gen. Because no combustion occurred, the levels of skin friction reduction measured for the 100% tangential injection tests were mainly due to the film-cooling effects of hydrogen injection. Rowan (2003) also noted in his experiments that the level of skin friction reduction decreases when the equivalence ratio of cross-stream hydrogen injection is increased (see Figure 2.4a). Rowan (2003) attributes the decrease in skin friction reduction to be due to the increased flow disturbances brought by cross-stream

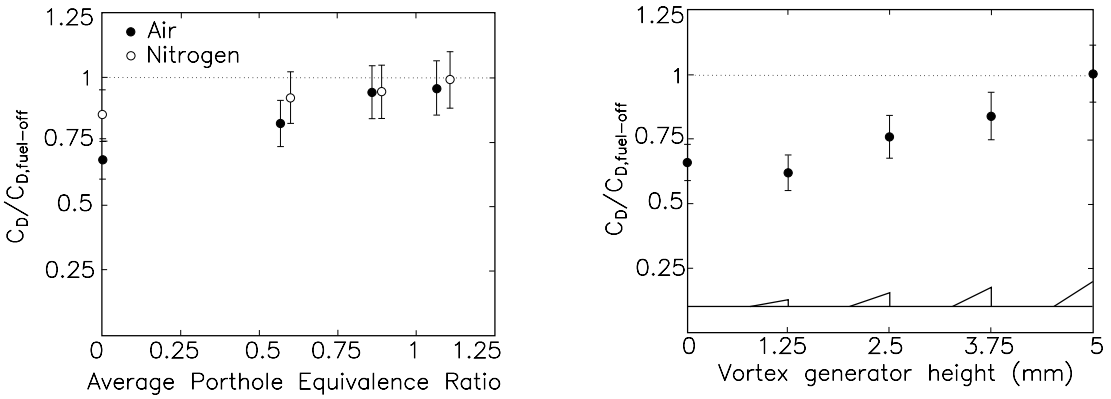

(a) Effect of equivalence ratio of cross-stream injection.

(b) Effect of height of vortex generator.

Figure 2.4: Effects of equivalence ratio of cross-stream fuel injection and vortex generator height on skin friction coefficient (adapted from Rowan and Paull, 2006).

fuel injection. To confirm that the detrimental effect of cross-stream injection on the film-cooling-induced skin friction reduction is brought about by the flow disturbances and not by combustion or mass addition, tests were conducted with an injector that had vortex generators in place of the portholes for cross-stream injection. The vortex generators were semi-pyramidal in shape and were designed to generate pairs of counter-rotating vortices similar to those produced by the normal injection of hydrogen. Shown in Figure 2.4b, the trend in the measured viscous drag with increasing vortex generator height is similar to that observed with increasing porthole equivalence ratio in Figure 2.4a. This confirms that flow disturbances are responsible for the decrease in levels of skin friction reduction brought about by film-cooling.

In 2005, Stalker proposed a theoretical method for the estimation of skin friction and heat transfer when hydrogen is injected and burned in a supersonic turbulent boundary layer. Prior to this, no quantitative analysis of the boundary layer combustion phenomena on skin friction reduction in supersonic flows was available. Stalker (2005) used the Shvab-Zeldovich coupling of flow variables (Zeldovich, 1951) for the extension of Van Driest's theory of turbulent boundary layer skin friction (Van Driest, 1956) to include the injection and combustion of hydrogen in the boundary layer.

For Stalker's theoretical method, instantaneous and complete combustion is assumed to occur whenever hydrogen and oxygen come in contact. Although this assumption leads to an overprediction of the heat release, it does provide an upper limit for the potential for skin friction drag. Stalker presented two sets of equations for the analysis of skin friction reduction; one considering the effects of fuel injection and combustion, and the other considering only the effects of fuel injection. Stalker's theory neatly reduces to Van Driest's theory of turbulent boundary layer skin friction when no fuel injection is considered. Despite its approximate nature, this analysis was able to predict the experimental skin friction and heat transfer measurements presented by Goyne et al. (2000) to within 10 - 15% error bounds, as shown in Figure 2.5. An analysis of the

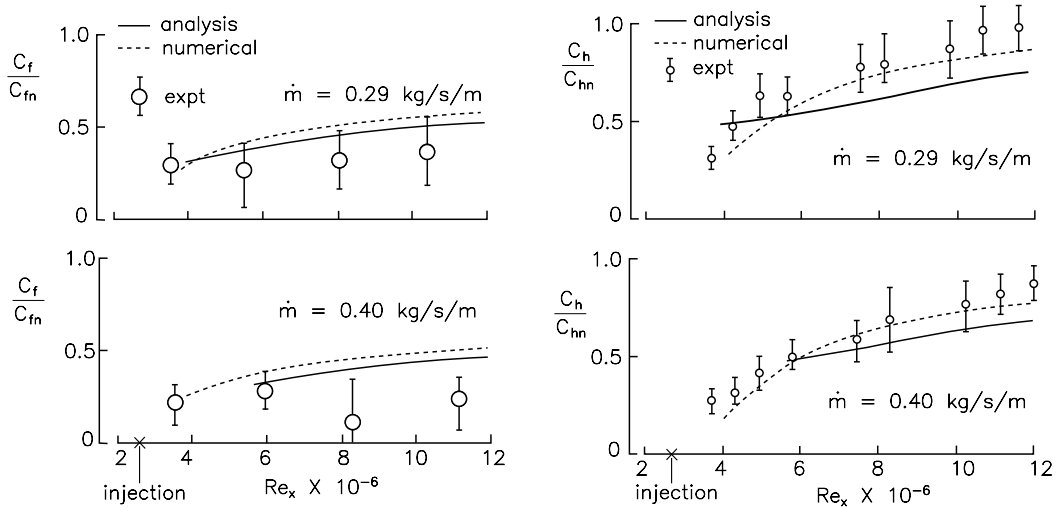

(a) Skin friction coefficient. **(b)** Heat transfer coefficient.

Figure 2.5: Comparison of Stalker's theory with experimental and numerical results of Goyne et al. (adapted from Stalker et al., 2005). The experimental configuration for these results is shown in Figure 2.2a.

results from Stalker's method shows that for flight velocities ranging from 2 - 6 km/s, the skin friction coefficient is less than half of that obtained when hydrogen is not injected, that there is a reduction in overall heat transfer from mainstream to the vehicle body when the combustion heat release in air is less than the stagnation enthalpy, and that both these benefits can be obtained with only modest hydrogen mass flows. It is also in this paper that Stalker suggests the important role played by the Reynolds stresses in supersonic skin friction reduction by boundary layer combustion.

Seeing the need to further research the effectiveness and further explore the effective operating range of reducing turbulent skin friction drag in hypersonic flight by boundary layer combustion, Suraweera (2006) conducted a parametric study to inves-

tigate how varying freestream flow conditions and fuel injection conditions will affect the level of skin friction reduction by boundary layer combustion. Parameters that were varied included the flight speed, flight altitude, fuel injection mass flow rate, fuel injection Mach number, and flight Mach number. The experimental setup is shown in Figure 2.6. Hydrogen was injected behind a backward-facing step into a turbulent

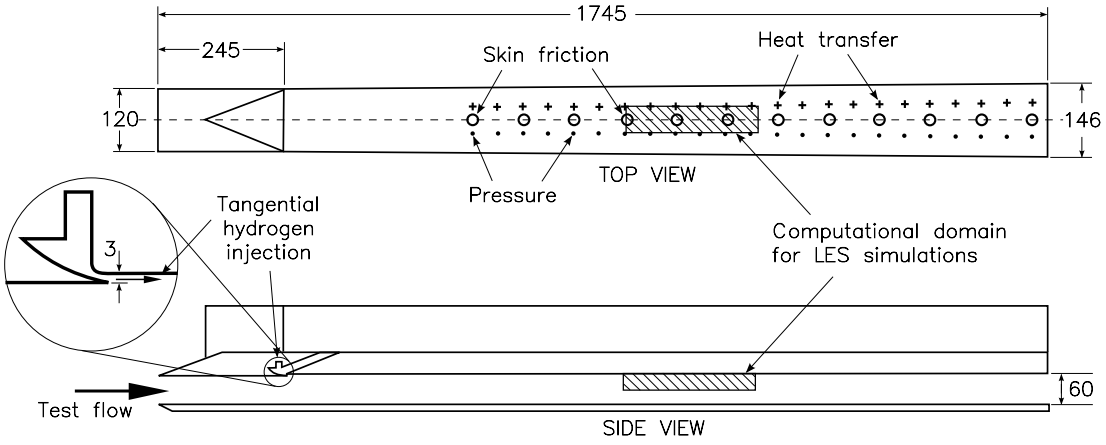

Figure 2.6: Experimental setup of Suraweera (2006). Also shown is the computational domain used by Denman (2007) for his LES simulations.

boundary layer in a 1.745 m long rectangular duct. Using the combustion-induced pressure rise as an indicator for the amount of combustion heat release, the experiments reveal that skin friction reduction increases with the amount of combustion heat release. The experiments also show that a local skin friction coefficient reduction of up to 70 - 80% can be achieved. In addition, the experiments also reveal that decreasing the simulated flight altitude increases the level of skin friction reduction and that increasing the fuel injection mass flows increases the ignition rate of the fuel-air mixture. These experiments also reveal a few limitations of the boundary layer combustion technique. Firstly, the skin friction reduction effect diminishes rapidly as stagnation enthalpies approach 10 MJ/kg. It is thought that this is the same phenomena previously described by Larin and Levin (2001) and Stephensen (2002) where the highly energised freestream flow limits the amount of heat that is released from combustion into the boundary layer. Secondly, the skin friction reduction effect also shows signs of diminishing as the stagnation enthalpy falls below 4.5 MJ/kg and diminishes as the static pressure falls from 50 kPa to 15 kPa. This phenomena is thought to be associated with a reduction in the rate at which combustion reactions take place.

In 2007, Denman conducted Large-Eddy Simulations (LES) to investigate the effects that heat addition through hydrogen combustion has on the turbulent struc-

tures within supersonic and hypersonic boundary layers. Because the use of dynamic subgrid-scale LES models requires no *a-priori* specification of model coefficients, the LES method presents itself as a high fidelity means of studying turbulent processes without the computational expense of Direct Numerical Simulations (DNS). In comparison with all previous numerical investigations of the boundary layer combustion technique performed using the Reynolds-averaged Navier-Stokes simulations, LES provides more insights into the turbulent mechanisms driving the skin friction reduction provided by the boundary layer combustion technique. Denman (2007) selected a computational domain to model a small portion of the rectangular duct used by Suraweera (2005) in his experiments. The computational domain is shown as the hatched areas in Figure 2.6. Hydrogen combustion was modelled using two methods - heat addition from a bulk thermal energy source and the 8-reactions finite-rate reaction scheme of Evans and Schexnayder (1980). For simulations with the 8-reactions finite-rate reaction scheme, the inflow was assumed to be pre-mixed hydrogen and air. Figure 2.7 shows the instantaneous contour plots of static temperature that have been obtained from simulations without heat addition, with bulk thermal energy addition and with combustion modelled using a finite-rate reaction scheme. Other than show-

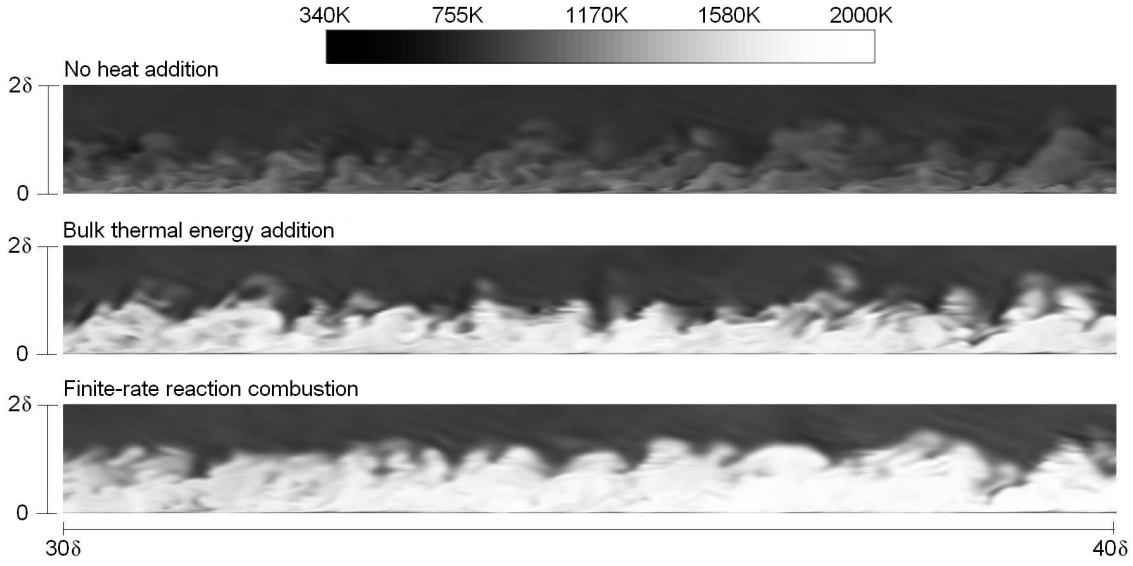

Figure 2.7: Instantaneous contour plot of static temperature. Flow is from left to right. (adapted from Denman, 2007)

ing the effects of heat addition to a turbulent boundary layer, these plots also indicate that the two approaches used to model the combustion processes produce similar results. Figure 2.8 shows a comparison of the localised skin friction coefficient that has been obtained from the simulations of Denman (2007), the experiments of Suraweera (2005) and the predictions from Stalker's 2005 theory. For the case without heat ad-

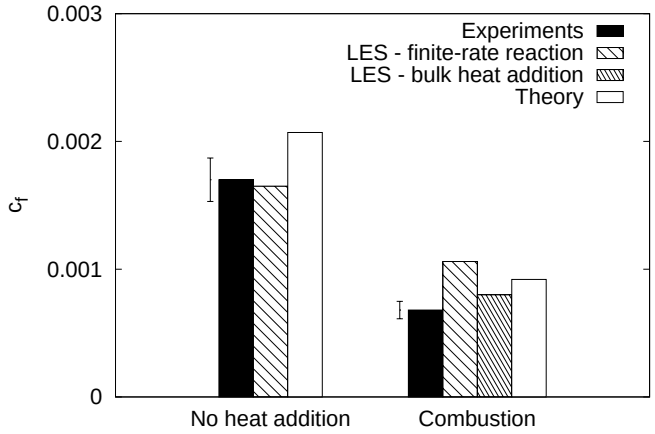

Figure 2.8: Comparison of localised skin friction coefficients (adapted from Denman, 2007).

dition, the skin friction coefficient estimated from the simulations matches that measured in Suraweera's experiments and that predicted using Stalker's theory. However, for the combusting case, the numerically-estimated skin friction coefficient is higher than the experimental measurements and theoretical predictions. Because the injection of hydrogen in Suraweera's experiments is not correctly modelled by either the bulk thermal energy addition method or the pre-mixed finite-rate reaction method in Denman's LES simulations, the possible drag reductions from the film-cooling effects of the surface hydrogen film are not accounted for in the simulations. This explains why the numerically-estimated skin friction coefficient values are higher than those in the experiments and theoretical predictions. Nonetheless, the simulations still estimate a reduction in the skin friction coefficient of about 20 - 40% when combustion occurs. More importantly, this numerical study confirms the suggestion by Stalker (2005) of the important role played by the Reynolds stresses in supersonic skin friction reduction by boundary layer combustion. Figure 2.9 shows the effects of heat addition on Reynolds shear stress with density scaling and on Reynolds shear stress without density scaling. With heat addition, the peak Reynolds shear stress with and without density scaling decreases from that when no heat is added. Denman (2007) postulates that a reduction in Reynolds shear stresses limits the transport of momentum to the wall which then reduces the wall shear stress. The reduction in peak Reynolds shear stress without density scaling in Figure 2.9b also suggests that reductions in skin friction from the addition of heat in the boundary layer are brought about not only by changes to density, but also by the changes in the turbulent transport properties.

Kirchhartz (2010) examined the effect of oncoming boundary layer thickness and entropy layer on boundary layer combustion for skin friction reduction. The experimental configuration used (Figure 2.10) was similar to that of Rowan (2003), in which

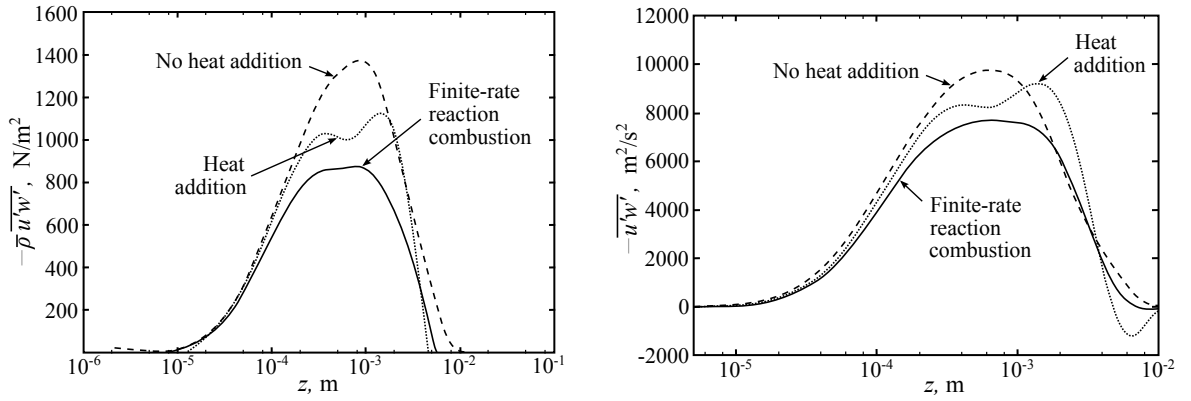

(a) Reynolds shear stress with density scaling. **(b)** Reynolds shear stress without density scaling.

Figure 2.9: Effect of heat addition on Reynolds shear stresses (adapted from Denman, 2007).

the integrated skin friction drag on the internal surface of a 500 mm constant-area combustor was measured using a stress wave force balance. To investigate the effects of upstream boundary layer properties on boundary layer combustion, a range of different inlets were used. Two sharp leading edge inlets with different lengths (60.5 mm and 244.5 mm) were used to study the effects of oncoming boundary layer thickness. In addition, both inlets had leading edges that could be interchanged for leading edges with 0.5 mm bluntness. For the sharp leading edge configurations, a comparison between the tests using a 60.5 mm inlet and 244.5 mm inlet shows that combustion occurs at a lower stagnation enthalpy when a longer inlet is used. The short inlet only produces combustion at a stagnation enthalpy of 7.8 MJ/kg. This result supports the findings

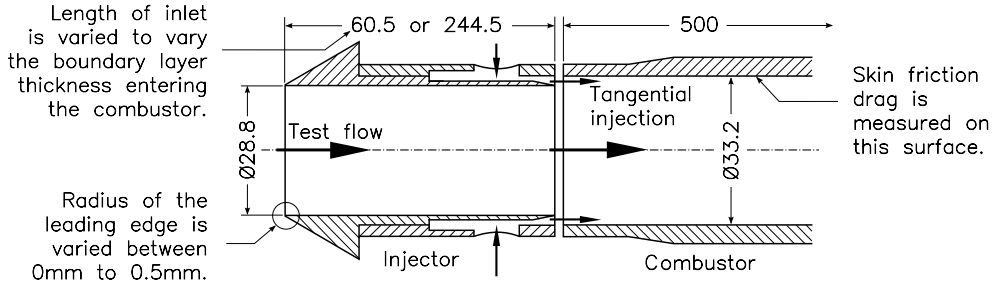

Figure 2.10: Experimental setup of Kirchhartz (2010).

of Rowan (2003), where no combustion occurred for tests that were conducted with a 60.5 mm inlet at stagnation enthalpies below 7.8 MJ/kg. A CFD analysis of the 60.5 mm and 244.5 mm inlets by Kirchhartz (2007) showed that due to the higher boundary layer temperatures, the ignition of hydrogen occurs earlier in the combustor fitted with the longer inlet. Kirchhartz (2007) demonstrated that blunted leading edges also promote an earlier ignition of hydrogen in the combustor. It is, however, not possible to deduce

whether the resulting stronger shock impingement or entropy layer from the bluntness is the main contributor to the improved ignition characteristics. The experiments of Kirchhartz (2010) show that when hydrogen burns, the integrated drag coefficent reduces by up to 77% from that when no hydrogen was injected. Kirchhartz (2010) also showed that the compression of the mainstream flow from boundary layer combustion can be modelled from the resulting growth of displacement thickness. In addition, Kirchhartz (2010) also demonstrated that by accounting for the combustion-induced pressure rise in the combustor with the use of local similarity, Stalker's boundary layer combustion theory can be used to predict the skin friction drag measurements.

It is clear from this review that there has been a considerable amount of research conducted to demonstrate the drag reduction potential of boundary layer combustion. However, as all the experiments and simulations undertaken so far focused only on the flow phenomena in the combustor, the effects of upstream flow disturbances were not accounted for. As such, there are still uncertainties with regards to how flow non-uniformities can affect the effectiveness of the boundary layer combustion technique in reducing skin friction. Section 2.2 reviews the types of flow disturbances that can be encountered in scramjets and discusses the possible effects that these disturbances can have on the drag reduction potential of the boundary layer combustion technique.

2.2 Flow disturbances & their possible effects on boundary layer combustion

There exist many different types of flow disturbances in realistic scramjet flowfields. Figure 2.11 shows a summary of the types of flow disturbances that may possibly affect the drag reduction capabilities of the boundary layer combustion technique.

Incident shock wave impingement and swept shock interaction are the most common form of disturbances that occur throughout the entire flowfield of scramjet engines. Although there has been no literature to date discussing the effects of incident shock wave impingement on the boundary layer combustion technique, there exists a wealth of literature that contains discussions on these effects on the film-cooling technique. Juhany and Hunt (1994) injected helium at Mach 2.2 into a Mach 2.4 mainstream airstream via a backward-facing step slot of height 1.5 mm. At 60 slot heights, a two-dimensional oblique shock is generated to impinge directly on the flow. Juhany and Hunt (1994) showed that shock wave impingement has a detrimental effect on the film-cooling effectiveness. Using visualisations by schlieren images and the inspection of the wall pressure distribution for an inflection point, Juhany and Hunt (1994) deduced

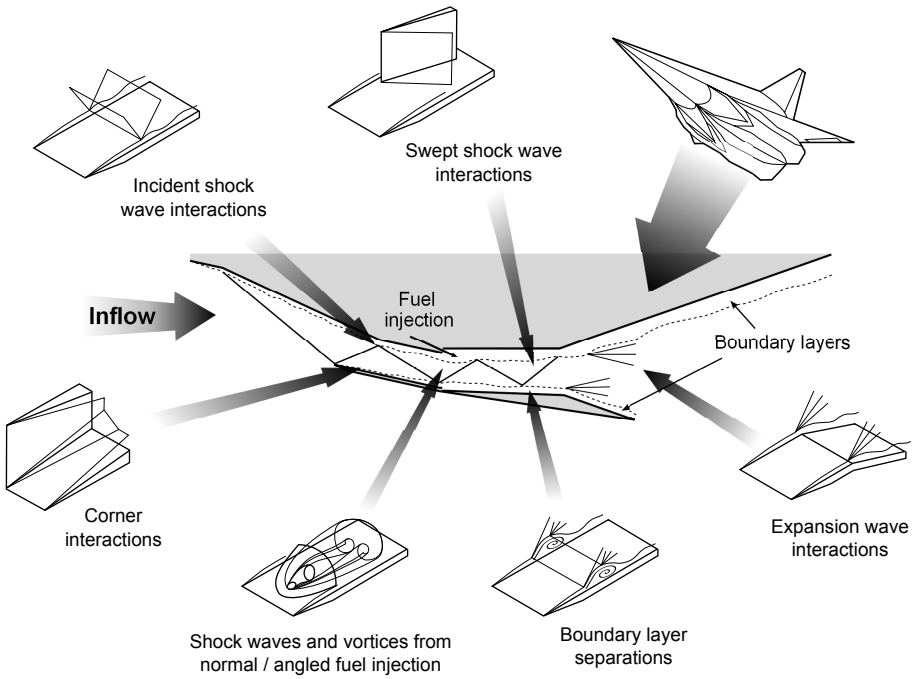

Figure 2.11: Typical flow disturbances encountered in scramjet flowfields (adapted from Hemsch, 1992).

that the injected helium separated upon shock wave impingement. Juhany and Hunt (1994) also noted that the injection of a fluid with a higher speed of sound (like helium or hydrogen) increases the speed of sound in the boundary layer, reducing the fullness of the Mach number profile, and therefore increasing the susceptability of the boundary layer to separate. The work of Kanda et al. (1996) and Kanda and Ono (1997), in which shocks generated from 6°, 7° and 8° wedges impinged on a nitrogen film, also showed that the coolant film separated when hit by a sufficiently strong shock wave. Like in the work of Juhany and Hunt (1994), they also measured a decrease in film-cooling effectiveness in the presence of shock-impingement. Kanda et al. (1996) attributed this to be a result of an increase of adiabatic wall temperature brought about by the decrease in local Mach number. This reduction of film-cooling effectiveness is also reported by Olsen and Nowak (1995), Takita and Masuya (2000) and Peng and Jiang (2009). However, none of these studies indicated whether the injected film was swept out of the boundary layer. To the author's knowledge, the effects of the interaction of a swept shock wave with the injected film have not been investigated before. The interaction of a swept shock wave with a turbulent boundary layer, however, is a well researched topic (Knight et al., 2003; Panaras, 1992; Settles and Dodson, 1991).

Kanda et al. (1996) suggested that the decrease in film-cooling effectiveness in the presence of shock wave interactions is due to the enhancment of mixing between the

injectant and mainstream. Several reports have shown that turbulence increases downstream of a shock wave interaction with a turbulent boundary layer (Anyiwo and Bushnell, 1982; Zang and Bushnell, 1984) and with a turbulent shear layer (Lu and Wu, 1991). Experimental investigations by Buttsworth (1994) and numerical simulations by Peng and Jiang (2009) have confirmed that these shock wave interactions can lead to enhanced mixing. For the boundary layer combustion technique, if the injected hydrogen does not get swept out of the boundary layer, the enhanced mixing brought about by the presence of shock wave interactions may actually be more beneficial to the drag reduction potential of boundary layer combustion.

The second most common form of disturbance is that of the flowfield resulting from the cross-flow injection of fuel. The complex flowfield (see Figure 2.12) contains regions of strong shock interactions and vortices. Viti et al. (2009) presents an excellent descrip-

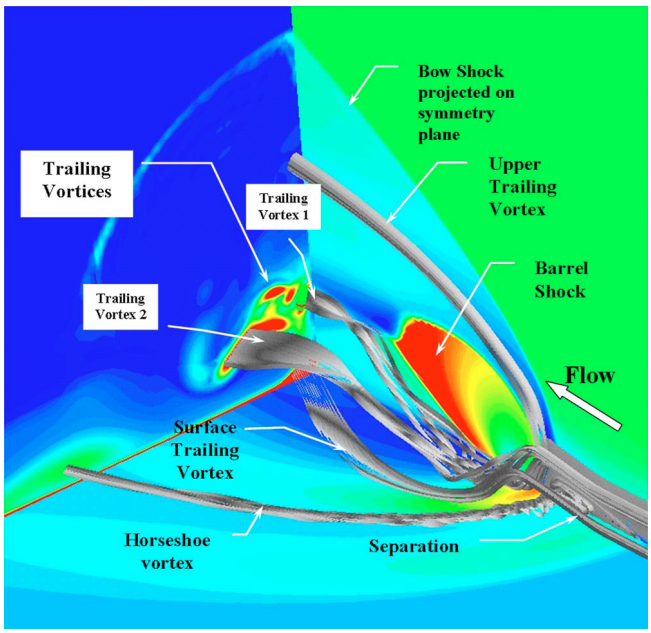

Figure 2.12: Complex flowfield resulting from the cross-flow injection of fuel (Viti et al., 2009)

tion of this complex flowfield. The main concern of relevance to the film-cooling and boundary layer combustion techniques is the effect of streamwise vorticity from this flowfield. Commonly used to improve the mixing of fuel and air for scramjet applications (Heiser and Pratt, 1994; Riggins and Vitt, 1995; Swithenbank and Chigier, 1969; Wheatley and Jacobs, 2010), streamwise vorticity can be detrimental to the drag reduction capabilities of boundary layer combustion. As mentioned in Section 2.1, Rowan (2003) demonstrated that disturbances from cross-stream fuel injection and from vortex generators decreased the levels of skin friction reduction. But because no combustion was observed in his experiments, the only definite conclusion that can be made is that

the vorticity affected the film-cooling-induced skin friction reduction. Whether the hydrogen remains in the boundary layer for combustion still remains unknown. Similar to the effects of incident shock wave impingement, the effects of mainstream vorticity on the film-cooling technique have also been extensively investigated in the turbomachinery industry (Haven et al., 1997; Leylek and Zerkle, 1994). The counter-rotating vortex pair generated from cross-flow injection has been known to lift the gas film needed for film-cooling away from the surface (Heidmann and Ekkad, 2008). Once again, none of these studies indicated to what extent the injected film was swept out of the boundary layer.

A review of the existing literature shows that despite the great potential of the boundary layer combustion technique for the reduction of skin friction drag, there lacks an understanding of how flow disturbances can affect the wall gas film required for this drag-reduction method. To address this, the effects of incident shock impingement, swept shock interactions and vorticity on the levels of skin friction reduction achievable by boundary layer combustion are investigated in the present study.

Chapter 3

Details of Experiments

The chapter starts with a description of the experimental model which includes details of the fuel delivery system and instrumentation. This is then continued with a description of the test facility. The test conditions and fuelling conditions together with their corresponding uncertainties are then presented. The chapter concludes with a description of the data reduction method used for the pressure and drag measurements obtained in the experiments.

3.1 Experimental model

Figure 3.1 shows the experimental model used in the current project. It consists of a Rectangular-to-Elliptical Shape Transition (REST) inlet, a fuel injection system and a circular constant-area combustor that is coupled to a stress wave force balance for skin friction drag measurements. The experimental setup used by Kirchhartz (2010) is shown in the lower half of Figure 3.1. The only significant difference between the current experiments and that of Kirchhartz's is that the current experiments include a more realistic scramjet inlet upstream of the combustor. This inlet has been designed to compress oncoming Mach 6 flow to combustor entry conditions similar to those in Kirchhartz's experiments. This then makes the comparison between the current experiments and those of Kirchhartz's possible, with the difference being the larger flow non-uniformities for the present experiments.

The T4 shock tunnel facility at The University of Queensland was used to supply the oncoming test flow to the experimental model. The first set of tests was performed at the design point stagnation enthalpy of 4.8 MJ/kg. By comparing the levels of skin friction reduction measured in the current tests with those measured in Kirchhartz's experiments, it can be found if flow disturbances from a REST inlet have affected the skin friction reduction potential of boundary layer combustion. The other tests that

were conducted included tests at lower and higher stagnation enthalpies, at higher freestream Mach numbers, and also tests with attached vortex generators to simulate the flow disturbances from cross-stream fuel injection.

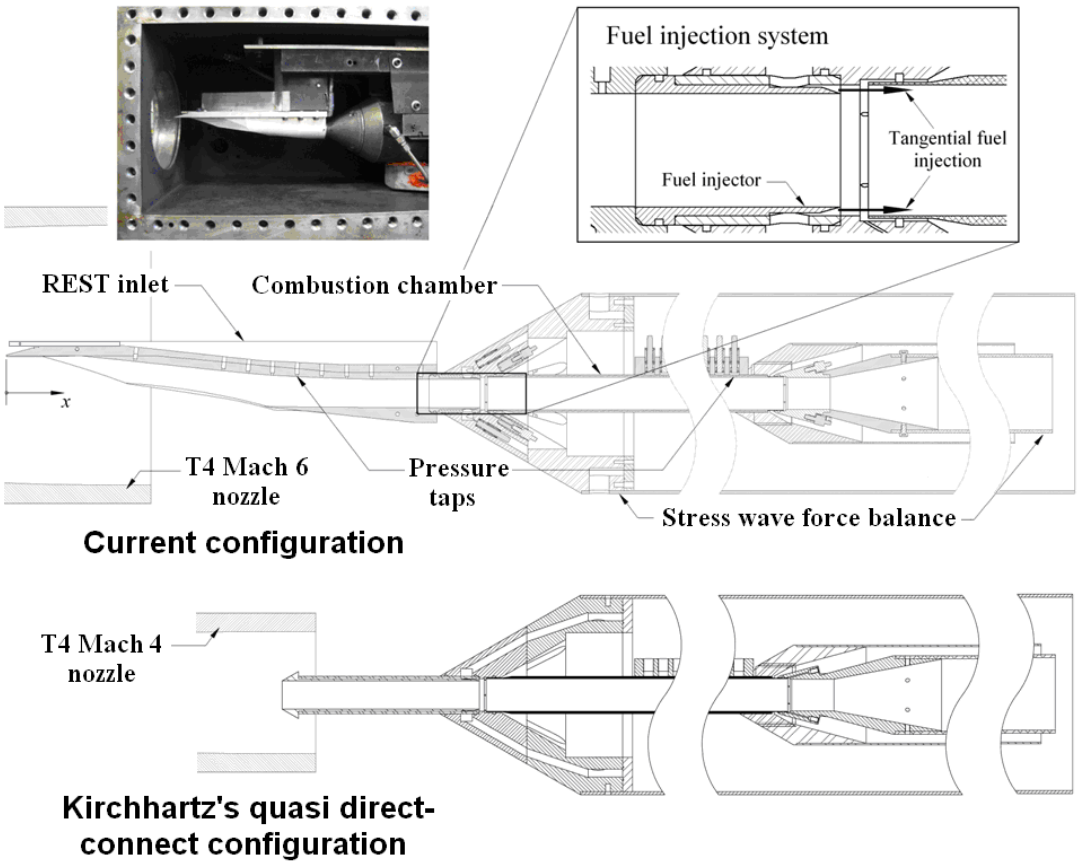

Figure 3.1: Experimental setup used in the current study. Also shown is the experimental setup of Kirchhartz (2010).

3.1.1 REST inlet

The REST inlet was chosen for this experiment because its design is typical of the type that have been proposed for self-starting scramjets (Eggers et al., 2009; Smart and Suraweera, 2009). This type of inlet is currently used on two of the nine flight experiments on the HIFiRE (Hypersonic International Flight Research Experiment) program (Auslender et al., 2009). Designed based on the quasi-stream-tracing technique of Smart (1999), these inlets have a rectangular capture area that smoothly transitions to an elliptical throat, as shown in Figure 3.2. For airframe-integrated scramjet engines of modular designs, it is desirable to have rectangular inlet capture shapes so that they can be easily mounted side-by-side and onto the airframe. It is also desirable for the in-

let to be used in combination with an elliptical combustor. Elliptical combustors are superior to their rectangular counterparts in several ways - the reduced structural weight required to contain a specified pressure, the reduced wetted area which reduces the levels of skin friction drag, and also the reduced complexity with flows related to hypersonic corner flows. In addition, the REST inlet also offers many advantages - it has a fixed geometry and no boundary layer bleed which results in greater scramjet system simplicity, it has been shown to be capable of starting at on-design conditions and self-starting after mechanically-induced inlet unstarts at on-design conditions (Smart, 2001), and it has been shown to be capable of operation at off-design conditions (Smart and Trexler, 2004). Several of these inlets have been successfully tested, including a Mach 7.1 REST scramjet in NASA Langley's combustion heated scramjet test facility (Smart and Ruf, 2006), a Mach 8.0 REST scramjet (Turner, 2010) and a Mach 12.0 REST scramjet (Suraweera and Smart, 2009) in The University of Queensland's T4 shock tunnel facility.

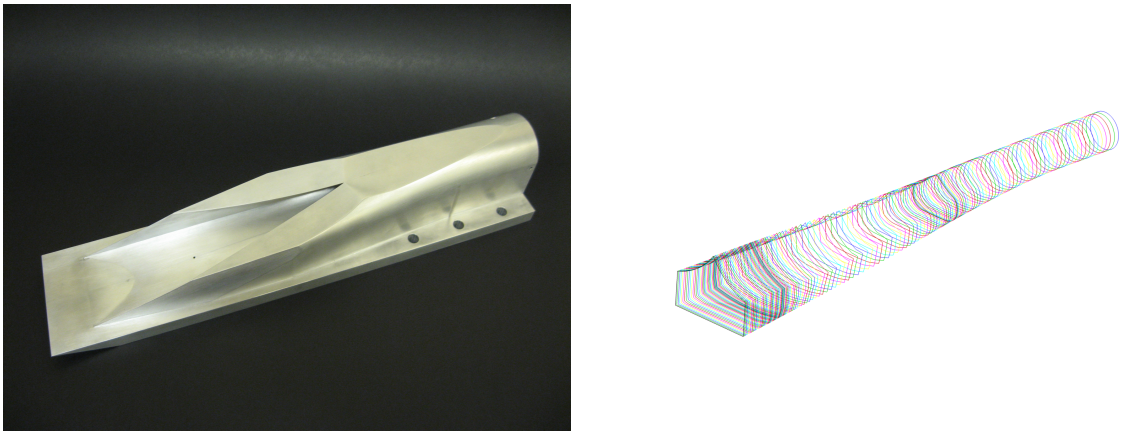

(a) Photograph of the REST inlet.

(b) Internal cross-sectional shape distribution of the REST inlet.

Figure 3.2: The REST inlet.

In order to allow a direct comparison of the results from the current experiments with those of Kirchhartz, the REST inlet was designed to produce combustor entry conditions similar to those obtained for the direct-connect inlet in Kirchhartz's 5 MJ/kg experiments. The REST inlet for the current experiments was designed to transition to a combustor of circular cross-section[1]. For the current experiments, the REST inlet was designed to compress flow from a Mach 6.2 condition to a Mach 4.5 condition[2].

[1] Note that a circle is an ellipse with an eccentricity of zero.

[2] The author wishes to acknowledge the helpful guidance of Dr James Turner and Prof Michael Smart in the design of the internal flowpath of the REST inlet.

The stagnation enthalpy for the design condition is 5 MJ/kg. This corresponds to a Mach 10 flight condition. Designing the inlet to compress from the outflow pressures produced by the Mach 10 nozzle of the T4 shock tunnel facility to the pressures entering Kirchhartz's combustor would require the compression ratio to be larger than 100. Large compression ratios of this order of magnitude can create unnecessary and onerous system constraints on the design of scramjet inlets, such as the need for variable geometry to start the inlet, or flow bleed to combat boundary later separation (Smart, 2012). Large compression ratios in scramjet inlets can also lead to significant aerothermodynamic losses and high external drag. By designing the inlet to compress from the outflow pressures produced by the T4 Mach 6 nozzle, a compression ratio of only 9.5 is required. This value of compression ratio is of the same order of magnitude as those of the REST inlets of Smart and Ruf (2006), Turner (2010) and Suraweera and Smart (2009). This explains why the REST inlet in the current project was designed to ingest a Mach 6.2 flow rather than a Mach 10 flow.

The 440-mm long inlet has a 70 mm wide frontal capture area of $2.5 \times 10^{-3}\,\mathrm{m}^2$ that contracts to a circular exit area of $6.5 \times 10^{-4}\,\mathrm{m}^2$. This gives a total geometric contraction ratio of 3.84. All leading edges have a 0.5 mm radius bluntness. The inlet has an internal contraction ratio of 1.61. The centreline of the upper (bodyside) surface of this inlet was instrumented with nine Kulite XTEL-100-190M pressure transducers at 130 mm, 220 mm, 245 mm, 269 mm, 294 mm, 319 mm, 345 mm, 370 mm and 420 mm from the leading edge (see Figure 3.1).

3.1.2 Fuel injector & supply system

A brass fuel injector was connected to the end of the REST inlet, as shown in Figure 3.3. The injector delivered hydrogen through an annular slot which had a throat area of $6.65 \times 10^{-5}\,\mathrm{m}^2$ that expanded by 17° to an exit area of $2.14 \times 10^{-4}\,\mathrm{m}^2$. Hydrogen was supplied to the annular slot from a Ludwieg tube fuel delivery system via a primary and secondary annular plenum chamber, as shown in Figure 3.3b. The use of a Ludwieg tube fuel delivery system ensured that a near-constant fuel flow rate was available during the test times in the current experiments (Gangurde et al., 2007; Ludwieg, 1955). An ASCO-Joucomatic SCB223A103 fast-acting solenoid valve separated the plenum chambers from the fuel delivery system and was used in the current experiments to control the timing of fuel injection.

3.1.3 Vortex generators

The effects of the vorticity generated by conventional cross-stream fuel injection on the

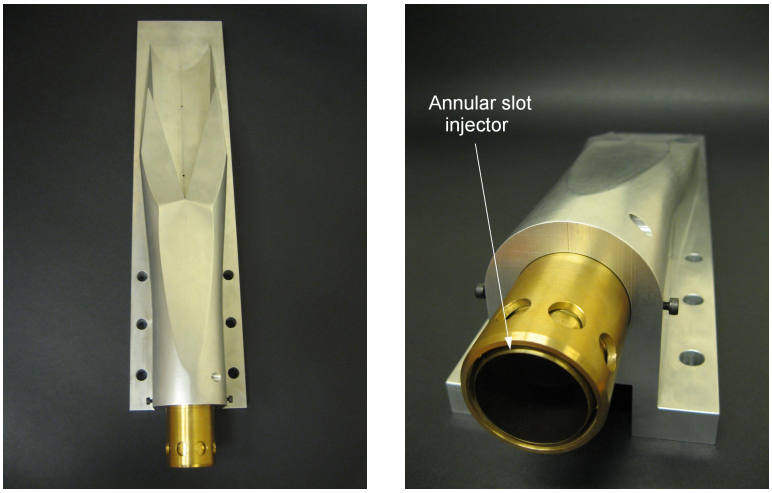

(a) Brass fuel injector shown attached to the end of the aluminium REST inlet.

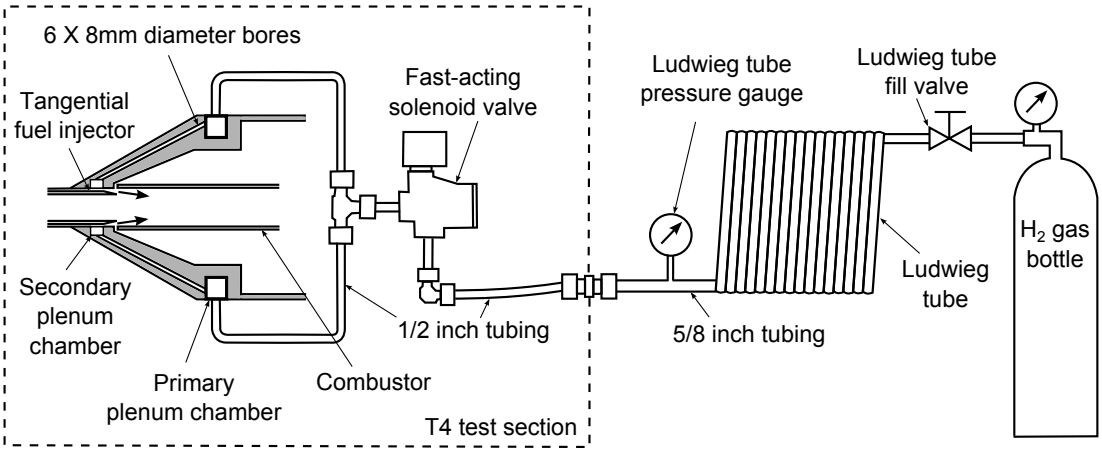

(b) Fuel supply system.

Figure 3.3: Fuel supply and injection system.

drag reduction potential of the boundary layer combustion technique are unknown. For the current experiments, instead of injecting fuel to generate the vorticity, 5-mm-by-5-mm-by-5-mm vortex generators of semi-pyramidal shape (Figure 3.4) were used. These vortex generators produced counter-rotating vortex pairs that are representative of those produced when fuel is injected cross-stream into the flow (Rowan, 2003). The height of these vortex generators was selected to create a flow obstruction similar to that brought about by a normally-injected fuel jet with a penetration height of 5 mm. For the current study, the use of fuel injection to generate vorticity adds complexity to the analysis of the results because the drag reduction potential of boundary layer combustion can be affected by both the addition of extra fuel and the generated vorticity.

The use of vortex generators in place of fuel injection is a good way to isolate the influence of the vorticity on the drag reduction potential of boundary layer combustion from that of the effects of extra fuel addition.

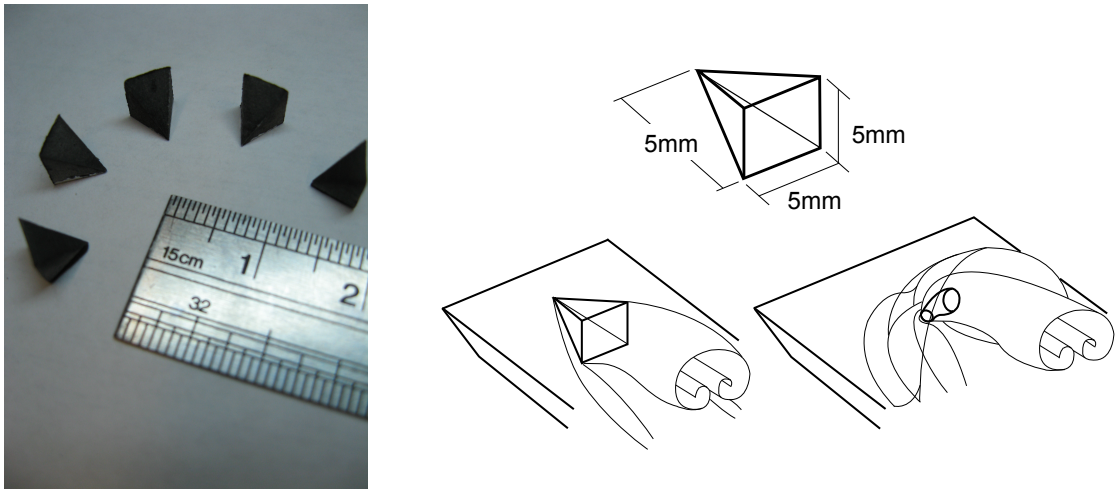

(a) Five vortex generators shown with a metal ruler.

(b) Using vortex generators to generate counter-rotating vortex pairs that are representative of those produced when fuel is injected cross-stream.

Figure 3.4: Vortex generators.

In scramjet engines, fuel injection is commonly employed either on the inlet (Turner, 2010) or near the entrance of the combustor (Curran and Murthy, 2000). Inlet injection is a viable scheme of injecting fuel that may aid the mixing and combustion process in the combustor by allowing more time for fuel to mix with air (Turner, 2010). To simulate the effects of this, three vortex generators were attached to the bodyside surface of the REST inlet at 0.157 m downstream of the leading edge, as shown in Figure 3.5. The tips of these vortex generators were located 13 mm apart. To simulate the effects of fuel injection near the entrance of the combustor, five vortex generators were attached at 49.5 mm upstream of the fuel injection plane in the fuel injector, as shown in Figure 3.6. These vortex generators were equally spaced at 72° around the inner circumference of the fuel injector.

3.1.4 Combustor

Figure 3.7 shows a schematic of the 500-mm long constant-area combustor used in the current experiments. The 33.2 mm internal diameter combustor was instrumented with twenty PCB 112A pressure transducers. Due to the spatial constraints in the experimental set up, the furthest upstream position that the first pressure transducer

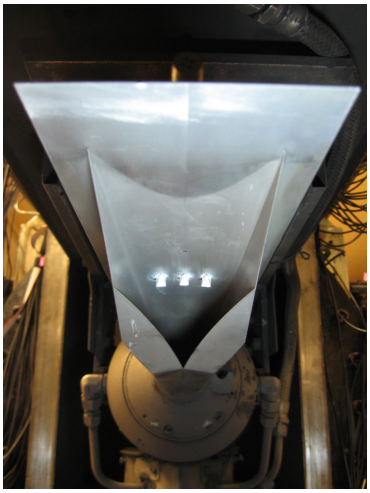

(a) Three vortex generators attached onto the bodyside surface of the REST inlet.

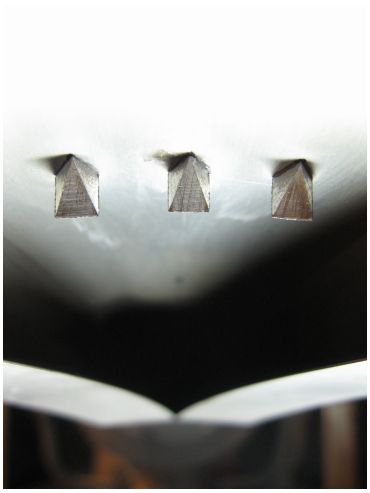

(b) Close-up view of the three vortex generators on the REST inlet.

Figure 3.5: Vortex generators on the REST inlet.

(a) Five vortex generators attached around the inner circumference of the injector.

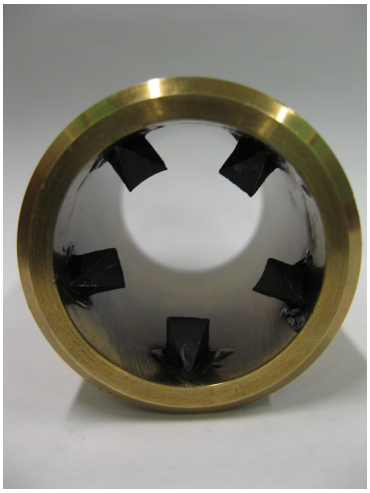

(b) Close-up view of the five vortex generators in the injector.

Figure 3.6: Vortex generators in injector.

could be located was at 160 mm from the leading edge of the combustor. Subsequent transducers were located at 15 mm streamwise spacing downstream of the first transducer. A stainless steel threaded adapter was used to attach the combustor to the force balance.

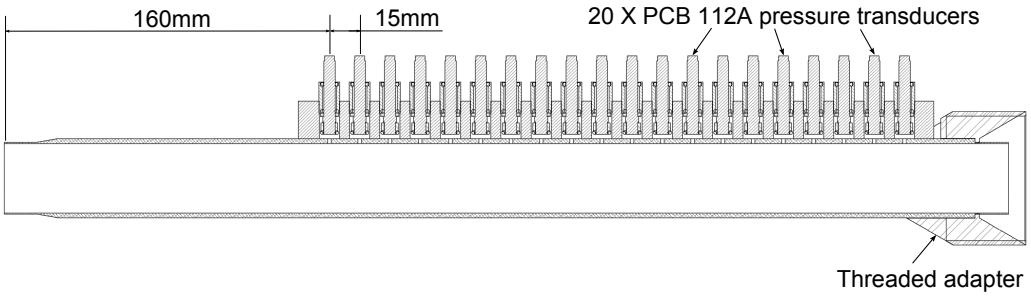

Figure 3.7: Combustor.

3.1.5 Stress wave force balance

A stress wave force balance was used to measure skin frictional drag forces in the combustor of the experimental model in the T4 shock tunnel facility. In comparison with local skin friction measurements made using skin friction gauges, a force balance measures the integrated effect of skin friction drag on the combustor. With the aim of this project being to show how much overall drag can be reduced by using boundary layer combustion, the force balance is the ideal instrument to use. The stress wave force balance, first proposed by Sanderson and Simmons (1991), is capable of measuring integrated forces on models tested in impulse test facilities with short test times in the order of 1 to 3 milliseconds. In impulse facilities, the limited duration of test flow is usually insufficient for the vibrations to be damped out sufficiently for accurate force measurements to be made with conventional force balances. Because the stress wave force balance technique infers the time history of aerodynamic forces from the stress wave activity in the model via strain time histories, the test model is not required to be in a state of force equilibrium. Experiments conducted in impulse facilities (Smith and Mee, 1996; Smith et al., 2001; Tanimizu et al., 2009; Tuttle et al., 1995) have shown that this technique can measure forces that agree well with theoretically calculated forces.

The stress wave force balance configuration used in the current experiments is shown in Figure 3.8. It is similar to that used by Tanno et al. (2001),Rowan (2003) and Kirchhartz (2010). The force balance configuration was used only to measure axial

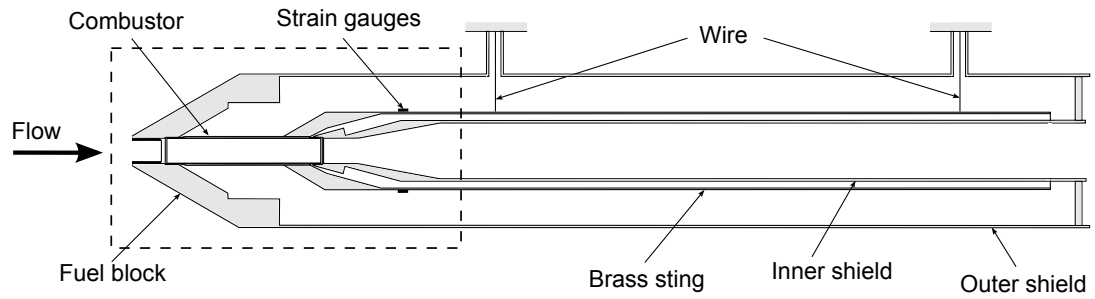

(a) Schematic of the stress wave force balance (not shown to scale).

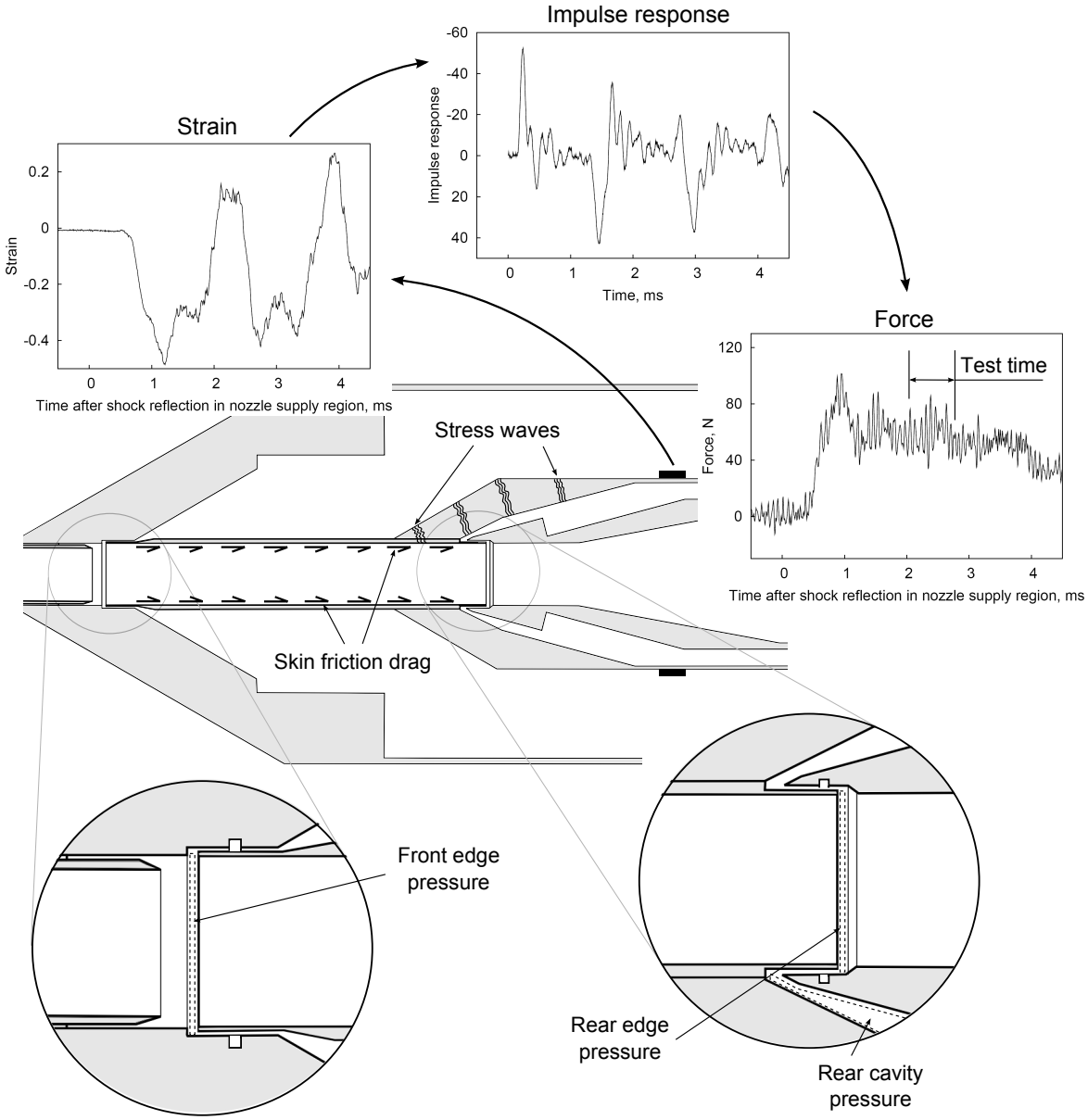

(b) Operational principle of the stress wave force balance.

Figure 3.8: Stress wave force balance.

forces, and consists of several components. The aluminium combustor, where skin friction drag on the internal surface are to be measured, was connected to a 2430-mm long brass sting via a stainless steel adapter. High viscosity grease (Dow Corning Molykote 111) was applied to the threads of the adapter prior to attachment to fill any air voids and maximise the transmission of stress waves (Chiu, 1996). The choice of materials for the combustor and sting represented the best compromise between low model flexibility, fast response time and high signal-to-noise ratio (Sanderson and Simmons, 1991). The sting was instrumented with piezo-electric film strain gauges and semi-conductor strain gauges in a layout as shown in Figure 3.9. The piezo-electric film, which was adhered around the circumference of the sting for bending compensation, was made from a poly-vinylidene fluoride film that had been coated with Nickel-Copper electrodes on either sides (Smith and Mee, 1996). The semi-conductor strain gauges were Micron Instruments SS-080-050-120PB-SSGH gauges.

The sting and attached combustor were suspended horizontally in the test section of the test facility by two thin wires, in a way that only movement in the axial direction is permitted. When an aerodynamic load is applied to the internal walls of the combustor, stress waves are initiated within the combustor. These stress waves then propagate and reflect within the structure of the combustor and the brass sting. Time histories of strain were recorded by the strain gauges.

Sample force traces are shown in Figure 3.8b. With prior knowledge of the system characteristics (impulse response) obtained through calibration, a deconvolution procedure was used to determine the time history of the applied aerodynamic load from the time history of measured strain (Mee, 2002b).

To ensure that only the skin friction drag on the internal surface of the combustor was measured, the remaining parts of the combustor and brass sting assembly were shielded from the test flow. The outer shielding isolated the exterior walls of the combustor, the sting and the strain gauges from forces generated by the oncoming hypervelocity flow during each test. The inner shield isolated the interior walls of the sting from forces generated by the flow exiting from the combustion chamber. The force balance was initially designed to have o-rings to seal the front and rear edges of the combustor to prevent flow leakage and pressure build-up. Tests by Kirchhartz (2010) showed that the removal of these o-rings had negligible effect on the pressure build-up in the front and rear cavities. This, too, allowed the combustor to move axially without any frictional resistance from the o-rings. Therefore, the o-rings were not used in the current experiments. Both the front and rear leading edges of the combustor were machined from a thickness of 2.4 mm to 0.75 mm to reduce the surface areas on

which extraneous pressure forces can act. Due to the finite thickness of the combustor leading and trailing edges, the front and rear edge surfaces of the combustor-sting assembly can still be exposed to some pressures when the test flow arrives. Six pressure transducers at each end of the combustor measured pressures in front and rear edge regions. In addition, the pressure in the rear cavity was also monitored by two pressure transducers. To ensure that only skin friction drag acting on the internal surface of the combustor was extracted, these pressures were measured and the extraneous forces due to the front edge, rear edge and rear cavity pressures were accounted for in the processing of the drag measurements. For tests without fuel injection, because the static pressures changed by less than the 1% from the front edge to the rear edge of the combustor, the resulting level of correction was typically less than 1% of the measured net skin friction drag. However, for tests in which combustion occurred, the static pressures at the rear edge of the combustor were usually three or four times higher than those at the front edge (see Figure 5.4). The typical level of correction that resulted from this pressure difference was 14% of the measured net skin friction drag for tests in which combustion occurred.

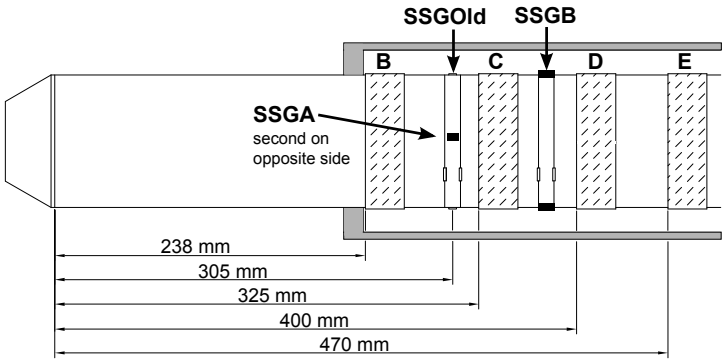

Figure 3.9: Layout of strain gauges on the brass sting (taken from Kirchhartz, 2010). Gauges B, C, D and E are the piezo-electric film strain gauges, while gauges SSGA, SSGB and SSGOld are the semi-conductor strain gauges.

3.2 Test facility

The T4 Stalker tube (Stalker, 1966, 1967, 1989, 2006; Stalker and Morgan, 1988; Stalker et al., 2005) was used to supply the oncoming test flow to the experimental model. The tunnel consists of five main sections (as shown in Figure 3.10a) - the reservoir, the compression tube, the shock tube, a convergent-divergent nozzle and the test section. A 90 kg piston separates the reservoir from the compression tube. A primary steel

diaphragm separates the compression tube from the shock tube. A secondary Mylar diaphragm separates the shock tube from the nozzle and test section.

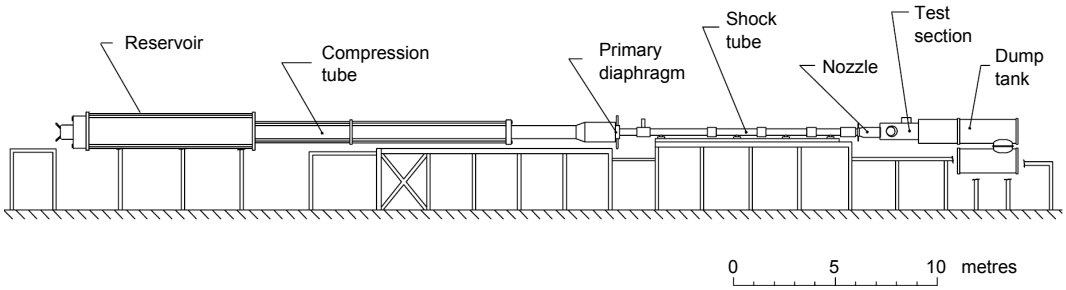

(a) Layout of the T4 Stalker tube (taken from Tanimizu, 2008).

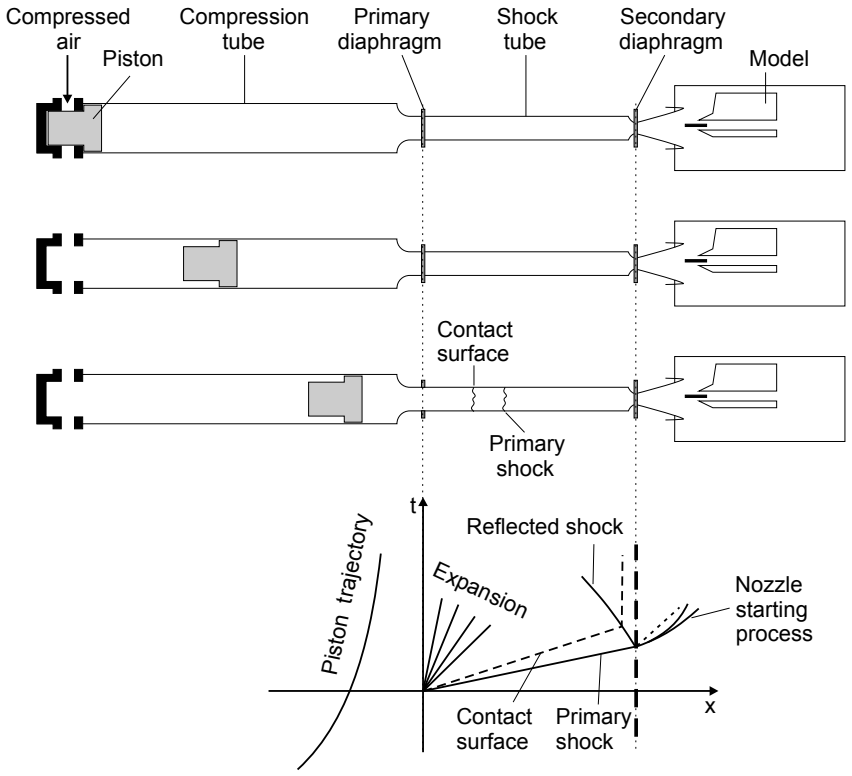

(b) Operational principles of a Stalker tube (taken from Kirchhartz, 2010).

Figure 3.10: T4 Stalker tube

Figure 3.10b shows schematically the operating principles of a Stalker tube. Prior to a test run, the shock tube is filled with the test gas (either air or nitrogen), the compression tube with driver gas (a mixture of helium and argon), and the reservoir with high-pressure air. On firing, the high-pressure gas drives the piston through the compression tube. This compresses the driver gas almost isentropically (to pressures of up

to 75 MPa in the present tests) until the burst pressure of the primary diaphragm is reached. When the primary diaphragm bursts, the large pressure differential between the driver gas and test gas drives a shock wave through the shock tube that compresses and accelerates the test gas towards the nozzle. Upon encountering the end of the shock tube, the incident shock wave reflects back towards compression tube and stagnates the test gas. This creates a region of hot and highly-pressurised gas which then expands through the convergent-divergent nozzle to the desired test conditions.

The convergent-divergent nozzles used for this experimental program were the Mach 6 and Mach 8 nozzles. The Mach 6 nozzle was used to provide design-point test conditions as well as conditions at higher stagnation enthalpies. This axisymmetric contoured nozzle, which was designed using the method-of-characteristics (Jacobs and Stalker, 1989), has a throat diameter of 0.025 m and exit diameter of 0.262 m and is about 0.8 m in length. On the other hand, the Mach 8 nozzle was used to provide conditions that were representative of over-speeding the engine. This axisymmetric contoured nozzle, which was designed by Craddock (2000), has a throat diameter of 0.0164 m and exit diameter of 0.27 m and is about 1.11 m in length.

To check the uniformity of the nozzle outflow, a survey using a Pitot rake was conducted prior to the experiments. Figure 3.11 overlays the schema of the experimental model on the measured ratio of Pitot-to-nozzle-supply pressure for the Mach 6 nozzle at $H_s = 5.4\,\mathrm{MJ/kg}$. As the REST inlet was designed assuming a uniform inflow, it is important that the flow ingested by the inlet was as uniform as possible to ensure that the inlet performs as it has been designed. As shown in Figure 3.11, the entire capture area of the REST inlet was located in the region of uniform flow where the Pitot-to-nozzle-supply pressure ratio was constant to within $\pm 6\%$. Note that at the first Pitot survey plane shown in Figure 3.11, there are two peaks located at 0.11 m from the axis in the Pitot-to-nozzle-supply pressure ratio profile. Because the Mach 6 nozzle is physically truncated to a length shorter than that for which it was originally designed[3], the outflow from the nozzle contains a region of under-expanded gas that is at a higher Pitot pressure than that in the core flow. This region of under-expanded gas travels downstream to $x \approx 0.22\,\mathrm{m}$ before it gets cancelled out by expansion waves from enamating from the corner of the nozzle exit. This explains the peaks in the Pitot-to-nozzle-supply pressure ratio profile at the first Pitot survey plane.

[3]In the original design profile of the Mach 6 nozzle, the exit diameter does not change significantly over the length of the last portion of the nozzle. Since a longer nozzle takes longer time to start, the Mach 6 nozzle was truncated to a shorter length to minimise the losses in test time durations, which comes at the expense of minor losses in the size of the test core flow.

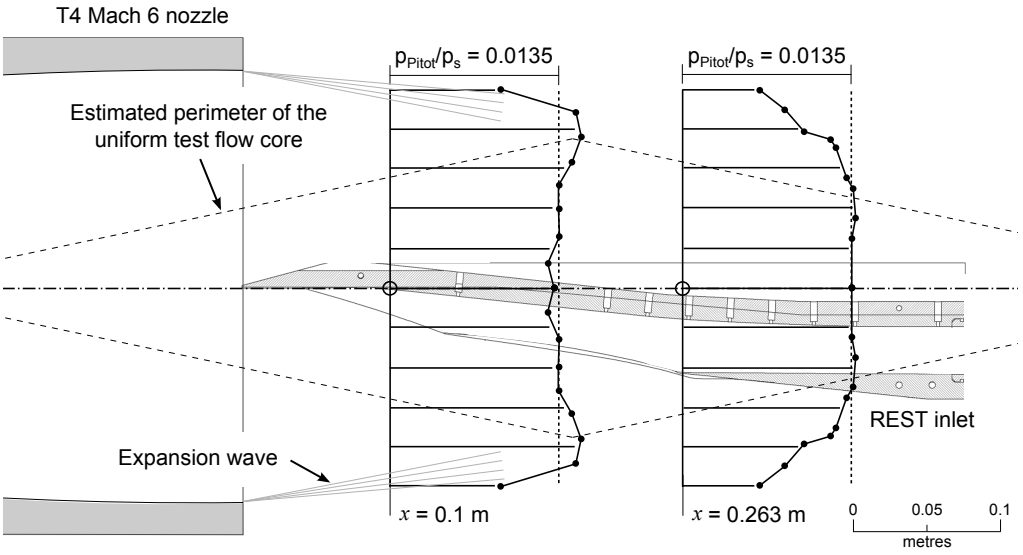

Figure 3.11: Uniform test flow core (estimated from a Pitot survey of the Mach 6 nozzle) shown in relation with the test model. Note that measurements have been replicated about the axis of the nozzle.

The value of Pitot-to-nozzle-supply pressure ratio is required to determine the nozzle exit freestream conditions. The Pitot-to-nozzle-supply pressure ratio obtained by averaging the measured values from the nozzle survey over the capture area of the REST inlet has been used for this purpose. The averaged values are used in Section 3.3.1 for the estimation of nozzle exit freestream conditions. For the tests with air as test gas, a mean value of the Pitot-to-nozzle-supply pressure ratio over the capture area of the REST inlet was 0.0135 for the Mach 6 and 0.0065 for the Mach 8 nozzle[4]. Measurements by Paull et al. (1995) and Knell (2003) show that the Pitot-to-nozzle-supply pressure ratio does not show significant variation with stagnation enthalpy between 3 MJ/kg and 9 MJ/kg conditions for the Mach 6 and 8 nozzles respectively. For the tests with nitrogen as test gas, a lower mean value of the Pitot-to-nozzle-supply ratio of 0.0124 was used for the Mach 6 and 0.00597 for the Mach 8 nozzle. The justification for the use of a lower Pitot-to-nozzle-supply pressure ratio for nitrogen tests is made based on measurements from Bakos in Mee (1993). Details are given in Appendix A. The value of Pitot-to-nozzle-supply pressure ratio was used to estimate the freestream properties for all the test conditions. This is discussed in Section 3.3.1.

[4]Results from the Pitot survey of the Mach 8 nozzle conducted in 2009 were kindly provided by Dillon Hunt.

3.3 Test conditions

3.3.1 Test conditions

Obtaining direct measurements of the freestream properties of the nozzle outflow without affecting the test flow itself is difficult. Therefore, these properties are inferred from measurements that can readily be obtained. These properties are estimated using the Equilibrium Shock Tube Conditions Junior (ESTCj) and Non-Equilibrium NozZle Flow (NENZF) (Lordi et al., 1966) codes. ESTCj, a modified version of ESTC (McIntosh, 1968), uses the CEA2 chemistry database (McBride et al., 2002) to compute the gas properties in the nozzle-supply region in thermal and chemical equilibrium. Due to the high pressures, high densities and low flow velocities in the nozzle-supply region, the assumption of thermal and chemical equilibrium is well justified. Using the shock tube fill pressure p_{fill}, fill temperature T_{fill}, and incident shock speed u_{shock}, the gas properties in the nozzle-supply region can be estimated with ideal normal shock relations in the ESTCj code. However, due to the minor losses, this tends to lead to higher estimations of nozzle-supply pressures than those measured experimentally. ESTCj then isentropically expands the estimates of the gas properties in the nozzle-supply region until the corresponding nozzle-supply pressure matches the experimentally measured quantity. The assumption of an isentropic expansion of the stagnated gas in the nozzle-supply region is shown by Hertzberg et al. (1961) and Copper (1962) to be a valid approximation. The nozzle-supply gas properties computed from ESTCj are then passed to the NENZF code. This code calculates the quasi-one-dimensional inviscid expansion of chemical equilibrium and non-equilibrium flows through hypersonic nozzles using curve-fits to thermo-chemical models. Since the flowfields in the axisymmetric contoured nozzles used in the T4 shock tunnel facility are expected to be relatively shock-free, the assumption of quasi-one-dimensional flow made in the NENZF computations is justified. In addition, because NENZF simulates only an inviscid flowfield, it is also necessary in the NENZF computations to account for the displacement of the core flow in the physical nozzle due to boundary layer growth. This is done by running NENZF iteratively with the nozzle-expansion ratio adjusted until the Pitot-to-nozzle-supply pressure ratio matches those that are measured experimentally. The corresponding properties are then taken to be the freestream properties in the nozzle core flow.

The inferred test conditions, the associated uncertainties and the equivalent flight conditions are shown in Table 3.1 for experiments with air test gas and Table 3.2 for

Table 3.1: Nominal experimental nozzle-supply, freestream conditions and equivalent flight conditions for tests with air as the test gas.

H_s	MJ/kg	3.7	±7.2%	4.8	±7.4%	8.0	±7.7%	4.8	±7.4%
M_∞	-	6.3	±2.2%	6.2	±2.2%	5.7	±2.1%	7.4	±2.5%
p_s	MPa	35.4	±3.0%	35.9	±3.0%	37.5	±3.0%	36.9	±3.0%
T_s	K	3206	±5.3%	3829	±5.0%	5317	±4.8%	3813	±5.0%
p_∞	kPa	9.4	±13.2%	9.8	±13.2%	12.5	±12.8%	3.1	±13.4%
T_∞	K	451	±9.6%	560	±10.4%	1087	±9.6%	395	±11.8%
ρ_∞	kg/m^3	0.0728	±11.3%	0.0610	±11.8%	0.0398	±11.3%	0.0275	±12.3%
u_∞	m/s	2660	±3.2%	2920	±3.6%	3673	±3.2%	2951	±4.0%
γ_∞	-	1.40		1.38		1.34		1.40	
M_f	-	8.4		9.6		12.5		-	
h_f	km	37		38		39		-	
q_f	kPa	22		24		36		-	

Table 3.2: Nominal experimental nozzle-supply and freestream conditions for tests with nitrogen as the test gas.

H_s	MJ/kg	3.8	±7.2%	4.9	±7.3%	8.5	±7.4%	4.9	±7.3%
M_∞	-	6.6	±2.1%	6.4	±2.0%	6.1	±1.7%	7.4	±2.0%
p_s	MPa	36.1	±3.0%	35.9	±3.0%	38.5	±3.0%	36.5	±3.0%
T_s	K	3353	±6.1%	4167	±6.3%	6489	±4.7%	4154	±6.3%
p_∞	kPa	8.0	±12.8%	8.5	±13.0%	10.2	±12.5%	3.1	±12.8%
T_∞	K	408	±8.9%	545	±9.0%	1025	±8.5%	409	±8.9%
ρ_∞	kg/m^3	0.0662	±11.0%	0.0524	±11.4%	0.0334	±11.5%	0.0253	±11.3%
u_∞	m/s	2697	±3.2%	3021	±3.6%	3903	±3.2%	3062	±4.0%
γ_∞	-	1.40		1.39		1.34		1.40	

experiments with nitrogen test gas. The uncertainties were computed following the procedures described by Mee (1993). Details of these calculations are shown in Appendix B.1. The equivalent flight conditions were approximated as shown in Appendix C. Detailed operating, nozzle-supply, nozzle-exit and fuelling conditions for each shot in this test campaign are shown in Appendix D. There are generally three types of tests done in this experimental campaign - fuel-off with air as the test gas, fuel-injection into a nitrogen test gas (combustion suppressed - film-cooling) and fuel-injection into an air test gas (boundary layer combustion). The main purpose of using nitrogen as the test gas was to suppress combustion when fuel was injected. When combustion occurs, effects on pressure and drag forces can be brought about by both fuel injection and combustion. The suppression of combustion can aid in distinguish-

ing the effects of fuel injection from those of combustion. Note that the freestream static pressure differs by 12% between the air tests and nitrogen tests, the static temperature by 7%, the density by 12% and the velocity by 4%. This is brought about by the difference in gas composition (and hence gas constant and hence speed of sound) in the test gas. From Figure 5.1, it can be seen that normalising the measured pressure against the freestream static conditions (as per Section 3.4) cancels out this difference and allows comparisons between air and nitrogen tests to be made. The only difference occurs in the change in shock angles from the difference in Mach number. For a wedge at an arbitrary angle of 6°, a change of inflow Mach number from 6.2 to 6.4 only changes the shock angle by 0.2°. This difference is not expected to significantly affect the comparison between air and nitrogen tests.

3.3.2 Fuel injection conditions

To determine the freestream properties of the injected fuel, the mass flow rate has to be computed first. To determine the mass flow rate of hydrogen injected from the annular slot, the fuel injection system was calibrated. The calibration process (Robinson et al., 2003) produces an effective discharge coefficient for the annular slot injector. Assuming choked flow through the injector throat and an isentropic expansion of the fuel in the Ludwieg tube, this discharge coefficient can be obtained from Equation 3.1.

$$\alpha = \frac{\left(p_{LT,f} - p_{LT,i}\right) V_{LT}}{R\, T_{LT,i}\, p_{LT,i}^{\frac{\gamma-1}{2\gamma}} \int_{t,i}^{t,f} p_{\text{plenum}}^{\frac{\gamma+1}{2\gamma}} dt}. \tag{3.1}$$

Although the target fuelling equivalence ratio was 1.0, the calibration was conducted over a range of Ludwieg tube fill pressures. The results are shown in Figure 3.12. The plot demonstrates that the discharge coefficient was insensitive to the Ludwieg tube fill pressures and hence to the mass flow rate. As such, a discharge coefficient of 25.96 nms was used for the current experimental campaign. Figure 3.13 shows a typical fuel plenum chamber pressure trace in relation to the nozzle supply pressure trace for shot 10567. Hydrogen was deliberately injected prior to flow arrival to ensure that the hydrogen supply was approximately constant throughout the period of the test time. Although this meant the presence of hydrogen in the combustor prior to flow arrival, Kirchhartz (2010) shows that this does not significantly affect the experimental results.

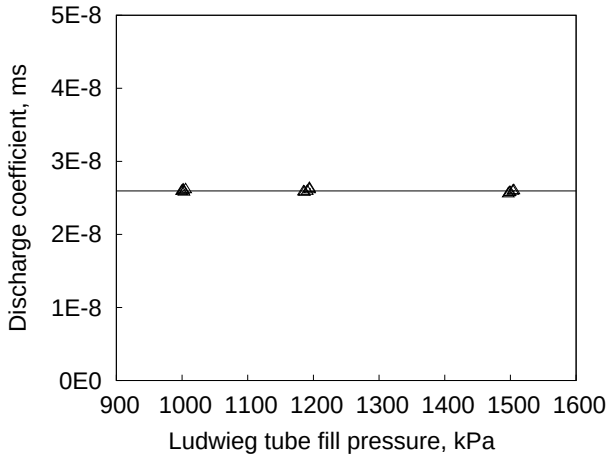

Figure 3.12: Ludwieg tube fill pressure versus discharge coefficient

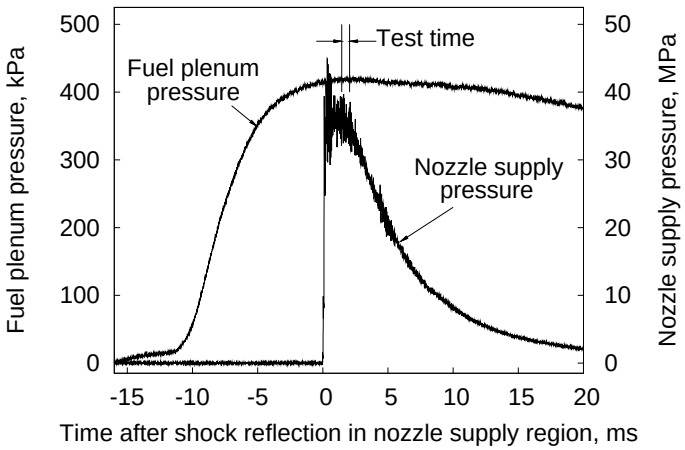

Figure 3.13: Timing of fuel injection for test 10567

The plenum pressure averaged during the test time duration is then used with the initial fill pressure of the Ludwieg tube and the discharge coefficient in Equation 3.2 to calculate the mass flow rate of hydrogen.

$$\dot{m}_{\mathrm{H_2}} = \alpha \, p_{LT,i}^{\frac{\gamma-1}{2\gamma}} \, p_{\mathrm{plenum}}^{\frac{\gamma+1}{2\gamma}} \tag{3.2}$$

The stoichiometric combustion reaction of hydrogen with the available oxygen in the inflow air represented by Equation 3.3.

$$2\,\mathrm{H_2} + \mathrm{O_2} \rightarrow 2\,\mathrm{H_2O} \tag{3.3}$$

Since the molar weight of molecular oxygen is 32 g/mol and that of molecular hydrogen is 2 g/mol, a stoichiometric combustion represented by Equation 3.3 would mean that the hydrogen mass flow rate that would consume all of the available oxygen is 1/8 of the oxygen mass flow rate. Assuming the mass fraction of oxygen in air to 0.232, the equivalence ratio can be calculated from Equation 3.4.

$$\phi = 8\,\frac{\dot{m}_{\mathrm{H_2}}}{0.232\,\dot{m}_{\mathrm{Air}}} = 8\,\frac{\dot{m}_{\mathrm{H_2}}}{0.232\,\rho_\infty u_\infty A_{\mathrm{capture}}} \tag{3.4}$$

For tests with nitrogen as the test gas, an equivalent value for the equivalence ratio[5] can be calculated from Equation 3.5.

$$\phi = \phi_{\mathrm{equivalent}} = 8\,\frac{\dot{m}_{\mathrm{H_2}}}{0.232\,\dot{m}_{\mathrm{N_2}}} = 8\,\frac{\dot{m}_{\mathrm{H_2}}}{0.232\,\rho_\infty u_\infty A_{\mathrm{capture}}} \tag{3.5}$$

The nominal fuel mass flow rate for the current experiments is 0.012 kg/s, which corresponds to a fuel equivalence ratio of approximately 1.0. Following the procedures described by Mee (1993), the uncertainty in equivalence ratio is calculated to be $\pm$13.7%. Details of this calculation are shown in Appendix B.2.

With the calculated hydrogen mass flow rate, the properties at the exit of the injector nozzle can then be estimated. This is shown in Appendix E. For an average hydrogen mass flow rate of 0.01255 kg/s, plenum pressures of 425.9 kPa, plenum temperatures of 300 K and isentropic flow from the plenum to the exit of the nozzle, the estimated conditions at the injector nozzle exit plane are as shown in Table 3.3.

Table 3.3: Estimated conditions at the fuel injector nozzle exit plane.

p_{jet}	8.5	kPa
u_{jet}	2405	m/s
T_{jet}	96	K
ρ_{jet}	0.0214	kg/m^3
M_{jet}	3.2	

[5] Note that the use of the terminology "equivalence ratio" is not entirely appropriate for tests with nitrogen test gas since there is no oxidiser present. However, to maintain simplicity in this thesis, this terminology is retained for tests with nitrogen test gas.

3.4 Data reduction

3.4.1 Pressure measurements

In impulse facilities where test times are in the order of milliseconds, the identification of the period of steady, established test flow is important. Figure 3.14 shows a typical pressure trace sampled from a transducer in the REST inlet. The flow through the nozzle requires a finite amount of time for the boundary layers to establish and for the shock and expansion waves to be swept out (Smith, 1966). This is taken to be about 0.78 ms after flow arrival and is denoted as "*Nozzle start-up time*" in Figure 3.14. After flow establishment in the nozzle, the flow then needs to become established throughout the experimental model. Studies by Jacobs et al. (1992) show that it takes about three flow lengths for turbulent boundary layers to fully develop. With the experimental model being 0.986 m long and freestream velocities of about 2700 - 3700 m/s, the flow establishment time in the model is approximately 1.1 - 0.8 ms. This is denoted as "*Flow establishment time*" in Figure 3.14. The end of test time is dictated by either

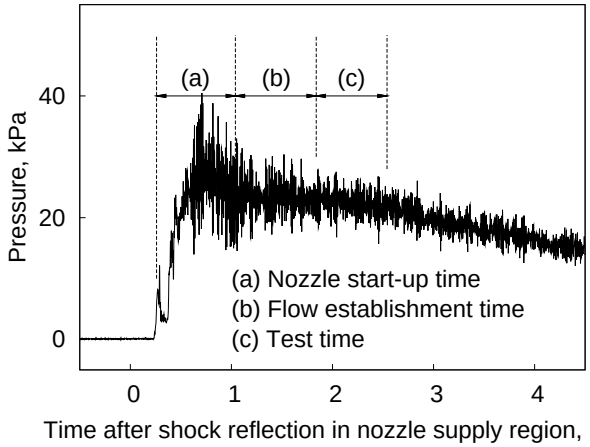

Figure 3.14: Typical pressure trace from shot 10568.

the arrival of driver gas in the test section or a significant drop (more than 5%) in the nozzle-supply pressure (Kirchhartz, 2010). Studies by Boyce et al. (2005) and Skinner (1994) have shown that for the T4 shock tunnel, the time taken for 10% driver gas contamination can be approximated by Equation 3.6 [6].

$$t_{10\%\,\text{contamination}} = 1.268 \times 10^{9}\, H_s^{-1.7183} \pm 38\% \tag{3.6}$$

[6]The original equation in the paper by Boyce et al. (2005) is re-written here in S.I. units.

For the range of stagnation enthalpies in this experimental campaign, 10% driver gas contamination[7] occurs approximately 6.6 ms after flow arrival for the 3.7 MJ/kg condition and 1.74 ms after flow arrival for the 8 MJ/kg condition. For 3.7 MJ/kg and 4.8 MJ/kg conditions, the end of available test time was dictated by the drop in nozzle-supply pressure. For the 8 MJ/kg condition, the end of available test time was dictated by driver gas contamination.

In the current study, the measured pressures are presented in the form of a pressure coefficient.

$$c_p = \frac{p - p_\infty}{\frac{1}{2}\rho_\infty u_\infty^2} \tag{3.7}$$

Presenting the pressure measurements in this way minimises the effects of shot-to-shot variations in the freestream conditions which primarily come from variations in the nozzle-supply pressure. It has been found in the current study that this also helps in eliminating the effect of the differences in the freestream static conditions between tests with air test gas and those with nitrogen test gas (see discussion in Section 3.3.1). Following the procedures for the analysis of uncertainties by Mee (1993), the uncertainty in c_p varies between 10% and 12%.

3.4.2 Drag measurements

From an analysis of the strain signals, the piezo-electric film strain gauge B has been ascertained to be the most reliable gauge of all the strain gauges shown in Figure 3.9 for the force measurements. The analysis is shown in Appendix F. All drag measurements presented in the following chapters are taken from the piezo-electric film strain gauge B.

Figure 3.15 shows a typical drag force trace obtained from the deconvolution of the measured strain history from strain gauge B with the impulse response. The extraneous thrust forces from the rear edge and rear cavity pressures, and the extraneous drag forces from the front edge pressures (as discussed in Section 3.1.5) have already been accounted for in the drag force trace shown in Figure 3.15. Note also that this trace

[7] In the T4 shock tunnel facility, it is common practice to use a threshold of 10% driver gas contamination to limit the test time. As the combustion phenomena is an important aspect in the current experiments, it is necessary to show that this level of driver gas contamination does not significantly affect combustion. This is shown in the analysis of supersonic reacting flow in a pipe with different levels of driver gas contamination in Appendix G. Results from this analysis demonstrate that the presence of 10% driver gas in the flow only acts to delay the ignition process, but does not significantly affect the other combustion processes, hence justifying the appropriateness of the use of 10% driver gas contamination to limit the test time in the current experiments.

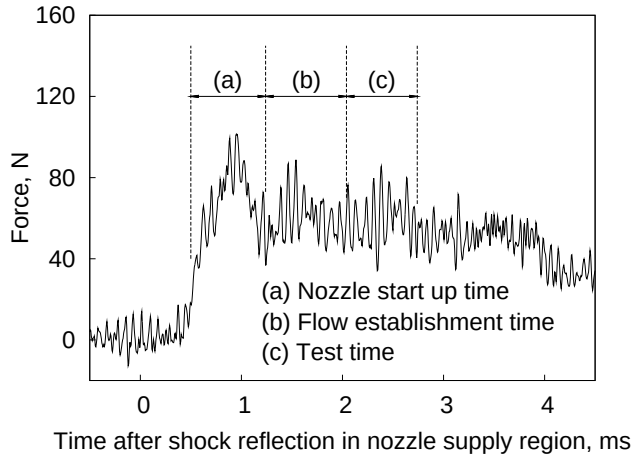

Figure 3.15: Typical drag trace from shot 10568.

has been filtered using a 100-μs moving-average filter. As per Figure 3.14, the nozzle startup, flow establishment and test times are marked.

In short-duration impulse facilities, there are usually small variations in freestream flow conditions during the nominal test period which may transcend into the aerodynamic flow properties in the experimental model. Instead of using the commonly-used form of drag coefficient (Equation 3.8),

$$c_D = \frac{D}{\frac{1}{2}\rho_\infty u_\infty^2 A_c} \tag{3.8}$$

Mee (2002b) showed that presenting drag measurements as per Equation 3.9 allows the effects of variations in the freestream flow to be accounted for. The derivation of this equation is shown in Appendix H.

$$c_D = \left[\frac{2}{p_{\text{Pitot}}/p_s} \left(\frac{\gamma+1}{2} \right)^{\frac{\gamma+1}{\gamma-1}} \gamma^{\frac{\gamma}{1-\gamma}} \right] \frac{D}{p_s A_c} \tag{3.9}$$

Presenting drag measurements in this way also eliminates the effect of shot-to-shot variations in the freestream conditions, and the effect of the differences in freestream conditions between tests with air test gas and those with nitrogen test gas. Note that D in Equation 3.9 is the measured drag that has already been corrected for extraneous pressure forces. The uncertainty in c_D, that has been analysed using the procedures of Mee (1993), is 11%.

Chapter 4

Details of Numerical & Analytical Tools

In general, conducting ground and flight experiments to explore the phenomena within hypersonic flowfields is useful, but can often be limited by difficulties in measuring all flow parameters of interest. The use of CFD and turbulent skin friction friction theories as tools for simulating and characterising these flowfields can complement the experiments and help reveal more insights into the flowfield. This chapter describes the numerical and analytical tools that are used to support the analysis of the experiments described earlier in Chapter 3. Details of the CFD flow solver, Eilmer3, and the newly implemented k-ω turbulence model are described. Results from validation test cases that have been conducted to demonstrate the suitability of Eilmer3 and the k-ω model for use in this project are also shown. This is then followed by a summary of the turbulent skin friction theories that are used in this project. The chapter then concludes with an example demonstrating the applicability of these theories to the current project.

4.1 Numerical tools

CFD simulations are used in two ways in this study. Firstly, simulations of the experimental flowfield are conducted. Since experiments are conducted in an enclosed environment, no visualisations of the internal flowfield are available. Instead, CFD results are compared to surface pressure measurements at discrete locations and integrated skin friction drag measurements. If they can be matched to within experimental uncertainties, an analysis of the numerical results can provide further insights to the flow phenomena in the enclosed combustor. Secondly, additional simulations are conducted to determine the type of flow conditions that would drive the fuel layer out of the boundary layer. Note that, for all simulations conducted in the current project, combustion reactions between the injected hydrogen and mainstream air flow are not considered.

4.1.1 Flow solver - Eilmer3

All simulations detailed in this thesis (with exception to those conducted for the REST inlet) were conducted using an inhouse code called Eilmer3 (Jacobs and Gollan, 2008; Jacobs et al., 2010). Eilmer3 is an integrated collection of programs that solves the compressible Navier-Stokes equations in multi-block structured grids to provide time-accurate simulations of compressible flows in two and three dimensions. In Eilmer3, the governing equations are expressed in integral form, as shown in Appendix I, over cell-centred, finite-volume cells, with the time rate of change of conserved quantities in each cell specified as a summation of the mass, momentum and energy flux through the cell interfaces. Inviscid fluxes are computed with up to third-order truncation error using an adaptive scheme (see Section 2.6 in Jacobs et al. (2010)) which applies the EFM scheme (Macrossan, 1989) in regions near shock waves and the AUSMDV scheme (Wada and Liou, 1994) in regions away from shocks, while viscous fluxes are mostly evaluated to second-order truncation error using the divergence theorem. At the boundaries, one-sided derivatives are evaluated. Eilmer3 has successfully been used for the simulation of transient scramjet flows (Kirchhartz et al., 2010; McGilvray et al., 2010; O'Byrne and Wittig, 2008; Tanimizu et al., 2009), hypersonic bluff body flows (Kulkarni et al., 2007; McGilvray et al., 2009b), hypersonic test facilities (McGilvray et al., 2009a; Wheatley et al., 2004), and more recently, turbine flows (Ventura et al., 2010).

4.1.2 The modelling of turbulence

As discussed in Chapter 2, the drag-reduction benefits of the boundary layer combustion technique can only be realised in turbulent boundary layers. This means that the simulations conducted using Eilmer3 must be able to model the turbulence present in the flowfield. Of the three common approaches for modelling turbulence (direct numerical simulation (DNS), large-eddy simulation (LES) and Reynolds-averaged Navier-Stokes (RANS) simulation), it is well known that the RANS approach is the most computationally efficient and has the highest chance of completely modelling realistic aerospace systems (Ladeinde, 2010). Prior to the implementation of Wilcox's k-ω model (Wilcox, 2006), turbulent simulations in Eilmer3 had to be conducted using the algebraic Baldwin-Lomax turbulence model (Baldwin and Lomax, 1978). For flowfields that are relevant to the current study, researchers have shown that algebraic turbulence models do not give accurate predictions of the flowfield. For example, Kuryachii (1998) showed that the algebraic Cebeci-Smith model (Smith and Cebeci,

1967) seriously overpredicted the skin friction coefficients when heat was added to turbulent boundary layers. In addition, Aupoix et al. (1998) also showed that the algebraic Cebeci-Smith and Baldwin-Lomax turbulence models did not correctly reproduce the key features of the flowfield, in which a nitrogen-air mixture was injected into a boundary layer. They suggested this was because algebraic models only deal with global information on the turbulence length scale deduced from the flow geometry, that these models assume that the wall boundary and mixing are essentially the same layer even before they have merged, and that the thickness of this layer gives the turbulence length scale. The models overestimate the turbulence length scale and the turbulent diffusion, and therefore they predict a very rapid mixing and a very quick relaxation toward an equilibrium boundary-layer solution. Both authors noted that two-equation turbulence models performed significantly better than the algebraic ones in their studies.

Of the many two-equation RANS turbulence models available, an ideal turbulence model is one that can be used to provide accurate predictions for a wide range of applications with minimal adjustments to its closure coefficients. Previous versions of Wilcox's k-ω models (Wilcox, 1988, 1998) have been shown to be suitable candidates for supersonic and hypersonic aerothermodynamic applications (Cutler et al., 2006; Parent and Sislian, 2004). However, several authors (Bardina et al., 1997; Roy and Blottner, 2003) have also noted the k-ω model's sensitivity to freestream turbulence conditions as one of its major shortcomings. The latest version of Wilcox's k-ω model, although not thoroughly validated for hypersonic applications, is quoted by (Wilcox, 2006) to be significantly improved from the previous versions - it has little sensitivity to inflow turbulence conditions and can provide improved predictions of supersonic separated flows. Considering the reliability of previous versions of the k-ω model and the quoted improvements in the latest version, Wilcox's 2006 k-ω model was thus chosen for use in the current project.

The equations defining the Wilcox's 2006 k-ω model, together with the mass, momentum and energy conservation equations, are as follows.

Mass Conservation:

$$\frac{\partial \bar{\rho}}{\partial t} + \frac{\partial}{\partial x_i}\left(\bar{\rho}\tilde{u}_i\right) = 0 \tag{4.1}$$

Species Mass Conservation:

$$\frac{\partial \bar{\rho} Y_\alpha}{\partial t} + \frac{\partial}{\partial x_i}\left(\bar{\rho}\tilde{u}_i Y_\alpha\right) = \frac{\partial}{\partial x_i}\left(\bar{\rho} D_\alpha \frac{\partial Y_\alpha}{\partial x_i}\right) + \dot{S}_\alpha \tag{4.2}$$

Momentum Conservation:

$$\frac{\partial}{\partial t}\left(\bar{\rho}\tilde{u}_i\right)+\frac{\partial}{\partial x_j}\left(\bar{\rho}\tilde{u}_j\tilde{u}_i\right)=-\frac{\partial p}{\partial x_i}+\frac{\partial}{\partial x_j}\left[\bar{t}_{ji}+\bar{\rho}\tau_{ji}\right] \tag{4.3}$$

Energy Conservation:

$$\begin{aligned}\frac{\partial}{\partial t}\left[\bar{\rho}\left(\tilde{e}+\frac{\tilde{u}_i\tilde{u}_i}{2}+k\right)\right]+\frac{\partial}{\partial x_j}\left[\bar{\rho}\tilde{u}_j\left(\tilde{h}+\frac{\tilde{u}_i\tilde{u}_i}{2}+k\right)\right]=\\ \frac{\partial}{\partial x_j}\left[\left(\frac{\mu}{Pr_L}+\frac{\mu_T}{Pr_T}\right)\frac{\partial\tilde{h}}{\partial x_j}+\left(\mu+\sigma^*\frac{\bar{\rho}k}{\omega}\right)\frac{\partial k}{\partial x_j}\right]+\frac{\partial}{\partial x_j}\left[\tilde{u}_i\left(\bar{t}_{ij}+\bar{\rho}\tau_{ij}\right)\right]\end{aligned} \tag{4.4}$$

Molecular and Reynolds-Stress Tensors:

$$\bar{t}_{ij}=2\mu\bar{S}_{ij}\qquad\bar{\rho}\tau_{ij}=2\mu_T\bar{S}_{ij}-\frac{2}{3}\bar{\rho}k\delta_{ij}\qquad\bar{S}_{ij}=S_{ij}-\frac{1}{3}\frac{\partial\tilde{u}_k}{\partial x_k}\delta_{ij} \tag{4.5}$$

Eddy Viscosity:

$$\mu_T=\frac{\bar{\rho}k}{\tilde{\omega}}\qquad\tilde{\omega}=\max\left\{\omega,\ C_{lim}\sqrt{\frac{2\bar{S}_{ij}\bar{S}_{ij}}{\beta^*}}\right\}\qquad C_{lim}=\frac{7}{8} \tag{4.6}$$

Turbulence Kinetic Energy:

$$\frac{\partial}{\partial t}\left(\bar{\rho}k\right)+\frac{\partial}{\partial x_j}\left(\bar{\rho}\tilde{u}_jk\right)=\bar{\rho}\tau_{ij}\frac{\partial\tilde{u}_i}{\partial x_j}-\beta^*\bar{\rho}k\omega+\frac{\partial}{\partial x_j}\left[\left(\mu+\sigma^*\frac{\bar{\rho}k}{\omega}\right)\frac{\partial k}{\partial x_j}\right] \tag{4.7}$$

Specific Dissipation Rate:

$$\begin{aligned}\frac{\partial}{\partial t}\left(\bar{\rho}\omega\right)+\frac{\partial}{\partial x_j}\left(\bar{\rho}\tilde{u}_j\omega\right) &= \alpha\frac{\omega}{k}\bar{\rho}\tau_{ij}\frac{\partial\tilde{u}_i}{\partial x_j}-\beta\bar{\rho}\omega^2+\sigma_d\frac{\bar{\rho}}{\omega}\frac{\partial k}{\partial x_j}\frac{\partial\omega}{\partial x_j}\\ &\quad+\frac{\partial}{\partial x_j}\left[\left(\mu+\sigma\frac{\bar{\rho}k}{\omega}\right)\frac{\partial\omega}{\partial x_j}\right]\end{aligned} \tag{4.8}$$

Closure Coefficients:

$$\alpha=\frac{13}{25}\qquad\beta=\beta_of_\beta\qquad\beta^*=\frac{9}{100}\qquad\sigma=\frac{1}{2}\qquad\sigma^*=\frac{3}{5}\qquad\sigma_{do}=\frac{1}{8} \tag{4.9}$$

$$\beta_o=0.0708\qquad Pr_T=\frac{8}{9}\qquad\sigma_d=\begin{cases}0, & \frac{\partial k}{\partial x_j}\frac{\partial\omega}{\partial x_j}\le 0\\ \sigma_{do}, & \frac{\partial k}{\partial x_j}\frac{\partial\omega}{\partial x_j}>0\end{cases} \tag{4.10}$$

$$f_\beta = \frac{1+85\chi_\omega}{1+100\chi_\omega} \qquad \chi_\omega = \left|\frac{\Omega_{ij}\Omega_{jk}\hat{S}_{ki}}{(\beta^*\omega)^3}\right| \qquad \hat{S}_{ki} = S_{ki} - \frac{1}{2}\frac{\partial \tilde{u}_m}{\partial x_m}\delta_{ki} \tag{4.11}$$

The most important differences between Wilcox's 2006 k-ω turbulence model and earlier versions (Wilcox, 1988, 1998) are the addition of a "cross diffusion" term and a "stress-limiter" modification. The addition of the "cross diffusion" term (see σ_d in Equation 4.8) is suggested as a remedy for the original k-ω model's sensitivity to the freestream value of ω, while the "stress-limiter" modification (see μ_T dependence on $\tilde{\omega}$ in Equation 4.6) is used to improve the model's capability to predict hypersonic- and supersonic-separated flows. The "stress-limiter" modification makes eddy viscosity a function of k, ω and, effectively, the ratio of turbulence-energy production to turbulence-energy dissipation, and is somewhat similar to the "realisability constraints" cited by Moore and Moore (1999), Thivet et al. (2001) and Thivet (2002). The current version of the k-ω model also includes Pope's round-jet/plane-jet anomaly modification (Pope, 1978). This modification corrects the anomaly seen in many turbulence models, which wrongly predicts that a round-jet spreads more rapidly than a plane-jet. The dilatation-dissipation modification, which improves compressible mixing-layer predictions (Parent and Sislian, 2004; Wilcox, 2006), has been omitted as recommended by Wilcox (2006) because it has a detrimental effect on shock-separated flow predictions.

In Eilmer3, the transport equations for k and ω are solved by a method that is the same as that used for the mass, momentum and energy conservation equations (as described in Section 4.1.1). The only differences are that the source (production and dissipation) terms for k and ω are updated implicitly using a single-step Euler update, and that the values of ω are corrected as recommended by Menter (1994) to improve the estimation of ω in cells that located near non-slip walls.

The newly implemented k-ω model in Eilmer3 is validated against test cases that have flowfields representative of those to be expected in the current experiments. The validation exercise will demonstrate the suitability of Eilmer3 and the k-ω turbulence model for use in the current project. The selected test cases, shown in Figure 4.1, are also representative of those to be expected in typical scramjet flowfields. The first and second test cases, which involve the development of a turbulent boundary layer on a flat plate and an axisymmetric cylinder, are the most commonly seen features throughout the entire scramjet. The third test case, which involves the flow over a backward-facing step, is a feature commonly used in scramjets for the injection of fuel and for

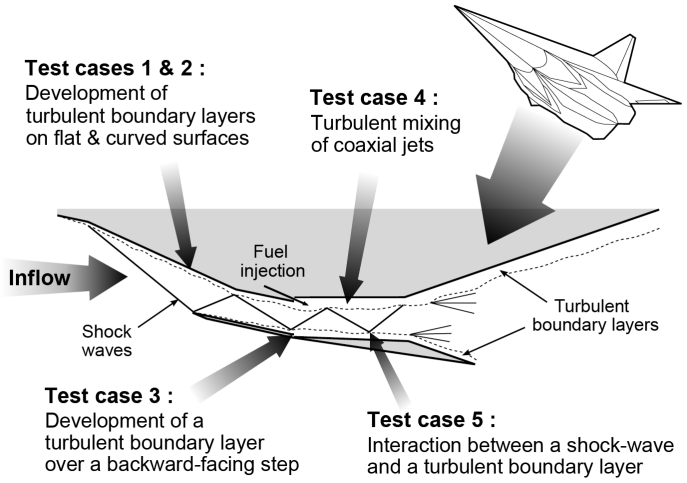

Figure 4.1: Overview of selected test cases.

flameholding. The fourth test case, which features the turbulent mixing of two coaxial jets, is commonly seen inside combustion chambers of scramjets where fuel mixes with air for combustion. The fifth test case involves the interaction between a swept shock wave and a turbulent boundary layer - a three-dimensional feature that commonly occurs throughout the entire scramjet. The first, second and fifth test cases are seen throughout the current experimental model, while the third and fourth test cases are seen near the fuel slot injector. Note that all validation test cases make up regions of the flowfield that are expected in the current study. In addition, since the flowfield expected in the current experiments has somewhat similar flow features to those in the experiments of Kirchhartz (2010), validation against these experiments is a definitive way of demonstrating the suitability of the numerical tools for use in the current study.

4.1.3 Test case 1 - 2D flat plate

The first validation test case is that of a two-dimensional Mach 4.5 flow of air over a flat plate. Experimental results of Mabey (from Fernholz and Finley (1977) test case 74021801) and turbulent skin friction correlations by Van Driest (1956) are used for comparison with Eilmer3 simulations. Due to its simplicity, this test case is used to explore the k-ω model's sensitivity to freestream turbulence properties. In this test case (Figure 4.2), a boundary layer formed on the top surface of a 1.65 m long and 0.889 m wide flat plate. This boundary layer was tripped by small glass spheres located 2.5 mm downstream of the plate's leading edge. The walls were insulated and can be assumed to be adiabatic. Air, modelled as an ideal gas at a static pressure of 3.2 kPa, static tem-

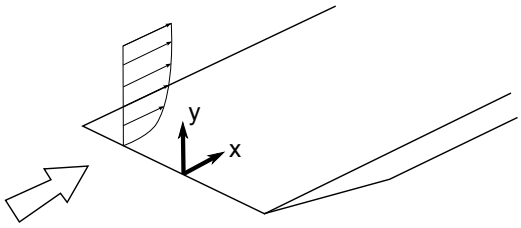

Figure 4.2: Schematic of the flat plate experiments.

Table 4.1: Test matrix for the different freestream turbulence properties tested.

	Turbulence intensity		
$\frac{\mu_T}{\mu_L}$	1e-5	1e-3	1e-2
1e-5	k_∞ = 7.6e-5 ω_∞ = 326490	Not tested*	Not tested*
1	k_∞ = 7.6e-5 ω_∞ = 3.2649	k_∞ = 0.76 ω_∞ = 32649	k_∞ = 76 ω_∞ = 3264900
10	k_∞ = 7.6e-5 ω_∞ = 0.32649	k_∞ = 0.76 ω_∞ = 3264.9	k_∞ = 76 ω_∞ = 326490
100	k_∞ = 7.6e-5 ω_∞ = 0.032649	k_∞ = 0.76 ω_∞ = 326.49	k_∞ = 76 ω_∞ = 32649

*This combination of freestream turbulence properties was not tested because the resulting ω value was larger than 1% of that expected in the boundary layer.

perature of 62 K and velocity of 713 m/s, is used as the inflow for these simulations. The inflow freestream turbulence intensity in the simulations is varied between 0.00001 and 0.01 while the turbulent-to-laminar viscosity ratio is varied between 0.00001 and 100 for the sensitivity studies. The corresponding values of k and ω are shown in Table 4.1. The use of freestream ω values that are larger than 1% of those in the boundary layer is considered to be unrealistic (Wilcox, 2006). Therefore, simulations with combinations of freestream turbulence intensity and turbulent-to-laminar viscosity ratio that generate unrealistic freestream values of ω have been omitted.

To check for grid convergence, simulations using a freestream k of 0.76 m^2/s^2 and freestream ω of 32649 /s are conducted on three grids (64×24 cells, 128×48 cells and 256×96 cells). For the three grid configurations, it is ensured that at least 15 cells in the wall-normal direction are within the boundary layer and that most wall cells have a y^+ value of less than 1. The entire computational domain is assumed to be turbulent. Figure 4.3a shows the estimated values of displacement thickness at $x = 0.368$ m

plotted against the representative cell size for the three grid configurations. In this two-dimensional simulation, the representative cell size, Δ is computed as $\sqrt{1/N_{\text{cells}}}$, where N_{cells} is the total number of cells for each grid. Also shown in Figure 4.3a is a line that has been fitted through the three points. The equation for this line follows the form

$$f(\Delta) = f_{limit} - C\Delta^{O} \tag{4.12}$$

where $f(\Delta)$ the flow parameter of interest, f_{limit} the limiting value for infinite resolution, C a constant and O the order of convergence. For about a second-order convergence, the limiting value for displacement thickness is 2.610 mm. A comparison of this value with that for the 256×96-cell grid indicates a grid-induced error of 1.3% when the 256×96-cell grid is used. Similarly, Figure 4.3b shows the values of skin friction coefficient averaged from $x = 0.1$ m to $x = 0.25$ m plotted against the representative cell size for the three grid configurations. For a first-order convergence, the limiting value for skin friction coefficient is 0.001309. A comparison of this value with that for the 256×96-cell grid indicates a grid-induced error of 0.3% when the 256×96-cell grid is used. As such, all subsequent simulations for this test case are conducted using the 256×96-cell grid.

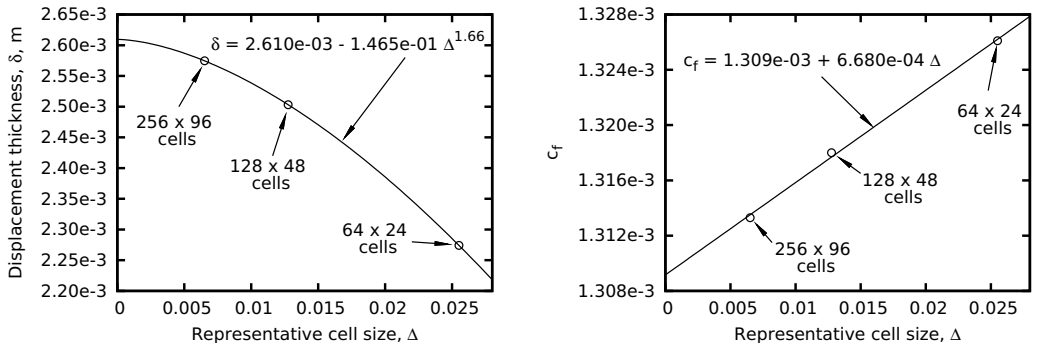

(a) Displacement thickness at $x = 0.368$ m **(b)** Skin friction coefficient

Figure 4.3: Grid convergence for the 2D flat plate test case.

Figure 4.4a shows the velocity profiles taken at $x = 0.368$ m. These profiles have been non-dimensionalised using van Driest's transformation (White, 2006), where u^+ is the dimensionless velocity and y^+_{cell} is the dimensionless normal distance of a cell from the wall. The numerical results shown in Figure 4.4a are for simulations conducted using different values of freestream turbulence intensities and turbulent-to-laminar viscosity ratios that are listed in Table 4.1. In the viscous sublayer and log-law regions ($y^+_{\text{cell}} < 300$), the numerical results match the experiments to within 4% difference and also do not exhibit any sensitivities to the freestream turbulence values. However,

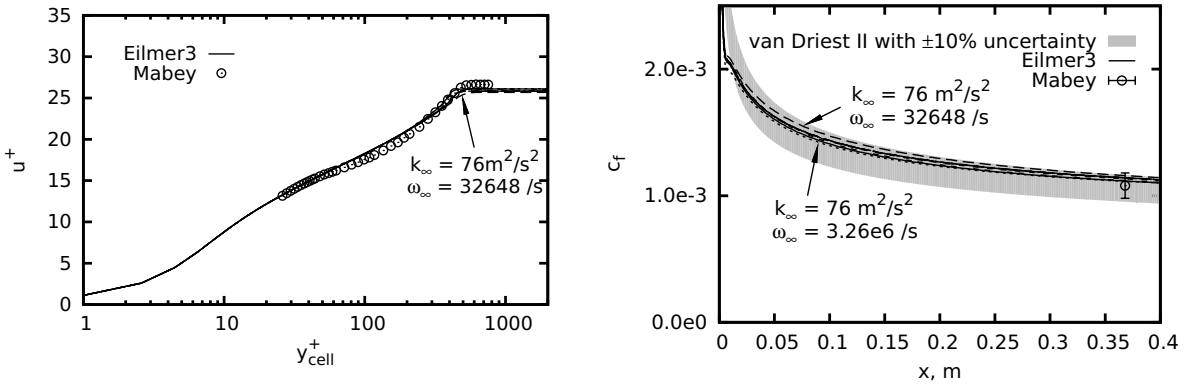

(a) Dimensionless velocity profiles.

(b) Distribution of skin friction coefficient along the surface.

Figure 4.4: Comparison of experimental, theoretical and numerical results. Numerical results are from simulations that have been conducted using freestream turbulence intensities listed in Table 4.1.

in the wake region ($y^+_{\text{cell}} > 300$), variations of about 2% in u^+ can be observed. Figure 4.4b shows the experimentally measured, theoretically predicted and numerically simulated values of skin friction coefficient along the flat plate. The theoretical values are computed using van Driest's flat plate turbulent skin friction theory. An estimation of the accuracy of this theory ranges from $\pm 3\%$ (Squire, 2000) to $\pm 10\%$ (Hopkins and Inouye, 1971). Although the numerically-predicted distributions of skin friction coefficient vary by about 4% for the range of freestream turbulence properties tested, all results still fall within the $\pm 10\%$ uncertainty bands of van Driest's theory and experimental results. This shows that the k-ω model in Eilmer3 can be used to predict turbulent skin friction coefficient on a flat plate, despite the model's sensitivity to freestream turbulence properties.

4.1.4 Test case 2 - Axisymmetric hollow cylinder

The second validation test case is the experiments of Mallinson et al. (2000) which involved a Mach 8.8 flow over a hollow cylinder. The experiments were performed in the Imperial College gun tunnel at a stagnation pressure of 60 MPa and stagnation temperature of 1150 K to supply a Mach 8.8 flow of nitrogen to the cylinder. The outflow from the tunnel's contoured nozzle has a slight divergence from the axis of the nozzle - at the nozzle exit plane, the flow deflection angle increases by about 0.005° per millimetre radial distance from the nozzle axis. This test case is an axisymmetric analogy of the flat plate test case and serves as an excellent exercise to test the axisymmetric formulation of the k-ω model. The turbulence model's sensitivity to y^+ values and maximum cell

aspect ratios are also investigated in this test case. The experimental setup is shown schematically in Figure 4.5. Static pressure and heat flux distributions were measured on the external surface of the sharp-nosed cylinder. The boundary layer that grew on this surface was allowed to transition naturally to turbulence from its laminar state. In this validation exercise, several grid configurations are used to explore the k-ω model's sensitivity to y^+ values and cell aspect ratios. Details of these grids are provided in the results. Nitrogen, modelled as an ideal gas with a turbulence intensity of 0.005 and a turbulent-to-laminar viscosity ratio of 0.5, is used as the inflow condition. The presence of flow angularity is also accounted for in this inflow. The wall of the cylinder is modelled to be at a constant temperature of 295 K. To trigger the transitioning of the boundary layer at about $x = 0.1$ m, the region from $x = 0$ m to $x = 0.05$ m is set to be a laminar region. For a turbulent Eilmer3 simulation, a laminar region is where the turbulent viscosity is set to zero, the turbulent kinetic energy and specific dissipation rate are transported, and the turbulence source terms not computed.

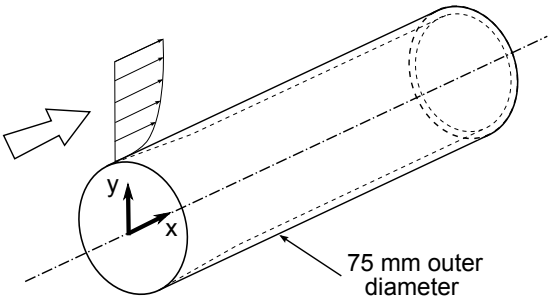

Figure 4.5: Schematic of the axisymmetric hollow cylinder experiments, where $x = 0$ m corresponds to the leading edge of the cylinder.

Figure 4.6 shows the numerical results for four different grid resolutions. The naming convention for the grids indicates the number of cells, y^+ value, maximum cell aspect ratio and wall-normal grid stretching rate. For example, the "*200×65cells-y+1.5-ar227-gs12*" grid has 200 streamwise cells, 65 wall-normal cells, a y^+ value of 1.5, a maximum cell aspect ratio of 227 and an average wall-normal grid stretching rate of 12% in the boundary layer regions. Note that the y^+ value is taken from an average of the y^+ values in the turbulent region (from $x = 0.18$ m to 0.8 m). In contrast to the boundary layer profiles in Figure 4.6a, the simulated surface static pressure and heat flux distributions in Figures 4.6b and 4.6c show greater sensitivity to grid resolution. If grid convergence is considered based only on the boundary layer profiles and sur-

face static pressure, then the "*200×65cells-y$^+$1.5-ar227-gs12*" grid is adequate. However, if the heat flux distributions are also considered, then this grid does not produce grid-independent results. To check for grid convergence, values of surface heat flux averaged from $x = 0.7$ m to $x = 0.8$ m are plotted against the representative cell size for the different grid configurations in Figure 4.6d. For a first-order convergence, the limiting value for surface heat flux is 65.1 kW/m^2. A comparison to this value indicates that the estimated surface heat flux for the "*520×169cells-y$^+$0.6-ar237-gs4*" grid has a grid-induced error of 3.6%, while that for the "*400×130cells-y$^+$0.8-ar235-gs6*" grid has a grid-induced error of 4.7%.

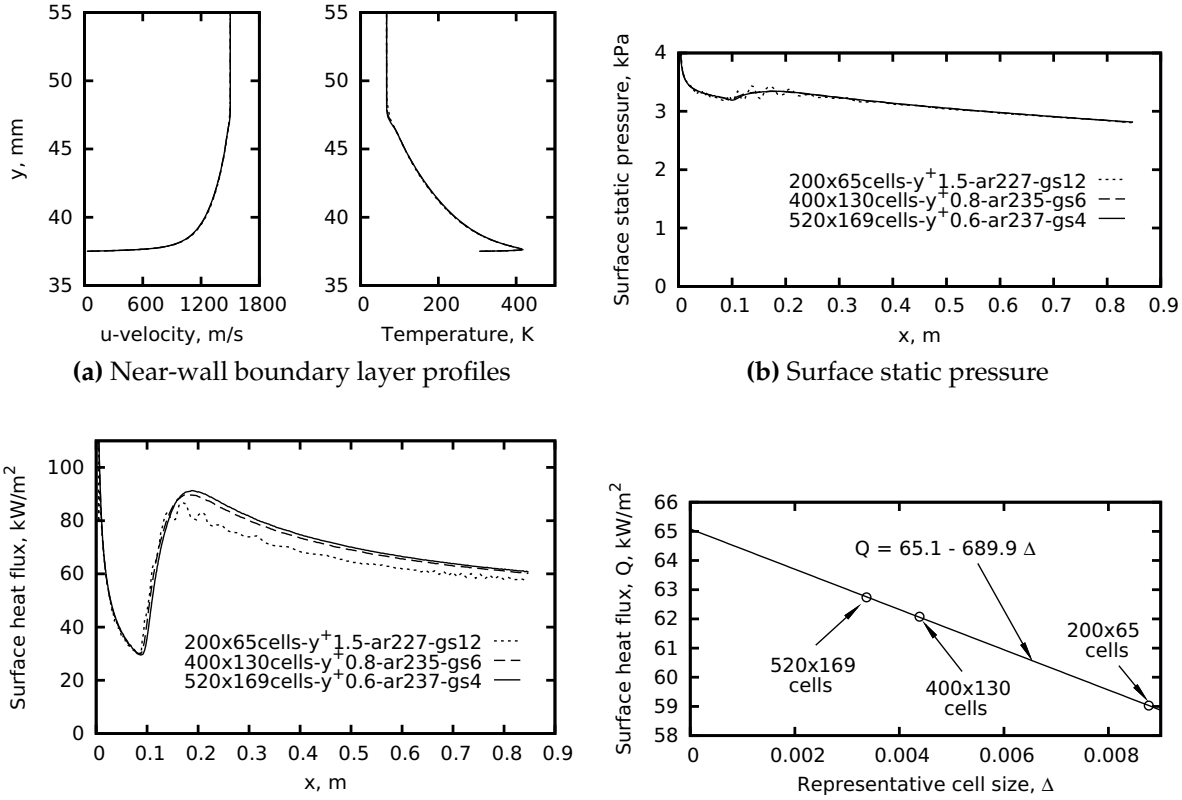

(a) Near-wall boundary layer profiles

(b) Surface static pressure

(c) Surface heat flux

(d) Grid convergence for average surface heat flux values

Figure 4.6: Comparison of results from grids with different resolutions.

In turbulent CFD simulations, the y^+ value and aspect ratio of the first wall-normal cell also need to be considered in grid-convergence studies. The y^+ criterion is important for adequate resolution of the laminar sublayer needed by the low-Reynolds number formulation of the turbulence model, while the maximum cell aspect ratio criterion is needed to ensure adequate resolution of the physics in the flowfield. To examine the influence of y^+ on the numerical results, the grid clustering for the "*400×130cells-y$^+$0.8-ar235-gs6*" grid is adjusted to vary the y^+ values. The simulated surface static

pressure and heat flux distributions are shown in Figure 4.7. It can be observed that only the heat flux distribution is truly sensitive to differences in y^+; the pressure distribution is similar for all three grids. To quantify the k-ω model's sensitivity to y^+ values, the value of y^+ at an arbitrary location ($x = 0.3$ m) is plotted against the value of surface heat flux for each grid in Figure 4.7, and shown in Figure 4.8. A line fitted through these points is extrapolated to estimate the wall heat flux value if an infinitesimally small y^+ is used. A comparison between this extrapolated wall heat flux value to that for $y^+ = 0.2$ gives a difference of approximately 1%. For a y^+ of 0.8, the difference is about 6% and for a y^+ of 1.7, this difference is about 13%. For this test case, where the experimental uncertainties for the heat flux measurements are about $\pm 5\%$, the use of the numerical results from grids with a y^+ less than 0.8 is acceptable.

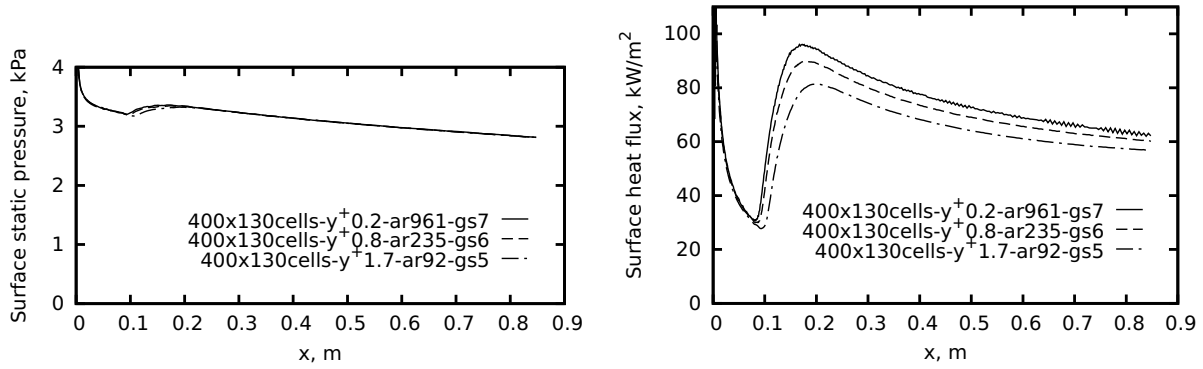

(a) Surface static pressure **(b)** Surface heat flux

Figure 4.7: Comparison of results from grids with different y^+ values.

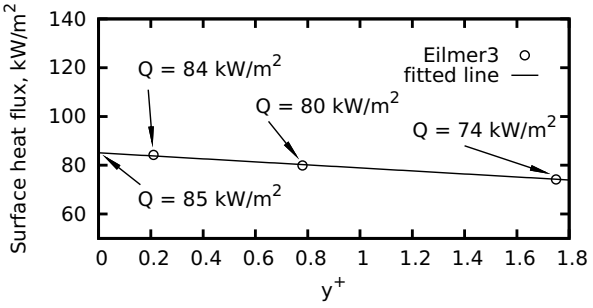

Figure 4.8: Surface heat flux values at $x = 0.3$ m for different y^+ values.

It can be seen in Figure 4.7 that the surface heat flux distribution for the "*400×130-cells-y+0.2-ar961-gs7*" grid becomes unstable downstream of $x = 0.3$ m. This instability is brought about by the high aspect ratios of the cells. Clustering to the surface to

achieve low y^+ values tends to lead to cells with high aspect ratios. To quantify the effects of cell aspect ratio on the simulations, results from grids with different cell aspect ratios are plotted in Figure 4.9. The grids with a maximum cell aspect ratio of around 200 produce stable results. When the maximum cell aspect ratio is around 577, small instabilities appear. For grids with maximum cell aspect ratio higher than 600, significant instabilities can be seen in the surface heat flux traces. For the numerical implementation in Eilmer3 described here, it is therefore recommended that maximum cell aspect ratios be kept below 600 for all simulations. Note that this value may depend on the details of the numerical scheme used. For example, in a different flow structure and with a different code, Hirsch (1988, 2007) quotes a value for maximum cell aspect ratio that is an order of magnitude larger than that stated in this paper. Note also that since the recommendation of 600 is deduced from a test case which has a relatively simple flow, it is likely that a smaller aspect ratio will be needed in cases with regions of strong flow gradients or flow separation.

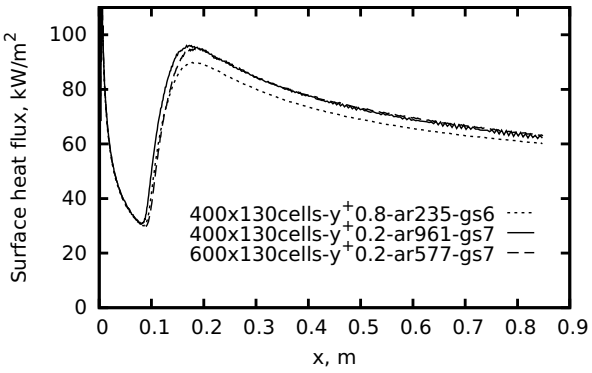

Figure 4.9: Comparison of results from grids with different maximum cell aspect ratios.

Among the different grid configurations tested, the "*520×169cells-y$^+$0.6-ar237-gs4*" grid is taken to be the most suitable one for comparison with the experimental data - it is sufficiently grid-converged for boundary layer profiles, surface pressure and surface heat flux distributions, it has a maximum aspect ratio of less than 600, and it has an average y^+ of 0.6. The numerical results for this grid are compared with the experimental data in Figure 4.10. The computed surface static pressures agree well with those measured. The small dip and rise in the surface static pressure at $x \approx 0.1$ m in Figure 4.10a is an artefact of the turbulence model transitioning the boundary layer from a laminar to a turbulent state.

The surface heat flux distribution in Figure 4.10b can be divided into three regions - laminar region between $x = 0.0$ m and 0.1 m, transitional region between $x \approx 0.1$ m and

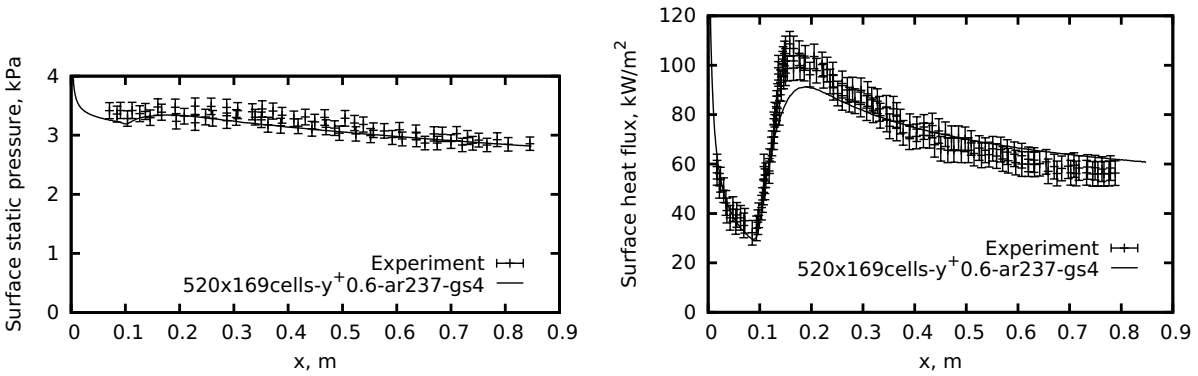

(a) Surface static pressure **(b)** Surface heat flux

Figure 4.10: Comparison of experimental and numerical results.

0.18 m, and turbulent region downstream of $x \approx 0.18$ m. The laminar surface heat flux distribution is well predicted by Eilmer3. The transitional region is also well modelled by the k-ω model in Eilmer3. An interesting point to note here is that even though the only variable fixed in this simulation is the location where transition initiates, the overall transitional process (the length of the transitional region) is predicted quite well by the k-ω model. The turbulence model underpredicts the peak in surface heat flux at $x \approx 0.16$ m by about 9%. In the turbulent region, the simulated surface heat flux distribution matches the experimental data to within experimental uncertainties. This good agreement deviates progressively from the experimental values downstream of $x \approx 0.5$ m.

4.1.5 Test case 3 - Backward-facing step

The third validation test case is the Mach 2 flow over a backward-facing step experiments of Eklund et al. (1995) and McDaniel et al. (1991). A two-dimensional Laval nozzle is used to supply air at a stagnation pressure of 274 kPa and stagnation temperature of 300 K to the backward-facing step (see Figure 4.11). The freestream static pressure, static temperature and velocity are 35 kPa, 167 K and 518 m/s respectively. As the dimensions of the Laval nozzle are not provided in the papers, the nozzle is not modelled in the current simulations. Instead, a two-dimensional duct with a 0.5° taper (to accommodate for boundary layer growth) and an arbitrary length is used. Air, modelled as an ideal gas with a turbulence intensity of 0.01 and a turbulent-to-laminar viscosity ratio of 100, is used as the inflow to the duct. The length of this duct was varied until the flow at one step height upstream of the step matched the experimentally measured profiles (see Figure 4.12). These profiles were then used as inflow conditions

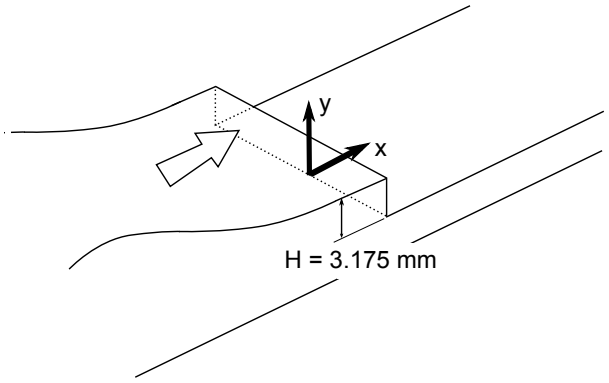

Figure 4.11: Schematic of the backward-facing step experiments.

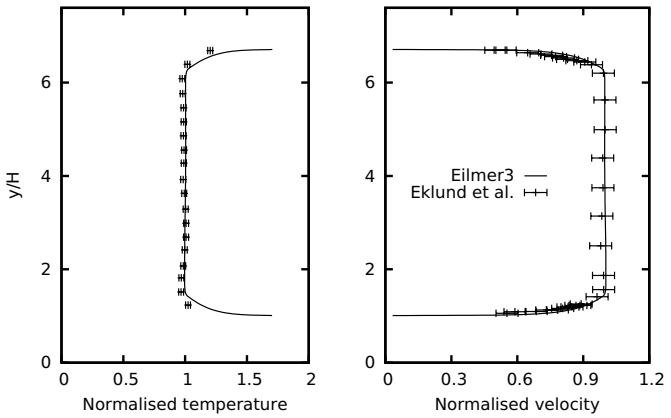

Figure 4.12: Comparison of profiles at x/H = -1. Note that temperatures and velocities have been normalised using freestream quantities quoted in the main text.

for the actual simulation of the flow past the step. Simulations were conducted on three grid resolutions (2685 cells, 10080 cells and 40080 cells) to check for grid convergence. For each of these grids, it was ensured that at least 15 cells were located in the wall-normal direction within the boundary layer and that most wall cells have a y^+ value of less than 1 (except for the first few wall cells just downstream of the step). The walls are assumed to be adiabatic for the simulations. Figure 4.13a shows the estimated displacement thickness at $x/H = -1$ plotted against the representative cell size for the three grid configurations while Figure 4.13b shows that for the estimated y-location of the expansion fan at $x/H = 10.8$. The limiting value for the displacement thickness is 3.86 mm with close to second-order convergence, while that for the y-location of the expansion fan is 8.75 mm with approximately third-order convergence. A comparison

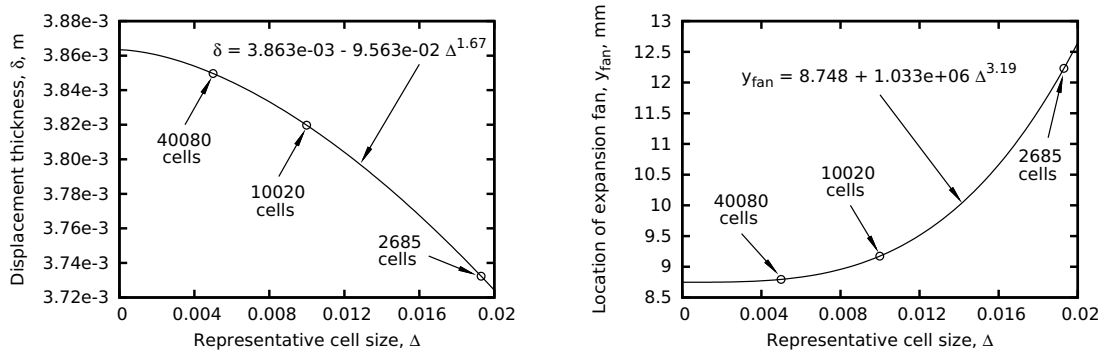

(a) Displacement thickness at $x/H = -1$ **(b)** y-location of expansion fan at $x/H = 10.8$

Figure 4.13: Grid convergence for the 2D backward-facing step test case.

of these values with those from the solutions of the 40080-cell grid indicates a grid-induced error of 0.3% for the displacement thickness and 0.5% for the y-location of the expansion fan.

Figure 4.14 shows the comparisons between experimentally measured and numerically computed pressure and temperature contours. These comparisons show that the degree of expansion, the position of the recompression shock and the size of the separation region are well estimated by Eilmer3. Only a subtle difference can be observed from these comparisons - the expansion fan is shown to centre around the step and does not extend as far upstream as measured in the experiments. Eklund et al. (1995) also observed this in their numerical simulations and attributed it to the small curvature at the corner of the step not being modelled in the simulations. Eilmer3 simulations with a 0.5 mm radius curvature at the corner of the step also failed to reproduce the upstream spreading of the expansion fan seen in the experiments.

Comparisons between the computed and measured (pointwise laser-induced iodine fluorescence) profiles of pressure, temperature and x-velocity at several axial locations are shown in Figures 4.15a - 4.15c. The expansion fan and recompression shock are well captured by Eilmer3 (see pressure plots at $y/H = 1.8$ in Figure 4.15a and $y/H = 2.4$ in Figure 4.15b for the expansion fan, and at $y/H = 0.8$ in Figure 4.15b and $y/H = 2.9$ in Figure 4.15c for the recompression shock). However, in the region where recompression starts (see pressure plot at $y/H < 0.7$ in Figure 4.15b), Eilmer3 underestimates the pressure near the walls by 13%. The temperatures at all three locations are also well estimated by Eilmer3. The only difference is in the near-wall region where Eilmer3 overestimates the temperatures by 5%. This mismatch is due to the erroneous near-wall PLIIF measurement of temperatures brought about by background scattering. The excellent agreement between the experiments and simulations is also seen in

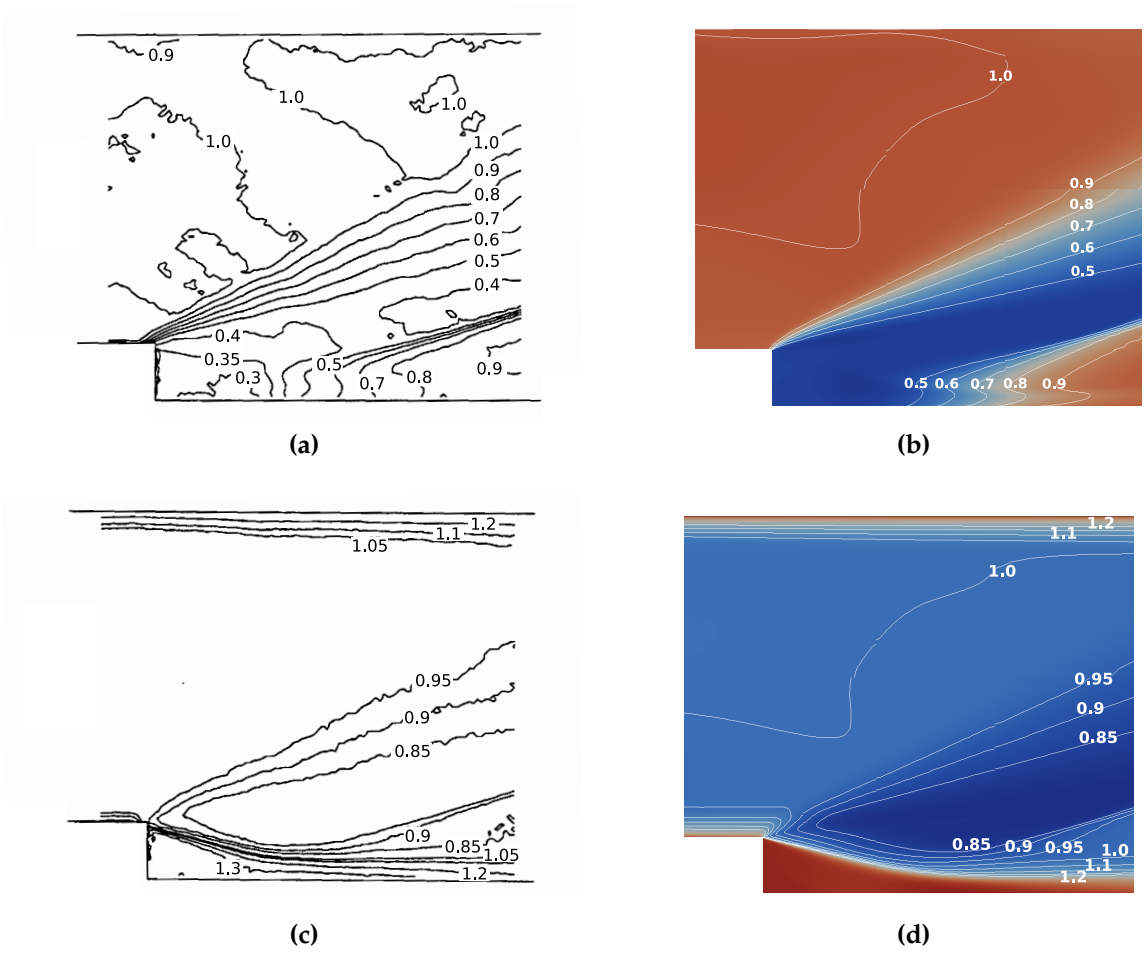

Figure 4.14: Comparison between **(a)** experimentally measured and **(b)** numerically simulated pressure contours, and **(c)** experimentally measured and **(d)** numerically simulated temperature contours. Note that the iso-contours have been normalised using freestream static properties.

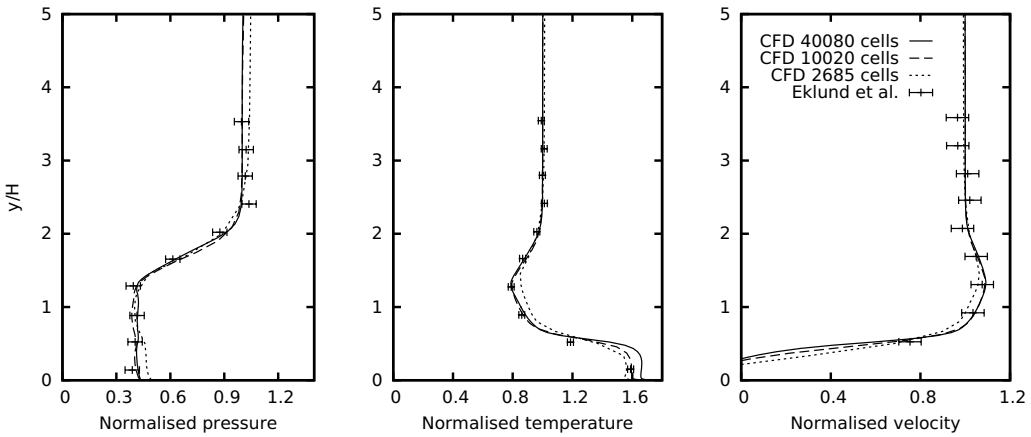

(a) Boundary layer profiles at $x/H = 1.7$.

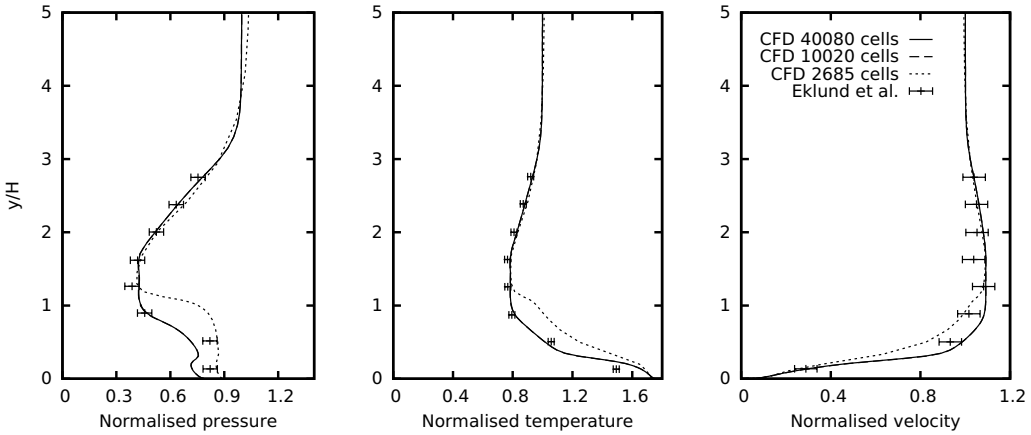

(b) Boundary layer profiles at $x/H = 3.9$.

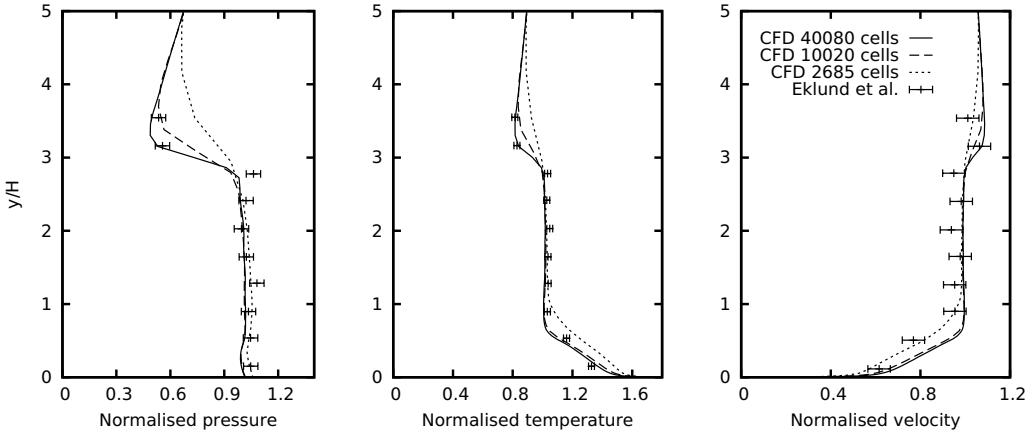

(c) Boundary layer profiles at $x/H = 10.8$.

Figure 4.15: Boundary layer profiles at several x/H locations. Note that pressures, temperatures and velocities have been normalised using freestream quantities.

the x-velocity profiles, where the only difference of about 22% occurs at $y/H = 0.5$ in Figure 4.15c.

4.1.6 Test case 4 - Mixing of coaxial jets

The fourth test case is the experiment of Cutler et al. (2006) that was conducted to study the turbulent mixing phenomena of two supersonic coaxial jets. Conducted at NASA Langley Research Centre, these experiments have been adopted by the NATO Research and Technology Organisation Working Group 10 as a test case for their CFD development and validation activities. As the exit static pressures of both jets have been tuned to be similar, the streamwise development of the flow is dominated by turbulent stresses rather than pressure forces (Cutler and White, 2001). As such, this set of experiments is considered to be an excellent test case for the turbulence model. The experimental setup (Figure 4.16), designed to discharge two coaxial jets at Mach 1.8 into stagnant air, is axisymmetric and consists of an outer body and centre body. The

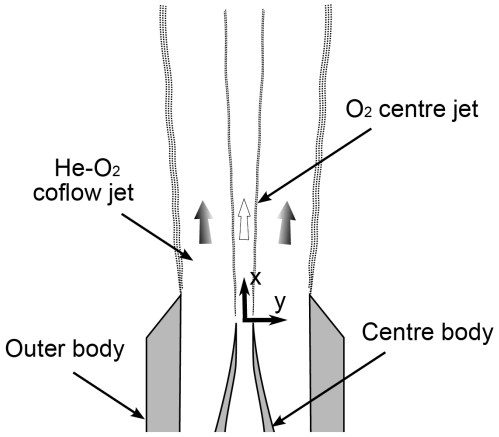

Figure 4.16: Schematic of the coaxial jets experiments.

passage between both bodies forms an exit nozzle for the coflow jet while the interior passage of the centre body forms an exit nozzle for the centre jet. The centre jet, which has a stagnation pressure of 615 kPa and stagnation temperature of 306 K, consists of a mixture of helium and oxygen (95% He and 5% O_2 by volume), while the coflow jet, which has a stagnation pressure of 580 kPa and stagnation temperature of 300 K, consists of air. An axisymmetric simulation of the flowfield is conducted with three grids with different total numbers of cells (22572 cells, 90288 cells, 361152 cells). Grid-independent solutions are obtained from the grid with a total of 90288 cells. The grids start from the throats of both nozzles and extend for 0.27 m downstream of the nozzle exit plane. The grids also extend out radially by 0.33 m to capture the interaction

between the coflow jet and the ambient air. The grids are clustered towards the walls of both nozzles to achieve y^+ values of less than 1. All gases used for this simulation are modelled as ideal gases. In addition, a modification to Fick's first law of diffusion (Bird et al., 2007) to allow for turbulent mass diffusion is used. The turbulent Prandtl and Schmidt numbers are assumed to be 0.75, as recommended by Cutler et al. (2006).

Figures 4.17 - 4.20 show the comparisons between experimentally measured and numerically simulated profiles of He-O_2 mole fractions, Pitot pressure, x-velocity and root-mean-square x-velocity fluctuations. Note in Figure 4.20 that the experimentally measured values of root-mean-square x-velocity fluctuations $\sqrt{\overline{u'^2}}$ are compared with numerically simulated $\sqrt{2k/3}$ values. This has to be carried out because $\sqrt{\overline{u'^2}}$ cannot be extracted fom RANS simulations. However, since $\sqrt{\overline{u'^2}}$ is equal to $\sqrt{2k/3}$ only in truly isotropic turbulence (in most shear flow cases, $\sqrt{\overline{u'^2}}$ is slightly larger than $\sqrt{2k/3}$), the comparison between both values should only be treated to be approximate (Hinze, 1975). Note also that there are two sets of numerical results for the plots in Figures 4.17 - 4.20. The "*Low* I_{turb}" results are from Eilmer3 simulations that have an inflow turbulence intensity of 0.01 and a turbulence-to-laminar viscosity ratio of 1. The "*High* I_{turb}" results are from simulations that have an inflow turbulence intensity of 0.035 for the coflow jet and 0.02 for the centre jet, and a turbulence-to-laminar viscosity of 5000 for both jets. This rather large value for turbulent-to-laminar viscosity ratio is needed to match the measured turbulence intensities at the nozzle exit plane. Specifically, the higher freestream turbulence quantities for the "*High* I_{turb}"case are obtained from adjustments of these values to match $\sqrt{2k/3}$ values with $\sqrt{\overline{u'^2}}$ values at the nozzle exit plane (see Figure 4.20a). In addition, Cutler's CFD results are also presented together with the experimental measurements and Eilmer3 results (see Figures 4.17 - 4.20f).

Figure 4.17 shows that the turbulent mixing of helium and oxygen between the coflow and centre jets is well predicted by the "*High* I_{turb}" Eilmer3 simulations, with a difference of 5% occurring at the last measurement plane (Figure 4.17f). Results from the "*Low* I_{turb}" Eilmer3 simulations and from Cutler's CFD simulations (which also used low freestream turbulence intensities) do not match the experiments as well as the '*High* I_{turb}" simulations. This shows that matching the turbulence intensities at the nozzle exit plane is important in achieving good agreement between the numerical and experimental results. Although the rate at which both jets mix in the numerical simulations can be controlled by adjusting the turbulent Schmidt number (Cutler and White, 2001), the way in which both jets mix is dependent on the turbulence model and diffusion model. The excellent agreement between the "*High* I_{turb}" Eilmer3 simulations

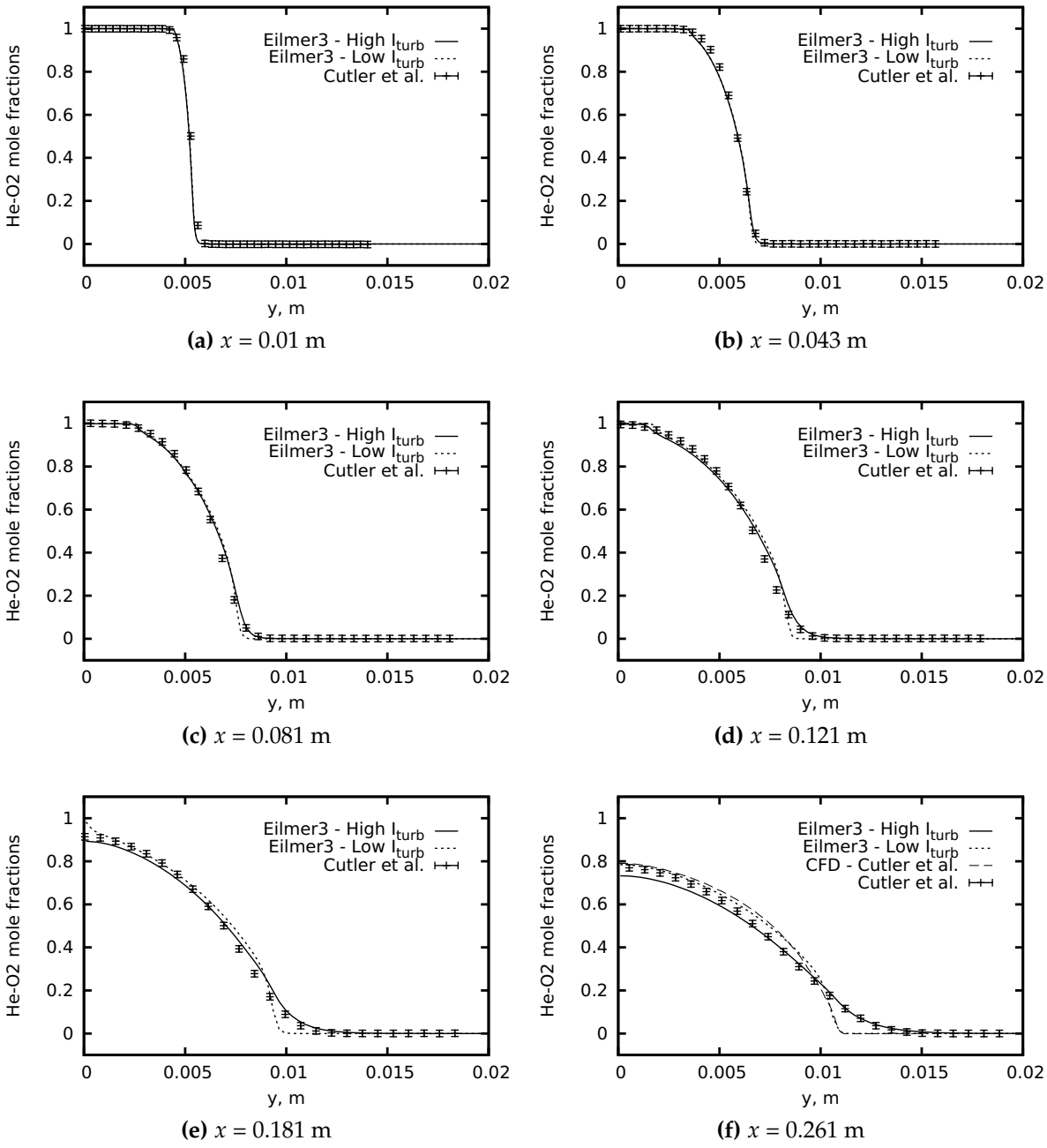

(a) $x = 0.01$ m **(b)** $x = 0.043$ m

(c) $x = 0.081$ m **(d)** $x = 0.121$ m

(e) $x = 0.181$ m **(f)** $x = 0.261$ m

Figure 4.17: He-O_2 mole fractions at several x-locations.

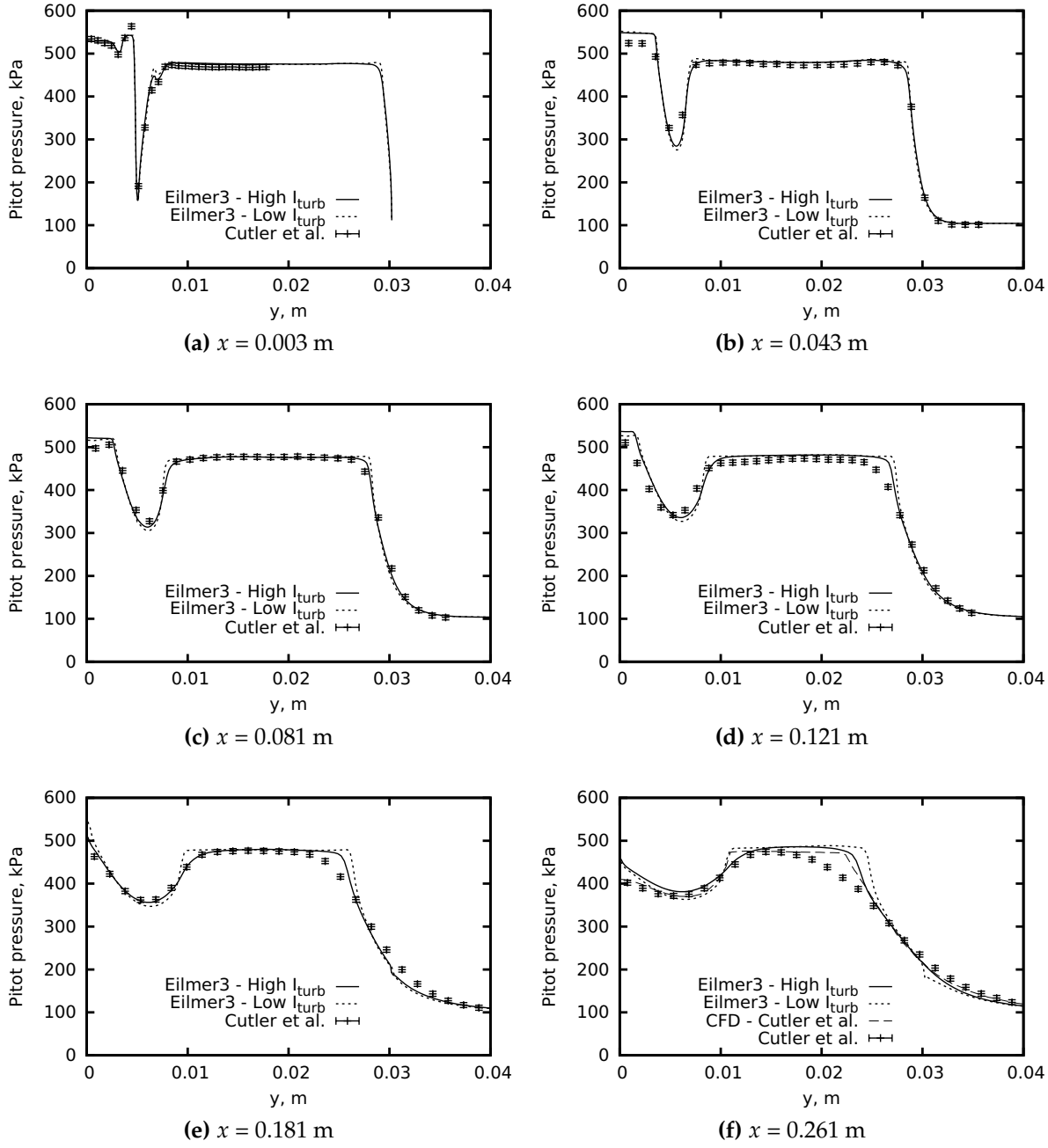

(a) $x = 0.003$ m **(b)** $x = 0.043$ m

(c) $x = 0.081$ m **(d)** $x = 0.121$ m

(e) $x = 0.181$ m **(f)** $x = 0.261$ m

Figure 4.18: Pitot pressure at several x-locations.

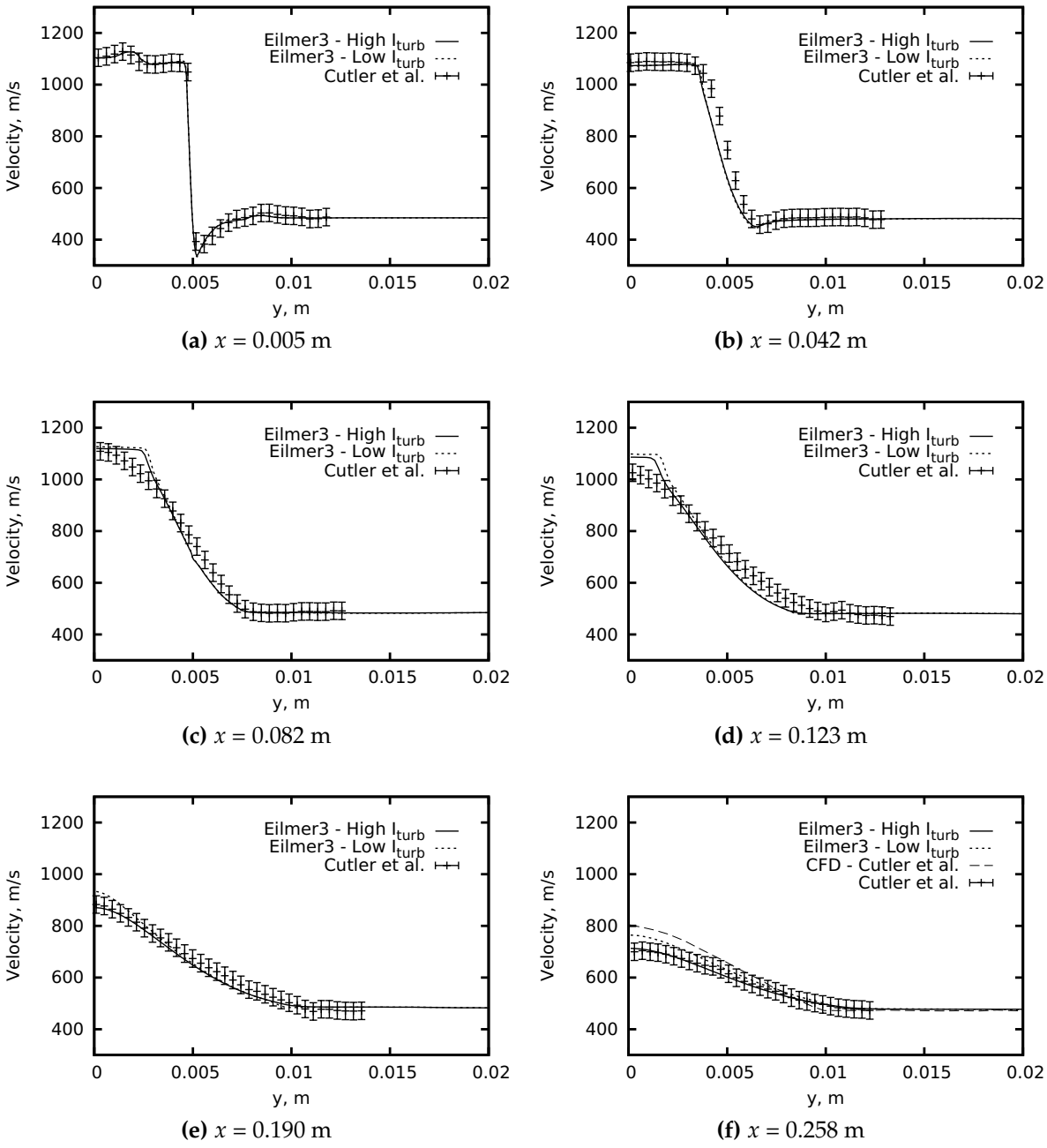

(a) $x = 0.005$ m **(b)** $x = 0.042$ m

(c) $x = 0.082$ m **(d)** $x = 0.123$ m

(e) $x = 0.190$ m **(f)** $x = 0.258$ m

Figure 4.19: x-velocity at several x-locations.

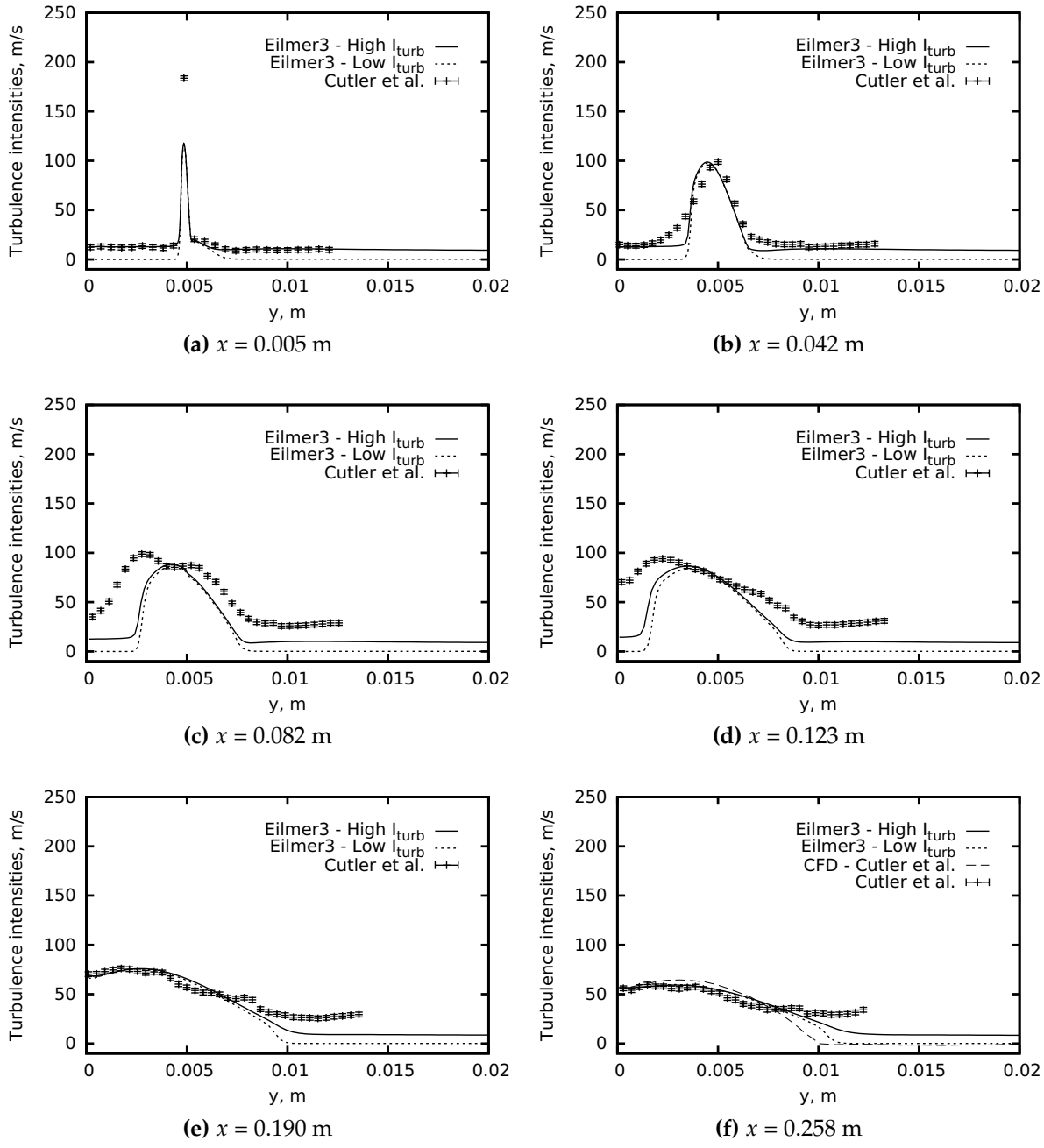

(a) $x = 0.005$ m **(b)** $x = 0.042$ m

(c) $x = 0.082$ m **(d)** $x = 0.123$ m

(e) $x = 0.190$ m **(f)** $x = 0.258$ m

Figure 4.20: Comparison of experimental turbulence intensity $\sqrt{\overline{u'^2}}$ from the experiments of Cutler et. al. and numerical turbulence intensity $\sqrt{2/3\,k}$ from Eilmer3 simulations.

and experiments indicates that the combination of the modified Fick's diffusion model and Wilcox's k-ω turbulence model works well in predicting the mixing phenomena of both jets.

Figure 4.18 shows that the Pitot pressures in the mixing region between both jets ($y = 0$ m to 0.015 m) are also well estimated by the "*High* I_{turb}" Eilmer3 simulations. The interaction between the coflow jet and the ambient air is well estimated up to $x = 0.081$ m. The simulations then deviate by up to 15% from the experimental measurements downstream of this location. For the x-velocities (Figure 4.19), Eilmer3 estimations of the experiments are good, with a maximum difference of 8% occurring at $x = 0.082$ m. Similar to the comparisons made in Figure 4.17, the "*High* I_{turb}" Eilmer3 simulations match the experiments better than the "*Low* I_{turb}" Eilmer3 simulations and Cutler's simulations. This, once again, demonstrates the importance of matching the turbulence intensities at the nozzle exit plane.

Figure 4.20 shows that the profiles of $\sqrt{\overline{u'^2}}$ and $\sqrt{2k/3}$ are in good agreement qualitatively. However, while $\sqrt{2k/3}$ in the region $y = 0.01$ m to 0.02 m stays almost constant, $\sqrt{\overline{u'^2}}$ increases in the streamwise direction. This increase in $\sqrt{\overline{u'^2}}$ values is attributed to increased streamwise interaction of the coflow jet with the ambient air. The mismatch between the $\sqrt{\overline{u'^2}}$ and $\sqrt{2k/3}$ values in this region could be the cause for the difference between experimentally measured and numerically computed Pitot pressure profiles in the $y = 0.01$ m to 0.02 m region (see Figure 4.18f).

4.1.7 Test case 5 - Shock-wave-turbulent-boundary-layer interaction

The fifth test case is that of the experiments of Kim et al. (1991) conducted to study the interaction between a swept shock wave and a turbulent boundary layer. The experimental setup is shown in Figure 4.21. Air at a freestream static pressure of 10.3 kPa,

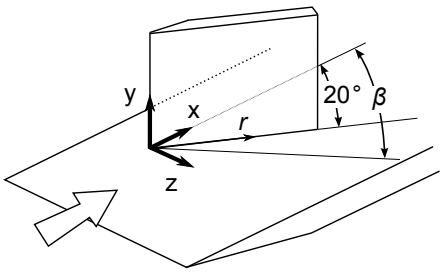

Figure 4.21: Schematic of the shock-wave-turbulent-boundary-layer interaction experiments.

static temperature of 70.4 K, velocity of 707 m/s and Mach number of 4 flows over the flat plate of length 0.216 m. The resulting boundary layer on the flat plate is turbulent upstream of the fin (Kim et al., 1991). This boundary layer then interacts with the shock wave generated by the 20° fin. To simulate this flowfield, three three-dimensional grids with different total numbers of cells are used. Grid-independent solutions are obtained for a grid with a total of 2985984 cells. Boundary layer profiles from two-dimensional turbulent flat plate simulations, which have been verified against those measured experimentally (Lu, 1988), are used as inflow conditions for these simulations. As no turbulence parameters were measured in the experiments, an arbitrary turbulence intensity of 0.01 and turbulent-to-laminar viscosity ratio of 1 are used to start the two-dimensional flat plate calculations. The surfaces of the flat plate and fin are modelled as non-slip walls at a constant temperature of 316.2 K. The grids are clustered towards these walls to ensure that the y^+ and z^+ values are below 1.

Figure 4.22 shows a comparison between experimentally measured and numerically computed values of static pressure on the flat plate surface at $r = 0.0889$ m. It can be observed that Eilmer3 simulations capture both the vortex in the near-fin region (note the pressure rise and drop for $20^\circ < \beta < 30^\circ$) and the vortex on the flat plate (note the pressure rise and drop for $30^\circ < \beta < 52^\circ$). Numerical results of Knight et al. (2003), which were obtained from simulations with the Wilcox-Durbin turbulence model, are also shown in Figure 4.22. The Wilcox-Durbin turbulence model (Durbin,

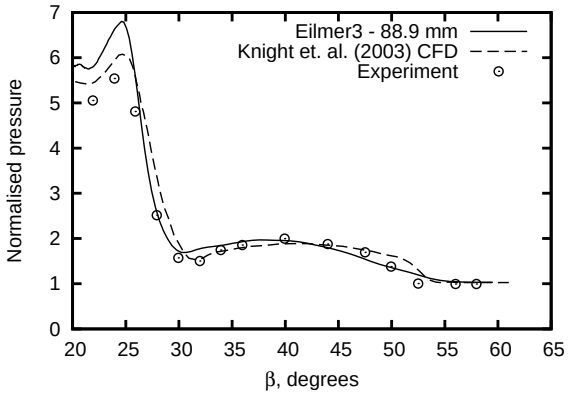

Figure 4.22: Static pressure on the flat plate surface at $r = 0.0889$ m. Note that static pressures have been normalised against freestream quantities.

1996) is essentially the Wilcox 1988 k-ω model (Wilcox, 1988) that uses a $C_{lim} = 1.03$ stress-limiter. Knight et al. (2003) showed that the use of the Wilcox-Durbin model improved the estimates for 3D shock-wave-turbulent-boundary-layer interaction in comparison with the Wilcox 1988 k-ω model. According to Wilcox (2006), the $C_{lim} = 7/8$

stress-limiter in the 2006 k-ω model should further improve these estimates. In the $30^\circ < \beta < 60^\circ$ region in Figure 4.22, the computed surface static pressure distribution for both turbulence models are in close agreement with the experiments. In the $25^\circ < \beta < 30^\circ$ region, the 2006 k-ω model performs better than the Wilcox-Durbin model in estimating the drop in static pressure. Both models overestimate the pressures in the near-fin region ($20^\circ < \beta < 25^\circ$) with the 2006 k-ω model performing worse than the Wilcox-Durbin model.

4.1.8 Test case 6 - Boundary layer combustion experiments of Kirchhartz

As described in Section 2.1, Kirchhartz (2010) used a circular constant-area inlet which was connected to a circular constant-area combustor with an annular slot fuel injector for his boundary-layer-combustion experiments 2.10 . To model this geometry, a grid which had total of 620400 cells was used. The location for boundary layer transition was taken to be at 0.122 m upstream of the fuel injection plane (Kirchhartz, 2010). Nitrogen, modelled as an ideal gas at a static pressure of 79.4 kPa, temperature of 1075 K, and velocity of 2860 m/s, was used as the inflow to the inlet. Hydrogen, modelled as an ideal gas at a static pressure of 9.3 kPa, static temperature of 86.7 K, and velocity of 2280 m/s, was used as the inflow at the exit of the fuel injector. The inflow profiles for the inlet and the fuel injection were assumed to be uniform. In addition, the freestream turbulence intensity was taken to be 0.01 and the freestream turbulent-to-laminar viscosity ratio to be 1. As Kirchhartz's tests were conducted in the T4 impulse facility, the surface temperature of the model is estimated to rise by less than 1 K due to the short test times. The inlet and combustor walls were hence modelled in the simulations to be at a constant temperature of 298 K. Although values of y^+ varied along the duct in these simulations, these values were kept below 1 for most parts of the duct, with exception to the first few cells at the leading edge and behind the backward-facing step. In comparison with grids with 310200 and 155100 cells, grid-converged results were obtained for the grid with 620400 cells. To account for turbulent diffusion, a modified version of Fick's diffusion model (Bird et al., 2007) was used. The combination of this model with the k-ω model was shown to successfully estimate the turbulent mixing phenomena of two coaxial jets in test case 4. Note that only the fuel-off and fuel-into-N_2 tests from Kirchhartz's experiments are simulated.

Figure 4.23a shows a comparison of the experimental (from tests 10167 and 10192) and numerical pressures along the combustor. For both the injection and no-injection cases, the experimental pressure distribution along the combustor is well estimated

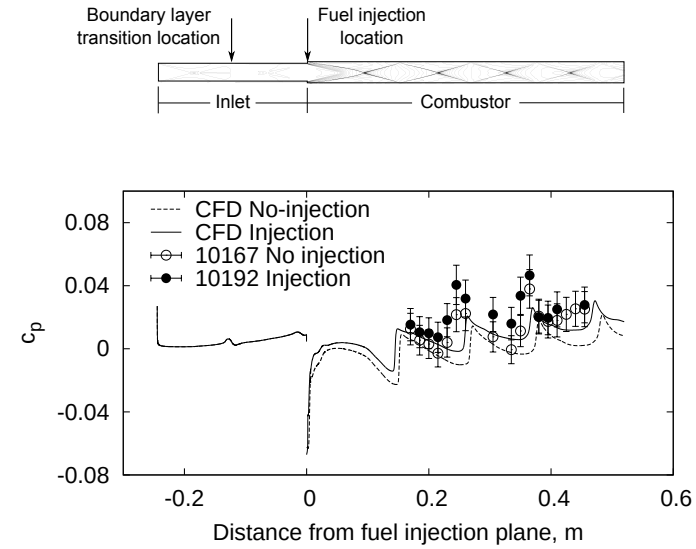

(a) Pressure coefficient

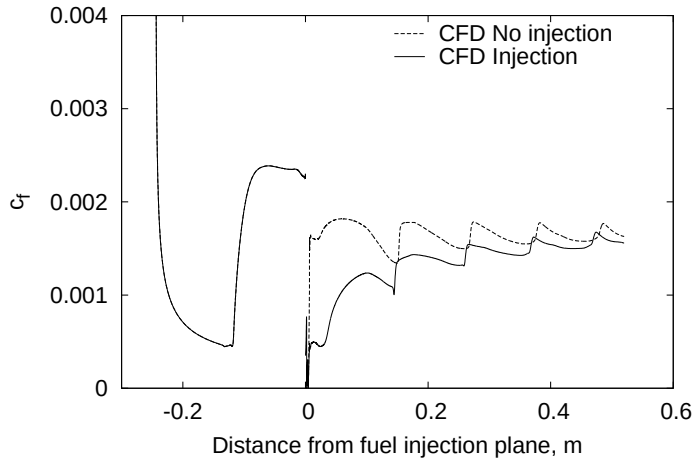

(b) Local skin friction coefficient

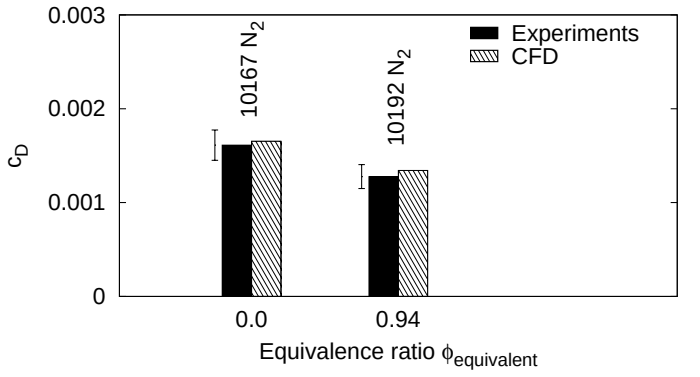

(c) Integrated skin friction coefficient

Figure 4.23: Comparison of experimental and numerical results.

by Eilmer3. The only difference is that Eilmer3 overpredicts the shock impingement locations by 0.015 m. This could be attributed to the assumption of a uniform inflow profile at the entrance of the inlet instead of accounting for the possible variations in the profile (Schloegel and Boyce, 2009). Note also that both the experimental and numerical pressures are higher for the injection case than for the no-injection case. This increase in pressure is brought about by the effect of mass addition. Figure 4.23b shows the numerically simulated local skin friction coefficient along the combustor. The rise in the values of skin friction coefficient at -0.122 m is brought about by the "switching-on" of turbulence. As expected, the skin friction coefficient upstream of fuel injection in the inlet for both injection and no-injection cases are identical. In the combustor, the reduction of the local skin friction coefficient is evident when hydrogen is injected. A reduction of 70% in the skin friction coefficient for the injection case from that for the no-injection case occurs in the region of 10 step heights from the fuel injection plane. Downstream of this region, the high level of skin friction reduction then diminishes to about 6% by the end of the combustor. The reduction in skin friction is brought about the film-cooling effect described in Chapters 1 and 2. The resulting drag integrated over the length of the combustor is then normalised as discussed in Section 3.4.2, and compared against experimentally measured values in Figure 4.23c. The integrated drag coefficients from the experiments for both injection and no-injection cases are well predicted by the numerical simulations. Because the level of drag reduction estimated by Eilmer3 is similar to that measured in the experiments, this is a good indication that Eilmer3 has also correctly estimated the levels of mixing between the injected hydrogen and mainstream nitrogen.

The excellent agreement observed between the numerical and experimental results in this and the other five test cases clearly demonstrates that Eilmer3, with the k-ω turbulence model implemented by the present author, can be used to simulate the type of flow relevant to the current study.

4.2 Analytical tools

Despite their simplicity, turbulent skin friction theories can be very useful tools for the prediction of skin friction drag. For the current project, these theories are used for the estimation of turbulent skin friction drag acting on the internal surface of the combustor. Although these theories do not take into account the effects of flow disturbances and hence may not be expected to give a highly accurate prediction of the skin friction drag in the presence of flow disturbances, the drag values predicted using these theories still provide a good baseline estimate for when boundary layer combustion works

and is hence a useful gauge for estimating how much skin friction reduction is affected by flow disturbances.

4.2.1 Turbulent skin friction theories

Of the many theories reviewed by Hopkins and Inouye (1971), Cary and Bertram (1974), Bradshaw (1977) and White (2006), the method commonly referred to as the van Driest II method is proposed to be the most accurate method for predicting compressible turbulent skin friction drag. For flows on very cold walls ($T_w/T_{aw} < 0.2$), several researchers have found that the theory of Spalding and Chi (1964) gave a more accurate prediction of skin friction drag than does the van Driest II method (Bradshaw, 1977; Goyne et al., 2003; Kirchhartz, 2010). For tests in hypersonic impulse facilities, the wall-to-adiabatic-wall-temperature ratio T_w/T_{aw} generally ranges from 0.02 to 0.1. Since T_w/T_{aw} in the combustor for the conditions used in the current experiments is expected to range from 0.05 to 0.08, it is also appropriate to consider the turbulent skin friction predictions from the theory of Spalding & Chi. For cases where hydrogen is injected and allowed to burn, skin friction is predicted using the theory of Stalker (2005), which is described in Section 2.1.

Van Driest (1956)

The local skin friction coefficient c_f can be estimated using Equation 4.13.

$$4.15 \log(c_f Re_x \mu_e/\mu_w) + 1.7 \quad = \quad F_0/\sqrt{c_f(T_{aw} - T_e)/T_e} \tag{4.13}$$

where

$$\begin{aligned} F_0 &= \sin^{-1}(b/Q) + \sin^{-1}\left[(2a^2 - b)/Q\right] \\ b &= (H_e - H_w)/H_w \\ a^2 &= u_e^2/(2.0 H_w) \\ Q &= \sqrt{b^2 + 4a^2} \end{aligned} \tag{4.14}$$

Spalding and Chi (1964)

The local skin friction coefficient c_f can be estimated using Equation 4.15.

$$c_{f,e} = (1/F_c)\, c_{f,e,inc} \tag{4.15}$$

where

$$\begin{aligned} F_c &= [(T_{aw}/T_e) - 1] \ / \ (\sin^{-1}\alpha + \sin^{-1}\beta)^2 \\ \alpha &= [(T_{aw}/T_e) + (T_w/T_e) - 2] \ / \ \sqrt{[(T_{aw}/T_e) + (T_w/T_e)]^2 - 4(T_w/T_e)} \\ \beta &= [(T_{aw}/T_e) - (T_w/T_e)] \ / \ \sqrt{[(T_{aw}/T_e) + (T_w/T_e)]^2 - 4(T_w/T_e)} \end{aligned} \tag{4.16}$$

The incompressible skin friction coefficient $c_{f,e,inc}$ can be computed using Equation 4.17.

$$\begin{aligned} Re_{x,inc} = (1/12)(2/c_{f,inc})^2 + (1/[K^3E])\Bigg\{ &\left[2 + \left(2 - K\sqrt{2/c_{f,inc}}\right)^2\right] \exp\left(K\sqrt{2/c_{f,inc}}\right) \\ &- 6 - 2K\sqrt{2/c_{f,inc}} - (1/12)\left(K\sqrt{2/c_{f,inc}}\right)^4 - (1/20)\left(K\sqrt{2/c_{f,inc}}\right)^5 \\ &- (1/60)\left(K\sqrt{2/c_{f,inc}}\right)^6 - (1/256)\left(K\sqrt{2/c_{f,inc}}\right)^7 \Bigg\} \end{aligned} \tag{4.17}$$

where

$$\begin{aligned} Re_{x,inc} &= Re_x / \left[F_c \, (T_e/T_{aw})^{-0.772} \, (T_e/T_w)^{1.474}\right] \\ K &= 0.4 \qquad \text{and} \qquad E = 12 \end{aligned} \tag{4.18}$$

Stalker (2005)

For cases when hydrogen is injected but combustion is suppressed, the local skin friction coefficient c_f can be estimated using Equation 4.19.

$$\begin{aligned} 4.15\log(c_f Re_x \mu_e/\mu_w) + 1.7 = \ & F_0/\sqrt{c_f(T_{aw} - T_e)/T_e} \\ & + 3.97\log\left[1.0 - c_{Hw} + c_{Hw}u_{\text{jet}}/u_e\right] \end{aligned} \tag{4.19}$$

where

$$\begin{aligned} F_0 &= \sin^{-1}(b/Q) + \sin^{-1}\left[(2a^2 - b)/Q\right] \\ b &= (H_e - H_w)/H_w \\ a^2 &= u_e^2/(2.0H_w) \\ Q &= \sqrt{b^2 + 4a^2} \end{aligned} \tag{4.20}$$

For cases when hydrogen is injected and allowed to burn, the local skin friction coefficient c_f can be estimated using Equation 4.21.

$$\begin{aligned} &4.15\log(c_f Re_x \mu_e/\mu_w) + 1.7 \quad = \\ &F_1/\sqrt{c_f(T_{aw}-T_e)/T_e} \\ &+ 3.97\log\left\{\left[1.0 - c_{Hw} + (c_{Hw} + f c_{oe})u_{\text{jet}}/u_e\right]/(1.0 + f c_{oe})\right\} \\ &+ 3.97\log\left\{1.0 + G\exp\left[(F_2 - F_1)K\sqrt{2}/\sqrt{c_f(T_{aw}-T_e)/T_e}\right]\right\} \end{aligned} \tag{4.21}$$

where

$$\begin{aligned} G &= 0.5(b_1 - b_2)g(1-g)/(1 + b_1 g - a^2 g^2) \\ F_1 &= \sin^{-1}(b_1/Q_1) + \sin^{-1}\left[(2a^2 - b_2)/Q_2\right] \\ &\quad + \sin^{-1}\left[(2a^2 g - b_1)/Q_1\right] - \sin^{-1}\left[(2a^2 g - b_2)/Q_2\right] \\ F_2 &= \sin^{-1}(b_1/Q_1) + \sin^{-1}\left[(2a^2 g - b_1)/Q_1\right] \\ b_1 &= (H_e - H_w + f c_{oe}\Delta Q)/H_w \\ b_2 &= (H_e - H_w - c_{Hw}\Delta Q)/H_w \\ a^2 &= U^2/(2.0 H_w) \\ \alpha &= c_{Hw}\Delta Q/H_w \\ Q_1 &= \sqrt{b_1^2 + 4a^2} \\ Q_2 &= \sqrt{b_2^2 + 4a^2(1.0 + \alpha)} \end{aligned} \tag{4.22}$$

Note that although these theories have been developed for boundary layers on flat plates, they are applied in this project for the estimation of skin friction drag on the curved internal surface of the combustor. For a boundary layer with a thickness that is small relative to the radius of the combustor, the flat plate assumption is approximately valid. Kirchhartz (2010) showed that for a 3.4 mm thick boundary layer in a combustor of radius 16.6 mm, these theories can be used to estimate the skin friction to within 10% accuracy for the experiments without fuel injection and to within 25% accuracy for the experiments with fuel injection. For the current experiments, where the combustor has the same radius as that of the combustor in Kirchhartz's experiments, the average boundary layer thickness is estimated to be 3.5 mm for about 90% of the combustor circumference and 8 mm for the remaining 10%. This is roughly comparable to the boundary layer thickness observed in Kirchhartz's experiments, and hence indicates

that the accuracy of the skin friction predictions will similar to that in Kirchhartz's analysis. For the current experiments, the effects of the flow disturbances are more likely to influence the accuracy of the skin friction predictions than that of the deviation from the flat plate assumption.

4.2.2 Modification of theories to account for flows with pressure gradients

In the current experiments, when combustion occurs, the pressure levels in the constant-area combustor rises to relatively high levels. This results in an adverse pressure gradient that acts on the boundary layer. However, the three skin friction drag theories described in Section 4.2.1 were developed for flows with low or no pressure gradients. To account for adverse pressure gradients, these theories are applied in this project using a local similarity principle proposed by Stollery and Coleman (1975). Stollery and Coleman (1975) suggest that for an arbitrary body with properties known at the edge of the boundary layer, the corresponding skin friction drag can be estimated by locally applying a skin friction prediction method on incremental slices over the body, as illustrated in Figure 4.24.

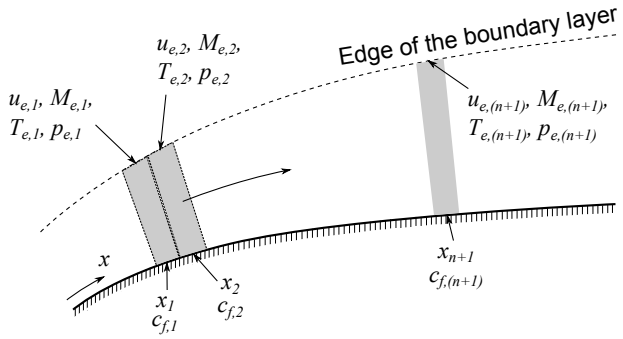

Figure 4.24: Schematic for the concept of local similarity (Anderson, 2006).

Using the reference enthalpy method by Eckert (1955) as the skin friction approximation method, Stollery (1976) shows that the local similarity approach can be used to predict skin friction drag on flat plates and axisymmetric bodies with pressure gradients. For the current experiments, the van Driest II, Spalding and Chi, and Stalker theories are applied using the local similarity approach, as follows.

1. Fit a line to the measured static pressure distribution in the combustor. Assuming that pressure remains constant across the boundary layer, the fitted line is the pressure at the edge of the boundary layer $p_e(x)$, where x is the distance along the combustor.

2. Since the oncoming freestream conditions (p_∞, T_∞, M_∞, ρ_∞, u_∞) are known, use isentropic relations to compute the other properties at the edge of the boundary layer ($T_e(x)$, $M_e(x)$, $\rho_e(x)$, $u_e(x)$).

3. Using the localised boundary layer edge conditions, compute the local skin friction coefficient by applying the turbulent skin friction theories of van Driest II, Spalding & Chi and Stalker.

4. Integrate the local skin friction coefficient over the internal surface of the combustor to obtain the integrated drag coefficient c_D.

To demonstrate the validity of this approach, the experimental results of Kirchhartz (2010) are used. Figure 4.25 shows a comparison between the experimental, numerical and theoretical values of integrated skin friction drag coefficient. The experimental

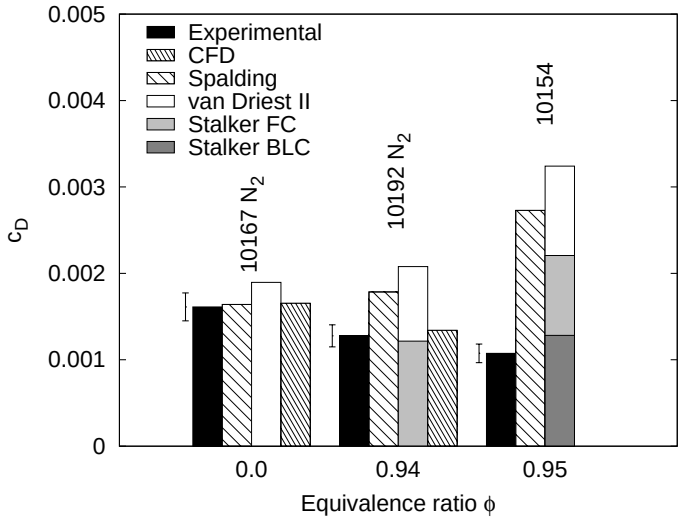

Figure 4.25: Comparison of experimental, numerical and theoretical results.

and numerical drag coefficients are similar to those shown in Figure 4.23c, while the theoretical values are computed using the local similarity approach. These values are shown for three cases - a fuel-off-N_2 test (10167), a fuel-into-N_2 test (10192) and a fuel-on test (10154). For test 10167, it can be seen that the Spalding & Chi method offers a better approximation of the skin friction drag than does the van Driest II method.

Since the value of T_w/T_{aw} is 0.15 for this test, this supports the findings of Bradshaw (1977), Goyne et al. (2003) and Kirchhartz (2010) that the theory of Spalding and Chi (1964) gives a more accurate prediction of skin friction drag for flows on very cold walls ($T_w/T_{aw} < 0.2$).

For the fuel-on test 10154, the theoretical level of drag reduction achievable by boundary layer combustion can be computed by comparing the drag coefficient predicted using Stalker's boundary layer combustion theory (dark grey bar titled "Stalker BLC" for test 10154 in Figure 4.25) with that predicted using the van Driest II method (white bar for test 10154 in Figure 4.25)[1]. This gives a theoretical drag reduction of 60%. However, the experimentally-measured level of drag reduction is only 33% (compare the black bar for fuel-on test 10154 with the black bar for fuel-off-N_2 test 10167 in Figure 4.25). Kirchhartz (2010) shows that, by accounting for the increased drag from the combustion-induced pressure rise, a more appropriate comparison between the experiments and the analytical predictions can be made[2]. This is done by comparing the experimentally-measured drag coefficient (black bar for fuel-on test 10154) with that predicted using the Spalding & Chi theory for the fuel-on test (hatched bar for fuel-on test 10154). The resulting level of drag reduction obtained from this comparison is 61%. This compares very well with the theoretical level of drag reduction of 60% predicted using Stalker's method. Note also that the Spalding & Chi theory predicts a higher drag coefficient for the fuel-on test (hatched bar for test 10154) than for the fuel-off-N_2 test (hatched bar for test 10167) because of the higher pressure gradients present in the fuel-on test.

By using the same approach as that used in the fuel-on test, Stalker's film-cooling theory predicts a drag coefficient reduction of 41%. The level of drag reduction inferred from a comparison of the experimental drag coefficient with that predicted by the Spalding & Chi theory is 29%. This slightly poorer performance for the fuel-into-N_2

[1] As stated in Kirchhartz (2010), the theoretical levels of drag reductions achievable with film-cooling and boundary layer combustion can be inferred by comparing the drag coefficient predicted using Stalker's theory with that predicted using the van Driest II method. This comparison is justified because the theory of Stalker is developed from that of van Driest II and collapses to that of van Driest II when fuel injection is not considered.

[2] It should be noted that the drag increment can only be brought about by the growth in displacement thickness which occurs when fuel burns in the boundary layer. This is shown by Kirchhartz (2010) in his experiments where a conical spike is located axially inside a cylindrical duct to bring about a gradual reduction in the cross-sectional area which is similar to that caused by a growth in displacement thickness. Kirchhartz's experiments show that the constriction of the mainstream flow brings about an adverse pressure gradient which then causes an increase in the skin frictional drag in the duct. In the event where combustion occurs across the entire duct, it was shown in the experiments of Goyne et al. (1999) and of Tanno et al. (2001) and the numerical simulations in Section 5.1.3 that the skin frictional drag does not increase.

test in comparison with that for the fuel-on test is also seen in the analysis of Kirchhartz (2010).

The generally good agreement between the experimental, numerical and theoretical results, which is also seen in Kirchhartz (2010), demonstrates that the theories of van Driest II, Spalding & Chi and Stalker, when applied with the local similarity approach, can be used to provide a baseline value for the skin friction drag acting on the internal surface of the combustor in flows with minimal disturbances.

Chapter 5

Results & Discussions

This chapter presents the results from the experimental program. The analysis of the results, supported with CFD simulations and turbulent skin friction theories, is also reported. The chapter starts in Section 5.1 with an examination of the results for tests conducted at a freestream stagnation enthalpy of 4.8 MJ/kg and Mach number of 6.2. This is a good starting point, since the REST inlet has been designed to operate at this condition. To check that the REST inlet is performing as it has been designed, its performance is verified against its design point in Section 5.1.1. A comparison of the measured pressures in the inlet and the combustor with those from the CFD simulations is shown in Section 5.1.2. This is then continued in Section 5.1.3 with a comparison of the measured drag with that estimated using CFD simulations and skin friction theories. Section 5.1 then concludes with a comparison of the results from the current experiments with those from the experiments of Kirchhartz (2010), in which the test flow contains minimal disturbances. This will demonstrate how flow disturbances from the REST inlet affect the drag reduction potential of the boundary layer combustion technique.

The measured pressures and drag for the experiments conducted with vortex generators attached on the inlet and the fuel injector are presented in Sections 5.2 and 5.3. As the vortex generators are used to generate flow disturbances similar to those generated by cross-stream fuel injection, the results from these experiments will reveal how the disturbances from cross-stream fuel injection affect the drag reduction potential of the boundary layer combustion technique. All results in Sections 5.2 to 5.3 are presented in the same way to those in Sections 5.1.2 and 5.1.3. Lastly, the findings from experiments conducted at off-design test conditions are presented in Section 5.4. These experiments are conducted to investigate how flow disturbances brought about by changes in inflow conditions affect the drag reduction potential of the boundary

layer combustion technique. For conciseness, only a summary of the results is presented. More details of the results from these experiments can be found in Appendix J.

5.1 Tests at design point - 4.8 MJ/kg condition

5.1.1 Verification of the performance of the inlet against its design point

One of the key points in the design process of the REST inlet was to produce combustor-entry conditions that are similar to those in the experiments by Kirchhartz (2010). The comparison of a single-point measurement of the surface static pressure at entrance of the combustor for both cases is not sufficient. As such, the numerical simulation of the REST inlet has to be compared with those of Kirchhartz's constant-area inlet. Figure 5.1 shows pressure measurements taken on the bodyside of the REST inlet for tests

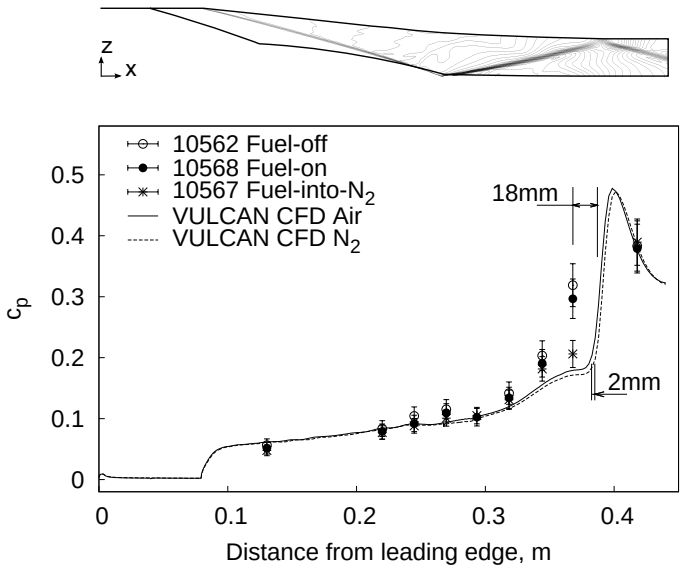

Figure 5.1: Pressure coefficients in the inlet

with air test gas and nitrogen test gas. Results from VULCAN CFD simulations[1] that have been conducted using air and nitrogen as test gases are shown on the same plot.

[1] These simulations were conducted by Professor Michael Smart with the NASA Langley Research Centre's hypersonic CFD code VULCAN (White and Morrison, 1999). Note that VULCAN was used instead of Eilmer3 for the simulation of the REST inlet because the automated grid-generation process, which was proposed by Smart and White (2002) to remove the complexity of generating grids for REST inlets, was built only to be used with VULCAN. Adapting this automated grid-generation process to enable simulations of REST inlets to be conducted with Eilmer3 is not within the scope of this project, and is hence not undertaken.

Other than at 0.37 m from the leading edge of the inlet, the experimental pressure coefficients agree well with the numerical predictions. Pressure levels in that region are highly sensitive to the location of the cowl shock impingement. It is postulated that the mismatch between the numerical and experimental results at 0.37 m in Figure 5.1 is brought about because the bluntness of the leading edges of the REST inlet are not modelled in the VULCAN CFD simulations. To investigate this further, Figure 5.2b shows two-dimensional numerical simulations of three flat plates with leading edges of different bluntness radii (0 mm, 0.5 mm and 1 mm radius). The inflow condition was chosen to match that near the cowl closure point in the inlet - x-velocity is 1987 m/s, z-velocity is -482 m/s, static pressure is 22.7 kPa and static temperature is 719 K.

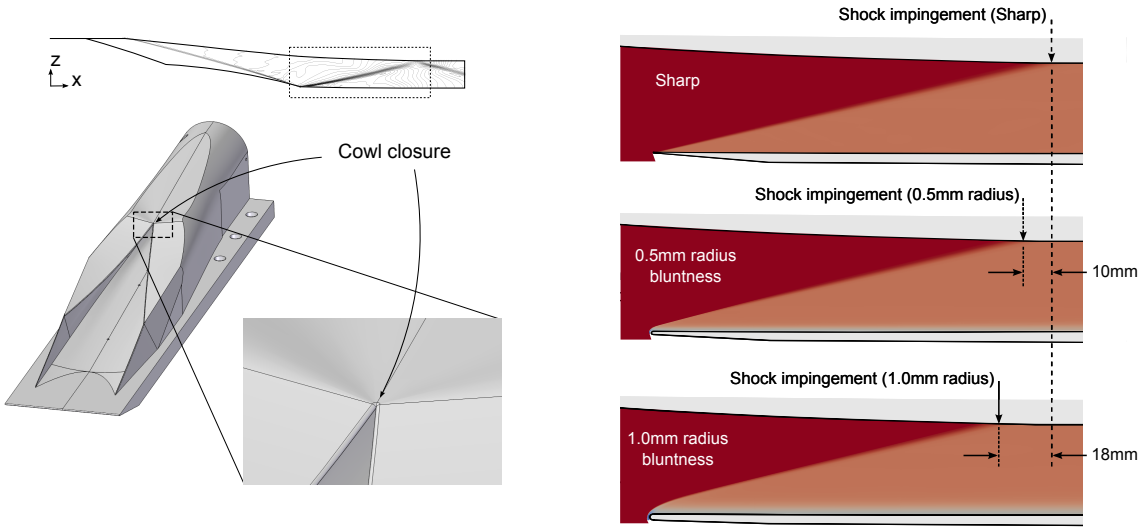

Figure 5.2: Effects of leading edge bluntness on cowl shock impingment location.

These results show that a leading edge with a bluntness radius of 0.5 mm shifts the location of the cowl shock impingement on the bodyside surface by about 10 mm upstream from that of a sharp leading edge. For a leading edge with a bluntness radius of 1 mm, the impingement location of the cowl shock on the bodyside surface shifts by about 18 mm upstream from that of a sharp leading edge. Although the leading edge bluntness for the REST inlet is 0.5 mm, the geometry of the cowl closure is such that the flow is not relieved as much as in the 2D simulation (see the enlarged diagram of REST inlet at cowl closure in Figure 5.2a). One would then expect the impingement location of the cowl shock to shift upstream by more than the length of 10 mm estimated from the CFD simulations. This therefore indicates that the lack of the modelling of the

leading edge bluntness to be the cause for the mismatch between the numerical and experimental results at 0.37 m in Figure 5.1.

Note also that both experimental results and numerical results show that for the air tests, the cowl shock impingement on the bodyside surface occurs about 2 mm upstream of that for the nitrogen tests. This is attributed to the difference in freestream Mach number between the air and nitrogen tests (see Tables 3.1 and 3.2). A Mach number of 6.2 for the air tests, which is 0.2 lower than that in nitrogen tests, generates a less inclined shock. A simple inviscid oblique shock analysis shows that this difference in Mach number of 0.2 shifts the cowl shock by 2 mm.

With the CFD results being a reasonably good approximation of the flow in the inlet, a comparison of these results with those of Kirchhartz can be made. Figure 5.3a shows contour plots of the static pressure distribution taken on the symmetry plane of the numerical simulations for the REST inlet in the current experiments and for the constant-area inlet in Kirchhartz's experiments, while Figures 5.3b and 5.3c show contour plots of static pressure and streamwise vorticity taken on an axial plane 45 mm upstream of the hydrogen injection plane for both inlets. These plots clearly show that the inflow to the combustor from the REST inlet is more non-uniform than that from the constant-area inlet. Figures 5.3d and 5.3e show the temperature and velocity profiles taken 45 mm upstream of the hydrogen injection plane. Figure 5.3 shows that thicker and hotter boundary layers, which are favourable for the boundary layer combustion technique (Kirchhartz et al., 2010), are present on the bodyside surface of the inlet. Although the boundary layer on the cowlside surface of the REST inlet is about the same thickness as that in the constant-area inlet, the peak temperatures in the boundary layer are lower than those in Kirchhartz's inlet. As mentioned in Chapter 2, the peak temperatures and thickness of the boundary layer have a significant effect on the ignition of the injected hydrogen (Rowan, 2003; Schetz and Gilreath, 1967; Stephensen, 2002). To check if the lower temperatures in the boundary layer on the cowl side of the inlet would affect the ignition of hydrogen, the ignition-delay length correlation for a hydrogen-air mixture of Pergament (1963) is used.

$$L_{ignition} = \frac{8 \times 10^{-9}\, e^{9600/T}}{p/101300} \times u \tag{5.1}$$

For the current experiments, at the location of the peak temperature of 1370 K, the velocity is 1713 m/s and static pressure is 72.8 kPa. This results in an ignition length of 21 mm. For the inlet used by Kirchhartz (2010), the velocity is 1771 m/s and static pressure is 90.7 kPa at the location of peak temperature of 1610 K. This results in an

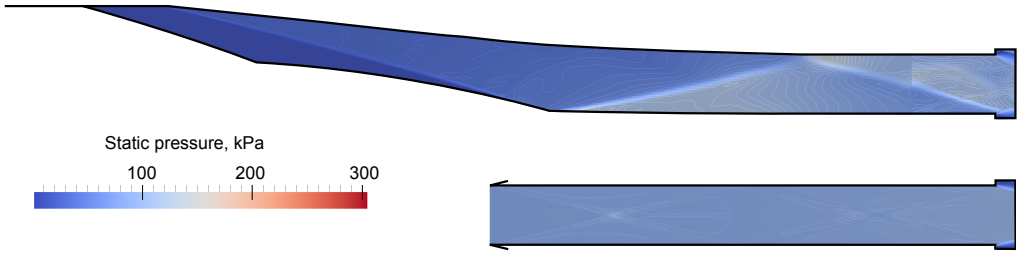

(a) Contours of static pressures in the REST inlet and constant-area inlet.

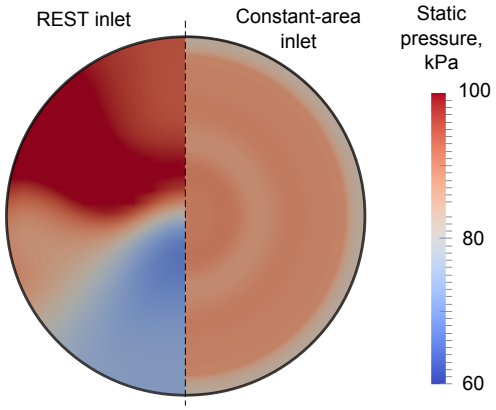

(b) Contours of static pressures at 45 mm upstream of hydrogen injection plane. (Left half: REST inlet. Right half: Constant-area inlet.)

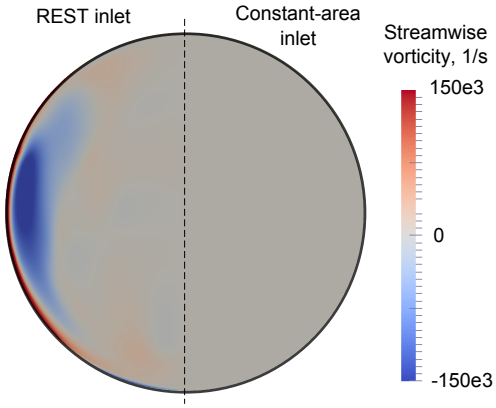

(c) Contours of streamwise vorticity at 45 mm upstream of hydrogen injection plane. (Left half: REST inlet. Right half: Constant-area inlet.)

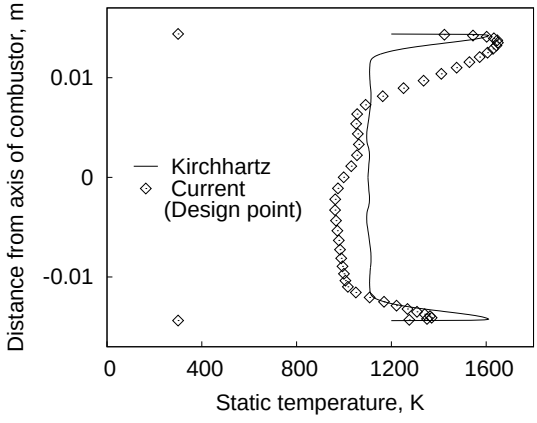

(d) Static temperature profiles.

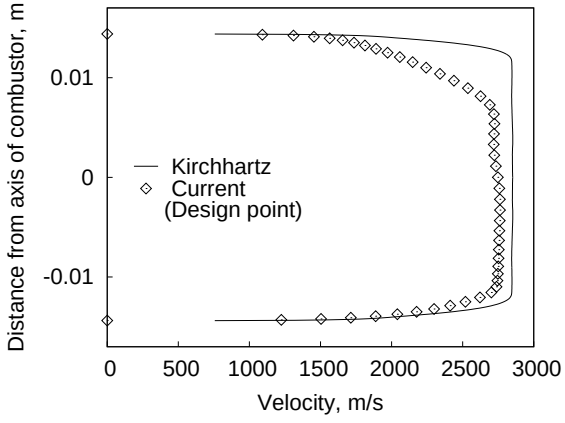

(e) x-velocity profiles.

Figure 5.3: Comparison of results from the numerical simulations of the current experiments and Kirchhartz's experiments.

ignition length of 6 mm. In a combustor of length 500 mm, a difference of 15 mm in the ignition length between the current experiments and that of Kirchhartz (2010) is not expected to be significant. Note that since the conditions used to estimate the ignition lengths are localised conditions, the predicted ignition lengths are not expected to be comparable with those estimated from the experimental measurements.

Since the combustor-entry conditions in Kirchhartz's experiments were axisymmetric while those in the current experiments are expected to be three-dimensional, a one-dimensionalised form of comparison has to be made. Of the different methods available for the one-dimensionalisation of multi-dimensional data sets, mass-flux-weighted averaging is a simple approach that has been shown by Baurle and Gaffney (2008) to be suitable for the examination of how properties vary through a flowpath. This can be written as

$$F_{\text{avg}} = \frac{\int F \rho u \mathrm{dA}}{\int \rho u \mathrm{dA}} \tag{5.2}$$

where F is the flow property to be averaged and F_{avg} is the mass-flux-weighted averaged value of F. Table 5.1 shows the conditions averaged 45 mm upstream of the fuel injection plane. The comparison shows that most flow properties in the current experiments differ from those of Kirchhartz by about 2% - 4%, with the largest difference of 7% occurring for u_{avg}. Since one of the key points in the design process of the REST inlet was to produce combustor-entry conditions that are similar to those in the experiments by Kirchhartz (2010), these results demonstrate that the REST inlet is performing as designed.

Table 5.1: Comparison of one-dimensionalised flow properties at 45 mm upstream of fuel injection plane.

		Kirchhartz	Current	Difference
p_{avg}	kPa	90.0	88.5	+1.6%
T_{avg}	K	1159	1126	+2.8%
ρ_{avg}	kg/m^3	0.273	0.279	+2.4%
u_{avg}	m/s	2770	2576	+7.0%
M_{avg}	-	4.17	3.98	+4.5%

5.1.2 Inlet & combustor pressure measurements

Figure 5.4 shows the experimental and numerical pressure measurements taken on the bodyside of the REST inlet and combustor. Note that unlike Figure 5.1, the pressure

coefficients for the REST inlet are now shown relative to the fuel injection plane rather than to the leading edge of the inlet. The numerical results were from Eilmer3 CFD simulations conducted using a test gas of air without fuel injection and a test gas of nitrogen with fuel injection. For the fuel-off and fuel-into-N_2 tests, the pressure coefficients in the combustor estimated by Eilmer3 are about 6% lower than those measured experimentally, but they still match to within experimental uncertainties. Eilmer3 also over-estimates the distance to the second shock impingement on the bodyside surface by about 40 mm for both the fuel-off and fuel-into-N_2 tests. The slight increase in pressure levels for the fuel-into-N_2 case from those for the fuel-off case is evident in both the experimental and numerical results. This is attributed to the addition of mass from the injection of hydrogen in the combustor.

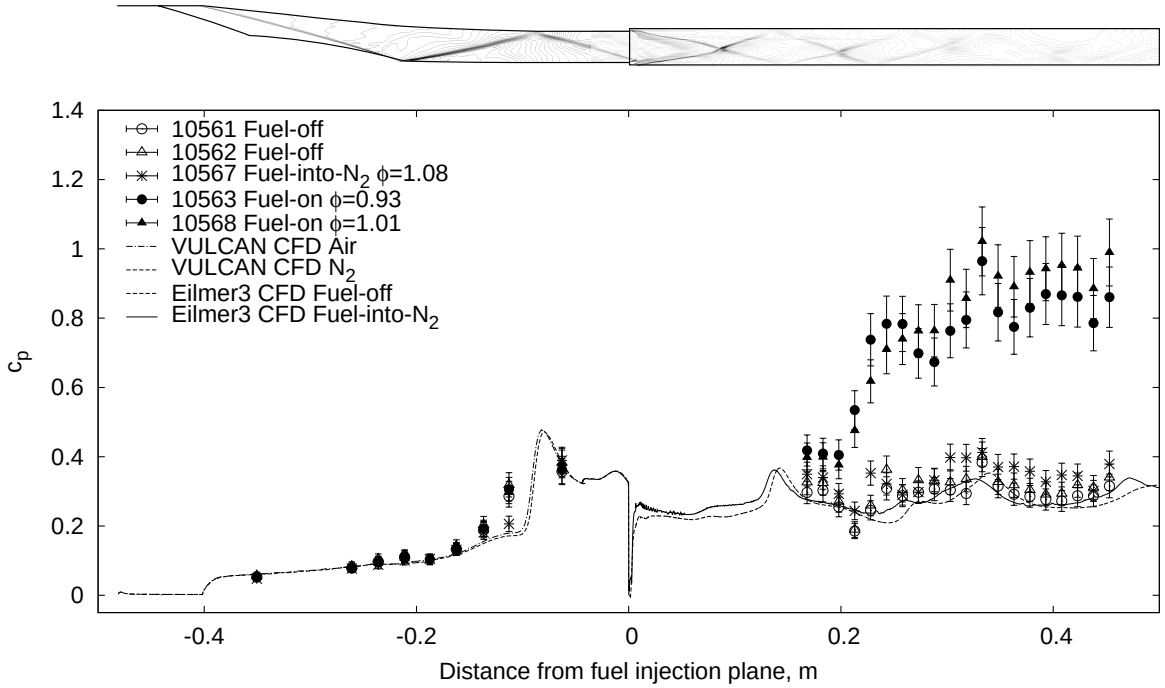

Figure 5.4: Pressure coefficients in the inlet and combustor for H_s = 4.8 MJ/kg condition.

For the fuel-on tests, the pressure rises steeply from the fuel-off and fuel-into-N_2 levels at about 0.2 m downstream of the fuel injection plane. The rapid increase in pressure is similar to that observed when the combustion is reaction-controlled. Stalker et al. (2005) suggest that this occurs when the freestream temperatures are low and the reaction lengths are large, which in turn allows for more mixing and creation of radicals to occur before a delayed but rapid energy release. The rapid increase in pressure coincides with a shock impingement location at about 0.2 m from the fuel injection

plane. This suggests that the rapid release of energy from combustion may be triggered by the increase in local temperatures from shock impingement. A similar observation was also made by Kirchhartz et al. (2010) for the experiments with the semi-direct connect inlets. In addition, the difference in pressures between combusting and non-combusting tests at the first three pressure measurement locations suggests that a small level of combustion could be occurring upstream of that location.

5.1.3 Combustor drag measurements

Figure 5.5 shows the experimental, numerical and theoretical values for the skin friction drag coefficient on the internal surface of the combustor. The experimental skin friction drag coefficient was obtained as described in Section 3.4.2.

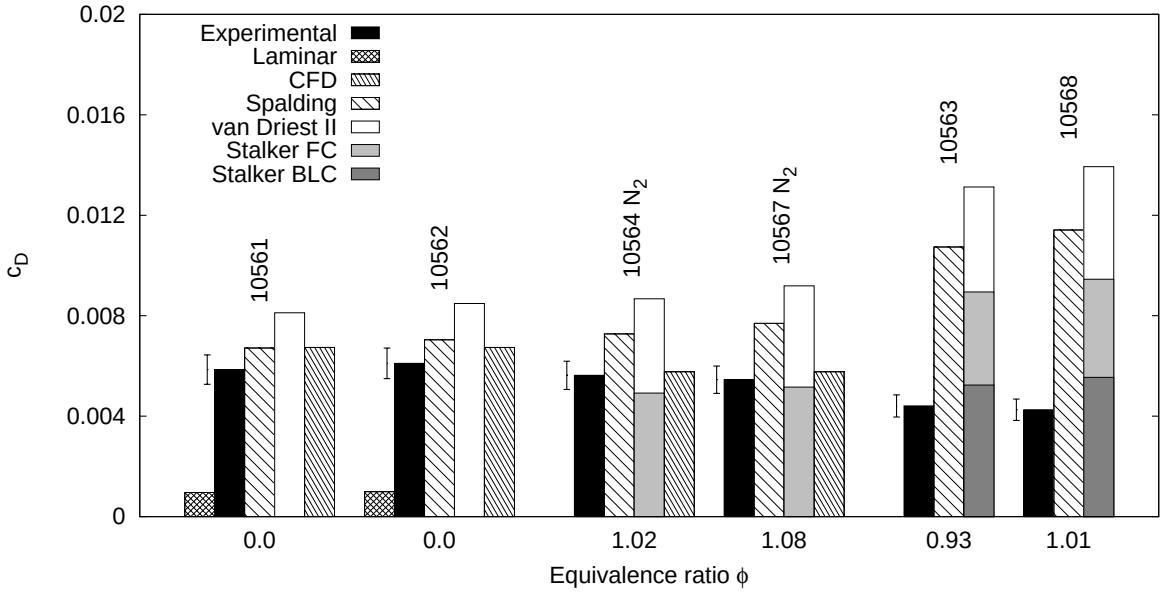

Figure 5.5: Combustor drag coefficients for $H_s = 4.8\,\mathrm{MJ/kg}$ condition.

For the fuel-off tests (shots 10561 and 10562), the experimentally measured drag coefficient is overpredicted by 15% by Spalding & Chi's theory and by 39% by the van Driest II theory. As discussed in Section 4.2.1, the method of Spalding & Chi performs better than the method of van Driest II due to the low T_w/T_{aw} value of 0.07 in the combustor. Note how both theories overpredict the measured drag coefficients for the fuel-off tests. In the current experiments, the boundary layer developing on the internal curved surface of the combustor is expected to be less "relieved" than that developing on a flat plate. This results in a thicker boundary layer in the combustor than that on a flat plate, which causes the drag in the combustor to be lower than that

on a flat plate. Since the methods of Spalding & Chi and van Driest II were developed for predicting drag on flat plates, it is expected that the predicted drag coefficients will tend to be higher than those measured experimentally in the combustor. The CFD simulations, on the other hand, perform better than the analytical theories at estimating the viscous drag levels. The numerical estimate of c_D is about 10% higher than the measured level, but still match to within experimental uncertainties.

Noting that the drag reduction benefits of the boundary layer combustion technique can only be realised in turbulent boundary layers, one question that is raised is whether the boundary layers entering the combustor are turbulent or laminar. Based on correlations for boundary layer transition developed for tests in the T4 shock tunnel facility (He and Morgan, 1994; Mee, 2002a), the boundary layer is expected to transition at a Reynolds number of 1.4×10^6, which corresponds to a transition length of 0.226 m. Since the REST inlet is 0.44 m in length, this means that the boundary layer should be turbulent at entry to the combustor. However, since the correlations have been developed for flat plates and also since the boundary layers on the cowlside of the inlet have a shorter distance to develop than those on the bodyside surface, it is worth checking the levels of drag coefficient expected for laminar boundary layers. Shown in Figure 5.5 for the fuel-off tests are estimated levels of drag coefficient if the boundary layers are assumed to be fully laminar throughout the combustor. These estimates are made based on the reference temperature method of Eckert (1955). The drag coefficients measured from the experiments are more than 6 times higher than those estimated for fully laminar boundary layers. This result supports the earlier suggestion, made based on the transition correlations, that the boundary layers entering the combustor are turbulent.

For the fuel-into-N_2 tests (shots 10564 and 10567), the measured drag coefficients are about 7% lower than those measured in the fuel-off tests. From the discussions in Section 4.2.2, it was shown that a more appropriate comparison between the skin frictional drag estimated from Stalker's theory and that measured from the experiments can be made by accounting for the increased drag brought about by increased pressures when hydrogen is injected. To account for the pressure-induced drag increment, a comparison between the experimentally measured drag coefficient and that predicted using the Spalding & Chi theory has to be made. The resulting level of drag reduction of 25% to 29% is lower than the 44% predicted using Stalker's film-cooling theory. This poorer estimation of the drag reduction levels for the fuel-into-N_2 tests is also seen in the experiments of Kirchhartz (2010). In comparison with the theoretical predictions, the Eilmer3 CFD simulations offer a better estimate of drag coefficient,

with the numerical estimate of drag coefficient matching that measured in the experiments to within 6%.

For the fuel-on tests (shots 10563 and 10568), the measured drag coefficients are 28% lower than those measured in the fuel-off tests. In comparison with the drag coefficients predicted using the Spalding & Chi theory, those measured experimentally are about 61% lower. This agrees well with the 60% drag reduction predicted using Stalker's theory for boundary layer combustion. This excellent agreement is a good indication that the drag reduction observed in these tests are brought about by the combustion of hydrogen in the boundary layer.

Another question that then arises is whether the injected fuel is being burnt in the boundary layer or in the mainstream. This is investigated here by examining CFD simulations of a circular constant-area duct with heat addition in the boundary layer, heat addition everywhere in the duct and without heat addition, as shown in Figure 5.6. For the first case, the heat addition is distributed over a thin volume inside the boundary layer that spans the full length of the duct. For the second case, the heat addition is distributed everywhere for the full length of the duct. The heat addition zones are shown as hatched areas in Figure 5.6. The amount of heat added for the first and second cases

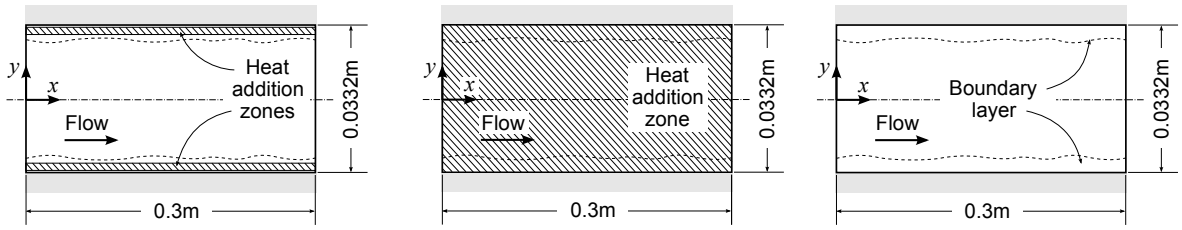

(a) Heat addition in boundary layer. **(b)** Heat addition everywhere. **(c)** No heat addition.

Figure 5.6: CFD simulations of a circular constant-area duct with heat addition at different locations in the flowfield.

is assumed to be 720 kW. This amount corresponds to the maximum combustion heat release possible for an equivalence ratio of 0.5 in the current experiments. The inflow of air to the duct is at a static pressure of 88.5 kPa, velocity of 2576 m/s and temperature of 1126 K, and contains a 3.4 mm thick turbulent boundary layer. The profile for the boundary layer was generated using the *eddybl.exe* boundary-layer code (Wilcox, 2006). These inflow conditions approximately correspond to those entering the combustor in the current experiments.

Figure 5.7a shows the pressure distribution along the surface of the duct for the three cases. For both the heat-addition cases, the pressure levels rise above those for the case without heat addition. Note that the shock impingements at x-locations of 0.1 m, 0.19 m and 0.27 m are stronger when heat is added to the boundary layer than when heat is added everywhere in the duct. This is attributed to the difference in the way heat addition contributes to the pressure rise in the duct. When heat is added everywhere, the pressure rises throughout the entire duct in an almost one-dimensional way. However, when heat is added to the boundary layer, the pressure rises as a result of the thickening of the boundary layer. Because the thickening of the boundary layer acts like a constriction to the mainstream flow, this causes the stronger shocks that are seen when heat is added in the boundary layer.

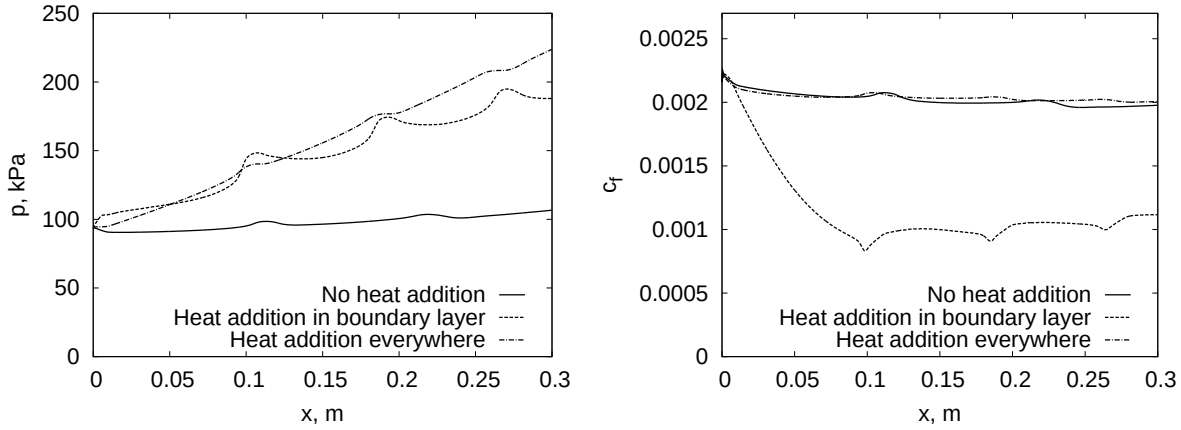

(a) Surface static pressure.

(b) Skin friction coefficient.

Figure 5.7: Effects of heat addition at different locations in the flowfield.

Figure 5.7b shows the distribution of skin friction coefficient along the surface of the duct for the three cases. When heat is added in the boundary layer, the skin friction coefficient decreases by about 50% from that when heat is not added. This shows that if fuel is burned in the boundary layer, then the reduction of skin frictional drag is possible. However, this is different when heat is added everywhere in the duct. In the first 0.1 m of the duct, the skin friction coefficient is about 1-2% lower than that when heat is not added. It is postulated that, in the first 0.1 m of the duct, the drag reduction from heat addition in the boundary layer is slightly higher than the increased drag from the increased pressure gradient, hence causing a slightly lower skin friction coefficient than that when heat is not added. Downstream of this, the contribution from the drag increment brought about by increased pressure gradients starts to dominate that from the drag reduction brought about by heat addition in the boundary layer.

Despite this, the skin friction coefficient when heat is added everywhere does not differ by more than 5% of that when no heat is added. This is also shown by Goyne et al. (1999) and Tanno et al. (2001) in separate experiments that, to within the uncertainties of the experiments, the skin friction drag in a constant-area combustor does not change when hydrogen is injected into the mainstream and allowed to burn. This analysis demonstrates that if fuel is burned anywhere else other than in the boundary layer, the skin friction drag is likely to remain similar to that when no fuel is injected. This clearly shows that the reductions in skin friction drag observed in the fuel-on tests in Figure 5.5 are brought about by the combustion of hydrogen in the boundary layer and not in the mainstream.

The significant role played by the Reynolds shear stress in the skin friction reduction phenomena in the boundary layer combustion technique can also be highlighted in the results from these simulations. Figure 5.8 shows a comparison of the weighted Reynolds shear stress profiles at several x-locations. For the results from a RANS simu-

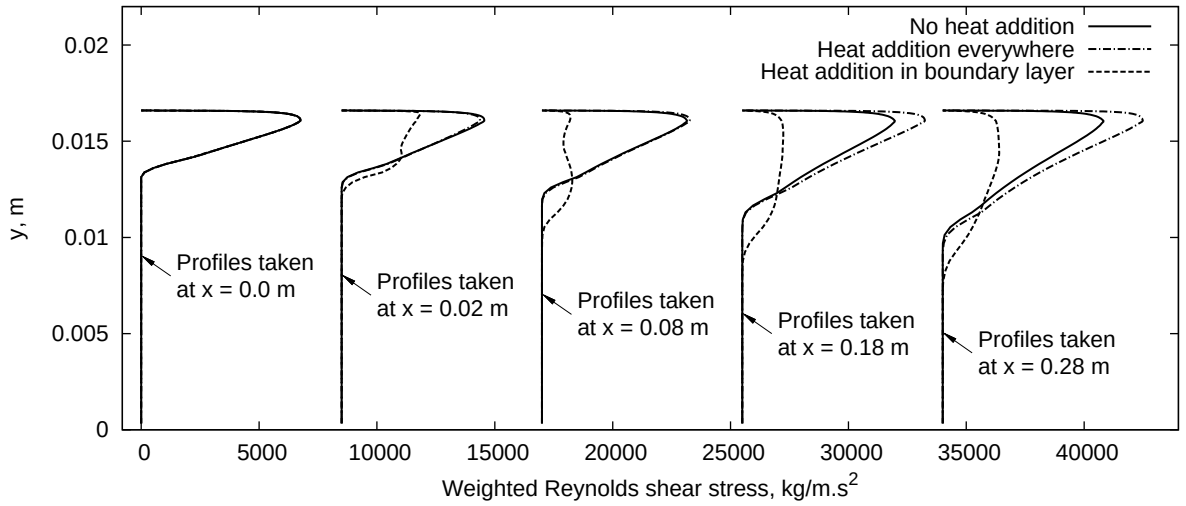

Figure 5.8: Comparison of the weighted Reynolds shear stress profiles at several x-locations. The false zero offset between each set of weighted Reynolds shear stress profiles is equivalent to 8500 kg/m.s^2.

lation, the Reynolds shear stress can be computed by multiplying the density with the turbulent viscosity and the wall normal velocity gradient (Wilcox, 2006). The value of Reynolds shear stress is weighted by the distance from the wall, where the weighting factor is equals to $2r^2$ at the walls and zero at the axis of the duct (Fukagata et al., 2002). Recall from Section 2.1 that the skin friction coefficient in a turbulent boundary layer is almost directly related to the Reynolds shear stress and that the contribution of the Reynolds shear stress to the skin friction coefficient can be computed by integrating

the weighted Reynolds shear stress profiles. Figure 5.8 shows that, when heat is added in the boundary layer, the weighted Reynolds shear stress profiles are shallower than when heat is not added. This then indicates that the resulting skin friction coefficient for the case with heat addition in the boundary layer should be lower than that for the case without heat addition. This is clearly seen in the c_f distributions for both cases in Figure 5.7b. For the case where heat is added everywhere in the duct, the weighted Reynolds shear stress profile at $x = 0.08$ m is similar to that when heat is not added. This explains the similar levels of c_f seen at $x = 0.08$ m in Figure 5.7b. Downstream of $x = 0.08$ m, the weighted Reynolds shear stress profile increases slightly relative to that for the case without heat addition. The resulting effect of this can also be seen in Figure 5.7b, where downstream of $x = 0.12$ m, the skin friction coefficient when heat is added everywhere increases slightly relative to that when no heat is added. It is clear from these results that the reduction of the Reynolds shear stress is the main driver for the drag reduction phenomena observed in the boundary layer combustion technique. It is also clear that for the drag reduction potential to be realised, heat addition from the combustion of fuel must occur in the regions of the boundary layer where there are large near-wall values of Reynolds shear stress.

5.1.4 Comparison with Kirchhartz's direct-connect experiments

Although the results in Sections 5.1.2 and 5.1.3 indicate that drag reduction from boundary layer combustion still occurs when a more realistic compression inlet is used, a comparison of the measured skin friction drag with that of Kirchhartz's experiments is still needed to reveal if the flow non-uniformities from the inlet affect the drag reduction potential of boundary layer combustion, and if so, by how much. As the pressure and drag levels for the current experiments are presented as coefficients based on the exit conditions from the Mach 6 nozzle and the coefficients for Kirchhartz's experiments are based on the exit conditions from the Mach 4 nozzle, the same level of absolute pressure will result in two different values of pressure coefficient for the two experiments. To make the pressure and drag data from both experiments comparable, the coefficients have to be based on the flow properties that are similar in both experiments. This can be done by basing the coefficients for both data sets on their respective mass-flux-weighted averaged values at 45 mm upstream of the fuel injection plane (as shown in Table 5.1). The re-normalised results are shown in Figure 5.9.

Figure 5.9a shows that the re-normalised pressure coefficients for the fuel-off and fuel-into-N_2 tests for the current experiments are similar to those of Kirchhartz. When fuel is injected and combustion occurs, the rise in pressure levels are also similar for

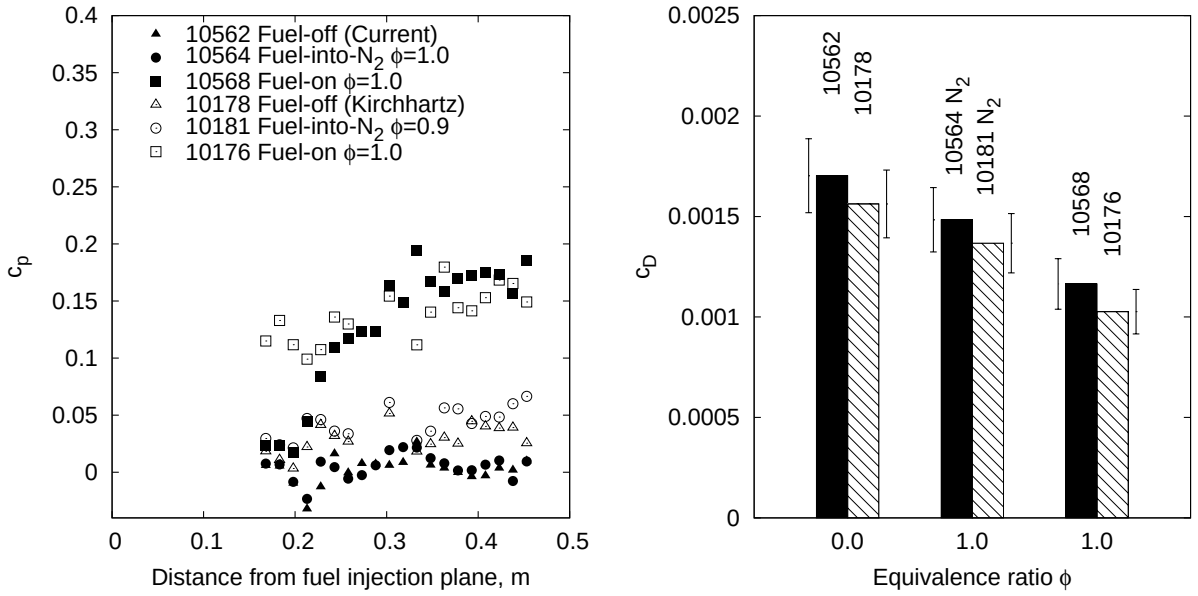

(a) Pressure coefficient. **(b)** Drag coefficient.

Figure 5.9: Comparison of re-normalised pressure and drag coefficients for the current experiments and Kirchhartz's experiments. In both plots, the filled symbols and bars are for the current experiments, while the unfilled symbols and bars for Kirchhartz's experiments.

both the current experiments and those of Kirchhartz's. This suggests that similar amounts of heat are added from the combustion process. However, the ignition occurs earlier in Kirchhartz's experiments. Figure 5.9b shows that the measured drag coefficients for fuel-off, fuel-into-N_2 and fuel-on tests are about 10% higher than those measured in Kirchhartz's experiments. The relative levels of drag reduction brought about by the film-cooling effect and boundary layer combustion effect are similar between the current experiments and those of Kirchhartz. This is an important result as it clearly shows that the skin friction drag reduction brought about by boundary layer combustion is not significantly affected by the flow disturbances generated from the REST inlet.

The similar levels of viscous drag reduction observed in both the current experiments and Kirchhartz's experiments can be explained with the aid of information from the CFD simulations of the fuel-into-N_2 tests. The profiles of hydrogen mass fractions taken at several x-locations on the symmetry plane in the combustor from the simulations of Kirchhartz's experiments are shown in Figure 5.10a and those from the simulations of the current experiments are shown in Figure 5.10b. The shaded regions in Figure 5.10 represent the location of the boundary layer. For the drag reduction potential of boundary layer combustion to be realised, it is crucial that the fuel remains in

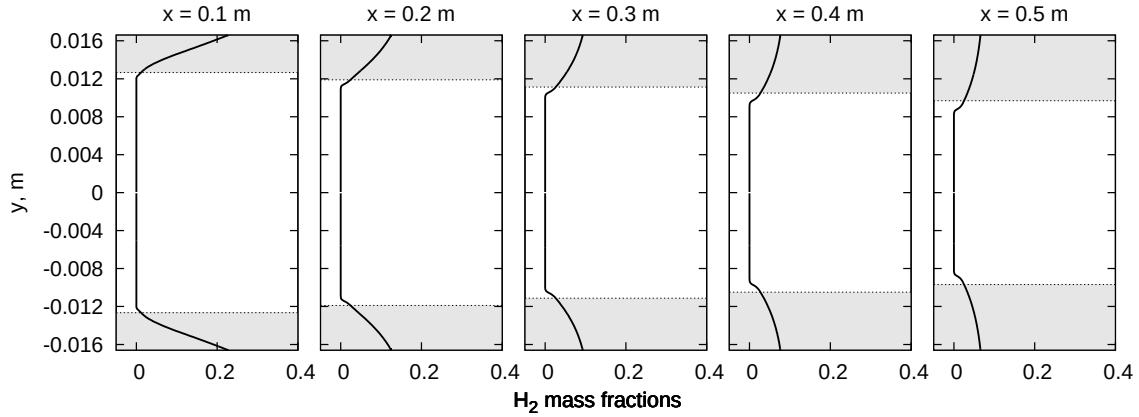

(a) Kirchhartz's experiments.

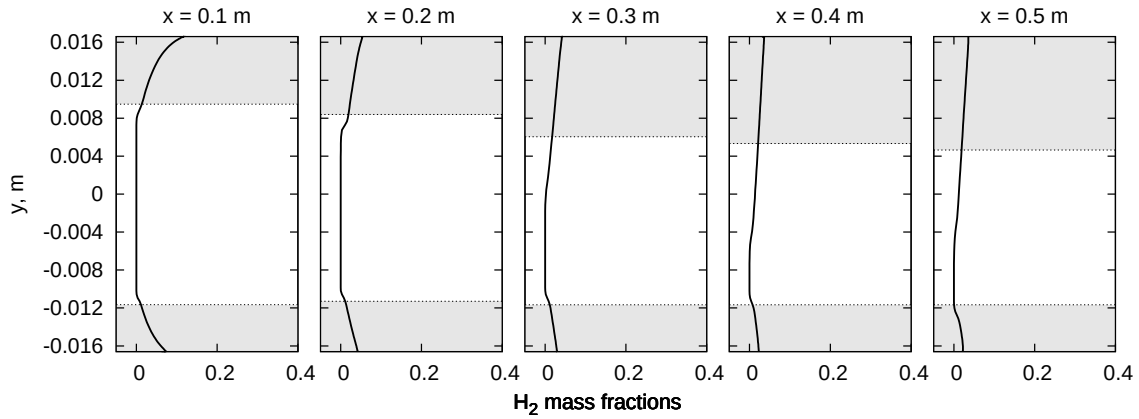

(b) Current experiments.

Figure 5.10: Profiles of hydrogen mass fractions at several x-locations taken from the CFD simulations of Kirchhartz's experiments and of the current experiments. The shaded regions represent the location of the boundary layer.

the boundary layer for combustion to occur. To determine if the hydrogen still remains in the boundary layer, the edge of the boundary layer needs to be defined. Common methods used to define the edge of the boundary layer include the use of 99% of the freestream velocity, the displacement thickness or the momentum thickness (White, 2006). However, in terms of the study of drag reduction by boundary layer combustion, the more appropriate method of defining the edge of the boundary layer is to use the Reynolds shear stress profile. Recall from Chapter 2 that the near-wall Reynolds stresses play an important role in the contribution to turbulent skin frictional drag. Fukagata et al. (2002) and Gomez et al. (2009) show that Reynolds shear stress contributes to at least 70% of the skin friction, and that 90% of this contribution comes from the near-wall region ($z^+ \approx 100$). By identifying the region where the Reynolds shear stress contributes to a significant proportion of skin friction, and then by examining the hydrogen mass fractions in that region, the potential of combustion in the part

of the boundary layer that is significant for viscous drag reduction can be identified. The shaded regions in Figure 5.10 are defined by the following steps.

1. Compute the Reynolds shear stress.
2. Weight the Reynolds shear stress by the distance from the wall, where the weighting factor is equals to $2r^2$ at the walls and zero at the axis of the duct. r is the radius of the combustor.
3. Cumulate the values of weighted Reynolds shear stress starting from the walls.
4. Locate the distance normal to the wall where the cumulative weighted Reynolds shear stress contributes to 99% of the total value of the weighted Reynolds shear stress. Define this distance as the edge of the boundary layer.

Figure 5.10 shows that throughout the entire length of the combustor for both the current experiments and Kirchhartz's experiments, large proportions of the injected hydrogen remain in the regions of the boundary layer which have the potential of reducing the Reynolds shear stress, and hence the skin frictional drag, when combustion occurs. This explains why there is a negligible difference in the levels of viscous drag reduction measured in the fuel-on tests for the current experiments and Kirchhartz's experiments.

5.2 Simulating the effects of inlet fuel injection

As mentioned in Section 3.1.3, vortex generators are used in the current study to investigate the effects of flow disturbances brought about by cross-stream fuel injection on the drag reduction potential of the boundary layer combustion technique. This section presents the results for the experiments in which three vortex generators were attached at 0.157 m downstream of the leading edge of the REST inlet. The experiments were conducted at the same test conditions as those in Section 5.1.

5.2.1 Inlet & combustor pressure measurements

Figure 5.11 shows the experimental pressure measurements taken on the bodyside of the REST inlet and combustor. Also shown are the pressure measurements for the tests conducted at the same test conditions without vortex generators. When compared with the tests without vortex generators, the pressure distribution in the inlet for the

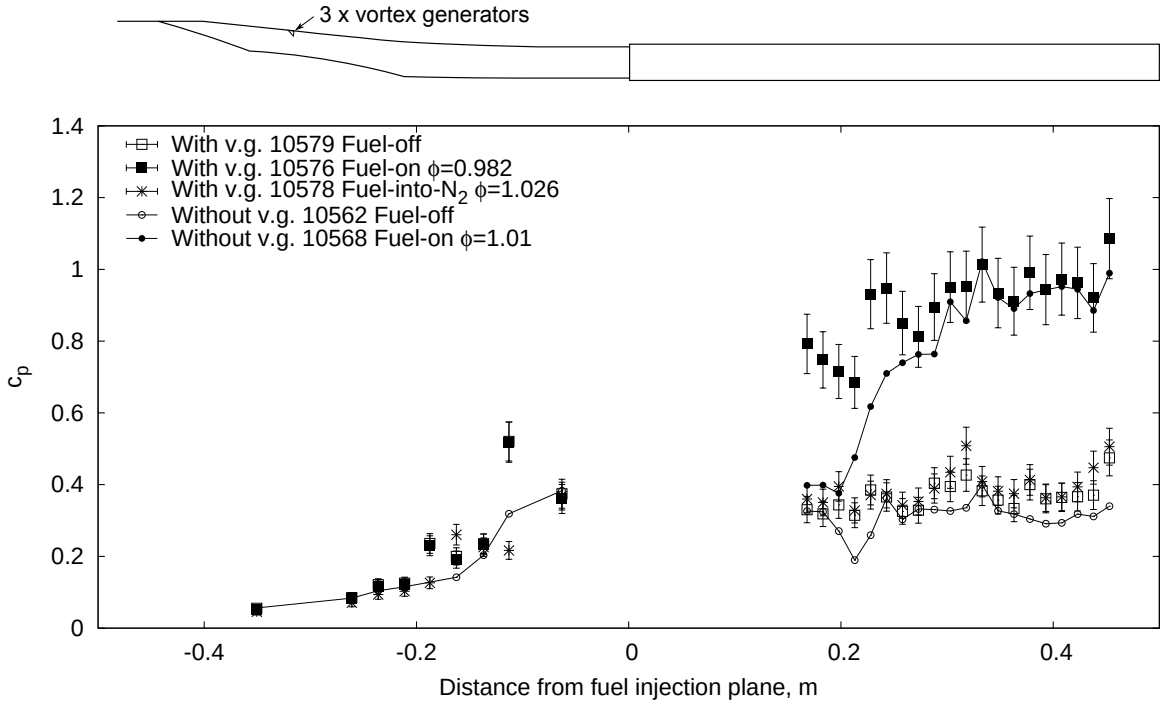

Figure 5.11: Pressure coefficients in the inlet and combustor for tests with vortex generators in the inlet (with v.g.) and without vortex generators (without v.g.) at the $H_s = 4.8\,\mathrm{MJ/kg}$ Mach 6.2 test condition.

tests with vortex generators clearly show that the flow disturbances from the vortex generators are present in the REST inlet.

In the combustor, for the fuel-off tests, the pressure coefficients are about 12% higher for the tests with vortex generators than they are for the tests without vortex generators. The three shocks which are evident for tests without vortex generators (at about 0.23 m, 0.32 m and 0.45 m from the fuel injection plane) also appear for the tests with vortex generators. These shocks appear to be impinging earlier for the tests with vortex generators than for those without vortex generators. This, together with the slightly higher pressure levels in the combustor, indicates that the boundary layers entering the combustor are thicker for the tests with vortex generators than for those without vortex generators. It is postulated that the swirling motion of the flow brought about by the vortex generators causes more mixing between the boundary layer and the mainstream flow, which then causes the boundary layers to become thicker. For fuel-into-N_2 tests, the slight rise in pressure from fuel mass addition is evident.

When fuel is injected and allowed to burn, the pressure rises to levels similar to those in the tests without vortex generators. The ignition of the fuel, however, occurs further upstream than in the tests without vortex generators. The earlier ignition of

the hydrogen is attributed to the regions of higher pressures and temperatures and the increased mixing of the fuel and air brought about by the vortex generators.

5.2.2 Combustor drag measurements

Figure 5.12a shows a comparison of the experimental and theoretical drag coefficients for the tests with vortex generators in the inlet. The experimental results are also compared with those for the tests conducted at the same conditions but without the vortex generators in Figure 5.12b.

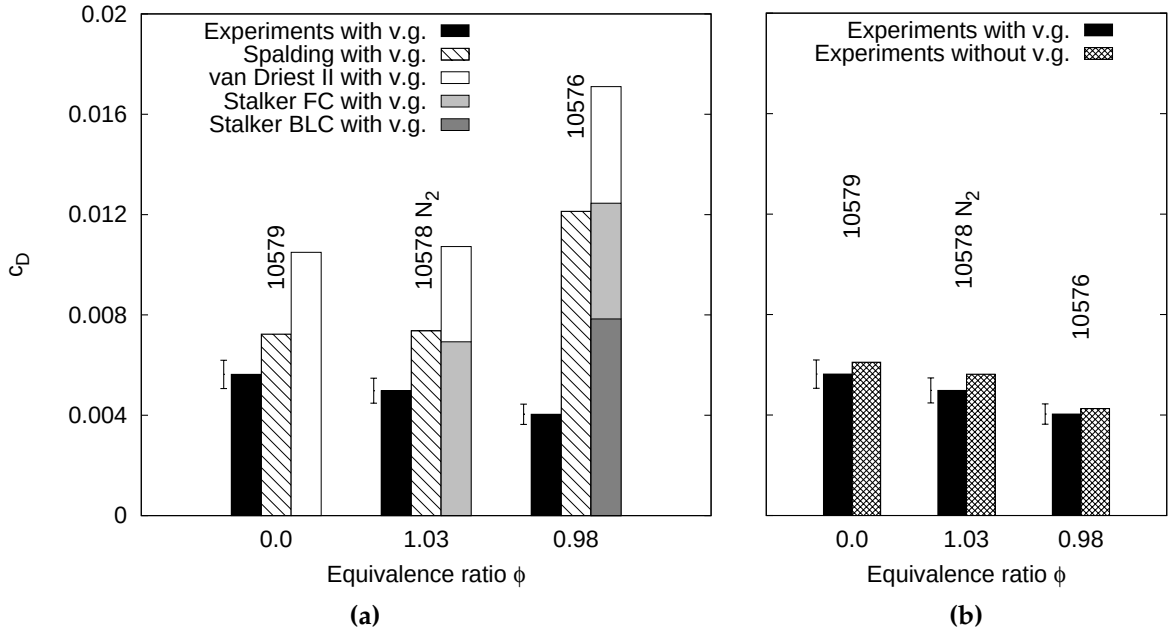

Figure 5.12: Comparison of experimentally measured combustor drag coefficients for tests with vortex generators in the inlet (with v.g.) **(a)** with those predicted using skin friction theories and **(b)** with those for tests without vortex generators (without v.g.).

For the fuel-off test, both the Spalding & Chi and van Driest II theories overpredict the measured drag coefficient. It is postulated that this is caused by the inability of both theories to predict the highly three-dimensional flowfield brought about by the vortex generators. Figure 5.12b shows that, for the fuel-off test, the drag coefficient is lower than that for the test without vortex generators. This supports the suggestion in Section 5.2.1 that the boundary layers entering the combustor are thicker for tests with vortex generators, since thicker turbulent boundary layers result in lower drag coefficients than thinner ones.

For the fuel-into-N_2 test, the measured drag coefficient decreases from that in the fuel-off test by 12%. A plausible explanation for this is that the thicker boundary layers

entering the combustor for tests with vortex generators offer more protection for the hydrogen layer near the walls, thus allowing the film-cooling effect to persist over a larger downstream distance from the injection plane. To allow for a comparison with Stalker's film-cooling theory, the measured drag coefficient is compared with that predicted using the Spalding & Chi theory. The resulting drag reduction level of 32% agrees well with the 35% drag reduction that is predicted using Stalker's film-cooling theory.

For the fuel-on test, the measured drag coefficient decreases from that in the fuel-off test by 28%. This level of decrement in the drag coefficient is similar to that measured in the test without vortex generators. To allow for a comparison with Stalker's boundary layer combustion theory, the measured drag coefficient is compared with that predicted using the Spalding & Chi theory. The resulting drag reduction level of 67% is higher than the 54% drag reduction that is predicted using Stalker's boundary layer combustion theory. Kirchhartz (2010) suggests that this is brought about by a small proportion of hydrogen burning outside the boundary layer. Kirchhartz (2010) postulates that this reduces the momentum in the mainstream, which in turn further reduces the momentum transfer to the combustor walls. However, results from the simulations of heat addition in a 0.3 m duct (as shown in Section 5.1.3) suggest otherwise - when heat is added in both the mainstream and in the boundary layer, the skin friction changes by less than 5% of that when heat is not added. It is suggested that CFD simulations, which include the modelling of combustion, be conducted to further verify the drag measurements. Nonetheless, a substantial level of reduction in viscous drag still occurs when the injected hydrogen burns.

These results clearly show that the flow disturbances generated from the three vortex generators on the inlet do not have a significant effect on the drag reduction potential of the boundary layer combustion technique. These results also show that these disturbances can promote an earlier ignition of fuel in the combustor, which is desirable for scramjet operation as it allows for combustors to be shorter in length. This, in turn, reduces the area for skin friction to act on. An important implication of these results is that cross-stream fuel injection in the inlet can be used in conjunction with tangential fuel injection at the start of the combustor. Using this combined fuel injection scheme in a scramjet engine provides the potential to obtain not only the benefits of thrust addition and viscous drag reduction from boundary layer combustion, but also those of thrust addition from mainstream combustion.

5.3 Simulating the effects of throat fuel injection

This section presents the results for the experiments in which five vortex generators were attached in the throat region of the REST inlet at 49.5 mm upstream of the hydrogen injection plane. Because of the presence of more vortex generators and of the closer proximity of the vortex generators to the combustor, the levels of flow disturbances entering the combustor for these experiments are expected to be higher than those for the experiments shown in Section 5.2.

5.3.1 Inlet & combustor pressure measurements

Figure 5.13 shows the experimental and numerical pressure measurements taken on the bodyside of the REST inlet and combustor for tests with five vortex generators located at the throat. Also shown are the pressure measurements for the tests conducted at the same test conditions without vortex generators. The pressures in the inlet are ex-

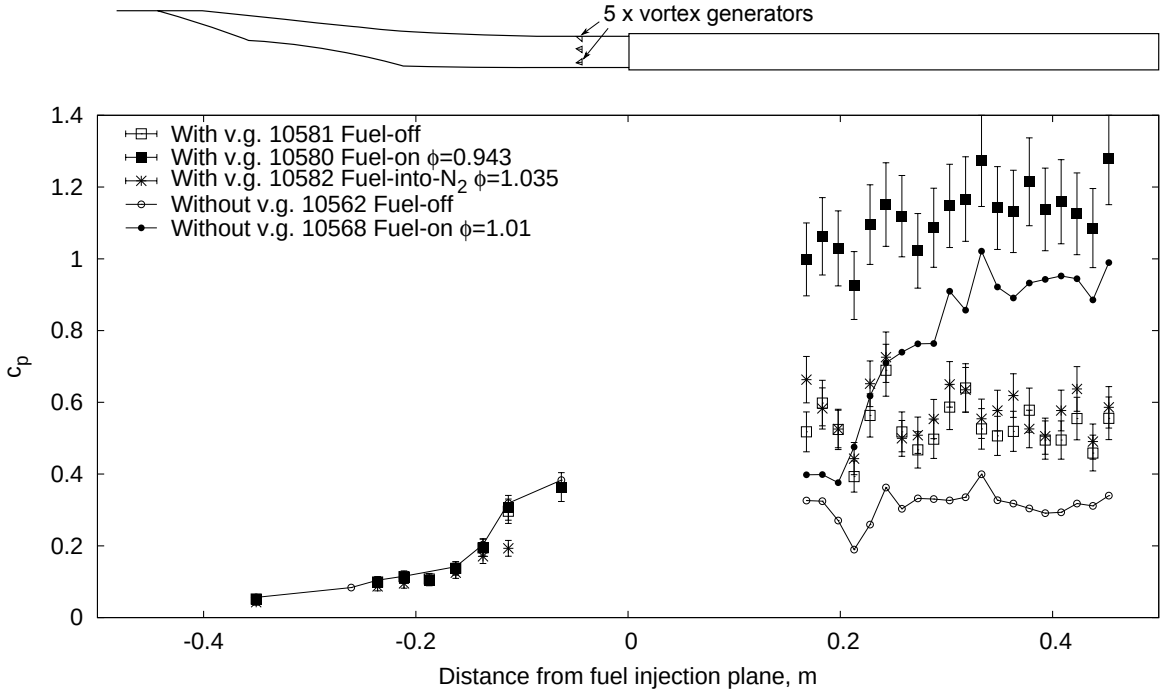

Figure 5.13: Pressure coefficients in the inlet and combustor for tests with vortex generators in the throat (with v.g.) and without vortex generators (without v.g.) at the $H_s = 4.8\,\mathrm{MJ/kg}$ Mach 6.2 test condition.

actly the same as in the tests without vortex generators, since the vortex generators are located downstream of all pressure transducers in the inlet. This indicates that downstream effects from the boundary layer interacting with either the vortex generators or

the resulting shock waves from the vortex generators are not travelling upstream into the inlet. With the flow passing through the vortex generators, the static pressure in the combustor is expected to rise higher than in the tests without vortex generators. This can be seen in the pressure distributions in the combustor for both combusting and non-combusting cases, where the pressure coefficients in the combustor rises by approximately 60% in the presence of the vortex generators. In comparison with tests without vortex generators, the flowfield in the combustor appears more disturbed in the tests with vortex generators. Due to the addition of extra mass from fuel injection, the pressure coefficients measured in the combustor for the fuel-into-N_2 test are slightly higher than those of the fuel-off test.

When fuel is injected and allowed to burn, the pressure coefficients in the combustor rise by about 0.6 from those for the fuel-off test. This is similar to the absolute rise in the pressure coefficient when combustion occurs in the tests without vortex generators. In relative amounts, the combustion-induced rise in pressure coefficient is 210% for tests with vortex generators and 290% for tests without vortex generators. By performing a simple Rayleigh analysis, it can be shown that the heat release from combustion for the test with vortex generators is less than that for the test without vortex generators. This is to be expected since the heat release from combustion is limited by the higher combustor temperatures in the tests with vortex generators. The higher temperatures and pressures, and the lower flow velocities contribute to the earlier ignition of hydrogen observed in the tests with vortex generators.

5.3.2 Combustor drag measurements

Figure 5.14a shows a comparison of the experimental and theoretical drag coefficients for the tests with vortex generators in the throat. The experimental results are also compared with those for the tests conducted at the same conditions but without the vortex generators in Figure 5.14b.

For the fuel-off test, the van Driest II theory overpredicts the drag coefficient. In contrast, the Spalding & Chi theory predicts the experimentally measured drag coefficient to within 3%. This is unexpected, since the Spalding & Chi theory performs much poorer for experiments with lower levels of flow disturbances (see Figure 5.12a) than for the current experiments. In addition, Figure 5.14b shows that the measured drag coefficient for the fuel-off test is similar to that for fuel-off tests without vortex generators.

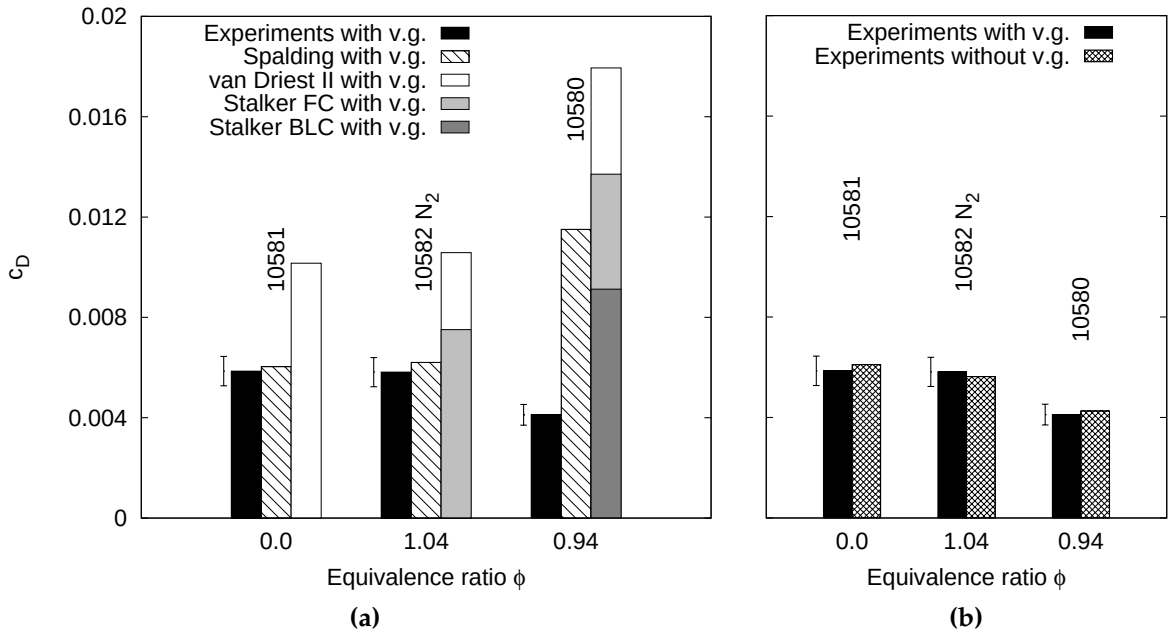

Figure 5.14: Comparison of experimentally measured combustor drag coefficients for tests with vortex generators in the throat (with v.g.) **(a)** with those predicted using skin friction theories and **(b)** with those for tests without vortex generators (without v.g.).

For the fuel-into-N_2 test, the measured drag coefficient decreases from that for the fuel-off test by only 0.7%. This is much lower than the 7% decrement in the drag coefficient measured in the experiments without the vortex generators and the 12% decrement in the drag coefficient for the experiments with three vortex generators in the inlet. The level of drag reduction inferred from a comparison of the measured drag coefficient with that predicted by the Spalding & Chi theory is 6%. This is much lower than the 30% drag reduction predicted using Stalker's film-cooling theory. Both comparisons strongly suggest that the drag reduction from the film-cooling effect is affected by the flow disturbances from the vortex generators.

For the fuel-on test, the measured drag coefficient decreases from that in the fuel-off test by 30%. This level of decrement in the drag coefficient is similar to the 28% decrement measured in the experiments without vortex generators and the experiments with vortex generators in the inlet. To allow for a comparison with Stalker's boundary layer combustion theory, the measured drag coefficient is compared with that predicted using the Spalding & Chi theory. The resulting drag reduction level of 67% is higher than the 50% drag reduction that is predicted using Stalker's theory for boundary layer combustion. This underprediction of the drag reduction levels is also observed in the experiments in Section 5.2.

These experiments demonstrate that even in the presence of stronger flow disturbances from the five vortex generators, the drag coefficient decreases significantly when hydrogen is injected and allowed to burn. These experiments also show that although locating the vortex generators in close proximity to the tangential fuel injection plane does not affect the drag reduction potential of boundary layer combustion, it does remove almost all possible drag reductions that comes from film-cooling effects.

5.4 Tests at off-design conditions

It is common for hypersonic vehicles to be designed to operate over a range of conditions. Operating at off-design conditions can bring about different flow disturbances, and it is of interest to see whether these disturbances affect the drag reduction potential of boundary layer combustion. The results from experiments conducted at off-design test conditions are reported in detail in Appendix J. In particular, Appendix J.1 presents results from experiments conducted at a lower stagnation enthalpy of 3.7 MJ/kg, Appendix J.2 of experiments conducted at a higher stagnation enthalpy of 8 MJ/kg and Appendix J.3 of experiments conducted at a higher freestream Mach number of 7.4.

Figure 5.15a shows the experimentally measured drag coefficients for tests that were conducted at different stagnation enthalpies. The results show that other than for tests conducted at a stagnation enthalpy of 3.7 MJ/kg, the drag coefficient decreases when fuel is injected into a test gas of nitrogen. More importantly, the results show that when fuel is injected and allowed to burn, the drag coefficients for the fuel-on tests are 28% - 30% lower than those for the fuel-off tests. This demonstrates that the levels of drag reduction brought about by boundary layer combustion are not affected by the flow disturbances generated when the experimental model is tested at stagnation enthalpies ranging from 3.7 MJ/kg to 8 MJ/kg.

For the experiments conducted at a higher freestream Mach number of 7.4, the experimentally measured drag coefficients are shown in Figure 5.15b. Also shown are the drag coefficients for tests conducted at on-design test conditions (at the same stagnation enthalpy but lower Mach number of 6.2). For the fuel-off test, the drag coefficient measured for the Mach 7.4 test is higher than that for the Mach 6.2 test. The flow through the inlet and combustor for the Mach 7.4 test develops differently in comparison with that for the Mach 6.2 test, which in turn causes a difference in the flow properties in the combustor. It is postulated that the difference in the flow properties causes the difference in the drag coefficients observed in the Mach 7.4 and Mach 6.2 tests. When fuel is injected into a nitrogen test gas at an equivalence ratio of 2, the drag

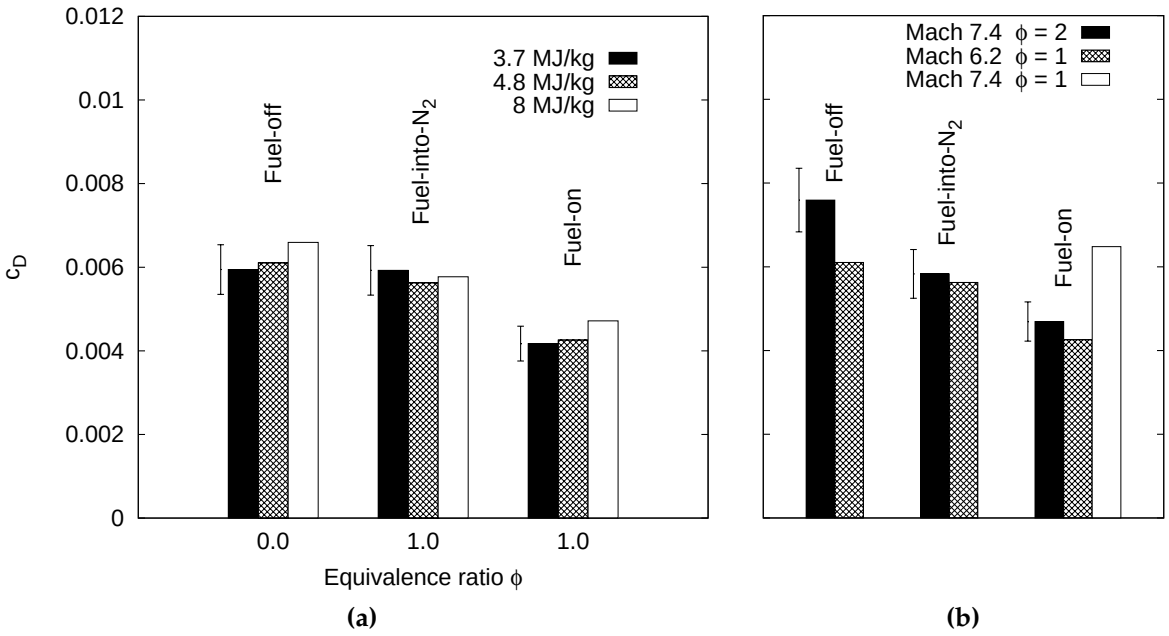

Figure 5.15: Experimentally measured combustor drag coefficients for tests **(a)** at different stagnation enthalpies and **(b)** at different Mach numbers.

coefficient decreases by about 23% from that for the fuel-off test. When fuel is injected at an equivalence ratio of 2 and allowed to burn, the drag coefficient decreases by about 38% from that for the fuel-off test. For the test at a lower equivalence ratio of 1, the measured level of drag reduction is lower but still significant. These results, together with those for the tests at different stagnation enthalpies demonstrate that even when the experimental model is tested at off-design conditions, viscous drag reduction is still possible when boundary layer combustion occurs for the range of conditions tested.

5.5 Summary

These experiments demonstrate that, for the conditions tested, the drag reduction potential of the boundary layer combustion technique is not affected by the flow disturbances generated from the REST inlet and the vortex generators. On the other hand, the levels of drag reduction brought about by film-cooling effects are shown to be more sensitive to the presence of flow disturbances, with the drag reduction levels almost fully diminishing in the presence of vortex generators in the throat region of the inlet and from testing at the condition with a stagnation enthalpy of 3.7 MJ/kg.

Although the results from these experiments demonstrate that the reduction of viscous drag is still possible, it is also important to characterise the levels of flow distur-

bances that may be required to sweep the fuel layer out from the boundary layer, and that may hence reduce the drag reduction potential of boundary layer combustion. This study is presented in Chapter 6.

Chapter 6

Characterisation of the Effects of Flow Disturbances

To assess the levels of flow disturbances that may be required to sweep the fuel layer out from the boundary layer, and that may hence reduce the drag reduction potential of boundary layer combustion, a series of CFD simulations was conducted. The focus of these simulations was to provide insights into how different inflow disturbances can perturb the injected film of hydrogen. Combustion phenomena are not considered in these simulations.

The idea behind these simulations was to provide information that could be applicable to a range of combustor geometries. Therefore a section of a combustor with symmetry boundary conditions on the sides was chosen (see Figure 6.1). In order to be able to relate the results to the current experiments, the height of the duct in these simulations was chosen to match that of the radius of the combustor in the present experiments, and the width of the duct chosen to be approximately 1/10 of the circumference of the combustor. In addition, the length of the duct was chosen to be 1/5 of the length of the combustor in the present experiments.

Nitrogen, modelled as an ideal gas with a freestream static pressure of 88.5 kPa, static temperature of 1126 K and velocity of 2576 m/s, was used as the inflow to the duct. The inflow boundary layer has a thickness of 3.4 mm and a turbulent profile generated using the *eddybl.exe* boundary-layer code (Wilcox, 2006). Hydrogen is injected behind the backward-facing step at the conditions listed in Table 3.3. The inflow conditions for the nitrogen and hydrogen correspond approximately to those entering the combustor in the experiments shown in Section 5.1. The freestream turbulence intensity for the hydrogen jet was assumed to be 0.01 and the freestream turbulent-to-laminar viscosity ratio to be 1. The isolator and combustor walls were modelled as

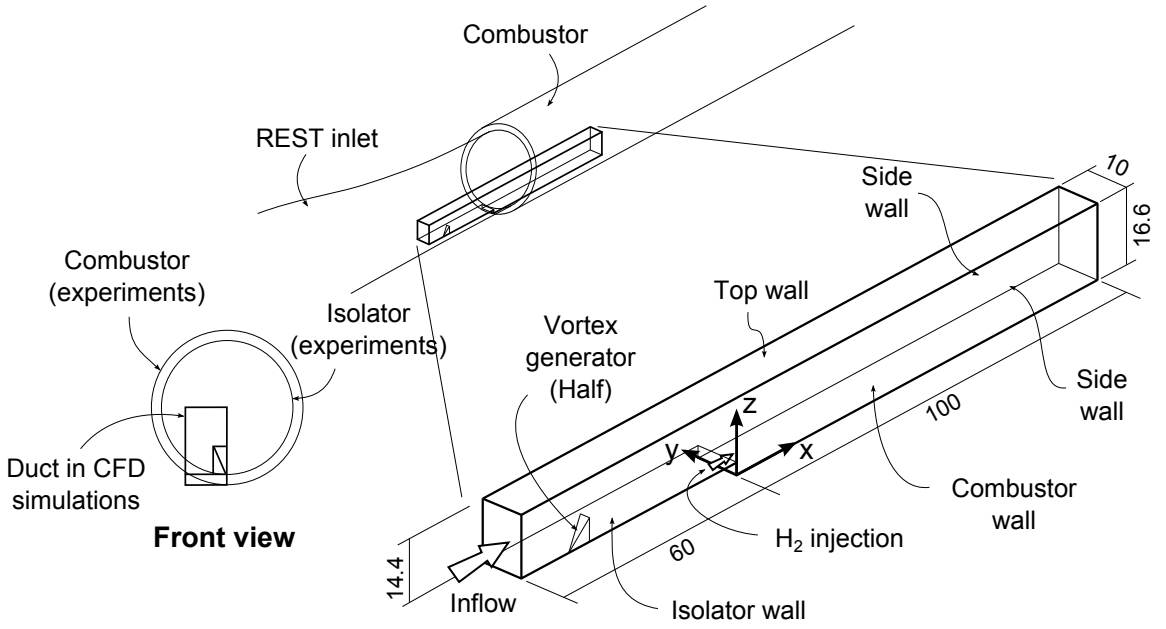

Figure 6.1: Schematic of computational domain. Dimensions are shown in mm. The vortex generator is not modelled for the undisturbed test case.

non-slip walls at a constant temperature of 298 K, while the top and side walls were modelled as slip walls. As per the simulations in Sections 4.1.6 and 4.1.8, a modified version of Fick's diffusion model (Bird et al., 2007) was used to account for turbulent diffusion.

The test cases that were examined include the following.

Undisturbed case - This case uses the nominal inflow and hydrogen injection conditions. Because the vortex generator is not modelled in this simulation, the hydrogen jet experiences minimal upstream flow disturbances. The results from this simulation is hence used as a baseline for comparison with the other test cases that have stronger upstream flow disturbances.

Vortex generator case - The nitrogen inflow and hydrogen injection conditions are the same as in the undisturbed case. In this test case, the vortex generator that is described in Section 3.1.3 is modelled. Because the vortex generator is symmetrical, only half of it is modelled. In addition, the tip of the vortex generator is modelled to be at 49.5 mm upstream of the hydrogen injection location. Since the distance from the symmetry plane of the vortex generator to the outer edge of the duct in the simulations is similar to that of 1/10 of the circumference of the combustor in the experiments, this simulation is a good geometrical approximation of the experiments with the five vortex generators located in the throat of the REST inlet (see Section 5.3). The non-uniformity

of the inflow into the combustor can be seen in Figure 6.2a, where the y-z velocity vectors are mapped onto the contours of streamwise vorticity at $x = -0.001$ m. Note that the range for streamwise vorticity contours in Figure 6.2a have been adjusted to allow for a clearer presentation of the non-uniformity of the flowfield. The location and value of the maximum streamwise vorticity are also indicated in Figure 6.2a. It can be noted that the maximum level of streamwise vorticity for this case ($\Omega_{x,\max} \approx$ 350,000 1/s) is of the same order of magnitude as those observed by other researchers, for example, $\Omega_{x,\max}$ ranges from 140,000 1/s to 200,000 1/s in the simulations of twin jet injectors by Koike et al. (2006), $\Omega_{x,\max}$ is about 180,000 1/s in the simulations of aeroramp injectors by Maddalena et al. (2006), and $\Omega_{x,\max}$ is about 100,000 1/s in the simulations of 90° cross-stream injection by Viti et al. (2009).

Increased vorticity case - This case is used to explore how increasing the streamwise vorticity affects the injected hydrogen film. To increase the streamwise vorticity, the same simulation for the vortex generator case is restarted at 47.3 mm downstream of the tip of the vortex generator, with the inflow y and z-velocities increased by a factor of 1.5. The factor of 1.5 was picked because initial simulations with a factor of 2 generated disturbances so strong that the flow into the duct choked.

Thin inflow boundary layer case - This case is similar to that of the vortex generator case, except that the thickness of the inflow turbulent boundary layer is 0.5 mm instead of 3.4 mm. In comparison with a thicker boundary layer, a thinner boundary layer is expected to generate higher levels of flow disturbances because a larger frontal area of the 5 mm high vortex generator is exposed to higher velocity flows. The differences in the flow disturbances between the case with an inflow boundary layer thickness of 0.5 mm and that with a boundary layer thickness of 3.4 mm can clearly be seen in the comparison of the streamwise vorticity contours at 0.001 m upstream of the hydrogen injection plane, as shown in Figure 6.2. The comparison shows that a thinner boundary layer flowing past the vortex generator brings about a near-wall vortex at the entrance of the combustor that has a larger length scale and larger streamwise vorticity than that for a thicker inflow boundary layer.

Hydrogen injection at matched pressures case - For the first four test cases, the hydrogen is injected at an over-expanded condition. Because of this, the hydrogen jet gets pushed towards the wall by the mainstream flow which comes over the backward-facing step. There is a possibility that the vortices produced by the vortex generator may not be able to reach the hydrogen film that has been pushed down towards the combustor wall. It is interesting to further investigate if the hydrogen can get pulled out of the boundary layer when the vortices are in a sufficiently close proximity to

the hydrogen jet. To do this, the hydrogen injection conditions are adjusted using isentropic relations to a state where the static pressure of the hydrogen jet matches that of the mainstream flow. This means that the injected hydrogen jet does not get compressed towards the wall or expanded out into the mainstream. This then places the hydrogen jet closer to the vortices that have been produced by the vortex generator. For this test case, the nitrogen inflow conditions are similar to those used for the thin inflow boundary layer case. These inflow conditions are chosen because they generate the largest levels of flow disturbances at the entrance to the combustor.

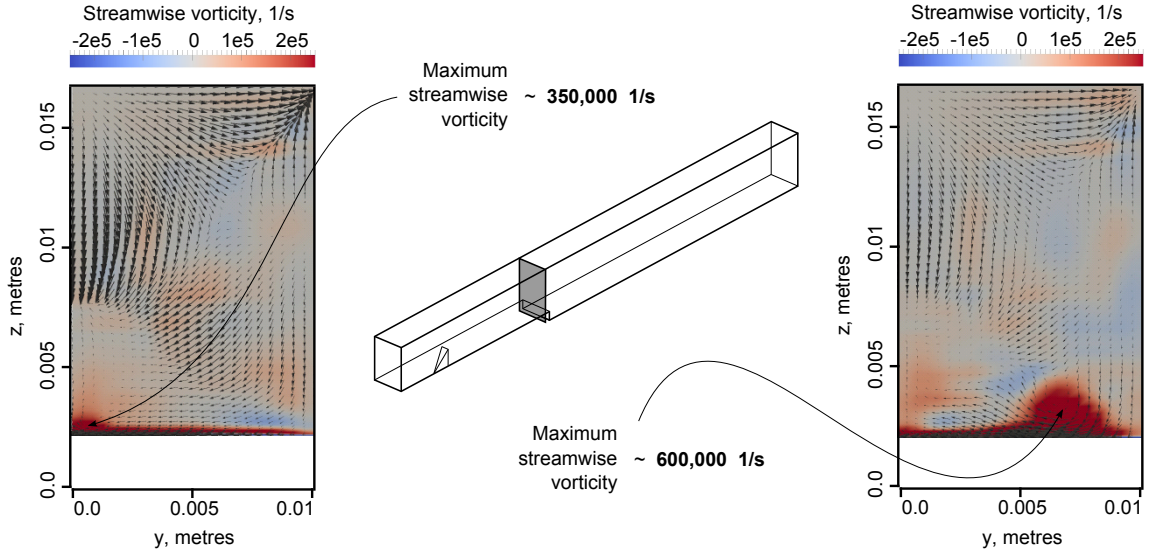

(a) Thick 3.4 mm boundary layer

(b) Thin 0.5 mm boundary layer

Figure 6.2: Differences in the streamwise vorticity at $x = -0.001$ m between the cases with different inflow boundary layer thicknesses. These cross-sections are with the observer looking upstream at the oncoming flow. The symmetry plane of the vortex generator is on the left of the cross-section.

In the results from the simulations of these test cases, the feature of the most relevance to the present study is that of where the injected hydrogen is located in the combustor. For the drag reduction potential of boundary layer combustion to be realised, it is crucial that the fuel remains in the boundary layer for combustion to occur. To determine if the hydrogen still remains in the boundary layer, the edge of the boundary layer needs to be defined. As per the method presented in Section 5.1.4, the edge of the boundary layer is defined as the distance normal to the duct wall where the cumulative weighted Reynolds shear stress contributes to 99% of the total value of the weighted Reynolds shear stress. By examining the levels of hydrogen mass fractions in the region bounded by the duct walls and the edge of the boundary layer, the potential of combustion to occur in the part of the boundary layer that is significant for viscous

drag reduction can then be estimated.

The results and findings from the simulations of the five test cases are presented in the following sections.

6.1 Undisturbed case

Streamwise slices at 12 locations in the duct (Figure 6.3) for the test case with no flow disturbances are shown in Figure 6.4. The contours are coloured by hydrogen mass fractions. Regions with a hydrogen mass fraction of 1 are in red and regions with a hydrogen mass fraction of 0 are in blue. Isolines for hydrogen mass fractions at intervals of 0.05 are also shown. In addition, the edge of the boundary layer, which is defined by the weighted Reynolds shear stress contribution, is indicated by the thick white line for each plot in Figure 6.4.

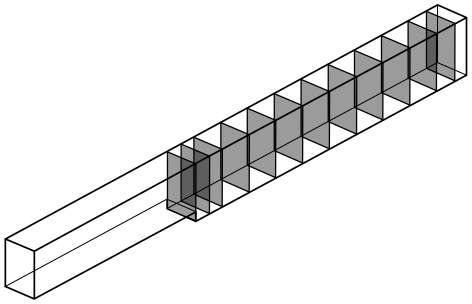

Figure 6.3: Streamwise slices.

At $x = 0\,\text{m}$, the edge of the boundary layer, which is defined using the weighted Reynolds shear stress contribution, is located about 3.4 mm above the isolator wall ($z = 0.0022\,\text{m}$). This value for boundary layer thickness is less than 1% different from that defined by the wall normal distance where the velocity is 99% of the freestream velocity. This is a good indication that the use of the weighted Reynolds shear stress contribution to define the edge of the boundary layer is appropriate. Downstream of $x = 0\,\text{m}$, the over-expanded jet gets recompressed by the mainstream flow which comes over the backward-facing step. This pushes the hydrogen film towards the duct wall, as shown at $x = 0.005\,\text{m}$. From $x = 0.005\,\text{m}$, the hydrogen film then mixes with the nitrogen in the boundary layer and diffuses slowly towards the mainstream. The mixing process is controlled by both molecular and turbulent diffusion. These results show that, by the end of the duct, the 0.05 hydrogen mass fraction line stays well within the boundary layer, thus indicating that most of the injected hydrogen remains in the

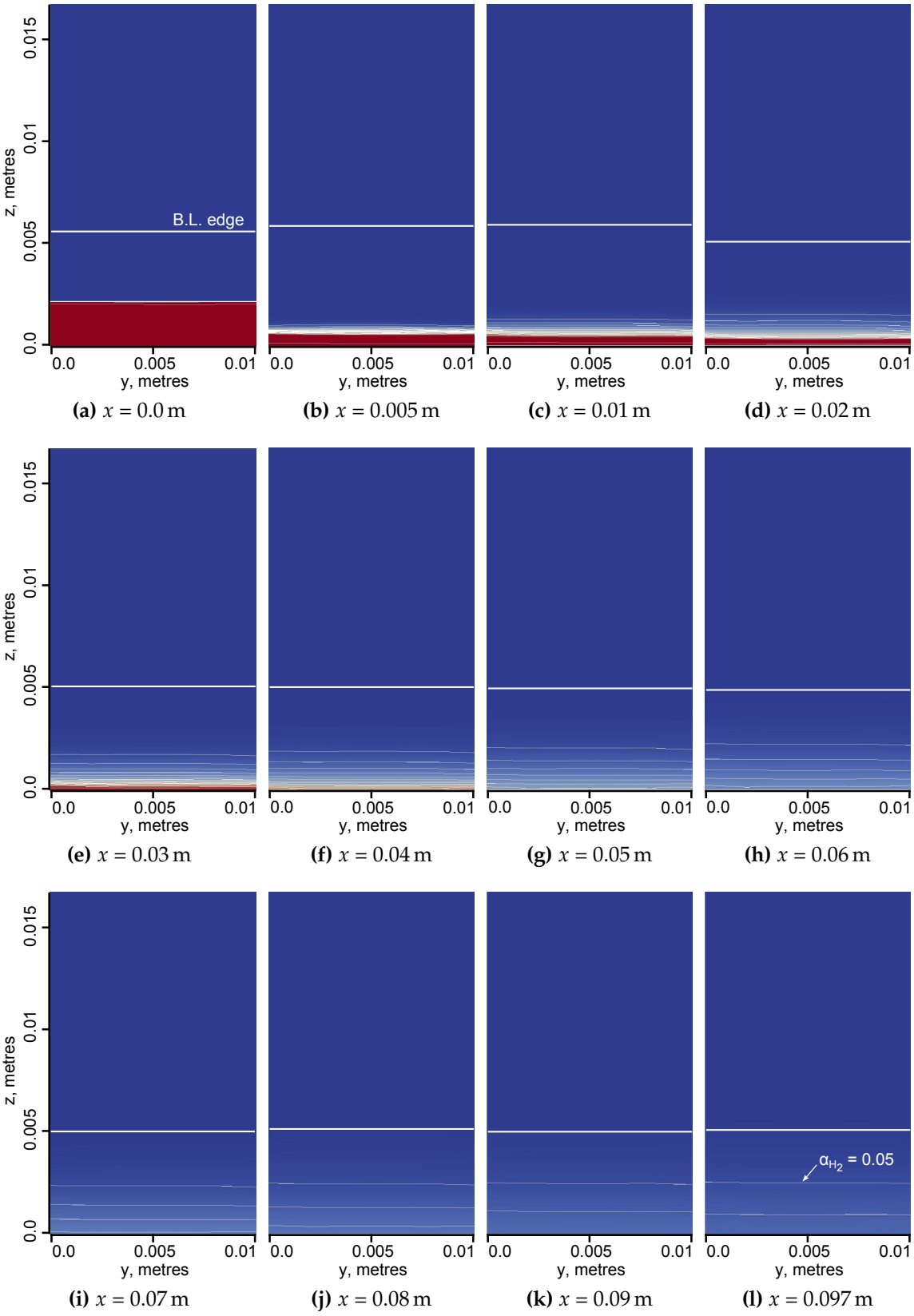

(a) $x = 0.0\,\text{m}$ **(b)** $x = 0.005\,\text{m}$ **(c)** $x = 0.01\,\text{m}$ **(d)** $x = 0.02\,\text{m}$

(e) $x = 0.03\,\text{m}$ **(f)** $x = 0.04\,\text{m}$ **(g)** $x = 0.05\,\text{m}$ **(h)** $x = 0.06\,\text{m}$

(i) $x = 0.07\,\text{m}$ **(j)** $x = 0.08\,\text{m}$ **(k)** $x = 0.09\,\text{m}$ **(l)** $x = 0.097\,\text{m}$

Figure 6.4: Undisturbed case, where α_{H_2} is the hydrogen mass fraction.

region of the flowfield that will induce a reduction in skin frictional drag when the hydrogen burns.

6.2 Vortex generator case

Streamwise slices at several locations in the duct for the test case with the vortex generator are shown in Figure 6.5. The coloured contours and isolines of hydrogen mass fraction, the line indicating the edge of the boundary layer, and the in-plane velocity vectors (vectors of the y and z-velocities) are also shown in Figure 6.5.

At $x = 0$ m, the boundary layer covers a larger area than that in the undisturbed case. In the region bounded by the boundary layer edge and the isolator wall, the velocity vectors show that there is a downward (negative z-direction) and outward (positive y-direction) motion of the fluid. From $x = 0$ m to 0.01 m, this motion nudges the hydrogen film away from the symmetry plane at $y = 0$ m. At $x = 0.02$ m, the outward motion changes direction and starts pushing the hydrogen film back towards the symmetry plane. As a result of this, the hydrogen near the symmetry plane gets pushed upwards in the positive z-direction. The inward and upward pushing motion persists downstream to about $x = 0.08$ m, causing the hydrogen plume to slightly lift off the wall and shift towards the symmetry plane. Downstream of $x = 0.08$ m, the upward and inward growth of the hydrogen plume stops. It can be noted that for the current case, the mixing between the hydrogen and nitrogen is primarily controlled by the large-scale swirling motions of the vortices. This is greatly different from the undisturbed case, where the mixing process is dominated by smaller-scale molecular and turbulent diffusion processes.

The experimental drag measurements in Section 5.3.2 show that the drag reduction from film-cooling effects is affected by the presence of flow disturbances from vortex generators. The CFD results for this test case support this finding. Figure 6.6 shows the contours of the hydrogen mass fractions near the combustor wall ($z = 0$ m) for the undisturbed case and vortex generator case. In the absence of flow disturbances from the vortex generator, the hydrogen diffuses slowly away from the wall. However, when flow disturbances from the vortex generator are present, the hydrogen is lifted away from the wall within 0.03 m from the injection plane. This leaves a larger wall surface area that is covered with low levels of hydrogen in comparison with that of the undisturbed case. As noted in Section 2.2, the removal of hydrogen from the surface reduces the drag reduction that can be obtained from the film-cooling effect. These results support the findings of the current experiments in Section 5.3.2

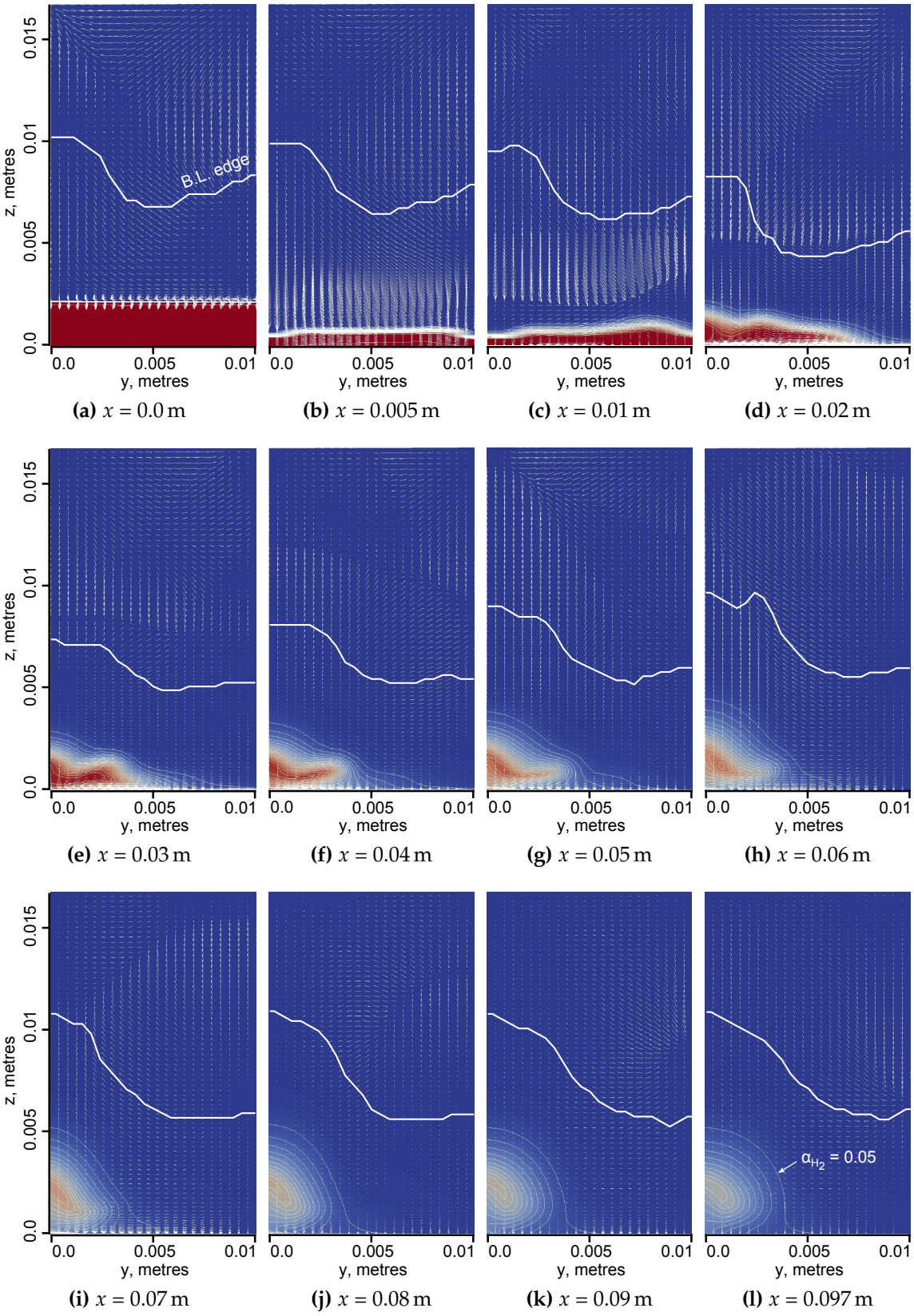

(a) $x = 0.0\,\mathrm{m}$ **(b)** $x = 0.005\,\mathrm{m}$ **(c)** $x = 0.01\,\mathrm{m}$ **(d)** $x = 0.02\,\mathrm{m}$

(e) $x = 0.03\,\mathrm{m}$ **(f)** $x = 0.04\,\mathrm{m}$ **(g)** $x = 0.05\,\mathrm{m}$ **(h)** $x = 0.06\,\mathrm{m}$

(i) $x = 0.07\,\mathrm{m}$ **(j)** $x = 0.08\,\mathrm{m}$ **(k)** $x = 0.09\,\mathrm{m}$ **(l)** $x = 0.097\,\mathrm{m}$

Figure 6.5: Vortex generator case, where α_{H_2} is the hydrogen mass fraction.

and of Rowan's experiments (2003), that the level of drag reduction achievable from film-cooling diminishes in the presence of flow disturbances from vortex generators which are located close to the hydrogen injection plane.

The results show that by the end of the duct, the 0.05 hydrogen mass fraction line stays well within the boundary layer. This finding is similar to that observed in the undisturbed case, suggesting that the resulting levels of drag reduction should be similar to those for the undisturbed case when all of the injected hydrogen burns completely. However, the results also show that most of the injected hydrogen gets swept towards the symmetry plane by the flow disturbances generated from the vortex generator, leaving behind regions in the boundary layer with lesser amounts of hydrogen

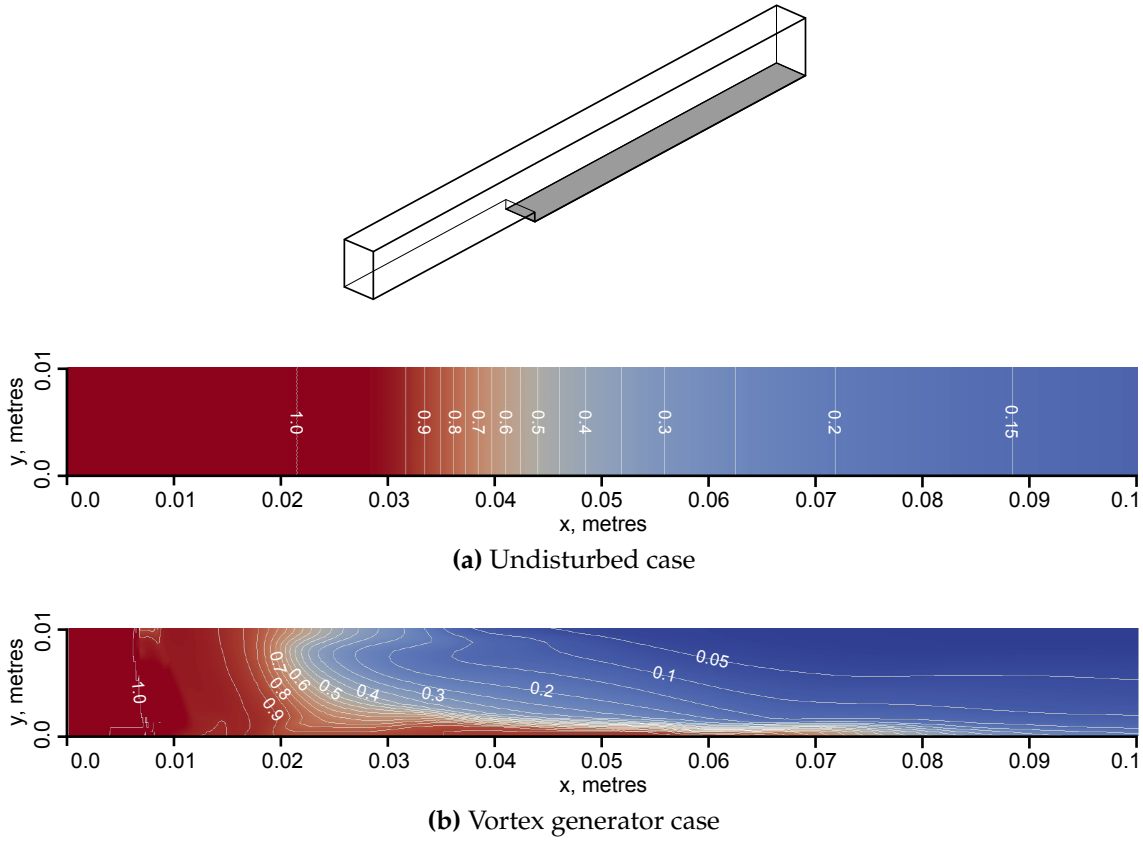

(a) Undisturbed case

(b) Vortex generator case

Figure 6.6: Contours of hydrogen mass fractions near the combustor wall.

available for combustion. This then suggests that the levels of drag reduction from boundary layer combustion for tests with vortex generators may be lesser than those for tests without vortex generators. However, the experiments in Chapter 5 indicate otherwise - that the levels of drag reduction brought about by boundary layer combustion for the tests with vortex generators are similar to those for the tests without vortex generators to within experimental uncertainty. It is possible that because com-

bustion is not considered in the CFD simulations, the results do not reveal a full picture of the processes involved in the drag reduction phenomena when hydrogen burns in the boundary layer. Therefore, without the modelling of the combustion processes in the simulations, it is not possible to deduce a definite conclusion for the difference observed between the simulations and the experiments.

6.3 Increased vorticity case

Figure 6.7 shows streamwise slices at several locations in the duct for the test case with increased inflow streamwise vorticity. The overall behaviour of the hydrogen jet is similar to that of the hydrogen jet in the vortex generator case. The major difference is that for the case with increased streamwise vorticity, the hydrogen plume is swept towards the symmetry plane at a faster rate (compare y-location of the hydrogen plume in Figure 6.5d with that in Figure 6.4d), and swept up higher in the z-direction (compare z-location of the hydrogen plume in Figure 6.5i with that in Figure 6.4i). These results show that when the inflow streamwise vorticity is increased, the 0.05 hydrogen mass fraction line shifts closer to the edge of the boundary layer. Despite this, the increased levels of flow disturbances in this test case are still not strong enough to sweep the hydrogen out of the boundary layer.

6.4 Thin inflow boundary layer case

Figure 6.8 shows streamwise slices at several locations in the duct for the test case with an inflow boundary layer thickness of 0.5 mm. It can be clearly seen in these plots that the flow disturbances in this test case affect the hydrogen film in a different way from that in the test case with a thicker inflow boundary layer. The hydrogen film gets nudged slightly away from the symmetry plane from $x = 0$ m to 0.01 m. At $x = 0.02$ m, the nitrogen gets inducted under the hydrogen film. This then pushes the hydrogen film back towards the symmetry plane. By examining the velocity vectors in Figure 6.8e, the two vortices that predominantly shape the hydrogen plume can be seen. The first vortex, centred at about $y = 0.0011$ m and $z = 0.0011$ m, rotates in a clockwise direction and is responsible for lifting the primary hydrogen plume in the z-direction. The second vortex, centred at about $y = 0.0047$ m and $z = 0.002$ m, rotates in a counter-clockwise direction and is responsible for sweeping the secondary hydrogen plume away from the symmetry plane.

These results show that, unlike the first three cases, the 0.05 hydrogen mass fraction line constantly breaches the edge of the boundary layer. This indicates that in the

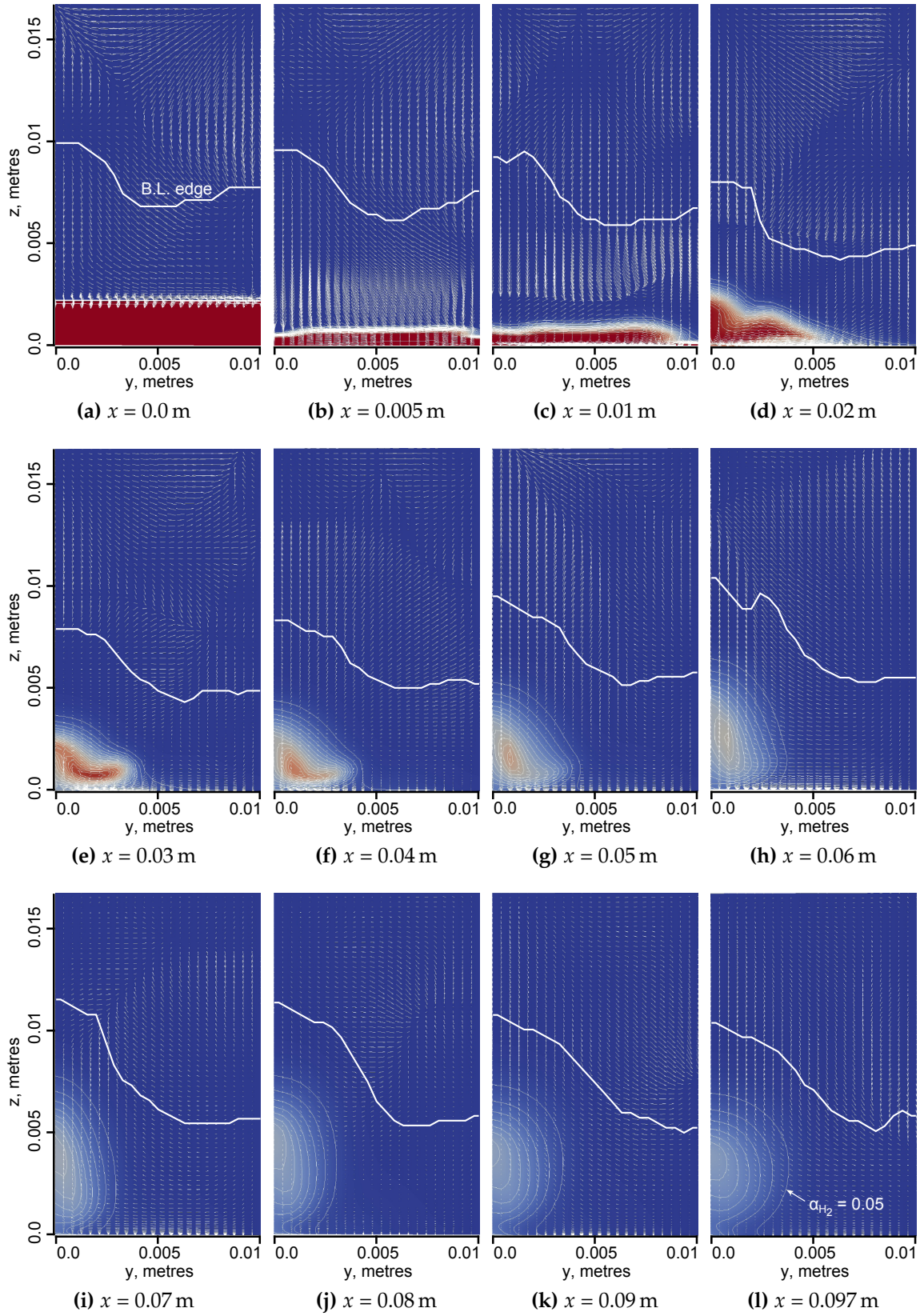

(a) $x = 0.0$ m **(b)** $x = 0.005$ m **(c)** $x = 0.01$ m **(d)** $x = 0.02$ m

(e) $x = 0.03$ m **(f)** $x = 0.04$ m **(g)** $x = 0.05$ m **(h)** $x = 0.06$ m

(i) $x = 0.07$ m **(j)** $x = 0.08$ m **(k)** $x = 0.09$ m **(l)** $x = 0.097$ m

Figure 6.7: Increased vorticity case, where α_{H_2} is the hydrogen mass fraction.

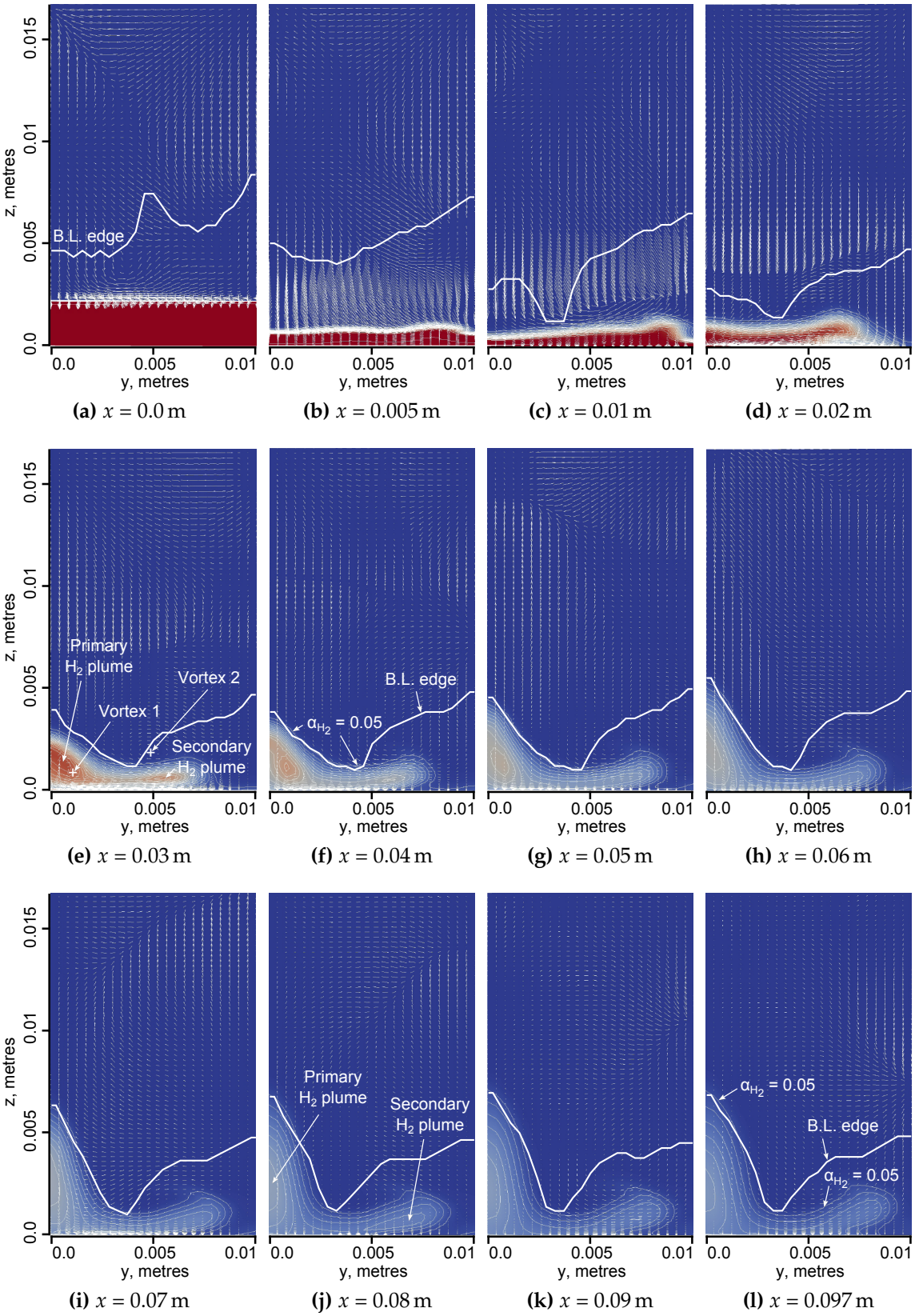

(a) $x = 0.0\,\mathrm{m}$ **(b)** $x = 0.005\,\mathrm{m}$ **(c)** $x = 0.01\,\mathrm{m}$ **(d)** $x = 0.02\,\mathrm{m}$

(e) $x = 0.03\,\mathrm{m}$ **(f)** $x = 0.04\,\mathrm{m}$ **(g)** $x = 0.05\,\mathrm{m}$ **(h)** $x = 0.06\,\mathrm{m}$

(i) $x = 0.07\,\mathrm{m}$ **(j)** $x = 0.08\,\mathrm{m}$ **(k)** $x = 0.09\,\mathrm{m}$ **(l)** $x = 0.097\,\mathrm{m}$

Figure 6.8: Thin inflow boundary layer case, where α_{H_2} is the hydrogen mass fraction.

presence of a stronger and larger length-scale vortex, some hydrogen can be swept outside the boundary layer. Nonetheless, most of the injected hydrogen still remains in the region of the flowfield that will induce a reduction in skin frictional drag when the hydrogen burns.

6.5 Hydrogen injection at matched pressures case

The results from the first four test cases show that it is extremely difficult to sweep the hydrogen jet out of the boundary layer. In the first four test cases, because the over-expanded hydrogen jet gets pushed towards the walls, it is possible that the vortices produced by the vortex generator may have a limited reach into the hydrogen film. To investigate if hydrogen can get swept out of the boundary layer when the vortices are closer to the hydrogen film, the hydrogen injection conditions were adjusted in the present test case to keep the hydrogen jet closer to the vortices produced by the vortex generator.

Figure 6.9 shows streamwise slices at several locations in the duct for the present test case. Being in closer proximity to the hydrogen film in the current case, the vortex, which is centred at $y = 0.0039$ m and $z = 0.0041$ m, now has a stronger effect on the hydrogen film than in the previous test cases. This can be observed in the different way that the hydrogen film develops in the current test case in comparison with that in the thin inflow boundary layer case. The injected hydrogen develops from a film in Figure 6.9a into a primary plume and secondary plume in Figure 6.9f. These plumes, which are more pronounced that those in the thin inflow boundary layer case, almost split into two separate plumes by the end of the duct. Downstream of $x = 0.06$ m, the flow non-uniformity begins to sweep some of the hydrogen out of the boundary layer. By the end of the duct, some portion of the 0.25 hydrogen mass fraction line sits outside the edge of the boundary layer. In comparison with the thin inflow boundary layer case, more hydrogen is displaced outside the boundary layer. This indicates that by shifting the vortex closer to the hydrogen jet, larger amounts of hydrogen can get swept out of the boundary layer. However, as in the case with the thin inflow boundary layer, the amount of hydrogen displaced outside the boundary layer represents only a small proportion of the total amount of hydrogen injected.

6.6 Summary

A series of CFD simulations have been conducted to further assess the levels of flow disturbances that may be required to sweep the fuel layer out from the boundary layer

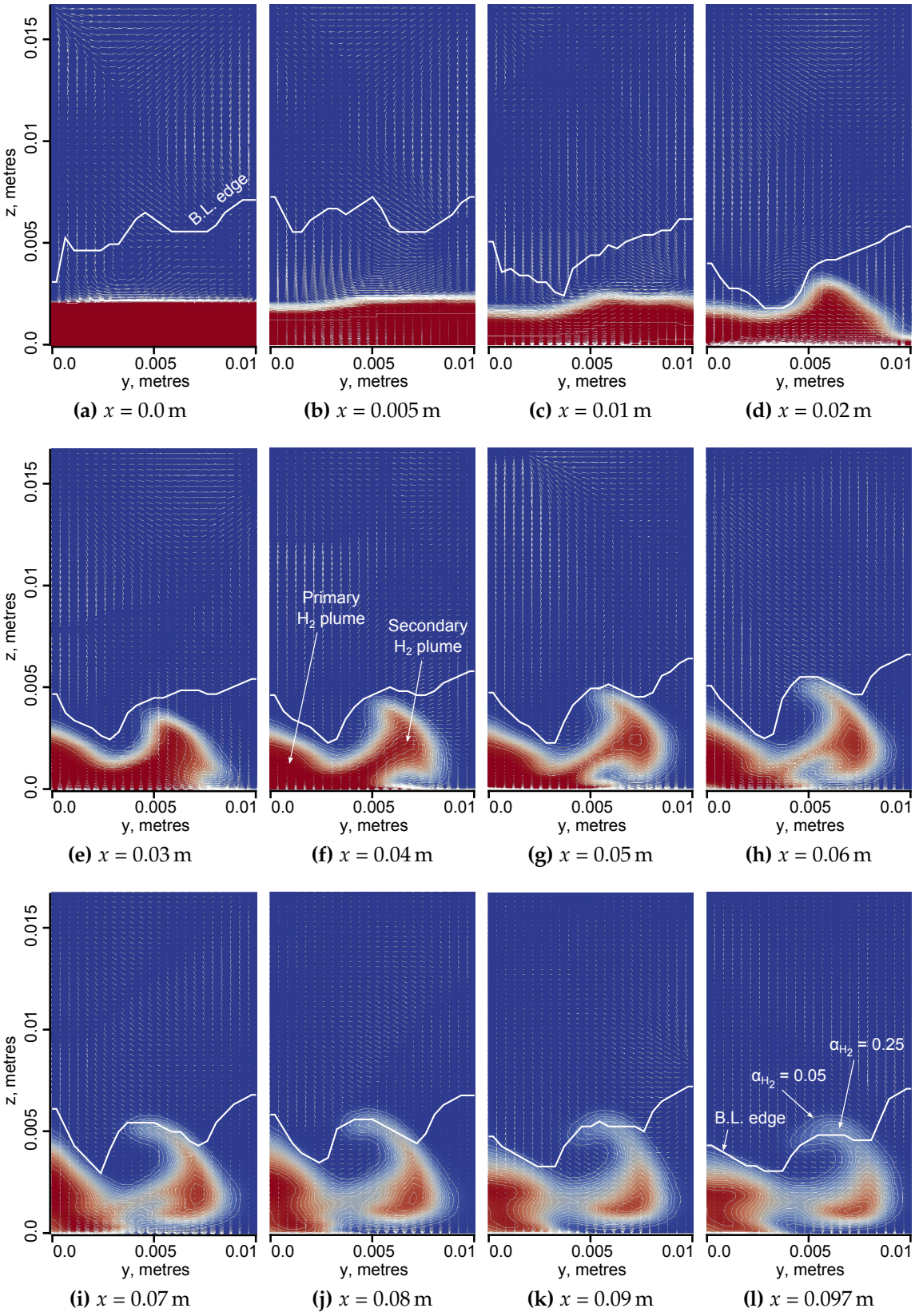

(a) $x = 0.0\,\text{m}$ **(b)** $x = 0.005\,\text{m}$ **(c)** $x = 0.01\,\text{m}$ **(d)** $x = 0.02\,\text{m}$

(e) $x = 0.03\,\text{m}$ **(f)** $x = 0.04\,\text{m}$ **(g)** $x = 0.05\,\text{m}$ **(h)** $x = 0.06\,\text{m}$

(i) $x = 0.07\,\text{m}$ **(j)** $x = 0.08\,\text{m}$ **(k)** $x = 0.09\,\text{m}$ **(l)** $x = 0.097\,\text{m}$

Figure 6.9: Hydrogen injection at matched pressures case, where α_{H_2} is the hydrogen mass fraction.

and that may therefore impede the drag reduction potential of boundary layer combustion. The results from the two cases in Sections 6.4 and 6.5 show that small amounts of the injected hydrogen can get displaced out of the boundary layer when a strong vortex with a large length-scale is sufficiently close to the hydrogen film. However, the amount of hydrogen displaced represents only a small proportion of the total amount of hydrogen injected. More importantly, the results demonstrate that it is generally very difficult to sweep large amounts of the injected hydrogen out of the region of the flowfield that will induce a reduction in skin frictional drag when the hydrogen burns. This supports the findings of the experiments in Chapter 5 that the drag reduction potential of the boundary layer combustion technique is not significantly affected by the presence of flow disturbances that are typical of those found in scramjet engines.

Chapter 7

Conclusions and Future Work

7.1 Conclusions

The aim of this thesis is to investigate if and how flow non-uniformities entering a scramjet combustor can affect the potential for boundary layer combustion to reduce skin friction. To achieve this aim, the project is approached experimentally and numerically.

Experiments were conducted on a circular constant-area combustor that was attached downstream of a REST inlet and an injector designed to deliver hydrogen into the boundary layer. Using a stress wave force balance, the integrated skin friction drag on the internal surface of the combustor was measured for three scenarios - one, where fuel is not injected, two, where fuel is injected but combustion is suppressed, and three, where fuel is injected and allowed to burn. The REST inlet was used to produce flow disturbances that are typical of those to be expected in operational scramjet inlets. In addition, the experimental model was also tested with vortex generators attached in the inlet. These vortex generators were used to induce flow disturbances similar to those brought about by conventional cross-stream fuel injection techniques. To support the analysis of the experiments, non-reacting RANS CFD simulations of the internal flowfield in the experimental model were conducted. Additional simulations were also conducted to characterise the levels of flow disturbances that may be required to sweep the fuel layer out from the boundary layer. These simulations were conducted using an in-house CFD code called Eilmer3. To allow for the simulation of the types of flows relevant to this study, the latest version of Wilcox's k-ω turbulence model had to be implemented in Eilmer3 and validated for two-dimensional, axisymmetrical and three-dimensional transient compressible flow typical of those experienced in scramjet flowfields.

The conclusions that can be drawn from this study are summarised below.

Wilcox's 2006 k-ω turbulence model can be used effectively for the simulation of scramjet flowfields. The newly implemented Wilcox's k-ω turbulence model was validated using six test cases that have flowfields representative of those to be expected in the experiments in this project. The test cases included a 2D flat plate, an axisymmetric cylinder, a backward-facing step, the mixing of a pair of coaxial jets, the interaction between a shock wave and turbulent boundary layer, and a film-cooling experiment. The generally good agreement between the numerical and experimental results obtained for all test cases demonstrates the suitability of Eilmer3 and the newly implemented k-ω turbulence model for scramjet flowfield simulations.

Flow disturbances from operating the REST inlet at on- and off-design conditions do not significantly affect the drag reduction potential of boundary layer combustion. When the experimental model was tested at on-design conditions, the experimentally measured drag coefficient for the fuel-on test was 28% lower than that for the fuel-off test. This level of skin friction reduction is similar to that measured in the experiments of Kirchhartz (2010) in which the only difference between both experiments is that the current experiments included a more realistic scramjet inlet upstream of the combustor. This therefore demonstrates that the drag reduction brought about by boundary layer combustion is not significantly affected by the flow disturbances generated from the REST inlet. Additional tests conducted at off-design conditions further demonstrate that the levels of drag reduction brought about by boundary layer combustion are not very sensitive to changes in the inflow conditions.

Flow disturbances similar to those from cross-stream fuel injection in the inlet do not significantly affect the drag reduction potential of boundary layer combustion. For the experiments with vortex generators attached at 0.157 m from the leading edge of the inlet and the experiments with vortex generators at 0.0495 m upstream of the tangential fuel injection plane, the measured levels of skin friction reduction due to boundary layer combustion are similar to those measured in the experiments without vortex generators. This demonstrates that flow disturbances similar to those from cross-stream fuel injection in the inlet do not affect the drag reduction potential of boundary layer combustion. An implication of these results is that cross-stream fuel injection in the inlet can be used in conjunction with tangential fuel injection at the start of the combustor. Using this combined fuel injection scheme in a scramjet engine provides the potential to obtain not only the benefits of thrust addition and viscous drag reduction from boundary layer combustion, but also those of thrust addition

from mainstream combustion.

In comparison with the drag reduction levels achievable from boundary layer combustion, those achievable from film-cooling effects are more sensitive to flow disturbances. The results for all experiments conducted in the present study show that when fuel is injected into the boundary layer and allowed to burn, the drag coefficients are about 28% - 30% lower than those measured in fuel-off tests. In contrast, when fuel is injected and combustion is suppressed, the drag coefficients are between 0.3% to 12% lower than those measured in fuel-off tests. This indicates that the levels of drag reduction brought about by film-cooling effects are more sensitive to the presence of flow disturbances than those from boundary layer combustion effects for the conditions of the present experiments. For the tests at a stagnation enthalpy of 3.7 MJ/kg and the tests with five vortex generators located 49.5 mm upstream of the fuel injection plane, the levels of drag reduction brought about by film-cooling effects almost fully diminish. Supporting CFD simulations of the tests with five vortex generators show that the hydrogen film gets lifted off the combustor wall by flow disturbances almost immediately after being injected into the combustor. Since the removal of hydrogen from the surface lowers the drag reduction levels that can be obtained from film-cooling effects, these numerical results provide an explanation for the drop in drag reduction levels seen in the corresponding experiments.

The skin friction coefficient decreases significantly only when combustion occurs in the boundary layer, and not when combustion occurs across the entire duct. Axisymmetric simulations of heat addition in a circular constant-area duct were conducted to explore the influence of the location of heat addition on the skin frictional drag in the combustor. These simulations demonstrate that a significant reduction in the skin frictional drag only occurs when heat is added in the boundary layer. The simulations also show that when heat is added across the entire duct, the skin frictional drag does not change from that when heat is not added. These results confirm the experimental findings of Goyne et al. (1999) and Tanno et al. (2001), that the skin friction drag in a constant-area combustor does not change when hydrogen is injected into the mainstream and allowed to burn.

For the drag reduction potential of the boundary layer combustion technique to be realised, heat addition from the combustion of fuel must occur in the regions of the boundary layer where there are large near-wall values of Reynolds shear stress. Another point that is highlighted in the axisymmetric simulations of heat addition in a circular duct is the significant role played by the Reynolds shear stress in the skin

friction reduction phenomena of the boundary layer combustion technique. The simulations show that the skin frictional drag decreases only when the large values of Reynolds shear stress in the near-wall region of the boundary layer are reduced by the addition of heat.

It is generally very difficult to sweep large portions of the injected hydrogen out of the boundary layer. Additional CFD simulations were conducted to further assess the levels of flow disturbances that may be required to sweep the fuel layer out from the boundary layer. In these simulations, a small section of the isolator and combustor that had been used in the experiments in Chapter 5 is modelled by a rectangular duct with the physical dimensions chosen to match that of a one-tenth radial slice of the experimental model. The levels of flow disturbances entering the combustor were varied between the typical levels expected in scramjet flowfields. The simulations show that while small amounts of hydrogen can get displaced from the boundary layer when the hydrogen film is sufficiently close to a vortex of adequately high vorticity and large length-scale, most of the injected hydrogen remains in the region of the flowfield that will induce a reduction in skin frictional drag if the hydrogen burns.

In summary, the experiments and simulations in this study clearly demonstrate that the boundary layer combustion technique is a robust method that can be used, even in the presence of flow disturbances, for the reduction of skin frictional drag.

7.2 Recommendations for Future Work

Over the course of this investigation, several issues that could not be resolved within the scope of the project were raised. These issues present themselves as opportunities for future research to be pursued.

Firstly, there were several instances in this project where CFD simulations that accounted for combustion would have assisted with the analysis of the results. However, as the conducting of reacting CFD simulations are not within the scope of this study, several questions could not be fully answered. It is suggested that a fully three-dimensional LES CFD simulation that uses finite-rate chemistry to model the combustion processes be conducted for the experiments in this project. The use of LES instead of RANS simulations is also recommended to provide better modelling of the mixing process between the mainstream flow and the injected hydrogen. Since the ignition and combustion processes are dependent on the mixing processes, the use of LES will help to improve the predictions made by these simulations.

Secondly, although Stalker's theory to predict flows with boundary layer combustion has been proven to be accurate for the prediction of the reduction in skin frictional drag, the theory is more appropriate for cases in which the wall-to-adiabatic-wall temperature is larger than 0.2. This is because the van Driest II method, on which Stalker's theory is constructed from, is most accurate for the prediction of skin friction when the wall-to-adiabatic-wall temperature is larger than 0.2 (Bradshaw, 1977; Goyne et al., 2003; Kirchhartz, 2010). For tests in hypersonic impulse facilities, where the wall-to-adiabatic-wall temperature generally ranges from 0.02 to 0.1, the theory of Spalding & Chi gives a better prediction of the skin friction drag. It is proposed that Stalker's theory be extended to incorporate the theory of Spalding & Chi to allow for a more accurate prediction of skin friction to be made for the experiments conducted in impulse facilities.

In addition, there also remains several questions that need to be addressed before the boundary layer combustion technique can be implemented in operational scramjet-powered vehicles.

Firstly, over the past few years, several other methods have been proposed for the injection of fuel into the boundary layer. These include the tangential porthole injectors of Suraweera and Smart (2009), the multiport injector array of Pudsey and Boyce (2010) and the porous wall injectors of Van Staden (2011). It is suggested that an investigation be conducted to characterise each injection method and to find the method that provides the best levels of skin friction reduction from boundary layer combustion. The consideration of the flow losses, the amount of heat addition, and the mechanical, thermal and structural design implications should also be factored into this investigation.

Secondly, one of the topics that has not been thoroughly examined for the boundary layer combustion technique is that of the conditions of fuel injection. The fuel injection conditions are important parameters that will affect how the fuel interacts with the mainstream flow and that will eventually affect the effectiveness of the boundary layer combustion technique in the reduction of skin frictional drag. It is suggested that an investigation be conducted to find the optimum fuel injection condition for the range of flight conditions that scramjets are expected to operate in.

Thirdly, although hydrogen has often been cited as the fuel of choice for scramjets due to its rapid burning and high mass-specific energy content, the use of hydrogen raises handling, packaging and safety issues (Lewis, 2001). It would be worthwhile investigating whether other fuels can bring about the same or even better levels of drag reduction if they are burned in turbulent boundary layers. For example, hydrocarbons

such as ethylene and kerosene are popular alternatives fuels for scramjets due to their superior aerodynamic and volumetric characteristics (Lewis, 2001). Some preliminary experiments by Suraweera (2006) and theoretical analysis by Barth et al. (2011) have suggested that the skin frictional drag reduces when ethylene burns in a turbulent boundary layer. It is suggested that these investigations be pursued in more detail to confirm the viability of using other fuels for the boundary layer combustion technique.

Fourthly, the results from this thesis suggest that cross-stream fuel injection, which allows for better fuel penetration into the mainstream flow, can be used in conjunction with boundary layer fuel injection. Using this combined fuel injection scheme in a scramjet engine provides the potential to obtain not only the benefits of thrust addition and viscous drag reduction from boundary layer combustion, but also those of thrust addition from mainstream combustion. It is suggested that an investigation be conducted to show how a combined fuel injection scheme can be used to improve the net thrust potential of a scramjet engine.

Finally, it is also noted that all the tests of boundary layer combustion performed in shock tunnels so far have been made with models with the walls remaining at about room temperature during the test duration. In flight, the surfaces of a scramjet-powered vehicle will be hot, possibly even exceeding 3000 K in the combustor (Powell et al., 2001). A hot surface will lead to a larger amount of hot air near to the surface, which may promote an earlier ignition of the fuel-air mixture in the boundary layer. If this can be achieved, it will lead to an extension of the range of conditions over which skin friction reduction can be achieved. Thus, a study needs to be conducted to investigate the effects of a hot wall on the ignition delay of the fuel-air mixture in the boundary layer and the subsequent effects on the levels of skin friction reduction that is achievable with boundary layer combustion.

References

Ames Research Staff (**1953**). "Equations, tables and charts for compressible flow". Tech. Rep. NACA Report 1135, Ames Research Center.

Anderson, J.D. (**2006**). *Hypersonic and high-temperature gas dynamics*. American Institute of Aeronautics and Astronautics, Reston, Virginia, USA, 2nd ed.

Anyiwo, J.C. and **Bushnell, D.M.** (**1982**). "Turbulence amplification in shock-wave boundary-layer interaction". *AIAA Journal*, **vol. 20, no. 7**, pp. 893–899.

Aupoix, B.; **Mignosi, A.**; **Viala, S.**; **Bouvier, F.** and **Gaillard, R.** (**1998**). "Experimental and numerical study of supersonic film cooling". *AIAA Journal*, **vol. 36, no. 6**, pp. 915–923.

Auslender, A.; **Suder, K.L.** and **Thomas, S.R.** (**2009**). "An overview of the NASA FAP Hypersonics Project Airbreathing Propulsion Research". In *16th AIAA/DLR/DGLR International Space Planes and Hypersonic Systems and Technologies Conference*. AIAA-2009-7277, American Institute of Aeronautics and Astronautics Inc., Bremen, Germany.

Bakos, R.J. (**1994**). *An investigation of test flow nonequilibrium effects on scramjet combustion*. PhD thesis, The University of Queensland, Queensland, Australia.

Baldwin, B.S. and **Lomax, H.** (**1978**). "Thin layer approximation and algebraic model for separated turbulent flows". In *AIAA 16th Aerospace Sciences Meeting*. AIAA-78-257, American Institute of Aeronautics and Astronautics Inc., Huntsville, Al.

Bardina, J.E.; **Huang, P.G.** and **Coakley, T.J.** (**1997**). "Turbulence modeling validation, testing, and development". Technical Memorandum NASA TM 110446, NASA.

Barth, J.E.; **Wheatley, V.** and **Smart, M.K.** (**2011**). "Effects of ethylene combustion in a hypersonic turbulent boundary layer". In *11th Australian Space Science Conference*. National Committee for Space Science & National Space Society of Australia, Canberra, ACT, Australia.

Baurle, R.A. and **Gaffney, R.L.** (**2008**). "Extraction of one-dimensional flow properties from multidimensional data sets". *Journal of Propulsion and Power*, **vol. 24, no. 4**, pp. 704 – 714.

Bird, R.B.; **Stewart, W.E.** and **Lightfoot, E.N.** (**2007**). *Transport phenomena*. John Wiley & Sons, New York, 2nd ed.

Bittker, D.A. and **Scullin, V.J.** (**1972**). "General chemical kinetics computer program for static and flow reactions, with application to combustion and shock tube kinetics". Technical Note NASA TN D-6586, NASA Lewis Research Center.

Boyce, R.R.; **Takahashi, M.** and **Stalker, R.J.** (**2005**). "Mass spectrometric measurements of driver gas arrival in the T4 free-piston shock-tunnel". *Shock Waves*, **vol. 14, no. 5/6**, pp. 371–378.

Bradshaw, P. (**1977**). "Compressible turbulent shear layers". *Annual Review of Fluid Mechanics*, **vol. 9**, pp. 33–54.

Bushnell, D.M. and **Hefner, J.N.** (**1990**). *Viscous drag reduction in boundary layers*. American Institute of Aeronautics and Astronautics, Washington D.C., USA.

Buttsworth, D.R. (**1994**). *Shock induced mixing and combustion in scramjets*. PhD thesis, The University of Queensland, Queensland, Australia.

Cary, Aubrey M., J. and **Bertram, M.H.** (**1974**). "Engineering prediction of turbulent skin friction and heat transfer in high-speed flow". Technical Note NASA TN D-7507, NASA.

Cary, Aubrey M., J. and **Hefner, J.N.** (**1972**). "Film-cooling effectiveness and skin friction in hypersonic turbulent flow". *AIAA Journal*, **vol. 10, no. 3**, pp. 1188–1193.

Chiu, H.S. (**1996**). *Propagation of stress waves through screw joints*. Bachelor of Engineering Thesis, Division of Mechanical Engineering, The University of Queensland, Brisbane, Australia.

Copper, J.A. (**1962**). "Experimental Investigation of the Equilibrium Interface Technique Citation: Phys. Fluids 5, 844 (1962);". *Physics of Fluids*, **vol. 5, no. 7**, pp. 844–849.

Craddock, C.S. (**2000**). "Design of the axisymmetric HyShot nozzle for T4". Department of Mechanical Engineering Report 2/00, The University of Queensland.

Curran, E. and **Murthy, S.** (**2000**). *Scramjet propulsion*. American Institute of Aeronautics and Astronautics,, Reston, Virginia, USA.

Cutler, A.D.; **Diskin, G.S.**; **Drummond, J.P.** and **White, J.A.** (**2006**). "Supersonic coaxial jet experiment for computational fluid dynamics code validation". *AIAA Journal*, **vol. 44, no. 3**, pp. 585–592.

Cutler, A.D. and **White, J.A.** (**2001**). "An experimental and CFD study of a supersonic coaxial jet". In *39th Aerospace Sciences Meeting and Exhibit*. AIAA 2001-0143, American Institute of Aeronautics and Astronautics Inc., Reno, Nevada, USA.

Denman, A.W. (**2007**). *Large-eddy simulation of compressible turbulent boundary layers with heat addition*. PhD thesis, The University of Queensland, Queensland, Australia.

Denman, A.W.; **Jacobs, P.A.** and **Mee, D.J.** (**2005**). "Compressible turbulent flow with boundary-layer heat addition". In *43rd AIAA Aerospace Sciences Meeting and Exhibit*. AIAA 2005-1097, American Institute of Aeronautics and Astronautics Inc., Reno, Nevada, USA.

Dershin, H.; **Leonard, C.A.** and **Gallaher, W.H.** (**1967**). "Direct measurement of skin friction on a porous flat plate with mass injection". *AIAA Journal*, **vol. 5, no. 11**, pp. 1934 – 1939.

Durbin, P.A. (**1996**). "On the k-ϵ stagnation point anomaly". *International Journal of Heat and Fluid Flow*, **vol. 17, no. 1**, pp. 89–90.

Eckert, E.R.G. (**1955**). "Engineering relations for friction and heat transfer to surfaces in high velocity flow". *Journal of the Aeronautical Sciences*, **vol. 22**, pp. 585–587.

Eggers, T.; **Silvester, T.B.**; **Paull, A.** and **Smart, M.K.** (**2009**). "Aerodynamic design of hypersonic re-entry flight HIFiRE 7". In *16th AIAA/DLR/DGLR International Space Planes and Hypersonic Systems and Technologies Conference*. AIAA 2009-7256, American Institute of Aeronautics and Astronautics Inc., Bremen, Germany.

Eklund, D.R.; **Fletcher, D.G.**; **Hartfield, J.R.J.**; **Northam, G.B.** and **Dancey, C.L.** (**1995**). "A comparative computational/experimental investigation of Mach 2 flow over a rearward-facing step". *Computers & Fluids*, **vol. 24, no. 5**, pp. 593–608.

Evans, J.S. and **Schexnayder, C.J.** (**1980**). "Influence of chemical-kinetics and unmixedness on burning in supersonic hydrogen flames". *AIAA Journal*, **vol. 18, no. 2**, pp. 188–193.

Fernholz, H.H. and **Finley, P.J.** (**1977**). *AGARDograph No. 223 - A critical compilation of compressible turbulent boundary layer data*. AGARD-AG-223, Neuilly Sur Seine, France : Advisory Group for Aerospace Research & Development, North Atlantic Treaty Organization.

Ferri, A.; **Libby, P.A.** and **Zakkay, V.** (**1964**). "Theoretical and experimental investigations of supersonic combustion". In *Proceedings of the International Council of the Aeronautical Sciences, Third Congress, Stockholm, 1962*, (pp. 1089 – 1155). Spartan, New York, USA.

Fukagata, K.; **Iwamoto, K.** and **Kasagi, N.** (**2002**). "Contribution of Reynolds stress distribution to the skin friction in wall-bounded flows". *Physics of Fluids*, **vol. 14, no. 11**, pp. L73–L76.

Gangurde, D.Y.; **Mee, D.J.** and **Jacobs, P.A.** (**2007**). "Numerical simulation of a Ludwieg-tube fuel delivery system for scramjet experiments in shock tunnels". In *16th Australasian Fluid Mechanics Conference*. School of Engineering, The University of Queensland, Gold Coast, Queensland, Australia.

Goldstein, R.J. (**1971**). "Film cooling". *Advances in Heat Transfer*, **vol. 7**, pp. 321–379.

Gomez, T.; **Flutet, V.** and **Sagaut, P.** (**2009**). "Contribution of Reynolds stress distribution to the skin friiction in compressible turbulent channel flows". *Physical Review E*, **vol. 79**, pp. 035301–1 – 035301–4.

Goyne, C.P.; **Stalker, R.J.** and **Paull, A.** (**1999**). "Shock-tunnel skin-friction measurement in a supersonic combustor". *Journal of Propulsion and Power*, **vol. 15, no. 5**, pp. 699–705.

Goyne, C.P.; **Stalker, R.J.**; **Paull, A.** and **Brescianini, C.P.** (**2000**). "Hypervelocity skin-friction reduction by boundary-layer combustion of hydrogen". *Journal of Spacecraft and Rockets*, **vol. 37, no. 6**, pp. 740–746.

Goyne, C.; **Stalker, R.** and **Paull, A.** (**2003**). "Skin-friction measurements in high-enthalpy hypersonic boundary layers". *Journal of Fluid Mechanics*, **vol. 485**, pp. 1–32.

Haven, B.A.; **Yamagata, D.K.**; **Kurosaka, M.**; **Yamawaki, S.** and **Maya, T.** (**1997**). "Anti-kidney pair of vortices in shaped holes and their influence on film cooling effectiveness". In *IGTI Turbo Expo*. ASME paper 97-GT-45, American Society of Mechanical Engineers, Orlando.

He, Y. and **Morgan, R.G.** (**1994**). "Transition of compressible high enthalpy boundary layer flow over a flat plate". *Aeronautical Journal*, **vol. 98, no. 972**, pp. 25–34.

Heidmann, J.D. and **Ekkad, S.** (**2008**). "A novel antivortex turbine film-cooling hole concept". *Transactions of the ASME: Journal of Turbomachinery*, **vol. 130**, pp. 031020–1 – 031020–9.

Heiser, W.H. and **Pratt, D.T.** (**1994**). *Hypersonic airbreathing propulsion*. American Institute of Aeronautics and Astronautics, Washington D.C., USA.

Hemsch, M.J. (**1992**). *Tactical Missile Aerodynamics: General Topics*, vol. 141 of *Progress in Astronautics and Aeronautics*. American Institute of Aeronautics and Astronautics, Washington DC, USA.

Hertzberg, A.; **Wittliff, C.E.** and **Hall, J.G.** (**1961**). "Summary of shock tunnel development and application to hypersonic research". Tech. Rep. AD-1052-A-12 (also AFOSR TR 60-139), Cornell Aeronautical Laboratory, Inc., Buffalo 21, New York, USA.

Hinze, J.O. (**1975**). *Turbulence*. McGraw-Hill, New York, USA.

Hirsch, C. (**1988**). *Numerical computation of internal and external flows*. Wiley, Chichester, England.

Hirsch, C. (**2007**). *Numerical computation of internal and external flows*. Butterworth-Heinemann, Oxford, UK, 2nd ed.

Hopkins, E.J. and **Inouye, M.** (**1971**). "An evaluation of theories for predicting turbulent skin friction and heat transfer on flat plates at supersonic and hypersonic Mach numbers". *AIAA Journal*, **vol. 9, no. 6**, pp. 993–1003.

Hornung, H.G. (**1988**). "28th Lanchester Memorial Lecture - Experimental Real-Gas Hypersonics". *Aeronautical Journal*, **vol. 92, no. 920**, pp. 379–389.

Jacobs, P.A. and **Gollan, R.J.** (**2008**). "The Eilmer3 code: User guide and example book". Department of Mechanical Engineering Report 2008/07, The University of Queensland.

Jacobs, P.A.; **Gollan, R.J.**; **Denman, A.W.**; **O'Flaherty, B.T.**; **Potter, D.F.**; **Petrie-Repar, P.J.** and **Johnston, I.A.** (**2010**). "Eilmer's Theory Book: Basic models for gas dynamics and thermochemistry". Department of Mechanical Engineering Report 2010/09, The University of Queensland.

Jacobs, P.A.; **Rogers, R.C.**; **Weidner, E.H.** and **Bittner, R.D.** (**1992**). "Flow establishment in a generic scramjet combustor". *Journal of Propulsion and Power*, **vol. 8, no. 4**, pp. 890–899.

Jacobs, P.A. and **Stalker, R.J.** (**1989**). "Design of axisymmetric nozzles for reflected shock tunnels". Department of Mechanical Engineering Report 1/89, The University of Queensland.

Juhany, K.A. and **Hunt, M.L.** (**1994**). "Flowfield measurements in supersonic film cooling including the effect of shock-wave interaction". *AIAA Journal*, **vol. 32, no. 3**, pp. 578–583.

Kanda, T. and **Ono, F.** (**1997**). "Experimental studies of supersonic film cooling with shock wave interaction (II)". *Journal of Thermophysics and Heat Transfer*, **vol. 11, no. 4**, pp. 590–593.

Kanda, T.; **Ono, F.**; **Takahashi, M.**; **Saito, T.** and **Wakamatsu, Y.** (**1996**). "Experimental studies of supersonic film cooling with shock wave interaction". *AIAA Journal*, **vol. 34, no. 2**, pp. 265–271.

Kazakov, A.V.; **Kogan, M.N.** and **Kuryachii, A.P.** (**1997**). "Effect of local heat supply to a turbulent boundary layer on the friction". *Fluid Dynamics*, **vol. 32, no. 1**, pp. 39–45.

Kim, K.S.; **Lee, Y.**; **Alvi, F.S.**; **Settles, G.S.** and **Horstman, C.C.** (**1991**). "Skin-friction measurements and computational comparison of swept shock/boundary-layer interactions". *AIAA Journal*, **vol. 29, no. 10**, pp. 1643–1650.

Kirchhartz, R.M. (**2007**). *Enhancing scramjet performance by boundary layer combustion*. Confirmation of candidature report, The University of Queensland, Queensland, Australia.

Kirchhartz, R.M. (**2010**). *Upstream wall layer effects on drag reduction with boundary layer combustion*. PhD thesis, The University of Queensland, Queensland, Australia.

Kirchhartz, R.M.; **Mee, D.J.**; **Stalker, R.J.**; **Jacobs, P.A.** and **Smart, M.K.** (**2010**). "Supersonic boundary-layer combustion: Effects of upstream entropy and shear-layer thickness". *Journal of Propulsion and Power*, **vol. 26, no. 1**, pp. 57–66.

Knell, M. (**2003**). "Calibration of a Mach 7.6 nozzle". Department of Mechanical Engineering Report 2003/13, The University of Queensland.

Knight, D.; **Yan, H.**; **Panaras, A.G.** and **Zheltovodov, A.** (**2003**). "Advances in CFD prediction of shock wave turbulent boundary layer interactions". *Progress in Aerospace Sciences*, **vol. 39**, pp. 121–184.

Koike, S.; **Suzuki, K.**; **Kitamura, E.**; **Hirota, M.**; **Takita, K.**; **Masuya, G.** and **Matsumoto, M.** (**2006**). "Measurement of vortices and shock waves produced by ramp and twin jets". *Journal of Propulsion and Power*, **vol. 22, no. 5**, pp. 1059–1067.

Kulkarni, V.; **Kulkarni, P.S.** and **Reddy, K.P.J.** (**2007**). "Drag reduction by a forward facing aerospike for a large angle blunt cone in high enthalpy flows". In *26th International Symposium on Shock Waves*, vol. 1, (pp. 565–570). Springer-Verlag, Berlin, Heidelberg, Gottingen, Germany.

Kuryachii, A.P. (**1998**). "Simulation of the thermal method for reducing turbulent friction". *Fluid Dynamics*, **vol. 33, no. 1**, pp. 48–55.

Ladeinde, F. (**2010**). "Advanced computational-fluid-dynamics techniques for scramjet combustion simulation". *AIAA Journal*, **vol. 48, no. 3**, pp. 513–514.

Larin, O.B. and **Levin, V.A.** (**2001**). "Energy addition to a gas in a turbulent supersonic boundary layer". *Journal of Applied Mechanics and Technical Physics*, **vol. 42, no. 1**, pp. 87–90.

Levin, V.A. and **Larin, O.B.** (**2003**). "Skin-friction reduction by energy addition into a turbulent boundary layer". In *41st AIAA Aerospace Sciences Meeting and Exhibit*. AIAA 2003-0036, American Institute of Aeronautics and Astronautics Inc., Reno, Nevada, USA.

Lewis, M.J. (**2001**). "Significance of fuel selection for hypersonic vehicle range". *Journal of Propulsion and Power*, **vol. 17, no. 6**, pp. 1214–1221.

Leylek, J.H. and **Zerkle, R.D.** (**1994**). "Discrete-jet film cooling: A comparison of computational results with experiments". *Transactions of the ASME: Journal of Turbomachinery*, **vol. 116**, pp. 358–368.

Lordi, J.A.; **Mates, R.E.** and **Moselle, J.R.** (**1966**). "Computer program for the numerical simulation of non-equilibrium expansions of reaction gas mixtures". NASA Contractor Report NASA-CR-472, Cornell Aeronautical Laboratory, Inc., Buffalo, NY.

Lu, F.K. (**1988**). *Mach number effects on fin-generated shock-wave boundary layer interactions*. PhD thesis, Pennsylvania State University, University Park, PA.

Lu, P.J. and **Wu, K.C.** (**1991**). "On the shock enhancement of confined supersonic mixing flows". *Physics of Fluids*, **vol. 3, no. 12**, pp. 3046–3062.

Ludwieg, H. (**1955**). "Der Rohrwindkanal". *Zeitschrift für Flugwissenschaften*, **vol. 3, no. 7**, pp. 206–216.

Macrossan, M.N. (**1989**). "The equilibrium flux method for the calculation of flows with non-equilibrium chemical-reactions". *Journal of Computational Physics*, **vol. 80, no. 1**, pp. 204–231.

Maddalena, L.; **Campioli, T.L.** and **Schetz, J.A.** (**2006**). "Experimental and computational investigation of light-gas injectors in Mach 4.0 crossflow". *Journal of Propulsion and Power*, **vol. 22, no. 5**, pp. 1027–1038.

Mallinson, S.G.; **Hillier, R.**; **Jackson, A.P.**; **Kirk, D.C.**; **Soltani, S.** and **Zanchetta, M.** (**2000**). "Gun tunnel flow calibration: defining input conditions for hypersonic flow computations". *Shock Waves*, **vol. 10**, pp. 313–322.

McBride, B.J.; **Zehe, M.J.** and **Gordon, S.** (**2002**). "NASA Glenn coefficients for calculating thermodynamic properties of individual species". NASA Technical Paper NASA-TP-2002-211556, NASA John H. Glenn Research Center at Lewis Field, Cleveland, Ohio.

McDaniel, J.C.; **Fletcher, D.G.**; **Hartfield, J.R.J.** and **Hollo, S.D.** (**1991**). "Staged transverse injection into Mach 2 flow behind a rearward-facing step: A 3-D compressible test case for hypersonic combustor code validation". In *AIAA 3rd International Aerospace Planes Conference*. AIAA-91-5071, American Institute of Aeronautics and Astronautics Inc., Orlando, Florida.

McGilvray, M.; **Austin, J.M.**; **Sharma, M.**; **Jacobs, P.A.** and **Morgan, R.G.** (**2009**a). "Diagnostic modelling of an expansion tube operating condition". *Shock Waves*, **vol. 19, no. 1**, pp. 59–66.

McGilvray, M.; **Jacobs, P.A.**; **Morgan, R.G.**; **Gollan, R.J.** and **Jacobs, C.M.** (**2009**b). "Helmholtz resonance of Pitot pressure measurements in impulsive hypersonic test facilities". *AIAA Journal*, **vol. 47**, pp. 2430–2439.

McGilvray, M.; **Morgan, R.G.** and **Jacobs, P.A.** (**2010**). "Scramjet experiments in an expansion tunnel: Evaluated using a quasi-steady analysis technique". *AIAA Journal*, **vol. 48, no. 8**, pp. 1635–1646.

McIntosh, M.K. (**1968**). "Computer program for the numerical calculation of frozen and equilibrium conditions in shock tunnels". Departmental Report, Department of Physics, Australian National University, Canberra, Australia.

Mee, D.J. (**2002**a). "Boundary-layer transition measurements in hypervelocity flows in a shock tunnel". *AIAA Journal*, **vol. 40, no. 8**, pp. 1542–1548.

Mee, D.J. (**1993**). "Uncertainty analysis of conditions in the test section of the T4 shock tunnel". Department of Mechanical Engineering Research Report 4/93, The University of Queensland.

Mee, D.J. (**2002**b). "Dynamic calibration of force balances". Department of Mechanical Engineering Research Report 2002/6, The University of Queensland.

Menter, F.R. (**1994**). "Two-equation eddy-viscosity turbulence models for engineering applications". *AIAA Journal*, **vol. 32, no. 8**, pp. 1598–1605.

Moore, J.G. and **Moore, J.** (**1999**). "Realizability in two-equation turbulence models". In *30th AIAA Fluid Dynamics Conference*. AIAA-99-2779, American Institute of Aeronautics and Astronautics Inc., Norfolk, VA.

O'Byrne, S. and **Wittig, S.** (**2008**). "Measurement of hypersonic inlet flow using diode laser absorption spectroscopy". In *Proceedings of the 8th Australian Space Science Conference*, (pp. 68–75). National Space Society of Australia Ltd, Canberra, Australia.

Oldenborg, R.; **Chinitz, W.**; **Friedman, M.**; **Jaffe, R.**; **Jachimowski, C.**; **Rabinowitz, M.** and **Schott, G.** (**1990**). "Hypersonic combustion kinetics, Status Report of the Rate Constant Committee". Technical Memorandum NASP TM-1107, NASP High Speed Propulsion Technology Team.

Olsen, G.C. and **Nowak, R.J.** (**1995**). "Hydrogen film cooling with incident and swept-shock interactions in a Mach 6.4 nitrogen free stream". Technical Memorandum NASA TM 4603, NASA Langley Research Center.

Panaras, A.G. (**1992**). "Numerical investigation of the high-speed conical flow past a sharp fin". *Journal of Fluid Mechanics*, **vol. 236**, pp. 607–633.

Parent, B. and **Sislian, J.P.** (**2004**). "Validation of Wilcox k-ω model for flows characteristic to hypersonic airbreathing propulsion". *AIAA Journal*, **vol. 42, no. 2**, pp. 261–270.

Parthasarathy, K. and **Zakkay, V.** (**1970**). "An experimental investigation of turbulent slot injection at Mach 6". *AIAA Journal*, **vol. 8, no. 7**, pp. 1302–1307.

Paull, A.; **Stalker, R.** and **Mee, D.** (**1995**). "Experiments on supersonic combustion ramjet propulsion in a shock tunnel". *Journal of Fluid Mechanics*, **vol. 296**, pp. 159–183.

Peng, W. and **Jiang, P.X.** (**2009**). "Influence of shock waves on supersonic film cooling". *Journal of Spacecraft and Rockets*, **vol. 46, no. 1**, pp. 67–73.

Perepechko, L.N. (**2003**). "Numerical study of the effect of methane combustion on heat and mass transfer and friction in the boundary layer". *Combustion, Explosion, and Shock Waves*, **vol. 39, no. 3**, pp. 255–260.

Pergament, H.S. (**1963**). "Theoretical Analysis of Non-Equilibrium Hydrogen-Air Reactions in Flow Systems". In *AIAA-ASME Hypersonic Ramjet Conference*, vol. No. 63113.

Pope, S.B. (**1978**). "An explanation of the turbulent round-jet/plane-jet anomaly". *AIAA Journal*, **vol. 16, no. 3**, pp. 279–281.

Powell, O.A.; **Edwards, J.T.**; **Norris, R.B.**; **Numbers, K.E.** and **Pearce, J.A.** (**2001**). "Development of hydocarbon-fueled scramjet engines: The Hypersonics Technology (HyTech) Program". *Journal of Propulsion and Power*, **vol. 17, no. 6**, pp. 1170–1176.

Pudsey, A.S. and **Boyce, R.R.** (**2010**). "Numerical investigation of transverse jets through multiport injector arrays in supersonic crossflow". *Journal of Propulsion and Power*, **vol. 26, no. 6**, pp. 1225–1236.

Razzaqi, S.A. (**2011**). *Oxygen enrichment in a hydrogen fuelled scramjet*. PhD thesis, The University of Queensland, Queensland, Australia.

Riggins, D.W. and **Vitt, P.H.** (**1995**). "Vortex generation and mixing in three-dimensional supersonic combustors". *Journal of Propulsion and Power*, **vol. 11, no. 3**, pp. 419–426.

Robinson, M.J.; **Rowan, S.A.** and **Odam, J.S.** (**2003**). *T4 free piston shock tunnel training program*. The University of Queensland, Queensland, Australia.

Rowan, S.A. (**2003**). *Viscous drag reduction in a scramjet combustor*. PhD thesis, The University of Queensland, Queensland, Australia.

Rowan, S.A. and **Paull, A.** (**2006**). "Performance of a scramjet combustor with combined normal and tangential fuel injection". *Journal of Propulsion and Power*, **vol. 22, no. 6**, pp. 1334–1338.

Roy, C.J. and **Blottner, F.G.** (**2003**). "Methodology for turbulence model validation: Application to hypersonic flows". *Journal of Spacecraft and Rockets*, **vol. 40, no. 3**, pp. 313–325.

Sanderson, S. and **Simmons, J.** (**1991**). "Drag balance for hypervelocity impulse facilities". *AIAA Journal*, **vol. 29, no. 12**, pp. 2185–2191.

Schetz, J. and **Gilreath, H.** (**1967**). "Tangential slot injection in supersonic flow". *AIAA Journal*, **vol. 5, no. 12**, pp. 2149–2154.

Schloegel, F. and **Boyce, R.R.** (**2009**). "CFD analysis of radical farming concept scramjet engine". In *16th AIAA/DLR/DGLR International Space Planes and Hypersonic Systems and Technologies Conference*. AIAA 2009-7416, American Institute of Aeronautics and Astronautics Inc., Bremen, Germany.

Settles, G.S. and **Dodson, L.J.** (**1991**). "Hypersonic shock/boundary-layer interaction database". Contractor Report NASA CR-177577, NASA.

Skinner, K. (**1994**). *Mass spectrometry in shock tunnel experiments of hypersonic combustion*. PhD thesis, The University of Queensland, Queensland, Australia.

Smart, M.K. (**1999**). "Design of three-dimensional hypersonic inlets with rectangular-to-elliptical shape transition". *Journal of Propulsion and Power*, **vol. 15, no. 3**, pp. 408–416.

Smart, M.K. (**2001**). "Experimental testing of a hypersonic inlet with rectangular-to-elliptical shape transition". *Journal of Propulsion and Power*, **vol. 17, no. 2**, pp. 276–283.

Smart, M.K. (**2012**). "How Much Compression Should a Scramjet Inlet Do". *AIAA Journal*, **vol. 50, no. 3**, pp. 610–619.

Smart, M.K. and **Ruf, E.G.** (**2006**). "Free-jet testing of a REST scramjet at off-design conditions". In *Collection of Technical Papers - 25th AIAA Aerodynamic Measurement Technology and Ground Testing Conference*, (pp. 190–201). AIAA 2006-2955, American Institute of Aeronautics and Astronautics Inc., San Francisco, California, USA.

Smart, M.K. and **Suraweera, M.V.** (**2009**). "HIFiRE 7 - Development of a 3-D scramjet for flight testing". In *16th AIAA/DLR/DGLR International Space Planes and Hypersonic*

Systems and Technologies Conference. AIAA 2009-7259, American Institute of Aeronautics and Astronautics Inc., Bremen, Germany.

Smart, M.K. and **Trexler, C.A.** (**2004**). "Mach 4 performance of hypersonic inlet with rectangular-to-elliptical shape transition". *Journal of Propulsion and Power*, **vol. 20, no. 2**, pp. 288–293.

Smart, M.K. and **White, J.A.** (**2002**). "Computational investigation of the performance and back-pressure limits of a hypersonic inlet". In *40th AIAA Aerospace Sciences Meeting and Exhibit*. AIAA 2002-0508, American Institute of Aeronautics and Astronautics Inc., Reno, Nevada, USA.

Smith, A.L. and **Mee, D.J.** (**1996**). "Drag measurements in a hypervelocity expansion tube". *Shock Waves*, **vol. 6**, pp. 161–166.

Smith, A.L.; **Mee, D.J.**; **Daniel, W.J.T.** and **Shimoda, T.** (**2001**). "Design, modelling and analysis of a six component force balance for hypervelocity wind tunnel testing". *Computers and Structures*, **vol. 79**, pp. 1077–1088.

Smith, A.M.O. and **Cebeci, T.** (**1967**). "Numerical solution of the turbulent boundary -layer equations". Division Report DAC 33735, Douglas Aircraft Company.

Smith, C.E. (**1966**). "The starting process in a hypersonic nozzle". *Journal of Fluid Mechanics*, **vol. 24, no. 4**, pp. 625–640.

Spalding, D.B. and **Chi, S.W.** (**1964**). "The drag of a compressible turbulent boundary layer on a smooth flat plate with and without heat transfer". *Journal of Fluid Mechanics*, **vol. 18**, pp. 117–143.

Squire, L.C. (**2000**). "The accuracy of flat plate, turbulent skin friction at supersonic speeds". *The Aeronautical Journal*, **vol. 104, no. 1036**, pp. 257–263.

Stalker, R.J. (**1966**). "The free-piston shock tube". *The Aeronautical Quarterly*, **vol. 17**, pp. 351–369.

Stalker, R.J. (**1967**). "A study of the free-piston shock tunnel". *AIAA Journal*, **vol. 5, no. 12**, pp. 2160–2165.

Stalker, R.J. (**1989**). "Recent developments with free piston drivers". In *Seventeenth International Symposium on Shock Waves and Shock Tube*, vol. AIP Conference Proceedings 208, (pp. 96 – 105). American Institute of Physics, Bethlehem, PA.

Stalker, R.J. (**2005**). "Control of hypersonic turbulent skin friction by boundary-layer combustion of hydrogen". *Journal of Spacecraft and Rockets*, **vol. 42, no. 4**, pp. 577–587.

Stalker, R.J. (**2006**). "Modern developments in hypersonic wind tunnels". *The Aeronautical Journal*, **vol. 110, no. 1103**, pp. 21–39.

Stalker, R.J. and **Morgan, R.G.** (**1988**). "The University of Queensland free piston shock tunnel T4 - Initial operation and preliminary calibration". In *4th National Space Engineering Symposium*. National Panel on Space Engineering, the Joint College Board of the Institution of Engineers, Australia., Adelaide, Australia.

Stalker, R.J.; **Paull, A.**; **Mee, D.J.**; **Morgan, R.G.** and **Jacobs, P.A.** (**2005**). "Scramjets and shock tunnels - The Queensland experience". *Progress in Aerospace Sciences*, **vol. 41, no. 6**, pp. 471–513.

Stephensen, D. (**2002**). *Controlling skin friction by boundary layer combustion*. Bachelor of engineering (Honours) thesis, The University of Queensland, Queensland, Australia.

Stollery, J.L. (**1976**). "Supersonic turbulent boundary layers: Some comparisons between experiment and a simple theory". *Aeronautical Quarterly*, **vol. 28**, pp. 87–98.

Stollery, J.L. and **Coleman, G.T.** (**1975**). "A correlation between pressure and heat transfer distributions at supersonic and hypersonic speeds". *Aeronautical Quarterly*, **vol. 26**, pp. 304–312.

Suraweera, M.V. (**2005**). "Skin friction reduction in hypersonic turbulent flow by boundary layer combustion". In *43rd AIAA Aerospace Sciences Meeting and Exhibit*. AIAA 2005-613, American Institute of Aeronautics and Astronautics Inc., Reno, Nevada, USA.

Suraweera, M.V. (**2006**). *Reduction of skin friction drag in hypersonic flow by boundary layer*. PhD thesis, The University of Queensland, Queensland, Australia.

Suraweera, M.V. and **Smart, M.K.** (**2009**). "Shock-tunnel experiments with a Mach 12 Rectangular-to-Elliptical Shape-Transition scramjet at off-design conditions". *Journal of Propulsion and Power*, **vol. 25, no. 3**, pp. 555–564.

Swithenbank, J. (**1964**). "Experimental investigation of hypersonic ramjets". In *Proceedings of the International Council of the Aeronautical Sciences, Third Congress, Stockholm, 1962*, (pp. 951 – 977). Spartan, New York, USA.

Swithenbank, J. and **Chigier, N.A.** (**1969**). "Vortex mixing for supersonic combustion". In *12th International Symposium on Combustion*, (pp. 1153–1162). The Combustion Institute.

Takita, K. and **Masuya, G.** (**2000**). "Effects of combustion and shock impingement on supersonic film cooling by hydrogen". *AIAA Journal*, **vol. 38, no. 10**, pp. 1899–1906.

Tanimizu, K. (**2008**). *Nozzle optimization study and measurements for a quasi-axisymmetric scramjet model*. PhD thesis, The University of Queensland, Queensland, Australia.

Tanimizu, K.; **Mee, D.J.**; **Stalker, R.J.** and **Jacobs, P.A.** (**2009**). "Drag force on quasi-axisymmetric scramjets at various flight Mach numbers: theory and experiment". *Shock Waves*, **vol. 19, no. 2**, pp. 83–93.

Tanno, H.; **Paull, A.** and **Stalker, R.J.** (**2001**). "Skin-friction measurements in a supersonic combustor with crossflow fuel injection". *Journal of Propulsion and Power*, **vol. 17, no. 6**, pp. 1333–1338.

Thivet, F. (**2002**). "Lessons learned from RANS simulations of shock-wave/boundary-layer interactions". In *40th AIAA Aerospace Sciences Meeting and Exhibit*. AIAA-2002-0583, American Institute of Aeronautics and Astronautics Inc., Reno, Nevada.

Thivet, F.; **Knight, D.D.**; **Zheltovodov, A.A.** and **Maksimov, A.I.** (**2001**). "Insights in turbulence modeling for crossing-shock-wave/boundary-layer interactions". *AIAA Journal*, **vol. 39, no. 6**, pp. 985–995.

Turner, J.C. (**2010**). *An experimental investigation of inlet fuel injection in a three-dimensional scramjet engine*. PhD thesis, The University of Queensland, Queensland, Australia.

Tuttle, S.L.; **Mee, D.J.** and **Simmons, J.M.** (**1995**). "Drag measurements at Mach 5 using a stress wave force balance". *Experiments in Fluids*, **vol. 19, no. 5**, pp. 336–341.

Van Driest, E.R. (**1956**). "The problem of aerodynamic heating". *Journal of the Aeronautical Sciences*, **vol. 15, no. 10**, pp. 26–41.

Van Staden, P.A. (**2011**). *Scramjet drag reduction from porous combustion chamber wall fuel injection*. Confirmation of candidature report, The University of Queensland, Queensland, Australia.

Ventura, C.; **Sauret, E.**; **Jacobs, P.A.**; **Petrie-Repar, P.**; **Gollan, R.G.** and **van der Laan, P.** (**2010**). "Adaption and use of a compressible flow code for turbomachinery design". In *5th European Conference on Computational Fluid Dynamics ECCOMAS CFD*

2010. European Community on Computational Methods in Applied Sciences, Lisbon, Portugal.

Viti, V.; **Neel, R.** and **Schetz, J.A.** (**2009**). "Detailed flow physics of the supersonic jet interaction flow field". *Physics of Fluids*, **vol. 21, no. 4**, pp. 046101–1 – 046101–16.

Volchkov, .P.; **Terekhov, V.V.** and **Terekhov, V.I.** (**2002**). "Boundary-Layer Structure with Hydrogen Combustion with Different Injection Intensities". *Combustion, Explosion, and Shock Waves*, **vol. 38, no. 3**, pp. 269–277.

Wada, Y. and **Liou, M.S.** (**1994**). "A flux splitting scheme with high-resolution and robustness for discontinuities". In *32nd Aerospace Sciences Meeting and Exhibit*. AIAA-94-0083, American Institute of Aeronautics and Astronautics Inc., Reno, Nevada. Also as NASA-TM-106452.

Weber, R.J. and **MacKay, J.S.** (**1958**). "An analysis of ramjet engines using supersonic combustion". Technical note NACA TN 4386, National Advisory Committee for Aeronautics, Washington.

Wheatley, V.; **Chiu, H.S.**; **Jacobs, P.A.**; **Macrossan, M.N.**; **Mee, D.J.** and **Morgan, R.G.** (**2004**). "Rarefied, superorbital flows in an expansion tube". *International Journal of Numerical Methods for Heat & Fluid Flow*, **vol. 14, no. 4**, pp. 512–537.

Wheatley, V. and **Jacobs, P.A.** (**2010**). "Fuel injection via rectangular cross-section injectors for mixing enhancement in scramjets". In *17th Australasian Fluid Mechanics Conference*.

White, F.M. (**2006**). *Viscous Fluid Flow*. McGraw-Hill, New York, USA, 3rd ed.

White, F.M. (**2008**). *Fluid Mechanics*. McGraw-Hill, New York, USA, 6th ed.

White, J.A. and **Morrison, J.H.** (**1999**). "A pseudo-temporal multi-grid relaxation scheme for solving the parabolized Navier-Stokes equations". In *14th AIAA Computational Fluid Dynamics Conference*. AIAA Paper 99-3360, American Institute of Aeronautics and Astronautics Inc.

Wilcox, D.C. (**1988**). "Reassessment of the scale-determining equation for advanced turbulence models". *AIAA Journal*, **vol. 26, no. 11**, pp. 1299–1310.

Wilcox, D.C. (**1998**). *Turbulence modelling for CFD*. DCW Industries, Inc, California, USA, 2nd ed.

Wilcox, D.C. (**2006**). *Turbulence modelling for CFD*. DCW Industries, Inc, California, USA, 3rd ed.

Zang, T.A. and **Bushnell, D.M.** (**1984**). "Numerical computations of turbulence amplification in shock-wave interactions". *AIAA Journal*, **vol. 22, no. 1**, pp. 13–21.

Zeldovich, Y.B. (**1951**). "On the theory of combustion of initially unmixed gases". Technical Memorandum NACA TM 1296, National Advisory Committee for Aeronautics (NACA).

Appendix A

Justification for the use of a lower Pitot-to-nozzle-supply pressure ratio for nitrogen tests

Figure A.1 shows a plot of the Pitot-to-nozzle-supply pressure ratio for the tests conducted with the T4 Mach 6 nozzle by Bakos (1994) in the T4 impulse facility. These results, which are for tests at a stagnation enthalpy of 14.2 MJ/kg, are referenced from the report by Mee (1993)[1]. The results from the current experimental campaign for tests at a stagnation enthalpy of 4.8 MJ/kg are also included in Figure A.1.

The results from both the tests of Bakos and the current tests show that the average Pitot-to-nozzle-supply pressure ratios for the shots with nitrogen test gas are about 0.92 times of those for the shots with air test gas. It is clear that the main cause of this difference in the Pitot-to-nozzle-supply pressure ratio comes about because of the difference in the gas properties of nitrogen and air. The differences are attributed to the differences in expansion through the nozzle for the different gases. It is suggested that CFD simulations of the nozzle-supply region and the nozzle in the T4 impulse facility be conducted in conjunction with a more detailed experimental survey of the nozzle to further investigate this. The nozzle calibration tests used to obtain the ratio of Pitot-to-nozzle-supply pressures used in processing the data were only performed with a test gas of air. Based on these results, all tests for the current campaign conducted with nitrogen test gas were processed using a value of Pitot-to-nozzle-supply pressure ratio that was 0.92 times that of the tests conducted with air as the test gas.

[1]Note that while the values of Pitot pressure from Bakos' tests have been normalised using only one nozzle-supply pressure measurement in Mee's report, the values shown in Figure A.1 have been normalised using the averaged value of two nozzle-supply pressure measurements

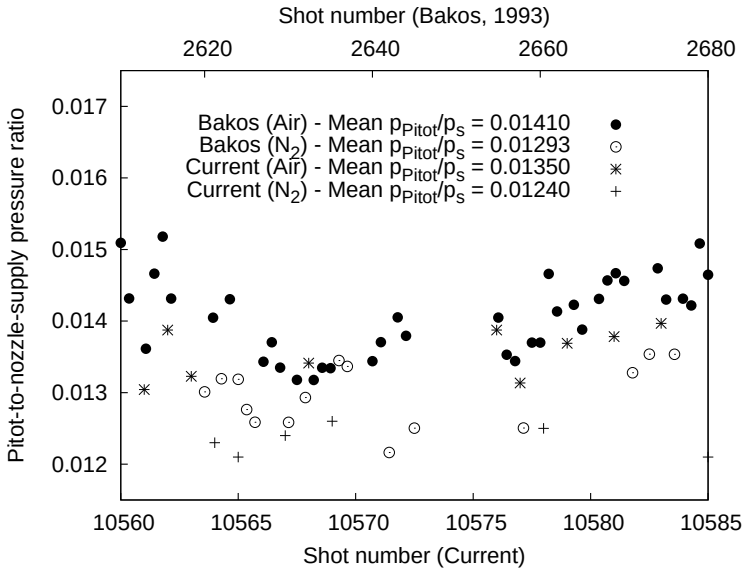

Figure A.1: A comparison of the Pitot-to-nozzle-supply pressure ratio for tests with air as the test gas and tests with nitrogen as the test gas.

Appendix B

Uncertainty Analysis

B.1 Uncertainties in the test conditions

The analysis of the uncertainties in the test conditions for the current test campaign is presented in this appendix. The uncertainty analysis was conducted following the method that is reported in Mee (1993).

For a quantity F, which is derived from a combination of measured quantities $\psi_1, .., \psi_i, .., \psi_n$ such that $F = f(\psi_1, .., \psi_i, .., \psi_n)$, the absolute uncertainty can be defined as

$$\delta F = \sqrt{\sum_{i=1}^{n} (\delta F)_i^2} \tag{B.1}$$

provided that the individual measured quantities are independent and normally distributed. The $(\delta F)_i$ term in Equation B.1 is the component of uncertainty in F due to the uncertainty in ψ_i which can be defined as

$$(\delta F)_i = \left(\frac{\partial F}{\partial \psi_i} \right) \delta \psi_i \tag{B.2}$$

where $\frac{\partial F}{\partial \psi_i}$ is the sensitivity of the derived quantity F to changes in the measured quantity ψ_i.

The relative uncertainty in the derived quantity F can then be defined as

$$X_F = \sqrt{\sum_{i=1}^{n} (X_F)_i^2} \tag{B.3}$$

where

$$(X_F)_i = \left(\frac{\partial X_F}{\partial X_{\psi_i}} \right) X_{\psi_i} \quad , \quad X_F = \frac{\delta F}{F} \quad , \quad X_{\psi_i} = \frac{\delta \psi_i}{\psi_i} \tag{B.4}$$

For the tests conducted in the T4 impulse facility, the derived quantities of interest include the nozzle-supply temperature T_s, nozzle-supply stagnation enthalpy H_s, the nozzle-exit static temperature T_∞, static pressure p_∞, static density ρ_∞, Mach number M_∞, velocity u_∞ and the ratio of specific heats γ_∞. The measured quantities include the shock tube fill pressure $p_{\text{fill,ST}}$, shock tube fill temperature $T_{\text{fill,ST}}$, incident shock speed u_{shock}, nozzle-supply pressure p_s, and nozzle-exit Pitot pressure p_{Pitot}.

To compute the $(X_F)_i$ in Equation B.4, the relative sensitivity $\frac{\partial X_F}{\partial X_{\psi_i}}$ and the relative uncertainty in the measured quantity δX_{ψ_i} need to be known. The relative sensitivity can be determined by

1. Perturbing ψ_i to get a positively perturbed value ψ_i^+ and a negatively perturbed value ψ_i^-,

2. Running ESTCj and NENZF with ψ_i, ψ_i^+ and ψ_i^- as the inputs to get F_{ψ_i}, $F_{\psi_i^+}$ and $F_{\psi_i^-}$, and

3. Computing the relative sensitivity by

$$\frac{\partial X_F}{\partial X_{\psi_i}} = \frac{\frac{F_{\psi_i^+} - F_{\psi_i^-}}{F_{\psi_i}}}{\frac{\psi_i^+ - \psi_i^-}{\psi_i}} \tag{B.5}$$

The relative sensitivities for each test condition listed in Table 3.1 are computed and shown in Table B.1. The values for the X_{ψ_i} term in Equation B.4 are taken to be similar to those stated in Kirchhartz (2010), and are listed in Table B.2. Values from both Tables B.2 and B.1 are then used with Equations B.3 and B.4 to compute the relative uncertainties in the derived flow parameters for each test condition. These uncertainties are shown in Table B.3.

B.2 Uncertainties in the fuelling conditions

The uncertainties in the fuelling conditions can also be computed using Equations B.3 and B.4. Since the correlations for the derived quantities of interest (the discharge coefficient α, mass flow rate of hydrogen $\dot{m}_{H_2}$, mass flow rate of oxygen $\dot{m}_{O_2}$ and equivalence ratio ϕ) are in the form $F = constant\ \psi_1^{m_1}\ \psi_2^{m_2}\ \psi_i^{m_i} .... \psi_n^{m_n}$, the relative sensitivity $\frac{\partial F}{\partial \psi_i}$ can be obtained directly by analytically differentiating F. This allows the step,

which involves the perturbation method described in Section B.1, to be skipped. Equation B.4 now becomes

$$(X_F)_i = \left(\frac{\partial X_F}{\partial X_{\psi_i}}\right) X_{\psi_i} = m_i \frac{\delta\psi_i}{\psi_i} \tag{B.6}$$

Equation B.3 can then be re-written as

$$X_F = \sqrt{\sum_{i=1}^{n} \left(m_i \frac{\delta\psi_i}{\psi_i}\right)^2} \tag{B.7}$$

The values for the relative uncertainties $\frac{\delta\psi_i}{\psi_i}$ are taken to be similar to those stated by Turner (2010). The only exception is that of the uncertainty in the volume of the Ludwieg tube, where the more conservative estimate given by Razzaqi (2011) is used. These uncertainties are listed in Table B.4. The resulting uncertainties in the fuelling conditions, which are computed with Equation B.7 and the values in Table B.4, are listed in Table B.5.

Table B.1: Relative sensitivities of the derived quantities F to perturbations in the measured quantities ψ_i.

Quantity		Condition			
	H_s	3.7	4.8	8.0	4.8
	M_∞	6.3	6.2	5.7	7.4
F	ψ_i	$\partial X_F / \partial X_{\psi_i}$			
H_s	$p_{\text{fill,ST}}$	-0.249	-0.229	-0.203	-0.231
	$T_{\text{fill,ST}}$	0.257	0.238	0.206	0.239
	u_{shock}	1.431	1.470	1.535	1.462
	p_s	0.248	0.233	0.204	0.233
	p_{Pitot}	0.000	0.000	0.000	0.000
T_s	$p_{\text{fill,ST}}$	-0.182	-0.154	-0.126	-0.156
	$T_{\text{fill,ST}}$	0.246	0.203	0.152	0.204
	u_{shock}	1.041	0.988	0.958	0.987
	p_s	0.185	0.169	0.164	0.169
	p_{Pitot}	0.000	0.000	0.000	0.000
T_∞	$p_{\text{fill,ST}}$	-0.307	-0.177	-0.235	0.018
	$T_{\text{fill,ST}}$	0.417	0.323	0.280	0.560
	u_{shock}	1.746	1.942	1.803	2.229
	p_s	0.301	0.423	0.218	0.274
	p_{Pitot}	0.402	0.388	0.337	0.409
p_∞	$p_{\text{fill,ST}}$	-0.094	0.067	-0.072	0.340
	$T_{\text{fill,ST}}$	0.130	0.010	0.074	0.207
	u_{shock}	0.493	0.510	0.598	0.639
	p_s	1.080	1.199	0.999	0.967
	p_{Pitot}	1.429	1.408	1.370	1.432
ρ_∞	$p_{\text{fill,ST}}$	0.212	0.240	0.171	0.310
	$T_{\text{fill,ST}}$	-0.289	-0.309	-0.221	-0.350
	u_{shock}	-1.254	-1.447	-1.267	-1.602
	p_s	0.779	0.778	0.790	0.693
	p_{Pitot}	1.025	1.021	1.030	1.018
u_∞	$p_{\text{fill,ST}}$	-0.110	-0.120	-0.083	-0.152
	$T_{\text{fill,ST}}$	0.149	0.153	0.100	0.158
	u_{shock}	0.630	0.711	0.627	0.784
	p_s	0.110	0.111	0.099	0.140
	p_{Pitot}	-0.026	-0.027	-0.034	-0.020
M_∞	$p_{\text{fill,ST}}$	0.038	-0.039	0.032	-0.164
	$T_{\text{fill,ST}}$	-0.064	0.000	-0.039	-0.110
	u_{shock}	-0.220	-0.223	-0.250	-0.307
	p_s	-0.038	-0.090	0.000	0.008
	p_{Pitot}	-0.221	-0.211	-0.192	-0.219

Table B.2: Relative uncertainties in the measured quantities X_{ψ_i}.

Quantity		Relative uncertainty (%)
Shock tube fill pressure	$p_{\text{fill,ST}}$	3.25
Shock tube fill temperature	$T_{\text{fill,ST}}$	2
Incident shock speed	u_{shock}	5
Nozzle-supply pressure	p_s	3
Pitot pressure	p_{Pitot}	8.8

Table B.3: Relative uncertainties in the test conditions.

	Condition				
	H_s	3.7	4.8	8.0	4.8
Quantity	M_∞	6.3	6.2	5.7	7.4
H_s		7.2%	7.4%	7.7%	7.4%
T_s		5.3%	5.0%	4.8%	5.0%
T_∞		9.6%	10.4%	9.6%	11.8%
p_∞		13.2%	13.2%	12.8%	13.4%
ρ_∞		11.3%	11.8%	11.3%	12.3%
u_∞		3.2%	3.6%	3.2%	4.0%
M_∞		2.2%	2.2%	2.1%	2.5%

Table B.4: Relative uncertainties in the measured quantities X_{ψ_i}.

Quantity		Relative uncertainty (%)
Initial fill pressure in the Ludwieg tube	$p_{LT,i}$	2
Initial temperature in the Ludwieg tube	$T_{LT,i}$	2
Final pressure in the Ludwieg tube	$p_{LT,f}$	2
Volume of the Ludwieg tube	V_{LT}	3
Pressure in the plenum chamber	p_{plenum}	3

Table B.5: Relative uncertainties in the fuelling conditions.

Quantity		Relative uncertainty (%)
Discharge coefficient	α	6.3
Mass flow rate of hydrogen	$\dot{m}_{\text{H}_2}$	3.8
Mass flow rate of oxygen	$\dot{m}_{\text{O}_2}$	11.9
Equivalence ratio	ϕ	13.7

Appendix C

Estimation of flight-equivalent conditions

The flight-equivalent conditions for each test condition are approximated using the following steps.

1. Assume that the REST inlet is attached to a vehicle that has a forebody with a wedge angle of 10°.

2. Specify an arbitrary flight altitude h_f and geometrical scaling factor η for which the test model scales with the actual flight model.

3. Use the 1976 U.S. Standard Atmosphere tables (Heiser and Pratt, 1994) to obtain the freestream static pressure $p_{\infty,f}$ and temperature $T_{\infty,f}$ at the specified flight altitude.

4. For the stagnation enthalpy at which the ground tests are conducted, compute the flight Mach number for the specified flight altitude.

$$u_{\infty,f} = \sqrt{2(H_{s,\text{ground}} - \frac{\gamma_{\infty,f}\, R_{\infty,f}}{\gamma_{\infty,f} - 1}\, T_{\infty,f})} \tag{C.1}$$

$$M_{\infty,f} = \frac{u_{\infty,f}}{\sqrt{\gamma_{\infty,f}\, R_{\infty,f}\, T_{\infty,f}}} \tag{C.2}$$

5. For the specified forebody wedge angle of 10°, use standard oblique shock relations to compute the pressure ratio $\frac{p_{\infty,f}}{p_{1,f}}$ and and the temperature ratio $\frac{T_{\infty,f}}{T_{1,f}}$, where $p_{1,f}$ and $T_{1,f}$ are the static pressure and static temperature at the entrance of the inlet in flight.

6. Compute $T_{1,f}$ from the temperature ratio $\frac{T_{\infty,f}}{T_{1,f}}$ and $T_{\infty,f}$.

7. If $T_{1,f}$ approximately matches the static temperature at the entrance of the inlet of the test model $T_{1,\text{ground},100\%}$, then proceed to step 8. Otherwise, specify another scaling factor for the test model and repeat step 6 until $T_{1,f}$ matches $T_{1,ground,100\%}$.

8. Compute $p_{1,f}$ from the pressure ratio $\frac{p_{\infty,f}}{p_{1,f}}$ and $p_{\infty,f}$.

9. With the use of p-L scaling[1], compute the static pressure at the entrance of the inlet for a 100% scale of the test model $p_{1,\text{ground},100\%}$ from that of the static pressure at the entrance of the inlet of the test model $p_{1,\text{ground,scaled}}$.

$$\begin{aligned} p_{1,\text{ground},100\%}\ L_{\text{char,ground},100\%} &= p_{1,\text{ground,scaled}}\ L_{\text{char,ground,scaled}} \\ \Rightarrow \qquad p_{1,\text{ground},100\%} &= \frac{L_{\text{char,ground,scaled}}}{L_{\text{char,ground},100\%}}\ p_{1,\text{ground,scaled}} \\ \Rightarrow \qquad p_{1,\text{ground},100\%} &= \eta\ p_{1,\text{ground,scaled}} \end{aligned} \tag{C.3}$$

10. If $p_{1,\text{ground},100\%}$ approximately matches $p_{1,f}$, then the flight Mach number and altitude can be used to work out the flight dynamic pressure.

$$q_{\infty,f} = \frac{\gamma_{\infty,f}\ p_{\infty,f}\ M_{\infty,f}^2}{2} \tag{C.4}$$

Otherwise, specify another flight altitude and repeat steps 3 to 10 until $p_{1,ground,100\%}$ matches $p_{1,f}$.

11. Repeat steps 1 to 11 for the other test conditions with different stagnation enthalpies.

[1] Hornung (1988) postulates that the product of density and characteristic length should remain constant when the characteristic length changes. The ρ-L scaling concept proposed by Hornung (1988) is also shown by Stalker et al. (2005) to be applicable to hydrogen-air flows with supersonic combustion, such as those present in the current experiments. This scaling concept is used to relate the flowfield in the small-scale model in the present experiments to that in larger-scale flight-size models. By assuming that the static temperature remains constant during the scaling process, the use of p-L scaling would then be similar to that of ρ-L scaling.

Appendix D

Detailed shot summary

The details of the operating, nozzle-supply, nozzle-exit and fuelling conditions for each shot conducted in the T4 impulse facility for this test campaign is shown in Table D.1. In addition, the chemical composition in the freestream flow at the exit of the nozzle is shown in Table D.2. The notation used in Table D.1 is as follows.

Res.	Reservoir
C.T.	Compression tube
S.T.	Shock tube
p_{fill}	Static pressure of the gas in the reservoir, compression tube or shock tube
T_{fill}	Static temperature of the test gas in the shock tube
Argon frac.	Volume fraction of argon in driver gas in the compression tube
Diaph.	Thickness of the primary diaphragm
u_{shock}	Shock speed
p_s	Nozzle-supply pressure
T_s	Nozzle-supply temperature
H_s	Nozzle-supply stagnation enthalpy
p_∞	Freestream static pressure at the exit of the nozzle
T_∞	Freestream static temperature at the exit of the nozzle
ρ_∞	Freestream static density at the exit of the nozzle
u_∞	Freestream velocity at the exit of the nozzle
M_∞	Freestream Mach number at the exit of the nozzle
Re_∞	Freestream unit Reynolds number at the exit of the nozzle
γ_∞	Freestream specific heats ratio at the exit of the nozzle
$\dot{m}_{\text{capture}}$	Mass flow rate entering the REST inlet
p_{plenum}	Static pressure in the fuel plenum chamber
$\dot{m}_{\text{H}_2}$	Mass flow rate of hydrogen
ϕ	Equivalence ratio

Table D.1: Nozzle-supply, nozzle-exit and fuelling conditions for each shot.

	Res.	C.T.		S.T.					Nozzle-supply conditions			Nozzle-exit conditions								Fuelling conditions		
Shot	p_{fill}	p_{fill}	Argon	p_{fill}	T_{fill}	Test	Diaph.	u_{shock}	p_s	T_s	H_s	p_∞	T_∞	ρ_∞	U_∞	M_∞	Re_∞	γ_∞	$\dot{m}_{\text{capture}}$	p_{plenum}	$\dot{m}_{\text{H}_2}$	ϕ
-	MPa	kPa	frac.	kPa	K	gas	mm	m/s	MPa	K	MJ/kg	kPa	K	kg/m^3	m/s	-	1/m	-	kg/s	kPa	kg/s	-
10558	4.65	67	60	140	300	Air	5	2208	32.98	3726	4.595	8.866	529.7	0.0583	2862	6.24	6.003×10^6	1.384	0.4178	0.000	0.00000	0.000
10559	4.80	67	51	130	300	Air	5	2434	37.07	4223	5.543	10.58	674.4	0.0547	3127	6.08	5.251×10^6	1.368	0.4283	0.000	0.00000	0.000
10560	4.80	67	55	150	300	Air	5	2265	35.36	3825	4.771	9.671	560.2	0.0601	2917	6.19	6.076×10^6	1.381	0.4391	0.000	0.00000	0.000
10561	4.80	67	55	150	300	Air	5	2276	34.98	3837	4.795	9.579	563.3	0.0592	2924	6.19	5.977×10^6	1.381	0.4334	0.000	0.00000	0.000
10562	4.85	67	55	150	300	Air	5	2276	35.72	3851	4.819	9.759	565.4	0.0601	2932	6.20	6.069×10^6	1.381	0.4413	0.000	0.00000	0.000
10563	4.85	67	55	150	300	Air	5	2253	36.03	3817	4.756	9.875	559.4	0.0615	2912	6.18	6.213×10^6	1.381	0.4483	409.7	0.01207	0.929
10564	4.85	67	55	150	300	N_2	5	2270	36.66	4213	4.928	8.681	553.3	0.0529	3038	6.37	5.821×10^6	1.387	0.4022	400.2	0.01190	1.020
10565	4.85	67	55	150	300	N_2	5	2253	35.11	4133	4.820	8.266	539.4	0.0516	3008	6.38	5.717×10^6	1.388	0.3889	424.3	0.01251	1.109
10566	4.85	67	55	150	300	N_2	5	2259	35.81	4164	4.863	8.450	544.9	0.0522	3020	6.38	5.768×10^6	1.388	0.3951	0.000	0.00000	0.000
10567	4.85	67	55	150	300	N_2	5	2247	35.36	4126	4.811	8.326	538.3	0.0521	3006	6.38	5.775×10^6	1.388	0.3922	418.1	0.01232	1.083
10568	4.85	67	55	150	300	Air	5	2236	34.98	3769	4.670	9.500	544.7	0.0608	2886	6.21	6.197×10^6	1.383	0.4391	436.4	0.01287	1.010
10569	4.85	67	55	150	300	N_2	5	2236	34.36	4075	4.742	8.067	529.5	0.0513	2986	6.39	5.712×10^6	1.389	0.3838	0.000	0.00000	0.000
10570	4.85	67	100	200	300	Air	5	2006	35.49	3223	3.737	9.496	455.4	0.0727	2668	6.26	7.739×10^6	1.400	0.4854	435.7	0.01282	0.911
10571	4.85	67	35	80	300	Air	5	2909	37.57	5335	8.074	12.53	1094	0.0397	3681	5.69	3.332×10^6	1.334	0.3657	439.1	0.01294	1.220
10572	4.85	67	35	80	300	Air	5	2890	37.47	5299	7.988	12.46	1080	0.0399	3665	5.70	3.359×10^6	1.335	0.3666	0.000	0.00000	0.000
10573	4.85	67	35	80	300	N_2	5	2949	38.52	6489	8.478	10.16	1025	0.0334	3903	6.11	3.210×10^6	1.341	0.3261	433.3	0.01277	1.350
10574	4.75	67	100	200	300	N_2	5	1992	36.37	3364	3.791	8.090	410.0	0.0665	2701	6.55	7.986×10^6	1.397	0.4497	410.7	0.01209	0.927
10575	4.75	67	100	200	300	Air	5	1988	35.27	3189	3.683	9.341	446.7	0.0728	2651	6.28	7.805×10^6	1.400	0.4836	0.000	0.00000	0.000
10576	4.85	67	55	150	300	Air	5	2294	37.07	3905	4.916	10.21	581.0	0.0612	2960	6.17	6.129×10^6	1.379	0.4534	438.5	0.01291	0.982
10577	4.85	67	55	150	300	Air	5	2270	36.78	3860	4.833	10.02	566.0	0.0617	2938	6.20	6.238×10^6	1.380	0.4537	0.000	0.00000	0.000
10578	4.85	67	55	150	300	N_2	5	2288	37.90	4285	5.026	9.019	565.9	0.0537	3066	6.36	5.873×10^6	1.385	0.4121	416.3	0.01227	1.026
10579	4.85	67	55	150	300	Air	5	2288	35.80	3872	4.858	9.838	573.2	0.0598	2943	6.18	6.006×10^6	1.380	0.4405	0.000	0.00000	0.000
10580	4.85	67	55	150	300	Air	5	2230	36.53	3788	4.700	9.886	546.8	0.0630	2898	6.22	6.428×10^6	1.383	0.4569	424.6	0.01249	0.943
10581	4.85	67	55	150	300	Air	5	2271	36.88	3862	4.836	10.09	568.7	0.0618	2938	6.19	6.228×10^6	1.380	0.4545	0.000	0.00000	0.000
10582	4.85	67	55	150	300	N_2	5	2270	37.15	4225	4.945	8.803	555.4	0.0534	3043	6.37	5.870×10^6	1.387	0.4069	414.5	0.01221	1.035
10583	4.85	67	55	150	300	Air	5	2259	36.35	3833	4.784	9.918	560.4	0.0616	2922	6.20	6.236×10^6	1.381	0.4508	0.000	0.00000	0.000
10584	4.75	67	100	200	300	N_2	5	1988	35.76	3342	3.762	7.938	406.4	0.0658	2692	6.56	7.923×10^6	1.397	0.4436	439.3	0.01295	1.006
10585	4.85	67	55	150	300	N_2	5	2247	34.93	4115	4.797	8.214	536.3	0.0516	3002	6.38	5.726×10^6	1.388	0.3878	0.000	0.00142	0.126
10586	4.85	67	55	150	300	Air	5	2247	34.97	3788	4.705	9.527	550.2	0.0603	2897	6.20	6.127×10^6	1.382	0.4374	0.000	0.00988	0.779
10587	4.85	67	55	150	300	Air	5	2247	35.40	3796	4.718	9.682	553.8	0.0609	2901	6.19	6.169×10^6	1.382	0.4423	0.000	0.00000	0.000
10588	4.85	67	55	150	300	Air	5	2230	36.64	3790	4.703	3.111	392.5	0.0276	2935	7.40	3.591×10^6	1.396	0.2027	0.000	0.00735	1.250
10589	4.85	67	55	150	300	Air	5	2230	37.13	3798	4.718	3.127	390.9	0.0279	2943	7.43	3.650×10^6	1.397	0.2052	429.1	0.01265	2.126
10590	4.85	67	55	150	300	Air	5	2265	36.94	3853	4.820	3.129	402.7	0.0271	2976	7.41	3.509×10^6	1.396	0.2016	0.000	0.00000	0.000
10591	4.85	67	55	150	300	N_2	5	2247	36.47	4154	4.849	3.065	408.8	0.0253	3062	7.44	3.451×10^6	1.397	0.1937	437.0	0.01288	2.293
10592	4.75	67	100	200	300	Air	5	1997	36.50	3225	3.739	3.879	350.7	0.0385	2708	7.22	5.017×10^6	1.400	0.2613	446.0	0.01314	1.734
10593	4.75	67	100	200	300	Air	5	1988	36.52	3210	3.715	3.000	323.5	0.0323	2710	7.52	4.474×10^6	1.400	0.2192	0.000	0.00000	0.000
10594	4.75	67	100	200	300	N_2	5	1992	38.00	3397	3.834	2.997	310.5	0.0325	2755	7.67	4.877×10^6	1.400	0.2243	413.9	0.01220	1.876
10595	4.85	67	55	150	300	Air	5	2247	35.87	3805	4.733	9.775	553.8	0.0615	2906	6.20	6.242×10^6	1.382	0.4473	0.000	0.00000	0.000

Table D.2: Freestream chemical composition at the exit of the nozzle for each shot.

Shot	E^-	N_2	O_2	Ar	N	O	NO	NO^+
10558	0.0000000	0.7206228	0.1917374	0.0128591	0.0000000	0.0004547	0.0741184	0.0000000
10559	0.0000000	0.7234077	0.1963577	0.0128591	0.0000000	0.0011284	0.0643484	0.0000000
10560	0.0000000	0.7234345	0.1951556	0.0128591	0.0000000	0.0005164	0.0679386	0.0000000
10561	0.0000000	0.7237608	0.1953305	0.0128591	0.0000000	0.0005414	0.0678105	0.0000000
10562	0.0000000	0.7237840	0.1956535	0.0128591	0.0000000	0.0005397	0.0669289	0.0000000
10563	0.0000000	0.7235515	0.1951051	0.0128591	0.0000000	0.0004937	0.0679284	0.0000000
10564	0.0000000	0.9998853	0.0000000	0.0000000	0.0001147	0.0000000	0.0000000	0.0000000
10565	0.0000000	0.9998838	0.0000000	0.0000000	0.0001162	0.0000000	0.0000000	0.0000000
10566	0.0000000	0.9998851	0.0000000	0.0000000	0.0001149	0.0000000	0.0000000	0.0000000
10567	0.0000000	0.9998862	0.0000000	0.0000000	0.0001138	0.0000000	0.0000000	0.0000000
10568	0.0000000	0.7222272	0.1937942	0.0128591	0.0000000	0.0004616	0.0702942	0.0000000
10569	0.0000000	0.9998852	0.0000000	0.0000000	0.0001148	0.0000000	0.0000000	0.0000000
10570	0.0000000	0.7553473	0.2317936	0.0128591	0.0000000	0.0000000	0.0000000	0.0000000
10571	0.0000000	0.7220120	0.1870105	0.0128591	0.0000000	0.0088447	0.0673989	0.0000000
10572	0.0000000	0.7218945	0.1874262	0.0128591	0.0000000	0.0084302	0.0673979	0.0000000
10573	0.0000000	0.9989730	0.0000000	0.0000000	0.0010270	0.0000000	0.0000000	0.0000000
10574	0.0000000	0.9999507	0.0000000	0.0000000	0.0000493	0.0000000	0.0000000	0.0000000
10575	0.0000000	0.7553473	0.2317936	0.0128591	0.0000000	0.0000000	0.0000000	0.0000000
10576	0.0000000	0.7249529	0.1961190	0.0128591	0.0000000	0.0005783	0.0656138	0.0000000
10577	0.0000000	0.7241720	0.1959742	0.0128591	0.0000000	0.0005258	0.0662722	0.0000000
10578	0.0000000	0.9998854	0.0000000	0.0000000	0.0001146	0.0000000	0.0000000	0.0000000
10579	0.0000000	0.7241171	0.1959169	0.0128591	0.0000000	0.0005633	0.0663384	0.0000000
10580	0.0000000	0.7230072	0.1946691	0.0128591	0.0000000	0.0004503	0.0688335	0.0000000
10581	0.0000000	0.7242275	0.1960121	0.0128591	0.0000000	0.0005256	0.0662019	0.0000000
10582	0.0000000	0.9998870	0.0000000	0.0000000	0.0001130	0.0000000	0.0000000	0.0000000
10583	0.0000000	0.7238752	0.1956021	0.0128591	0.0000000	0.0005043	0.0673919	0.0000000
10584	0.0000000	0.9999503	0.0000000	0.0000000	0.0000497	0.0000000	0.0000000	0.0000000
10585	0.0000000	0.9998846	0.0000000	0.0000000	0.0001154	0.0000000	0.0000000	0.0000000
10586	0.0000000	0.7228035	0.1943580	0.0128591	0.0000000	0.0004836	0.0695115	0.0000000
10587	0.0000000	0.7230993	0.1945370	0.0128591	0.0000000	0.0004829	0.0689796	0.0000000
10588	0.0000000	0.7160132	0.1856515	0.0128591	0.0000000	0.0006373	0.0853135	0.0000000
10589	0.0000000	0.7163372	0.1865503	0.0128591	0.0000000	0.0006234	0.0835309	0.0000000
10590	0.0000000	0.7183456	0.1885664	0.0128591	0.0000000	0.0007164	0.0794219	0.0000000
10591	0.0000000	0.9998084	0.0000000	0.0000000	0.0001916	0.0000000	0.0000000	0.0000000
10592	0.0000000	0.7553473	0.2317936	0.0128591	0.0000000	0.0000000	0.0000000	0.0000000
10593	0.0000000	0.7553473	0.2317936	0.0128591	0.0000000	0.0000000	0.0000000	0.0000000
10594	0.0000000	0.9999180	0.0000000	0.0000000	0.0000820	0.0000000	0.0000000	0.0000000
10595	0.0000000	0.7232915	0.1948551	0.0128591	0.0000000	0.0004823	0.0684905	0.0000000

Appendix E

Estimation of the conditions at the exit of the fuel injector nozzle

This appendix presents the calculations that have been used to estimate the conditions at the exit of the fuel injector nozzle. The procedure is illustrated for a nominal fuelling at an equivalence ratio of 1. Figure E.1 shows a schematic of the fuel injector used in the current study. The fuel injection system is modelled as a reservoir that is located upstream of a sonic throat and a diverging nozzle, with the plenum chamber being the reservoir.

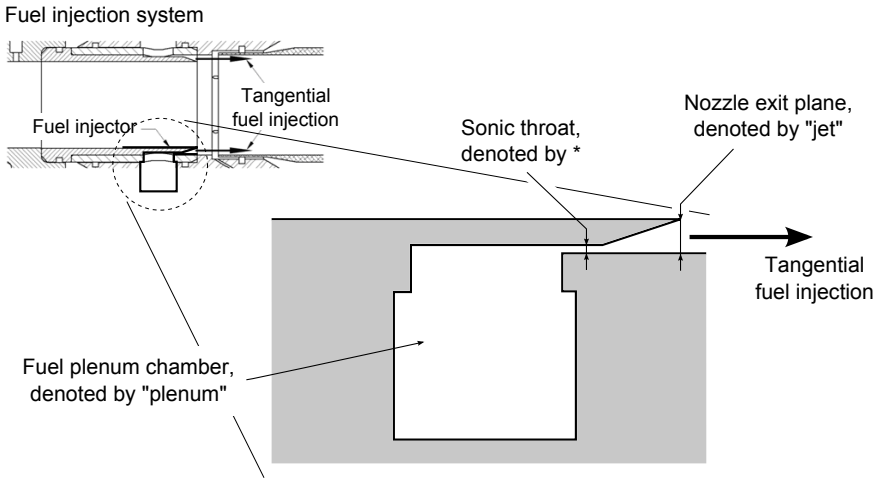

Figure E.1: Schematic of the fuel injector used in the current study.

To estimate the properties at the exit of the diverging nozzle, standard isentropic relations are used to calculate the expansion of the hydrogen in the plenum to the exit of the nozzle. In this process, it is assumed that the flow is sonic at the throat. In addition, because the hydrogen encounters losses when flowing from the plenum

chamber to the exit of the nozzle, the use of an effective throat area instead of the geometrical throat area allows for a better estimation of the nozzle exit conditions to be made. To compute the effective throat area $A^\star$, Equation 3.2 from Robinson et al. (2003)

$$\dot{m}_{\mathrm{H_2}} = \sqrt{\frac{\gamma}{R}\left(\frac{2}{\gamma+1}\right)^{\frac{\gamma+1}{\gamma-1}}} \frac{A^\star}{\sqrt{T_{LT,i}}}\, p_{LT,i} \left(\frac{p_{\mathrm{H_2}}}{p_{LT,i}}\right)^{\frac{\gamma+1}{2\gamma}} \tag{E.1}$$

is re-arranged to get the effective throat area

$$A^\star = \left[\frac{\sqrt{T_{LT,i}}}{\sqrt{\frac{\gamma}{R}\left(\frac{2}{\gamma+1}\right)^{\frac{\gamma+1}{\gamma-1}}}}\right] \left[\frac{1}{p_{LT,i}\left(\frac{p_{\mathrm{H_2}}}{p_{LT,i}}\right)^{\frac{\gamma+1}{2\gamma}}}\right] \tag{E.2}$$

The Ludwieg tube pressure $p_{LT,i}$ measured from the calibrations conducted in the present study is 1.035 MPa, the plenum pressure p_{plenum} is 425.9 kPa and the hydrogen mass flow rate $\dot{m}_{\mathrm{H_2}}$ is 0.01255 kg/s. Assuming that the Ludwieg tube temperature is 300 K, the gas constant for hydrogen R is 4124 J/kg.K and the specific heats ratio γ is 1.41, the resulting effective throat area $A^\star$ that is computed from Equation E.2 is $4.197\times10^{-5}\,\mathrm{m}^2$.

From White (2008), the Mach-number-area correlation for an isentropic flow with a perfect gas assumption is written as

$$\frac{A_{\mathrm{jet}}}{A^\star} = \frac{1}{M_{\mathrm{jet}}}\left[\frac{1+\frac{1}{2}(\gamma-1)M_{\mathrm{jet}}^2}{\frac{1}{2}(\gamma+1)}\right]^{\frac{\gamma+1}{2(\gamma-1)}} \tag{E.3}$$

Since the exit area of the fuel injector nozzle A_{jet} is $2.14\times10^{-4}\,\mathrm{m}^2$, and the values for $A^\star$ and γ are known, Equation E.3 is solved implicitly to obtain the Mach number at the exit of the injector nozzle M_{jet}.

Standard isentropic relations are then used, with the resulting M_{jet} of 3.122 and the conditions in the plenum chamber, to compute the static properties at the exit of the injector nozzle.

$$\frac{T_{\mathrm{plenum}}}{T_{\mathrm{jet}}} = 1+\frac{1}{2}(\gamma-1)M_{\mathrm{jet}}^2 \tag{E.4}$$

$$\frac{p_{\mathrm{plenum}}}{p_{\mathrm{jet}}} = \left[1+\frac{1}{2}(\gamma-1)M_{\mathrm{jet}}^2\right]^{\frac{\gamma}{\gamma-1}} \tag{E.5}$$

$$\frac{\rho_{\text{plenum}}}{\rho_{\text{jet}}} = \left[1 + \frac{1}{2}(\gamma - 1) M_{\text{jet}}^2\right]^{\frac{1}{\gamma - 1}} \tag{E.6}$$

$$u_{\text{jet}} = M_{\text{jet}} \sqrt{\gamma R T_{\text{jet}}} \tag{E.7}$$

The resulting static temperature of the hydrogen jet at the exit of the injector nozzle T_{jet} is 96 K, the static pressure p_{jet} is 8.5 kPa, the static density ρ_{jet} is 0.0214 kg/m^3 and the velocity u_{jet} is 2405 m/s.

Appendix F

A comparison of the strain gauges used

This appendix presents a comparison of the performance of the piezo-electric film and semi-conductor strain gauges that were used in the current experiments. The strain gauges used in the current experiments were those that had been used by Kirchhartz (2010) in his experiments. These gauges were applied in a configuration where the direction of the most sensitive axis of each gauge was aligned with the axis of the brass sting. This was done so that ideally only axial strains will be measured. However, the quality of the output from these gauges can be affected by several factors. One of these factors is the imperfections in the application of the gauges on the brass sting. These imperfections include the slight misalignment of the gauges, the age of the bonding layer between the gauge and the sting and the surface topology of the gauge (Kirchhartz, 2010). These imperfections are undesirable because they can reduce the gauge's sensitivity to axial strains and signal-to-noise ratio, and also increase the sensitivity to bending strains.

To evaluate the performance of the strain gauges, the combustor-sting arrangement was struck with an instrumented impulse hammer in a similar way to that in the calibration procedures for the stress-wave force balance (Mee, 2002b). As shown in Figure F.1, the combustor was struck at two separate locations to induce two different types of stresses - axial and bending.

The resulting strain outputs, which are normalised with the peak force levels of the hammer strike, are shown in Figure F.2 for the piezo-electric film strain gauges and in Figure F.3 for the semi-conductor strain gauges. Figures F.2a and F.3a show that of all the gauges tested, gauge B is the most sensitive to axial strains. Gauges SSGA, SSGOld and E have about half of gauge B's sensitivity to axial strains. In terms of the sensitivity to bending strains, gauge C is the least sensitive, followed by all the semi-conductor gauges and gauge B. An ideal strain gauge for axial force measurements in the current

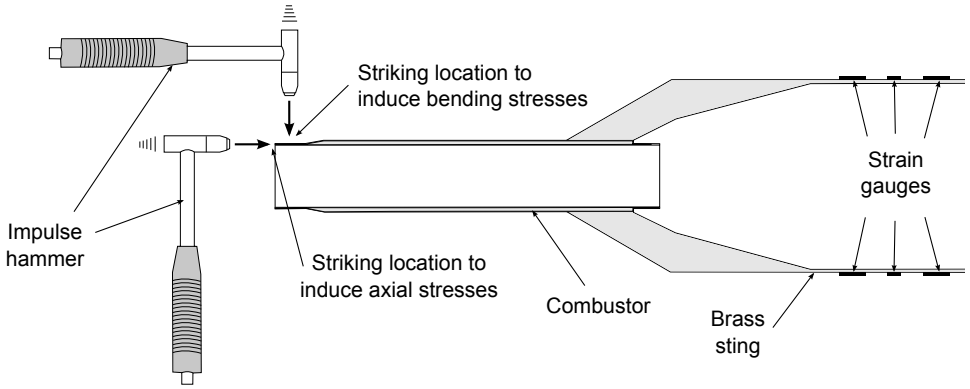

Figure F.1: Method used to generate axial and bending stresses.

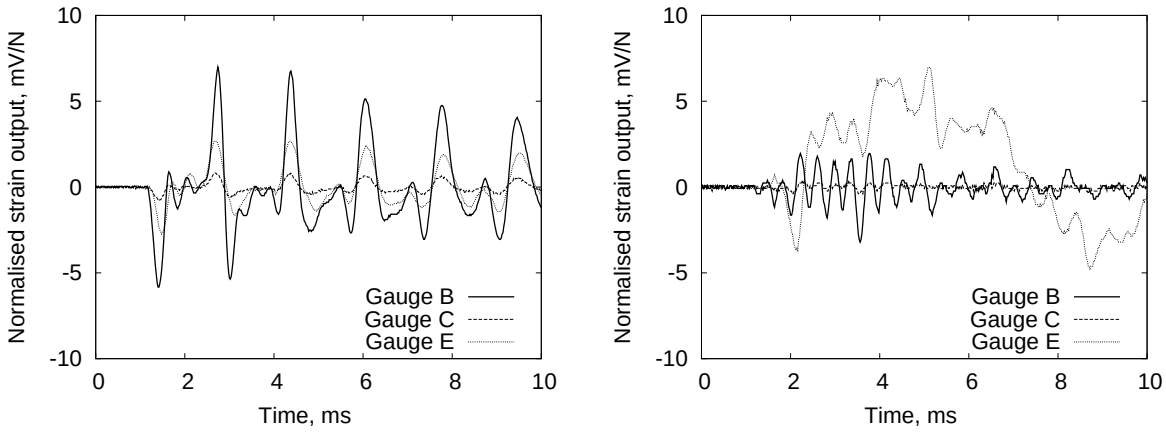

(a) Sensitivity to axial strains. **(b)** Sensitivity to bending strains.

Figure F.2: Normalised strain gauge output from piezo-electric film strain gauges.

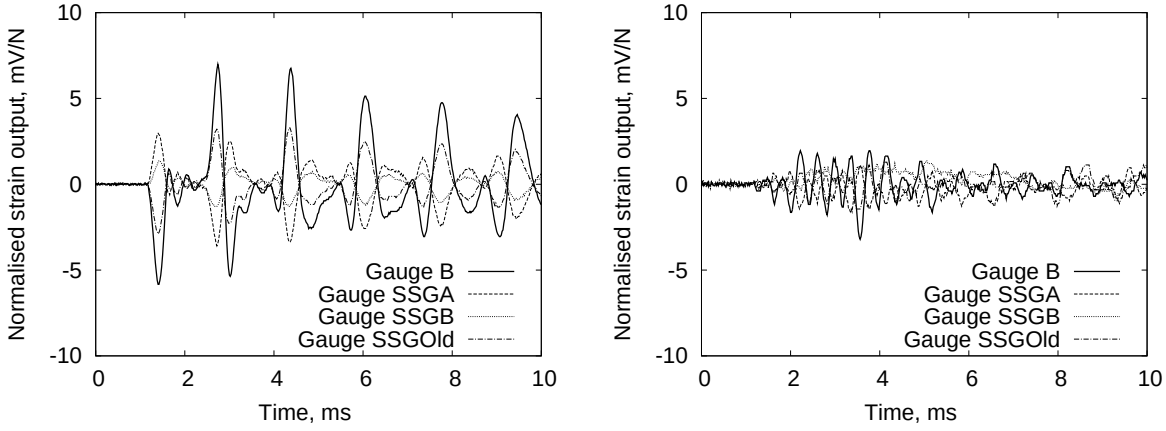

(a) Sensitivity to axial strains. **(b)** Sensitivity to bending strains.

Figure F.3: Normalised strain gauge output from semi-conductor strain gauges.

project is one that has the highest sensitivity to axial strains and the lowest sensitivity to bending strains. This then eliminates gauges C and E. Considering that gauge B has about twice the sensitivity to axial strains than the semi-conductor gauges and that it has a similar level of sensitivity to bending strains, it is concluded that gauge B is the most reliable gauge to be used for axial force measurements in the current project.

Appendix G

Justification of the use of 10% driver gas contamination to limit test times

In the T4 shock tunnel facility, it is common practice to use a threshold of 10% driver gas contamination to limit test times. As the combustion phenomena is an important aspect in the current experiments, it is necessary to show that this level of driver gas contamination does not significantly affect combustion. This is done by examining the effect that different levels of driver gas contamination have on the combustion of a hydrogen-air mixture in a supersonic stream.

To model the combustion of a hydrogen-air mixture in a supersonic stream, a one-dimensional finite-rate stream-tube analysis is used. This analysis is conducted with the use of a script, `reacting-pipe-flow.py`, which has been written by Dr Peter Jacobs with the use of Eilmer3's non-equilibrium chemistry module that has been written by Dr Rowan Gollan. This script has been verified against the numerical results of Bittker and Scullin (1972) and can be found in the "bittker-hydrogen-combustion" example in the Eilmer3 package. The analysis is conducted for a hydrogen-air mixture flowing through a 0.5 m-long inviscid constant-area pipe at a velocity of 2576 m/s, a static pressure of 88.5 kPa and a static temperature of 1126 K, as shown in Figure G.1. The inflow

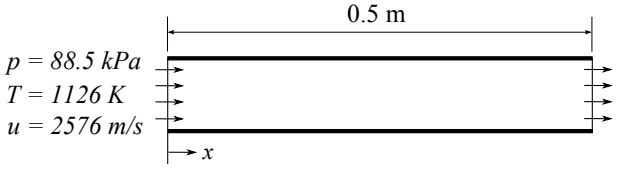

Figure G.1: Schematic for the stream-tube one-dimensional finite-rate stream-tube analysis.

conditions are representative of those entering the combustor for the current experiments (see Table 5.1). The finite-rate reaction scheme that is used for this analysis is the 9-species 18-reaction hydrogen-air reaction scheme of Bittker and Scullin (1972). The mass fraction of each individual species of the hydrogen-air mixture for three different driver gas compositions and five different contamination levels is shown in Table G.1. Note that the three different driver gas compositions correspond to those that are used for the T4 experiments in this project.

Table G.1: Mass fraction of each individual species of the hydrogen-air mixture for three different driver gas compositions and five different contamination levels.

		Driver gas composition (by volume)		
		100% argon 0% helium	55% argon 45% helium	35% argon 65% helium
0% contamination	O_2 mass fraction	0.226	0.226	0.226
	N_2 mass fraction	0.746	0.746	0.746
	H_2 mass fraction	0.028	0.028	0.028
	Ar mass fraction	0.000	0.000	0.000
	He mass fraction	0.000	0.000	0.000
2% contamination	O_2 mass fraction	0.221	0.221	0.221
	N_2 mass fraction	0.731	0.731	0.731
	H_2 mass fraction	0.028	0.028	0.028
	Ar mass fraction	0.020	0.018	0.016
	He mass fraction	0.000	0.002	0.004
5% contamination	O_2 mass fraction	0.214	0.214	0.214
	N_2 mass fraction	0.709	0.709	0.709
	H_2 mass fraction	0.028	0.028	0.028
	Ar mass fraction	0.049	0.045	0.040
	He mass fraction	0.000	0.004	0.009
10% contamination	O_2 mass fraction	0.203	0.203	0.203
	N_2 mass fraction	0.672	0.672	0.672
	H_2 mass fraction	0.028	0.028	0.028
	Ar mass fraction	0.097	0.090	0.080
	He mass fraction	0.000	0.007	0.017
50% contamination	O_2 mass fraction	0.113	0.113	0.113
	N_2 mass fraction	0.373	0.373	0.373
	H_2 mass fraction	0.028	0.028	0.028
	Ar mass fraction	0.486	0.449	0.400
	He mass fraction	0.000	0.037	0.086

Figure G.2 shows the distributions of static pressure, static temperature, velocity and H_2O mass fraction along the pipe for various driver gas contamination lev-

els for the driver gas composition with 100% argon. It can be seen that the static pressure, static temperature and velocity are the same in the post-combustion region (downstream of $x = 0.3$ m) for contamination levels that are below 10%. In the post-combustion region, the mass fraction of H_2O produced also varies by only 3% for contamination levels that are below 10%. The only significant effect of driver gas contamination that is clearly visible in these plots is the delay in the ignition process. The hydrogen-air mixture with 10% driver gas contamination ignites 0.012 m later than that with no driver gas contamination. This delay in ignition is considered to be insignificant for a combustor with a length of 0.5 m.

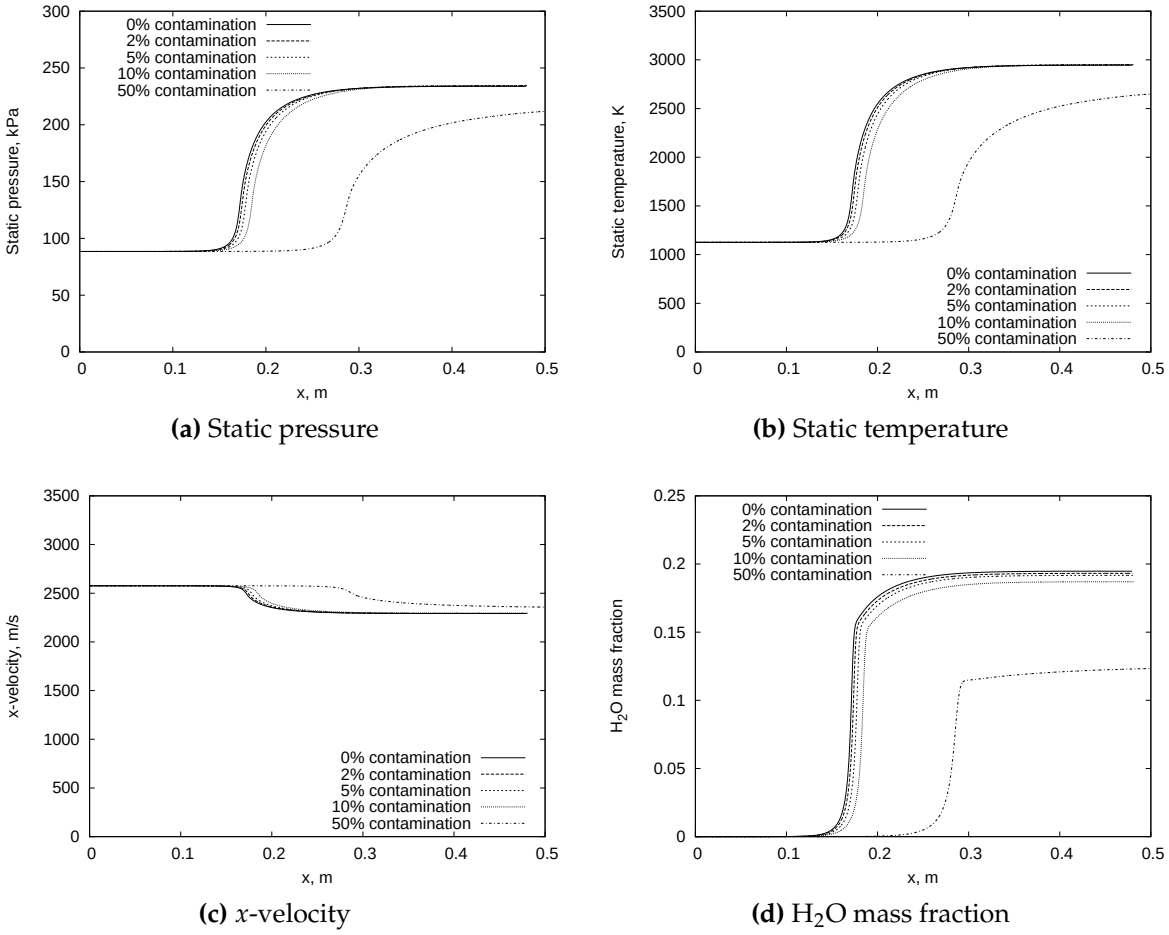

(a) Static pressure

(b) Static temperature

(c) x-velocity

(d) H_2O mass fraction

Figure G.2: Flow variables and H_2O production along the pipe for driver gas with 100% argon.

Figures G.3 and G.4 show distributions of static pressure, static temperature, velocity and H_2O mass fraction along the pipe for the other two driver gas compositions listed in Table G.1. The findings from these analyses are similar to those for the driver gas composition with 100% argon. For contamination levels that are below 10%, the

static pressure, static temperature and velocity in the post-combustion region (downstream of $x = 0.3$ m) are the same, and the mass fraction of H_2O produced varies by only 3%. These plots also show that an increase in the amount of helium in the driver gas increases the delay in ignition length. For a driver gas with a 45% volumetric fraction of helium, ignition for a hydrogen-air mixture with 10% driver gas contamination occurs 0.018 m later than for that with 0% driver gas contamination. For a driver gas with a 65% volumetric fraction of helium, ignition for a hydrogen-air mixture with 10% driver gas contamination occurs 0.026 m later than for that with 0% driver gas contamination.

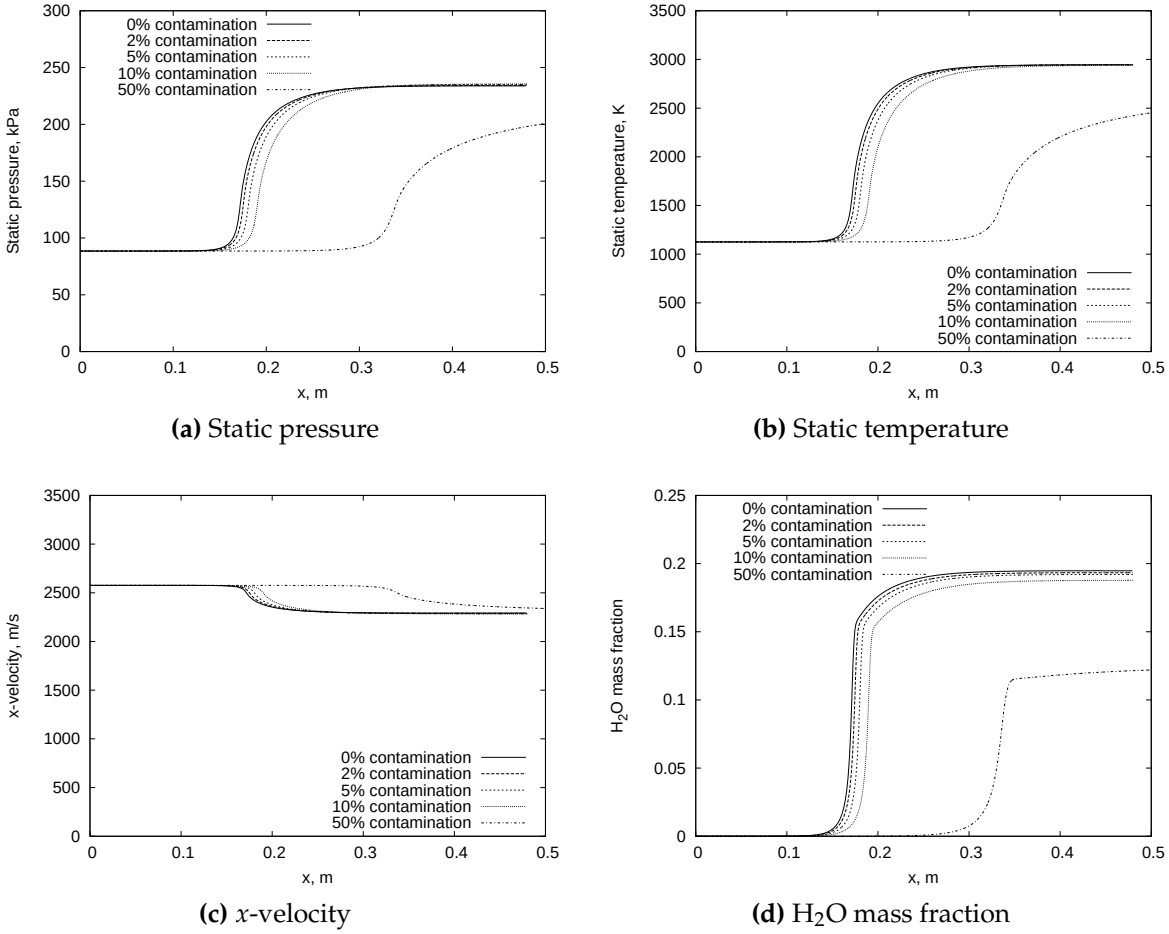

(a) Static pressure

(b) Static temperature

(c) x-velocity

(d) H_2O mass fraction

Figure G.3: Flow variables and H_2O production along the pipe for driver gas with 55% argon and 45% helium (by volume).

Results from this analysis demonstrate that the presence of 10% driver gas in the flow only acts to delay the ignition process, but does not significantly affect the other combustion processes, hence justifying the appropriateness of the use of 10% driver gas contamination to limit test times in the current experiments.

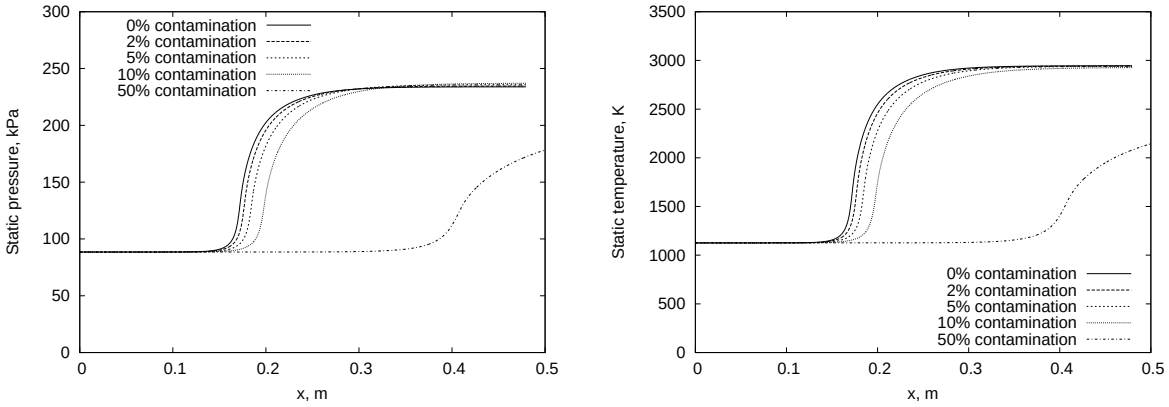

(a) Static pressure

(b) Static temperature

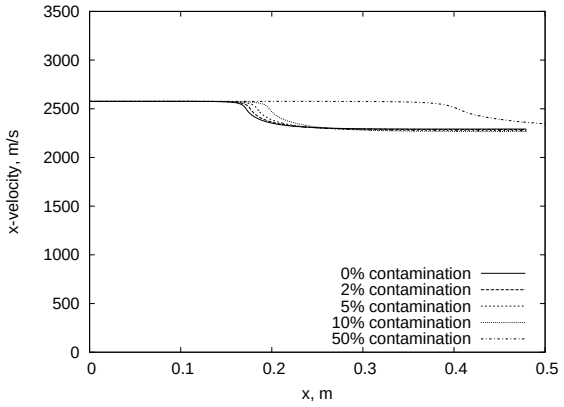

(c) x-velocity

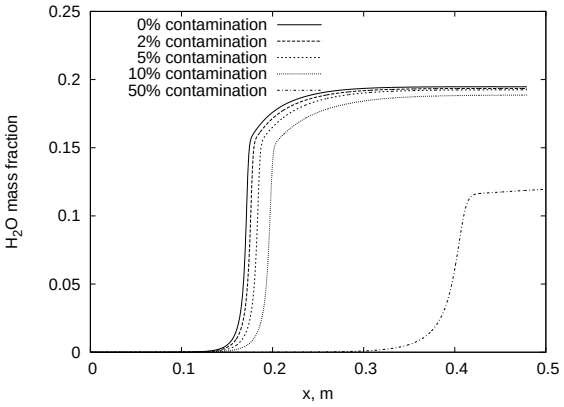

(d) H_2O mass fraction

Figure G.4: Flow variables and H_2O production along the pipe for driver gas with 35% argon and 65% helium (by volume).

Appendix H

Drag coefficient in terms of Pitot pressure

This appendix details the derivation of the alternate form of drag coefficient that was used in the presentation of the results in Chapter 5. This form of the drag coefficient is proposed by Mee (2002b) to account for the effects of fluctuations in the freestream flow on the aerodynamic forces on a model that is tested in a short-duration impulse facility. Mee (2002b) suggests that by re-formulating the drag coefficient to be in terms of Pitot pressure and by measuring the Pitot pressure simultaneously with the aerodynamic force, the fluctuations in the freestream flow can be accounted for in the force measurements.

The drag coefficient is commonly defined in terms of the measured drag force D, the freestream flow speed u_∞, the freestream density ρ_∞, and the area which the measured drag force acts on, A, as

$$c_D = \frac{D}{\frac{1}{2}\rho_\infty u_\infty^2 A} \tag{H.1}$$

The Rayleigh-Pitot formula (Ames Research Staff, 1953) gives the relationship between the Pitot pressure p_{Pitot}, the freestream static pressure p_∞, the freestream Mach number M_∞^2, and the ratio of specific heats of the test gas γ, as

$$p_{\text{Pitot}} = p_\infty \left[\frac{(\gamma+1)M_\infty^2}{2}\right]^{\frac{\gamma}{\gamma-1}} \left[\frac{\gamma+1}{2\gamma M_\infty^2-(\gamma-1)}\right]^{\frac{1}{\gamma-1}} \tag{H.2}$$

By noting that the Pitot pressure is approximately a constant fraction of the dynamic pressure for high Mach number flows, the Pitot pressure in Equation H.2 can be re-

written in terms of the dynamic pressure. When M_∞ is sufficiently large such that $2\gamma M_\infty^2 >> (\gamma - 1)$, the Pitot pressure can be approximated as

$$p_{\text{Pitot}} \approx p_\infty \left(\frac{\gamma+1}{2}\right)^{\frac{\gamma+1}{\gamma-1}} \gamma^{\frac{1}{1-\gamma}} M_\infty^2 \tag{H.3}$$

By the definition of Mach number and the equation of state for a thermally perfect gas, the term $p_\infty M_\infty^2$ in Equation H.3 can be written in terms of the dynamic pressure $\rho_\infty u_\infty^2$ as

$$p_\infty M_\infty^2 = \rho_\infty R T_\infty \frac{u_\infty^2}{\gamma R T_\infty} = \frac{\rho_\infty u_\infty^2}{\gamma} \tag{H.4}$$

This can then be substituted into Equation H.3 to yield

$$p_{\text{Pitot}} \approx \left(\frac{\gamma+1}{2}\right)^{\frac{\gamma+1}{\gamma-1}} \gamma^{\frac{\gamma}{1-\gamma}} \rho_\infty u_\infty^2 \tag{H.5}$$

Finally, Equation H.5 can be re-arranged in terms of the dynamic pressure and substituted back into Equation H.1. The resulting equation is that of the drag coefficient formulated in terms of the Pitot pressure.

$$c_D = \left[\frac{2}{p_{\text{Pitot}}/p_s}\left(\frac{\gamma+1}{2}\right)^{\frac{\gamma+1}{\gamma-1}} \gamma^{\frac{\gamma}{1-\gamma}}\right] \frac{D}{p_s A} \tag{H.6}$$

Appendix I

Integral form of the Navier-Stokes equations as implemented in Eilmer3

The integral form of the Navier-Stokes equations, as it is implemented in Eilmer3, is presented. A full description of the implementation of the governing equations can be found in the theory book for Eilmer3 (Jacobs et al., 2010).

The Eilmer3 code is formulated around the integral form of the Navier-Stokes equations, which can be expressed as

$$\frac{\partial}{\partial t}\int_V U dV = -\oint_S \left(\overline{F}_i - \overline{F}_v\right)\cdot \hat{n}\, dA + \int_V Q dV\ , \tag{I.1}$$

where S is the bounding surface and $\hat{n}$ is the outward-facing unit normal of the control surface.

For a three-dimensional flow, the array of conserved quantities is dependent on the thermal model under consideration, and for the thermal nonequilibrium models is

$$U = \begin{bmatrix} \rho \\ \rho u_x \\ \rho u_y \\ \rho u_z \\ \rho E \\ \rho e_{v_m} \\ \rho e_e \\ \rho f_s \end{bmatrix}\ . \tag{I.2}$$

Here, the conserved quantities are respectively density, x-momentum per volume, y-momentum per volume, total energy per volume, vibrational energy for mode m,

electronic-electron energy and mass density of species s. Note that ρe_e includes both bound and free electron energy. Both the total and individual species continuity equations are solved to add rigour to the flow solver: the redundant information gives a good idea when the numerics are running into trouble. Conversely, when only solving $n-1$ species equations, it is easier for undetected error in mass fractions to accumulate. Thus for 11 species air with 6 vibrating molecules and the inclusion of electrons, for example, there are 22 conserved quantities.

The flux vectors are divided into inviscid and viscous contributions. The inviscid component in thermal nonequilibrium is

$$\overline{F}_i = \begin{bmatrix} \rho u_x \\ \rho u_x^2 + p \\ \rho u_y u_x \\ \rho u_z u_x \\ \rho E u_x + p u_x \\ \rho e_{v_m} u_x \\ \rho e_e u_x + p_e u_x \\ \rho f_s u_x \end{bmatrix} \hat{i} + \begin{bmatrix} \rho u_y \\ \rho u_x u_y \\ \rho u_y^2 + p \\ \rho u_z u_y \\ \rho E u_y + p u_y \\ \rho e_{v_m} u_y \\ \rho e_e u_y + p_e u_y \\ \rho f_s u_y \end{bmatrix} \hat{j} + \begin{bmatrix} \rho u_z \\ \rho u_z u_x \\ \rho u_z u_y \\ \rho u_z^2 + p \\ \rho E u_z + p u_z \\ \rho e_{v_m} u_z \\ \rho e_e u_z + p_e u_z \\ \rho f_s u_z \end{bmatrix} \hat{k} \,. \tag{I.3}$$

The viscous component is

$$\overline{F}_v = \begin{bmatrix} 0 \\ \tau_{xx} \\ \tau_{yx} \\ \tau_{zx} \\ \tau_{xx}u_x + \tau_{yx}u_y + \tau_{zx}u_z + q_x \\ q_{x,v_m} \\ q_{x,e} \\ J_{x,s} \end{bmatrix} \hat{i} + \begin{bmatrix} 0 \\ \tau_{xy} \\ \tau_{yy} \\ \tau_{zy} \\ \tau_{xy}u_x + \tau_{yy}u_y + \tau_{zy}u_z + q_y \\ q_{y,v_m} \\ q_{y,e} \\ J_{y,s} \end{bmatrix} \hat{j} + \begin{bmatrix} 0 \\ \tau_{xz} \\ \tau_{yz} \\ \tau_{zz} \\ \tau_{xz}u_x + \tau_{yz}u_y + \tau_{zz}u_z + q_z \\ q_{z,v_m} \\ q_{z,e} \\ J_{z,s} \end{bmatrix} \hat{k} \,, \tag{I.4}$$

and the viscous stresses are

$$\begin{aligned}
\tau_{xx} &= 2\mu\frac{\partial u_x}{\partial x} + \lambda\left(\frac{\partial u_x}{\partial x} + \frac{\partial u_y}{\partial y} + \frac{\partial u_z}{\partial z}\right) , \\
\tau_{yy} &= 2\mu\frac{\partial u_y}{\partial y} + \lambda\left(\frac{\partial u_x}{\partial x} + \frac{\partial u_y}{\partial y} + \frac{\partial u_z}{\partial z}\right) , \\
\tau_{zz} &= 2\mu\frac{\partial u_z}{\partial z} + \lambda\left(\frac{\partial u_x}{\partial x} + \frac{\partial u_y}{\partial y} + \frac{\partial u_z}{\partial z}\right) , \\
\tau_{xy} = \tau_{yx} &= \mu\left(\frac{\partial u_x}{dy} + \frac{\partial u_y}{dx}\right) , \\
\tau_{xz} = \tau_{zx} &= \mu\left(\frac{\partial u_x}{dz} + \frac{\partial u_z}{dx}\right) , \\
\tau_{yz} = \tau_{zy} &= \mu\left(\frac{\partial u_y}{dz} + \frac{\partial u_z}{dy}\right) ,
\end{aligned} \tag{I.5}$$

where the secondary viscosity coefficient λ is expressed in terms of the primary coefficient μ via Stokes hypothesis, $\lambda = -\frac{2}{3}\mu$. The viscous heat fluxes are

$$\begin{aligned}
q_x &= k_{tr}\frac{\partial T}{\partial x} + \sum_{s=\text{mol.}} k_{v_s}\frac{\partial T_{v_s}}{\partial x} + k_e\frac{\partial T_e}{\partial x} + \sum_{s=\text{all}} J_{x,s}h_s , \\
q_y &= k_{tr}\frac{\partial T}{\partial y} + \sum_{s=\text{mol.}} k_{v_s}\frac{\partial T_{v_s}}{\partial y} + k_e\frac{\partial T_e}{\partial y} + \sum_{s=\text{all}} J_{y,s}h_s , \\
q_{x,v_m} &= k_{v_m}\frac{\partial T_{v_m}}{\partial x} + J_{x,m}h_{v_m} , \\
q_{y,v_m} &= k_{v_m}\frac{\partial T_{v_m}}{\partial y} + J_{y,m}h_{v_m} , \\
q_{x,e} &= k_e\frac{\partial T_e}{\partial x} + \sum_{s=\text{all}} J_{x,s}h_{e_s} , \\
q_{y,e} &= k_e\frac{\partial T_e}{\partial y} + \sum_{s=\text{all}} J_{y,s}h_{e_s} .
\end{aligned} \tag{I.6}$$

The vector of source terms is separated into geometric, chemistry, thermal energy exchange and radiation contributions in order to apply the operator-splitting integration approach, Equation I.7.

$$Q = Q_{\text{geom.}} + Q_{\text{chem.}} + Q_{\text{therm.}} + Q_{\text{rad.}} \tag{I.7}$$

For planar geometries $Q_{\text{geom.}}$, is a zero vector.

The chemistry source term vector is

$$Q_{\text{chem.}} = \begin{bmatrix} 0 \\ 0 \\ 0 \\ 0 \\ \Omega_m^{VC} \\ \sum_{s=\text{ion.}} \Omega_s^{EC} \\ \dot{\omega}_s \end{bmatrix}, \tag{I.8}$$

and the thermal energy-exchange source term vector is

$$Q_{\text{therm.}} = \begin{bmatrix} 0 \\ 0 \\ 0 \\ 0 \\ \Omega_m^{VT} + \Omega_m^{VV} + \Omega_m^{VE} \\ \sum_{s=\text{mol.}} \Omega_s^{EV} + \sum_{s=\text{all.}} \Omega_s^{ET} \\ 0 \end{bmatrix}, \tag{I.9}$$

The radiation source term vector is

$$Q_{\text{rad.}} = \begin{bmatrix} 0 \\ 0 \\ 0 \\ -\nabla \cdot q_{rad} \\ 0 \\ -\nabla \cdot q_{rad} \\ 0 \end{bmatrix}. \tag{I.10}$$

where any purely vibrational component of radiative heat loss (or gain) has been neglected. The transport, thermodynamic and chemical kinetic source term models are discussed in detail in Chapter 3 of the Eilmer3 theory book (Jacobs et al., 2010).

Appendix J

Tests conducted at off-design conditions

J.1 Tests at lower stagnation enthalpies - H_s = 3.7 MJ/kg

J.1.1 Inlet & combustor pressure measurements

Figure J.1 shows the experimental pressure measurements taken on the bodyside of the REST inlet and combustor. The pressure measurements for the 4.8 MJ/kg tests (shown in Section 5.1) are also shown in the same plot.

In the inlet, it can be observed that the shock impinges further downstream than in the tests conducted at $H_s = 4.8$ MJ/kg. Because the freestream Mach number for the 3.7 MJ/kg tests is slightly higher than that for the 4.8 MJ/kg tests[1], and because a higher Mach number produces a shock at a shallower angle, the cowl shock impinges further downstream in the inlet for the 3.7 MJ/kg tests than for the 4.8 MJ/kg tests.

In the combustor, the fuel-into-N_2 test shows slightly higher pressure coefficients in the combustor than the fuel-off tests, due to the fuel mass addition. For the fuel-on test, unlike the 4.8 MJ/kg tests, the ignition location of the hydrogen is located further upstream of the first pressure transducer in the combustor. Despite the lower fuel equivalence ratio for the 3.7 MJ/kg tests, the combustion-induced pressure rise is higher than that for the 4.8 MJ/kg tests. It is postulated that this is due to the difference in freestream static temperatures for different stagnation enthalpies. For the 3.7 MJ/kg tests, the freestream temperatures of 451 K are lower than those in the 4.8 MJ/kg tests (560 K), thus allowing more heat to be transferred from the combustion process into the flow. However, considering the lower freestream temperatures for the 3.7 MJ/kg tests,

[1] The Mach number at the exit of the Mach 6 nozzle varies as the nozzle-supply enthalpy varies. At higher enthalpies, the exit Mach number is lower because of the different real gas effects that occur in the expansion. This can be seen in the results in Table D.1

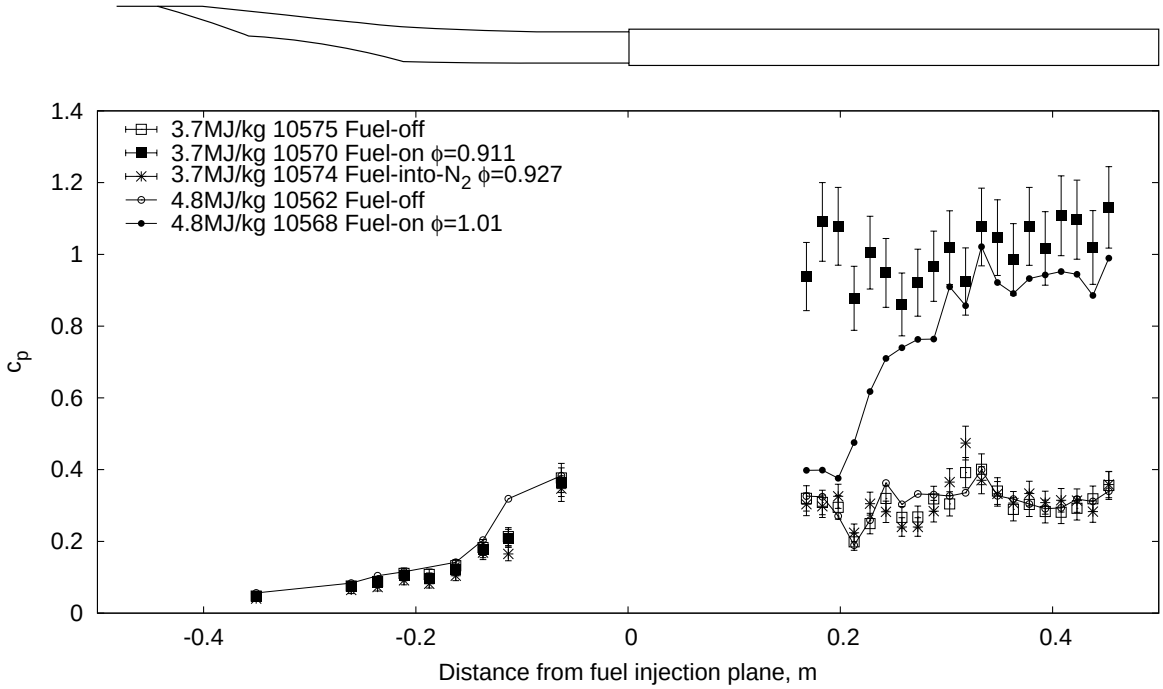

Figure J.1: Pressure coefficients in the inlet and combustor for H_s = 3.7 MJ/kg condition

the earlier ignition of the hydrogen is not expected. A plausible explanation for this is that because the reflected shock from the inlet impinges further downstream in the 3.7 MJ/kg tests, the shock just misses the backward-facing step and impinges directly on the wall hydrogen film. It is postulated that this may have caused the hydrogen film to separate and lift off the wall. This can potentially lead to better mixing between the hydrogen and air, which may, in turn, lead to the earlier ignition of the hydrogen-air mixture.

J.1.2 Combustor drag measurements

Figure J.2 shows the experimental and theoretical values for skin friction drag coefficient for the 3.7 MJ/kg tests. Also shown are the drag coefficients for the 4.8 MJ/kg tests.

For the fuel-off test, the measured drag coefficient is overpredicted by the Spalding & Chi theory by 13% and by the van Driest II theory by 9%. The drag coefficient measured for the 3.7 MJ/kg test is slightly lower than that for the 4.8 MJ/kg test, though the difference is in the order of the experimental uncertainties. Since the unit Reynolds number for the 3.7 MJ/kg tests of 7.8×10^6 is higher than that for the 4.8 MJ/kg tests and since a higher Reynolds number results in a lower drag coefficient for fully tur-

bulent boundary layers, the lower drag coefficient observed in the test conducted at a lower stagnation enthalpy is expected.

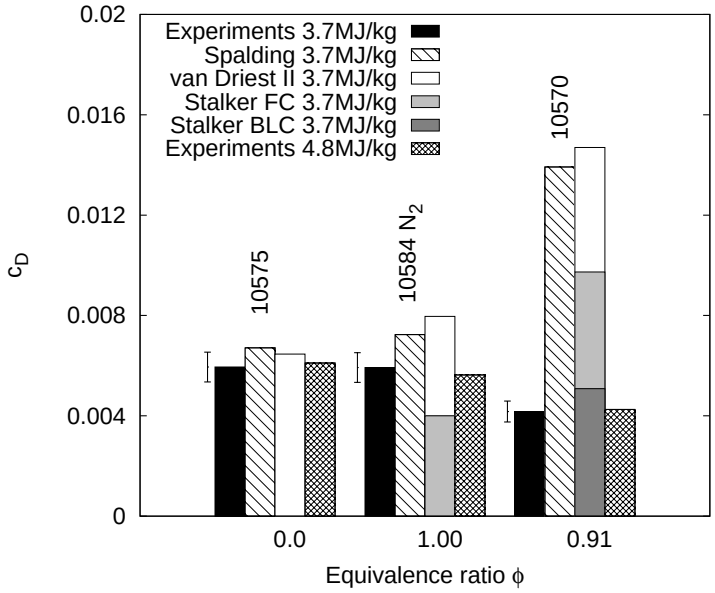

Figure J.2: Comparison of experimentally measured combustor drag coefficients for tests at the H_s = 3.7 MJ/kg condition with those predicted using skin friction theories and with those for tests at the H_s = 4.8 MJ/kg condition.

For the fuel-into-N_2 test, the measured drag coefficient is lower than that of the fuel-off test by only 0.3%. The level of drag reduction inferred from a comparison of the measured drag coefficient with that predicted by the Spalding & Chi theory is 18%. This is much lower than the 50% drag reduction predicted using Stalker's film-cooling theory. Both comparisons strongly suggest that the drag reduction from the film-cooling effect has been affected. It is suggested in Section J.1.1 that the reflected shock from the inlet may have impinged on the wall hydrogen film and caused the film to separate and lift off from the wall, thus leading to the earlier ignition of the hydrogen-air mixture. This too could have been the cause of the diminished drag reduction levels, since the removal of hydrogen from the surface reduces the drag reduction that can be obtained from the film-cooling effect.

For the fuel-on test, the measured drag coefficient is 30% lower than that measured in the fuel-off test. The level of drag reduction inferred from a comparison of the measured drag coefficient with that predicted by the Spalding & Chi theory is 70%. This is quite similar to the 65% drag reduction that is predicted using Stalker's boundary layer combustion theory. In addition, it can also be observed that the levels of drag

reduction due to boundary layer combustion for the 3.7 MJ/kg tests are slightly higher than those for the 4.8 MJ/kg tests. This occurs because the lowering of the stagnation enthalpy results in a larger amount of heat release from combustion, which then brings about a higher level of skin friction reduction when hydrogen burns in the boundary layer (Kirchhartz, 2010; Suraweera, 2006). From these tests, it can be concluded that the flow disturbances brought about by the lowering of the stagnation enthalpy does not affect the drag reduction capabilities of the boundary layer combustion technique.

J.2 Tests at higher stagnation enthalpies - H_s = 8 MJ/kg

J.2.1 Inlet & combustor pressure measurements

Figure J.3 shows the experimental pressure measurements taken on the bodyside of the REST inlet and combustor. The pressure measurements for the 4.8 MJ/kg tests are also shown in the same plot.

In the inlet, it can be observed that the shock impinges further upstream than in the tests conducted at $H_s = 4.8$ MJ/kg. Because the freestream Mach number for the 8 MJ/kg tests is slightly lower than that for the 4.8 MJ/kg tests, and because a lower Mach number produces a shock at a steeper angle, the cowl shock impinges further upstream in the inlet for the 8 MJ/kg tests than for the 4.8 MJ/kg tests.

In the combustor, the fuel-into-N_2 test shows slightly higher pressure coefficients in the combustor than the fuel-off tests, due to the fuel mass addition. For the fuel-on tests, the ignition location of the fuel-air mixture cannot be deduced from the measurements. However, pressure rises above the level for the fuel-into-N_2 test upstream of the first pressure transducer, like in the 4.8 MJ/kg tests. Despite the slightly higher fuel equivalence ratio for the 8 MJ/kg test, the combustion-induced pressure rise is significantly lower in the 8 MJ/kg tests than in the 4.8 MJ/kg tests. This occurs because the freestream static temperature in the 8 MJ/kg tests, which is higher than those in the 4.8 MJ/kg tests, limits the amount of heat that is being transferred from the combustion process to the boundary layer (Kirchhartz, 2010; Suraweera, 2006).

J.2.2 Combustor drag measurements

Figure J.4 shows the experimental and theoretical values for skin friction drag coefficient for the 8 MJ/kg tests. Also shown are the drag coefficients for the 4.8 MJ/kg tests.

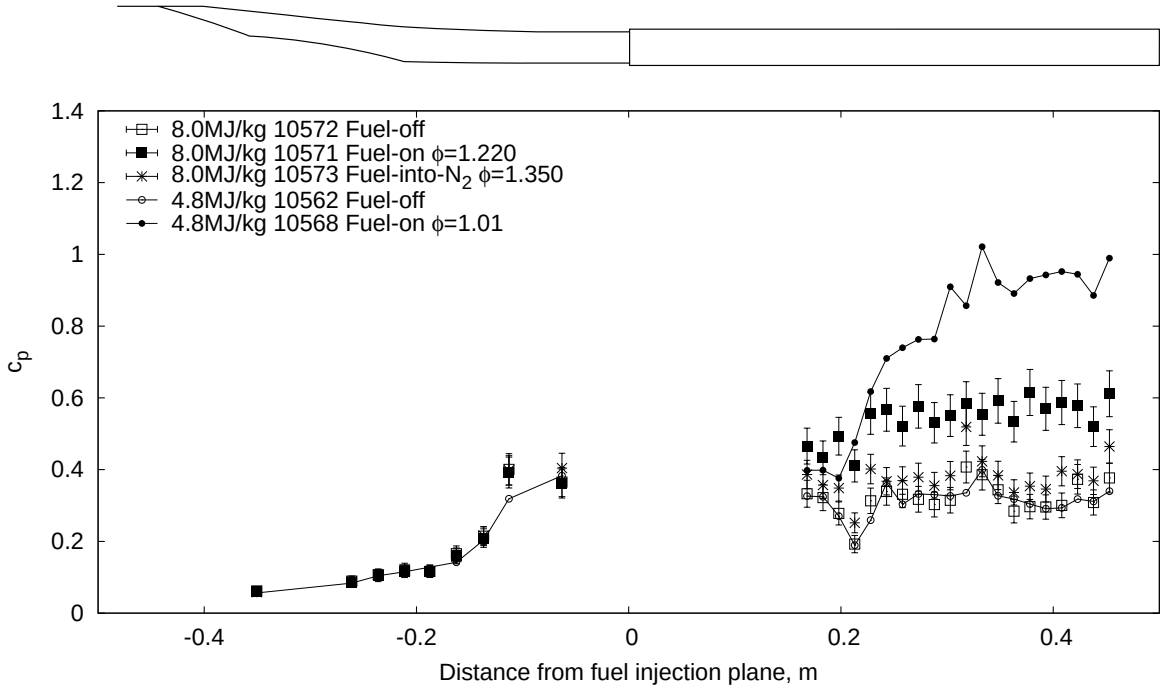

Figure J.3: Pressure coefficients in the inlet and combustor for $H_s = 8\,\mathrm{MJ/kg}$ condition.

For the fuel-off test, the measured drag coefficient is overpredicted by the Spalding & Chi theory by 15% and by the van Driest II theory by 51%. Because the capabilities of the van Driest II theory is expected to be lower with decreasing T_w/T_{aw} values (Bradshaw, 1977) and because the value of T_w/T_{aw} at the 8 MJ/kg condition is 38% lower than those at the 3.7 MJ/kg and 4.8 MJ/kg conditions, a poorer estimation of the drag coefficient by the van Driest II theory for this condition is expected. Note that since a lower Reynolds number results in a higher drag coefficient for fully turbulent boundary layers and since the unit Reynolds number for the 8 MJ/kg test is lower than that for the 4.8 MJ/kg test, the drag coefficient measured in the 8 MJ/kg test is higher than that measured in the 4.8 MJ/kg test.

For the fuel-into-N_2 test, the measured drag coefficient is lower than that of the fuel-off test by 12%. The level of drag reduction inferred from a comparison of the measured drag coefficient with that predicted by the Spalding & Chi theory is 34%. This is similar to the 35% drag reduction predicted using Stalker's film-cooling theory.

For the fuel-on test, the measured drag coefficient is 28% lower than that measured in the fuel-off test. Note that the level of drag reduction is about the same as that for the 4.8 MJ/kg tests. With a limited amount of heat release from combustion for the 8 MJ/kg tests, the level of drag reduction is expected to be lower than that for the

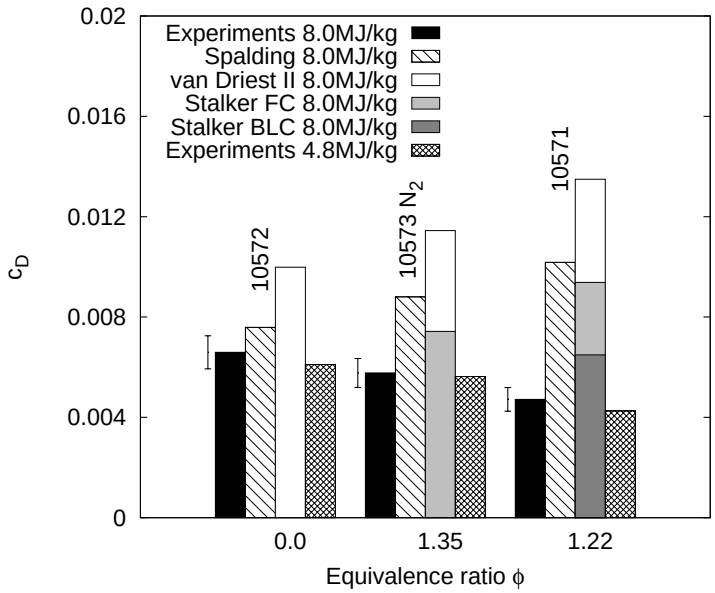

Figure J.4: Comparison of experimentally measured combustor drag coefficients for tests at the H_s = 8 MJ/kg condition condition with those predicted using skin friction theories and with those for tests at the H_s = 4.8 MJ/kg condition.

4.8 MJ/kg tests. A possible explanation for this is that the higher equivalence ratios and the earlier ignition of the fuel for the 8 MJ/kg tests are compensating for the lower levels of drag reduction obtained. In comparison with the 54% drag reduction inferred from a comparison of the measured drag coefficient with that predicted by the Spalding & Chi theory, the 52% drag reduction that is predicted using Stalker's boundary layer combustion theory is quite similar.

The results, together with those from Section J.2, demonstrate that the flow disturbances generated by the change of stagnation enthalpy of the flow between 3.7 and 8 MJ/kg does not significantly affect the drag reduction capabilities of the boundary layer combustion technique.

J.3 Tests at higher Mach numbers

J.3.1 Inlet & combustor pressure measurements

Figure J.5 shows the experimental pressure measurements taken on the bodyside of the REST inlet and combustor for the tests conducted at a Mach number of 7.4 and a stagnation enthalpy of 4.8 MJ/kg. The pressure measurements for tests conducted at the same stagnation enthalpy but lower Mach number are also shown in the plot.

In the inlet, it can be observed that the shock impinges further downstream on the bodyside surface for the tests conducted at a Mach number of 7.4. This is expected, since a higher Mach number produces a shock at a shallower angle. In the combustor,

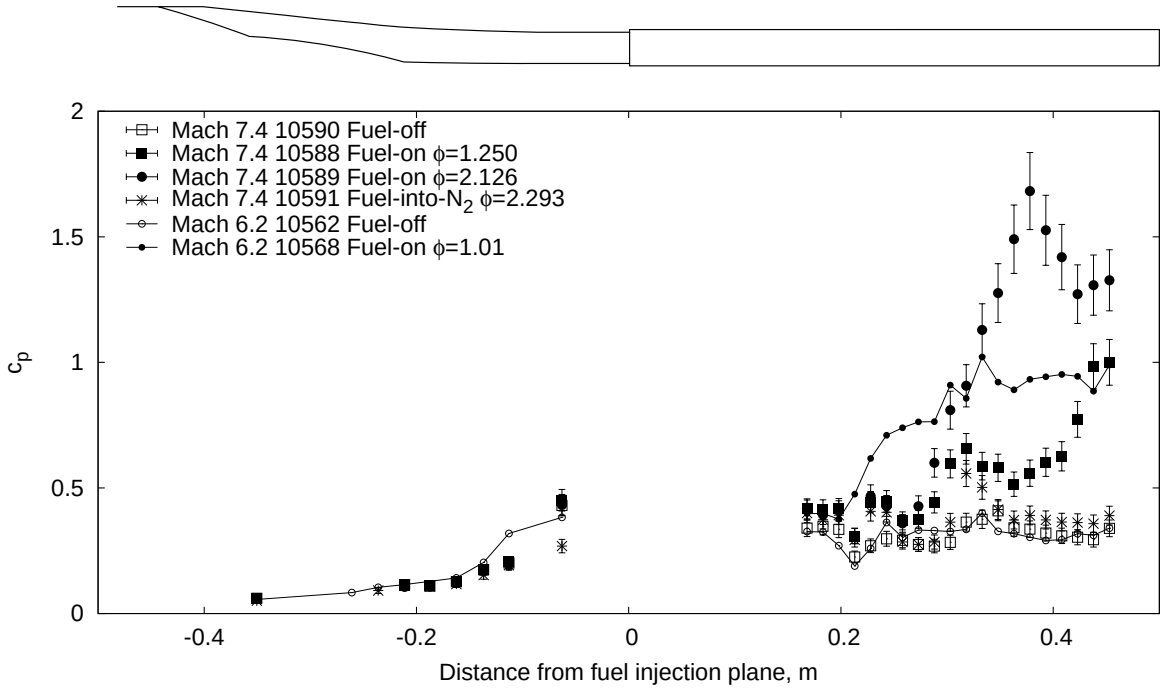

Figure J.5: Pressure coefficients in the inlet and combustor for H_s = 4.8 MJ/kg M = 7.4 condition.

the pressure levels at 0.22 m and 0.32 m from the fuel injection plane for the fuel-into-N_2 tests are higher than those for the fuel-off tests. These locations coincide with the shock impingement locations, hence suggesting that the boundary layer separates at these locations when fuel is injected. When fuel is injected at an equivalence ratio of 2.13 and allowed to burn, ignition occurs at about 0.25 m from the leading edge of the combustor. However, for an equivalence ratio of 1.25, the ignition location shifts downstream by more than 0.1 m. The ignition of the fuel-air mixture occurs about 0.15 m earlier for the tests conducted at lower Mach numbers with an equivalence ratio of 1. It is postulated that the later ignition of the fuel-air mixture for the tests conducted at a higher Mach number is brought about by the lower freestream temperatures entering the inlet and combustor.

J.3.2 Combustor drag measurements

Figure J.4 shows the experimental and theoretical values for skin friction drag coefficient for the tests conducted at a Mach number of 7.4 and a stagnation enthalpy of

4.8 MJ/kg. Also shown are the drag coefficients for tests conducted at the same stagnation enthalpy but lower Mach number.

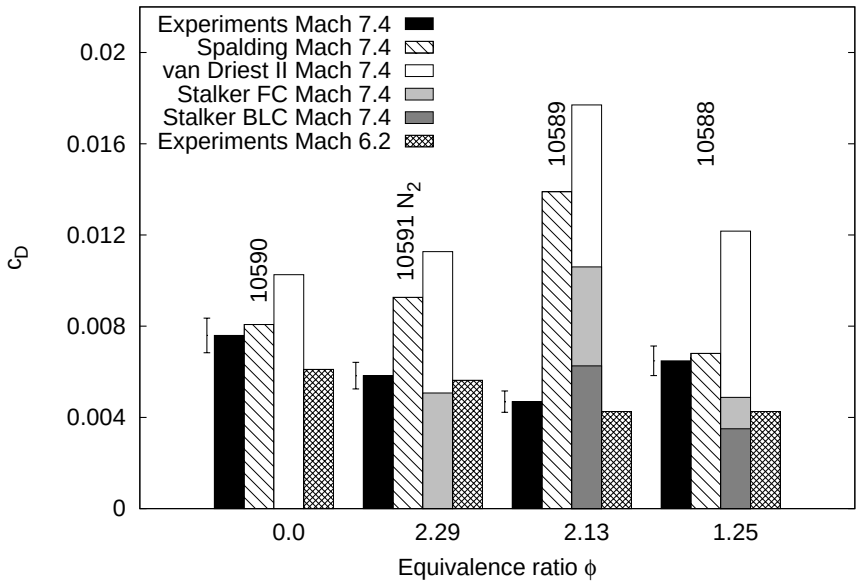

Figure J.6: Comparison of experimentally measured combustor drag coefficients for tests at the M = 7.4 condition condition with those predicted using skin friction theories and with those for tests at the M = 6.2 condition.

For the fuel-off test, the measured drag coefficient is overpredicted by the Spalding & Chi theory by 6% and by the van Driest II theory by 35%. Note also that the drag coefficient measured for the Mach 7.4 test is higher than that for the Mach 6.2 test. The flow through the inlet and combustor for the Mach 7.4 test develops differently in comparison with that for the Mach 6.2 test, which in turn causes a difference in the flow properties in the combustor. It is postulated that the difference in the flow properties causes the difference in the drag coefficients observed in the Mach 7.4 and Mach 6.2 tests.

For the fuel-into-N_2 test, the measured drag coefficient is lower than that of the fuel-off test by 23% when fuel is injected at an equivalence ratio of 2.3.

For the fuel-on test, the measured drag coefficient is 15% lower than that measured in the fuel-off test for an equivalence ratio of 1.25 and by 38% for an equivalence ratio of 2.13. For an equivalence ratio of about 1, the levels of drag reduction observed in the Mach 7.4 tests are much lower than the 28% reduction observed in the Mach 6.2 tests. This is attributed to the later ignition of the fuel-air mixture for the Mach 7.4 tests than for the Mach 6.2 tests.